Anti-idiotype antibodies for biomedical applications

TECHNISCHE UNIVERSITÄT DARMSTADT

Vom Fachbereich Chemie
der Technischen Universität Darmstadt

zur Erlangung des Grades
Doctor rerum naturalium
(Dr. rer. nat.)

Dissertation

Von

Jan Habermann, M. Sc.

Erstgutacher: Prof. Dr. Harald Kolmar

Zweitgutacherin: Prof. Dr. Evelyn Ullrich

Darmstadt 2023

Habermann, Jan: Anti-idiotype antibodies for biomedical applications
Darmstadt, Technische Universität Darmstadt,
Jahr der Veröffentlichung der Dissertation auf TUprints: 2024
URN: urn:nbn:de:tuda-tuprints-265409
URL: https://tuprints.ulb.tu-darmstadt.de/id/eprint/26540

Tag der Einreichung: 02. November 2023
Tag der mündlichen Prüfung: 15. Dezember 2023

Die vorliegende Arbeit wurde unter der Leitung von Herrn Prof. Dr. Harald Kolmar am Clemens-Schöpf-Institut für Organische Chemie und Biochemie der Technischen Universität Darmstadt im Zeitraum vom 15.09.2018 bis 31.07.2022 angefertigt.

Publications to related projects

Hinz SC, Elter A, Grzeschik J, **Habermann J**, Becker B, Kolmar H. (2021) Simplifying the Detection of Surface Presentation Levels in Yeast Surface Display by Intracellular tGFP Expression. Methods Mol Biol. 2020;2070:211-222. doi: 10.1007/978-1-4939-9853-1_12. PMID: 31625098.

Liebich VJ, Avrutina O, **Habermann J**, Hillscher LM, Langhans M, Meckel T, Biesalski M, Kolmar H. (2021) Toward Fabrication of Bioactive Papers: Covalent Immobilization of Peptides and Proteins. Biomacromolecules. 2021 Jul 12;22(7):2954-2962. doi: 10.1021/acs.biomac.1c00354. Epub 2021 Jun 8. PMID: 34101458.

Ali A, Happel D, **Habermann J**, Schoenfeld K, Macarrón Palacios A, Bitsch S, Englert S, Schneider H, Avrutina O, Fabritz S, Kolmar H. (2022) Sactipeptide Engineering by Probing the Substrate Tolerance of a Thioether-Bond-Forming Sactisynthase. Angew Chem Int Ed Engl. 2022 Sep 1. doi: 10.1002/anie.202210883. Epub ahead of print. PMID: 36049110.

Schoenfeld K, Harwardt J, **Habermann J**, Elter A and Kolmar H (2023) Conditional activation of an anti-IgM antibody-drug conjugate for precise B cell lymphoma targeting. Front. Immunol. 14:1258700. doi: 10.3389/fimmu.2023.1258700

Patents related to this work

Ullrich E, Wendel P, Wels W, Oberoi P, Kolmar H, Maccarón Palacios A, **Habermann J**, Schoenfeld K Personalized vNAR-based chimeric antigen receptors (vNAR-CAR) for the treatment of clonal B-and T cell malignancies, and methods for producing vNAR-CARs (2021) EP4141028A1 (Pending)

Contributions to Conferences

Poster

Habermann J, Grzeschik J, Traxlmayr M and Kolmar H (2018) Generation of a semi-synthetic combined library towards novel biparatopic binders *Protein Engineering Summit Europe*, Lisabon, Portugal

Habermann J, Grzeschik J, Traxlmayr M and Kolmar H (2019) Shark-derived nanobodies for biomedical applications *1st Bonn Nanobody Symposium*, Bonn, Germany

Lecture

Poster pitch in the context of the poster session (2019) Shark-derived nanobodies for biomedical applications *1st Bonn Nanobody Symposium*, Bonn, Germany

15-minute, short lecture (2019) Shark-derived nanobodies for biomedical applications *1st Bonn Nanobody Symposium*, Bonn, Germany

Table of content

1 Abstract

1.1 Zusammenfassung

Therapeutische Antikörper sind aus der heutigen Medizin nicht mehr wegzudenken. Neben dem Einsatz von Antikörpern bei der Behandlung einer Vielzahl verschiedener Krankheiten ist die Krebsbehandlung der wichtigste Anwendungsbereich. Zugelassene Antikörper haben alle den Nachteil, dass sie gegen tumorbezogene Antigene wirken, welche auf Tumorzellen überexprimiert sind, aber ebenfalls auf der Oberfläche gesunder Zellen vorkommen können. Aus diesem Grund können bei der Behandlung mit Antikörpern schwere Nebenwirkungen auftreten. Um die Risiken von Nebenwirkungen zu verringern, wurden verschiedene Ansätze verfolgt, darunter bispezifische, immunmodulatorische, pH-abhängige und proteaseaktivierbare Antikörper. Diese proteaseaktivierbare Antikörper werden später durch tumorassoziierte Proteasen aktiviert, die im gesunden Gewebe nur schwach exprimiert werden. Zusätzlich ist eine Maskierungsdomäne erforderlich. Diese Maskierungsdomänen können entweder aus Domänen bestehen, welche die Interaktion zwischen Antikörper und Antigen durch sterische Hinderung beeinträchtigen oder aus maßgeschneiderten, auf Affinität basierenden Maskierungsdomänen.

In dieser Arbeit wurden verschiedene Ansätze verfolgt, um Maskierungsdomänen zu erhalten, welche von Haien abgeleiteten Einzeldomänenantikörpern (vNARs) und von Hühnern abgeleiteten *single chain variable fragments* (scFvs) basieren, die gegen verschiedene therapeutisch relevante Antikörper gerichtet sind. Im Falle der vNARs basierte ein Ansatz auf einem bestehenden vNAR, der gegen Matuzumab gerichtet ist und eine hemmende Wirkung auf die Matuzumab-EGFR-Interaktion zeigt. Das Einfügen von Histidinen in die CDR3 des vNAR führte zu einem pH-abhängigen Bindungsverhalten mit stark verminderter Affinität. Der Verlust der Affinität konnte weder durch einen SEED-basierten noch durch einen Fusionsansatz an die schwere oder leichte Kette überwunden werden. Die Maskierungseigenschaft ging in diesem Fall bei Fusion an die schwere oder leichte Kette mit Einbau einer Proteaseschnittstelle verloren.

Ein weiterer Teil dieses Projekts zielte auf die *de novo* Isolierung von pH-abhängigen vNARs ab, die gegen Rituximab (Anti-CD20-Antikörper) und 5F9 (Anti-CD47-Antikörper) gerichtet sind. Die Isolierung von pH-abhängigen vNARs war für beide Antikörper erfolgreich. Zwei gegen 5F9 gerichtete vNARs wurden isoliert, während vier gegen Rituximab gerichtete vNARs erhalten wurden, von denen einer weiter charakterisiert wurde. Sowohl die gegen 5F9 gerichteten vNAR als auch der eine untersuchte vNAR gegen Rituximab zeigten Maskierungseigenschaften in Co-Inkubationsexperimenten des jeweiligen Antikörpers mit der jeweiligen Zielzelllinie. Während die Maskierungseigenschaften des gegen 5F9 gerichteten vNAR bei Fusion an den Antikörper nicht mehr beobachtet werden konnten, zeigte der gegen Rituximab gerichtete vNAR in SEED- und Leichte-Ketten-Konstrukten Maskierungseffekte. Der vNAR wurde über mehrere MMP-9-spaltbare Linker an die leichte Kette von Rituximab fusioniert. Im Falle der SEED-Konstrukte wurde eine pH-abhängige Wiederherstellung der Bindung beobachtet, während die

Bindung der Leichte-Ketten-Fusionen nach MMP-9-Spaltung wiederhergestellt wurde. Im Falle einer weiteren untersuchten Leichte-Ketten-Fusion konnte der Maskierungseffekt im Leichte-Ketten-Konstrukt auf den Linker und nicht auf den vNAR selbst zurückgeführt werden.

Das dritte Projekt im Rahmen dieser Arbeit zielte auf die Isolierung von Anti-Idiotyp-ähnlichen vNARs ab, die gegen einen T-Zell-Rezeptor (TCR) gerichtet sind. Während des Isolationsprozesses wurden vier vNARs erhalten, aber nur einer zeigte eine spezifische TCR-Bindung, während die anderen Varianten eine Bindung an konstanten Domänen zeigten.

Das letzte Projekt im Rahmen dieser Arbeit zielte auf die Isolierung von anti-idiotypischen Hühnern scFvs aus einer Immunbibliothek ab, die auf der Immunisierung eines Huhns mit dem scFv des therapeutischen Antikörpers 6G11 (Anti-CD32b-Antikörper) basiert. Durch die Einbeziehung von CD32b in den Sortierungsprozess konnten scFvs isoliert werden, welche die Interaktion zwischen 6G11 und CD32b stören bzw. nicht stören. Die Fusion der scFvs aus dem Screening-Verfahren an die leichte Kette von 6G11 führte zu einer 2700-fachen Reduzierung der Bindung im Vergleich zum unmaskierten 6G11. Nach der Abspaltung des scFvs durch MMP-9 wurde die Bindung wiederhergestellt. Für eine weitere Wiederherstellung der Bindung war die teilweise Entfernung des scFv erforderlich.

1.2 Abstract

Therapeutic antibodies have become an indispensable part of today's medicine. In addition to the implementation of antibodies in the treatment of a variety of different diseases, the most important area of application is cancer treatment. Approved antibodies all share the disadvantage of addressing tumor related antigens, which are overexpressed on tumor cells, but can also be found on the surface of healthy cells. Due to this fact, severe side effects can occur during antibody treatment. In order to decrease the risks of side effects, several approaches have been pursued including bispecific, immunomodulatory, pH-dependent and protease activatable antibodies. They are later activated by tumor-associated proteases that are weakly expressed in healthy tissue. Additionally, a masking domain is required. These masking domains can either consist of bulky domains interfering with target by steric hinderance or tailor-made affinity-based masking domains.

In this work different approaches were pursued to obtain masking domains based on shark-derived single domain antibodies (vNARs) and chicken-derived single-chain fragment variables (scFvs) directed against different antibodies of therapeutic relevance. In case of the vNARs one approach was based on an existing vNAR directed against matuzumab, which displayed an inhibitory effect on the matuzumab-EGFR interaction. Histidine-doping of the CDR3 of the vNAR resulted in a pH-dependent binding behavior with strongly decreased affinity. The loss of affinity could be overcome neither using a SEED-based nor a heavy or light chain fusion approach.

Another part of this project was aimed at the *de novo* isolation of pH-dependent vNARs directed against rituximab (anti-CD20 antibody) and 5F9 (anti-CD47 antibody). Isolation of pH-dependent vNARs was successful for both antibodies. Two vNARs directed against 5F9 were isolated, while four vNARs directed against rituximab were obtained; one of which has been further characterized. Both vNARs directed against 5F9 and the one analyzed vNAR against rituximab exhibited masking properties in co-incubation experiments of the respective antibody with the respective target cell line. While the masking properties of the vNAR directed against 5F9 could not be observed in any SEED or light chain construct, the vNAR directed against rituximab displayed masking effects in SEED and light chain constructs. The vNAR was fused to the light chain of rituximab *via* several MMP-9 cleavable linkers. In case of the SEED constructs pH-dependent restoration of binding was observed, while binding of light chain fusions was restored upon MMP-9 cleavage. In case of one further analyzed light chain fusion, the masking effect in the light chain construct could be attributed to the linker and not the vNAR itself.

The third project in this work was aimed at the isolation of anti-idiotype like vNARs directed against a T cell receptor (TCR). During the screening process, four vNARs were obtained, but only one revealed specific TCR binding, while the other variants displayed binding towards constant domains.

The last project in this work was aimed at the isolation of anti-idiotype chicken scFvs from an immune library based on the immunization of a chicken with the scFv of the therapeutic antibody 6G11 (anti-

CD32b antibody). By implementing CD32b into the screening process, scFvs interfering and non-interfering with the 6G11-CD32b interaction could be isolated. Fusion of the scFv obtained from the interfering screening approach resulted in 2700-fold reduction of binding compared to the unmasked 6G11. Upon MMP-9 cleavage, binding was restored, but partly removal of the scFv was required for further restoration of binding.

2 Introduction

2.1 Innate and adaptive immune system

The immune system represents a self-defense system developed by higher organisms, to antagonize pathogens such as microbes, viruses, fungi, and multi-cellular parasites. Distinction between foreign pathogens (non-self) and body cells (self) is of crucial importance (1). For this reason, several defense systems evolved, which are divided into the adaptive and innate immune system. The innate immune system recognizes pathogen-associated molecular patterns (PAMPs) *via* pattern recognition receptors (PRRs) (2). PRRs consist of various receptor subsets such as Toll-like receptors (TLR), NOD-like receptors (NLR), Rig-I-like receptors (RLR), and DNA receptors (3-6). This set of receptors is expressed on a variety of immune cells, among them dendritic cells (DCs), macrophages, natural killer (NK) cells, neutrophils, granulocytes, and mast cells (7-9). These cells can recruit other immune cells by secretion of chemo- and cytokines as well as detect and eliminate pathogens (10, 11). These processes are depended on the nature of the pathogen (12, 13). In the case of viruses major histocompatibility complex (MHC) class I is downregulated in infected cells (missing self), thereby preventing the recognition of viral peptides by cytotoxic T cells (14). The downregulation is identified and antagonized by NK cells due to more activating (NKG2D) than inhibitory signals (NKG2A) (**Figure 1A**) (13). Activated NK cells form an immunological synapse with the infected cell and release lytic granules, containing granzymes and perforin (15). Perforin is responsible to penetrate the cell membrane of the infected cell. Through the penetrated membrane, granzymes can enter the cell and induce apoptosis (16). At the same time, NK cells secret proinflammatory cytokines such as interferon gamma (IFN-γ) and macrophage inflammatory protein-1 alpha (MIP-1 α) for macrophage recruitment (17). Macrophages are responsible for neutralizing remaining infectious agents by phagocytosis, which in general is a major pathway to eliminate pathogens. For this reason, macrophages and dendritic cells exhibit a broad range of receptors to eliminate pathogens without requiring cell-mediated activation signals (18). Although these receptors and cells cover a wide range of PAMPs, some pathogens evolved escape mechanisms. For this reason, cells of the innate immune system can secrete chemo- and cytokines such as members of the interleukin 1 (IL-1) family and type I interferons to activate cells of the adaptive immune system (19).

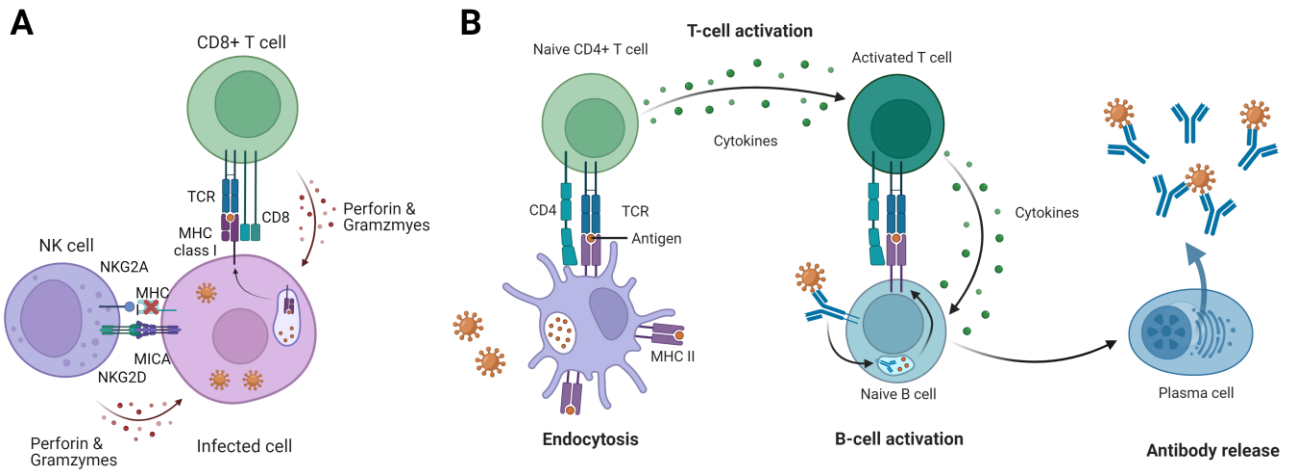

Figure 1: Innate and adaptive immune system. A) Elimination of virus-infected cell by a $CD8^+$ T cell and NK cell. The infection is recognized by either presentation of virus peptides *via* MHC I or missing MHC I due to downregulation by the virus. In both cases, immunological synapses form, and perforin and granzymes are released by the $CD8^+$ T or NK cell. **B)** Generation of antibodies by the adaptive immune system. Uptake and processing of pathogens by dendritic cells leads to the presentation of peptides *via* MHC II. Interaction of naive $CD4^+$ T cells with loaded MHC II leads to activation of the T cell and subsequent activation of naïve B cells. Activated B cells differentiate into plasma cells. Created with BioRender.com.

In contrast to the innate immune system, the adaptive immune system is able to react specifically towards foreign antigens. These antigens can be recognized by the B and T cell receptor (BCR/TCR) of B and T lymphocytes, respectively (20). T lymphocytes provide cell-mediated immunity. Therefore, T cells interact *via* their TCR with peptide loaded MHC class I, which is present on all nucleated cells. MHC class I presents proteolytically degraded peptides originating from cytosolic proteins. In case of a viral infection, peptides, originating from viral proteins, are presented on MHC class I and can be recognized by a T cell exhibiting a TCR specific for this viral peptide (21). The MHC-TCR interaction is stabilized by CD8 on $CD8^+$ cytotoxic T cells, which in turn eliminate the infected cell (**Figure 1A**) (22, 23). In contrast, $CD4^+$ T helper cell (T_H) specifically recognize MHC class II, expressed by antigen-presenting cells (APCs), such as macrophages and dendritic cells (24). By doing so, APCs link the innate and adaptive immune system (**Figure 1B**) (25). This interaction in combination with CD4 as a co-receptor leads to the formation of an immunological synapse (26). Thereby the T cell is primed and expression of various cytokines, like interleukin 2 (IL-2), interferon (IFN)-γ, and tumor necrosis factor (TNF)-β, leads to proliferation and differentiation of the T cell (27). Differentiation of T_H cells leads to different T_H subpopulations such as T_H1, T_H2, T_H9 and many others. The difference in the T_H populations lies within the cytokine expression profile. These expression profiles are very diverse and result in a variety of functions, such as response to extracellular parasites and activation of B cells (28). Activation by IL-5, which is secreted by T_H2 cells, leads to B cell proliferation and activation (29). Activated B cells secrete antibodies which represent the non-cell mediated humoral immune response. Furthermore, antibodies are secreted by differentiated B cells, so called plasma cells (**Figure 1B**), while immature B cells express membrane-bound IgM and IgD antibody isotypes as BCR. Upon antigen binding, the BCR antigen

complex is internalized, processed, and presented on MHC class II on the cell surface (30). TCRs of primed $CD4^+$ T cells towards the antigen, recognizing the peptides on the B cell surface *via* MHC class II and activate the B cell by subsequent cytokine secretion (31). Upon activation, proliferation, and differentiation, B cells transform into plasma cells. These plasma cells secret mono- or hexameric, but mainly pentameric IgM, consisting of either one, six or five IgMs. Conventionally, IgMs exhibit low affinity to its antigen, which is compensated by increased avidity (32). Furthermore, somatic hypermutation and recombination of the BCR DNA sequence takes place, to enhance affinity and facilitate the isotype switch to the IgG isotype (33). Further stimulation with the antigen results in further differentiation into B memory cells. These cells remain in the bloodstream or peripheral tissue and can be reactivated by a new exposure to the original antigen. In this case, proliferation and differentiation to plasma cells takes place and high affine and specific antibodies are secreted once more (34).

2.2 The structure and function of antibodies

Antibodies play an important role in the immune system, by connecting the high specificity of the adaptive immune system, with the outstanding pathogen removal system of the innate immune system. The removal of pathogens is carried out by mechanisms like antibody-dependent cytotoxicity (ADCC), complement-dependent cytotoxicity (CDC), and antibody-dependent cell-mediated phagocytosis (ADCP) (35-37). This variety of effector functions is covered by different antibody isotypes: IgA, IgD, IgE, IgG, and IgM (**Figure 2E**). The IgA isotype plays a major role in the immune response in mucous membranes (38). IgD antibodies are associated with the BCR of immature B cells. IgE plays a major role in allergic disease and protection from multi-cellular parasites (39). IgM is the first secreted antibody after antigen exposure (32). IgG is the most common isotype in the blood, which can make up to 20% of plasma proteins. The IgG class is further divided into four different subclasses: IgG1, IgG2, IgG3 and IgG4. The most common subtype is IgG1 with a half-life time of 21 days. Like IgG1, the IgG3 subtype is associated with an immune response towards soluble peptides and proteins. On the other hand, the IgG2 subtype is associated with an immune response towards polysaccharide antigens. The IgG4 subtype is produced after long-term exposure towards non-infectious antigens, such as allergens. All isotypes share the same Y shape, comprising of two light and two heavy chains (**Figure 2A**) (40). While IgD, IgE, and IgG reveal a bivalent structure, IgA and IgM show multi-valency (**Figure 2E**). IgA forms a dimer, while IgM exhibits a pentameric structure (32, 38). This multimerization is accomplished by linking the heavy chains of two or more antibodies *via* a peptide referred to as J chain. The structure of heavy chains consists of one variable domain (V_H), in the case of IgA, IgD, and IgG of three constant domains (C_H1-C_H3) and in the case of IgE and IgM of four constant domains (C_H1-C_H4). In contrast, light chains only consist of one variable domain (V_L) and one constant domain (C_L), which can be further divided into the

kappa and lambda subtype. The four chains of the antibody are connected *via* hydrophobic and electrostatic interactions and covalently coupled *via* disulfide bonds. These disulfide bonds between heavy and light chain are located at the C_L and C_H1 region. Additionally, the two heavy chains are connected within the flexible hinge region between C_H1 and C_H2 (41). Several protease cleavage sites such as for papain are located within this flexible region. By cleavage with these enzymes, two identical fragments of antigen binding (Fab) and one fragment crystallizable (Fc) are formed (42). While the Fc part is responsible for the effector function, the Fab part is responsible for antigen binding (41). This specific interaction is mediated by non-covalent interactions of six complementary determining regions (CDRs) (**Figure 2D**) (43). For this reason, CDRs reveal high structural and sequence diversity. Both V_L and V_H contain three CDRs each (CDR1-CDR3) (**Figure 2C**) (44). The six CDRs of one Fab form the so called a paratope and due to the two identical paratopes within one antibody molecule, antigen recognition is often driven by avidity. This avidity effect elevates the recruitment of immune cells by the Fc part. The Fc part of an antibody is responsible for the effector function and based on the isotype and the immune cell with which the antibody interacts, these effector functions can differ significantly (40). Among the most conventional effector functions are ADCC, CDC and ADCP (35-37). To facilitate this variety of effector functions, several receptors are required. Binding to IgA is carried out by FcαRI, binding towards IgE is facilitated by FcεRI, FcεRII and binding to IgG is enabled by FcγRI, FcγRIIa, FcγRIIb, FcγRIIc, FcγRIIIa, FcγRIIIb and FcRn (45, 46). While the other Fc receptors reveal effector function, FcRn is responsible for the recycling and thereby half-life extension of antibodies of the IgG isotype, which were internalized by pinocytosis. Upon internalization and transportation to the acidic environment of the early endosome, FcRn binds to the Fc and the complex is recycled to the cell surface, where the antibody is released under neutral conditions (47). Binding of Fc receptors takes place at the C_H3 domain in the case of IgE, while the other antibodies are bound in the C_H2 domain. Furthermore, glycosylation of Asn297 within the C_H2 domain plays a crucial role in protein stabilization, half-life extend, and effector function. The C_H2 domain is responsible for ADCC, CDC, and ADCP (48). ADCP and ADCC represent cell-mediated immune responses (37). ADCC is carried out by NK cells *via* crosslinking of FcγRIIIa (CD16) and subsequent secretion of perforin and granzymes. ADCP on the other hand leads to the engulfment of IgG-opsonized pathogens, due to the clustering of FcγRIIa. FcγRs clustering is not required for CDC. Upon binding of an antibody, C1q is recruited, the complement cascade is initialized, and a membrane attack complex is formed (49).

In order to obtain TCRs and BCRs addressing virtually every given antigen, high diversities of both receptors are required. Since the potential BCR repertoire is reported to be in the range of 10^{14} but the human genome only consists of about 20.000 genes, a special mechanism is required to archive this diversity. The genes for antibodies are encoded in different segments: variable (V), joining (J), diversity (D), and constant (C). The process of V(D)J recombination takes place in the early B cell development

and generates the native BCR (**Figure 2F**). Thereby, one variable segment is combined with a joining segment and in case of the heavy chain a diversity segment, before combination with the constant segment. This RAG1 and RAG2-mediated process leads to a diversity of about 10^6 different variants. To further expand the repertoire, nucleotides are added or removed during the recombination process by enzymes like terminal desoxyribonucleotidyl transferase (TdT) and Artemis nuclease, leading to a diversity of up to 10^{14} (50). After antigen challenge and activation by $CD4^+$ T cells, B cells undergo somatic hypermutation, caused by activation-induced cytidine deaminase (AID) to increase the affinity of the antibody. In this process, mutations are introduced into the CDRs of the antibody *via* cytosine deamination and subsequent replication of the arising uracil as thymidine or by the combination of mismatch repair and error-prone polymerases (51). Furthermore, AID assists in the class switch from IgM to IgG isotypes (52).

Each domain of an antibody exhibits the Ig fold, which is also found in the TCR and MHC molecules. Depending on the C or V-like Ig domain, the structure consists of 7-9 anti-parallel beta sheets (**Figure 2B**). Four beta sheets form the core of the Ig domain, two of these beta sheets are connected *via* a disulfide bond. The core is surrounded by three to five additional beta sheets (53). While the constant domains of an antibody are built by seven beta sheets, the variable domains consist of 9 beta sheets. Located within the variable domains are four frameworks regions and three CDRs (54).

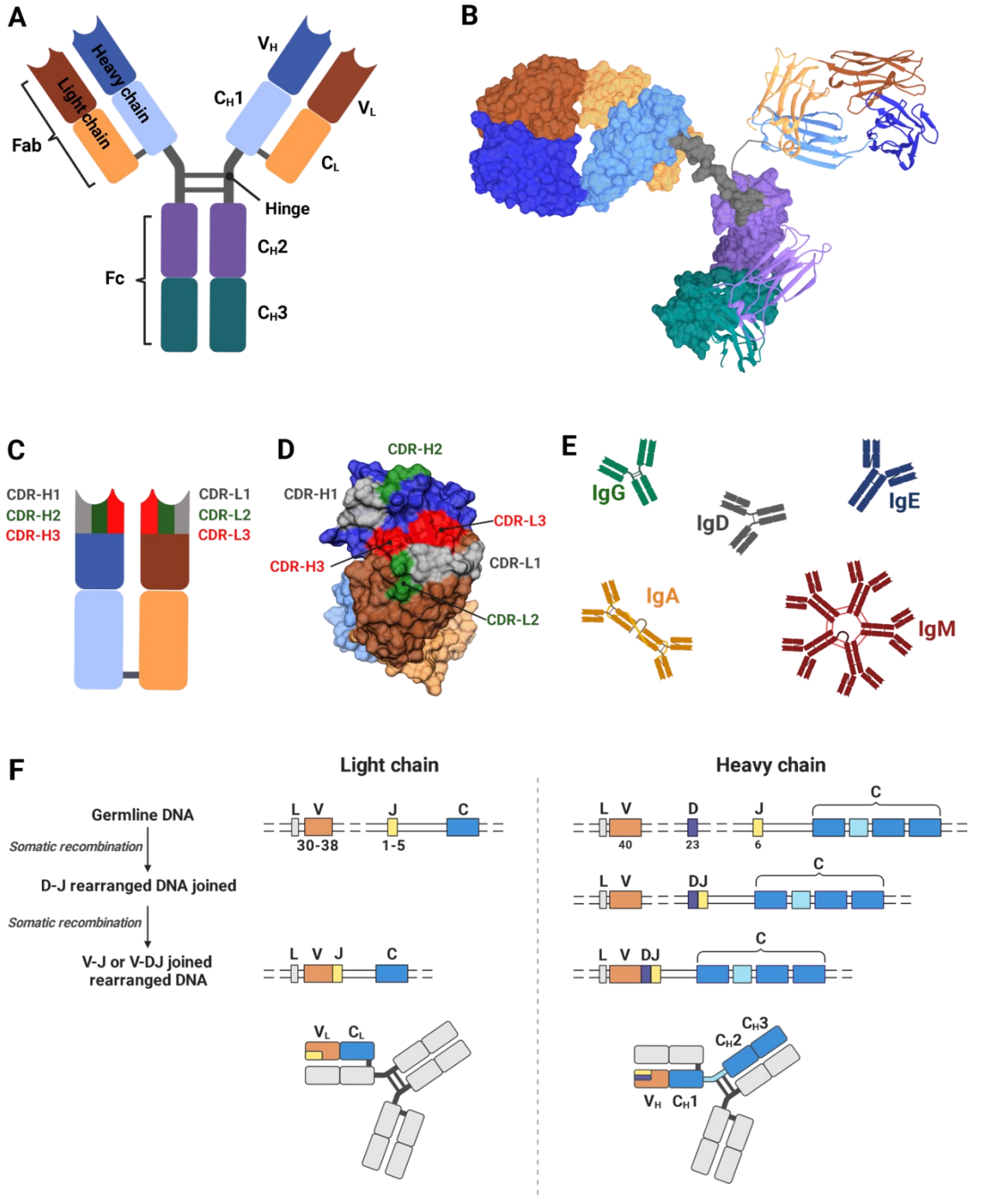

Figure 2: Antibody structure and diversification. A) Schematic overview of an IgG antibody. The heavy chain comprises of one variable domain (V_H, dark blue) and three constant domains C_H1–C_H3 (light blue, purple, and dark green). The light chain is formed by one variable domain (V_L, brown) and one constant domain (C_L, light brown). **B)** Structural overview of an IgG antibody as ribbon and surface model (PDB: 1IGT). The color code is identical to the schematic overview. **C)** Schematic overview of a Fab fragment. The CDR1–CDR3 of the V_H and V_L are shown in grey, green, and red respectively. **D)** Surface model of a Fab fragment with highlighted CDRs of V_H and V_L (PDB: 1IGT). The color code is identical to the schematic overview. **E)** Schematic overview of different Ig isotypes. IgA, IgD, IgE, IgG, and IgM are shown in yellow, grey, blue, green, and red respectively. **F)** V(D)J recombination process for diversification of heavy and light chain variable domains. Somatic recombination of germline DNA and V- J rearrangement leads to a functional light chain gene. In case of the heavy chain, an additional D- J rearrangement is required to form a functional heavy chain gene. Created with BioRender.com.

2.3 Antibody structure and generation in chickens

Besides the above-mentioned human antibody isotypes, different species developed their own unique isotypes (40, 55, 56). While humans exhibit a wide range of subtypes (IgA, IgD, IgE, IgG, and IgM), earlier-evolved species tend to a narrower spectrum of isotypes. Birds evolved about 150 million years prior to humans and reveal only three antibody isotypes: IgA, IgM, and IgY (56). The name IgY originates from egg yolk, where up to 50-100 mg of IgY can be found. IgY antibodies share functional similarity to mammalian IgG while sharing structural similarity to mammalian IgE (56). The heavy chain of IgY consists of five constant domains, with a shortened hinge region, leading to less flexibility (**Figure 3A**) (57). The heavy chain is connected *via* three inter-heavy chain disulfide bonds, two within the C_H2 domain and one in the C_H3 (58). Interestingly, avians reveal only a λ constant light chain domain, while the κ isotype is absent (59). Furthermore, the CDR1 of the light chain tends to be shorter than its mammalian counterpart, whereas the CDR3 of the heavy chain tends to be longer (60). Found within the CDRs of the V_H, is an increased number of cysteines, forming intra- and inter-CDR disulfide bonds (**Figure 3C**). Based on the number and connection of the disulfate bonds, six different types can be distinguished. Type 1 reveals a single inter CDR3 disulfide bond, while type 2 reveals no additional disulfide bonds. IgYs of type 3 contain an inter CDR1 to CDR3 disulfide bond. Type 4 is subdivided into classes a and b. While both subtypes reveal an inter CDR2 to CDR3 disulfide bond, the CDR2 cysteine in type a is located at position 55, while at position 58 in type b. Type 5 is defined by two disulfide bonds, one between CDR1 and CDR3, while the other forms within the CDR3. Subtype 6 exhibits two intra-CDR3 disulfide bonds. Due to these additional disulfide bonds, it is speculated, that this stabilizing factor contributes to the high thermal stability of avian antibodies (60).

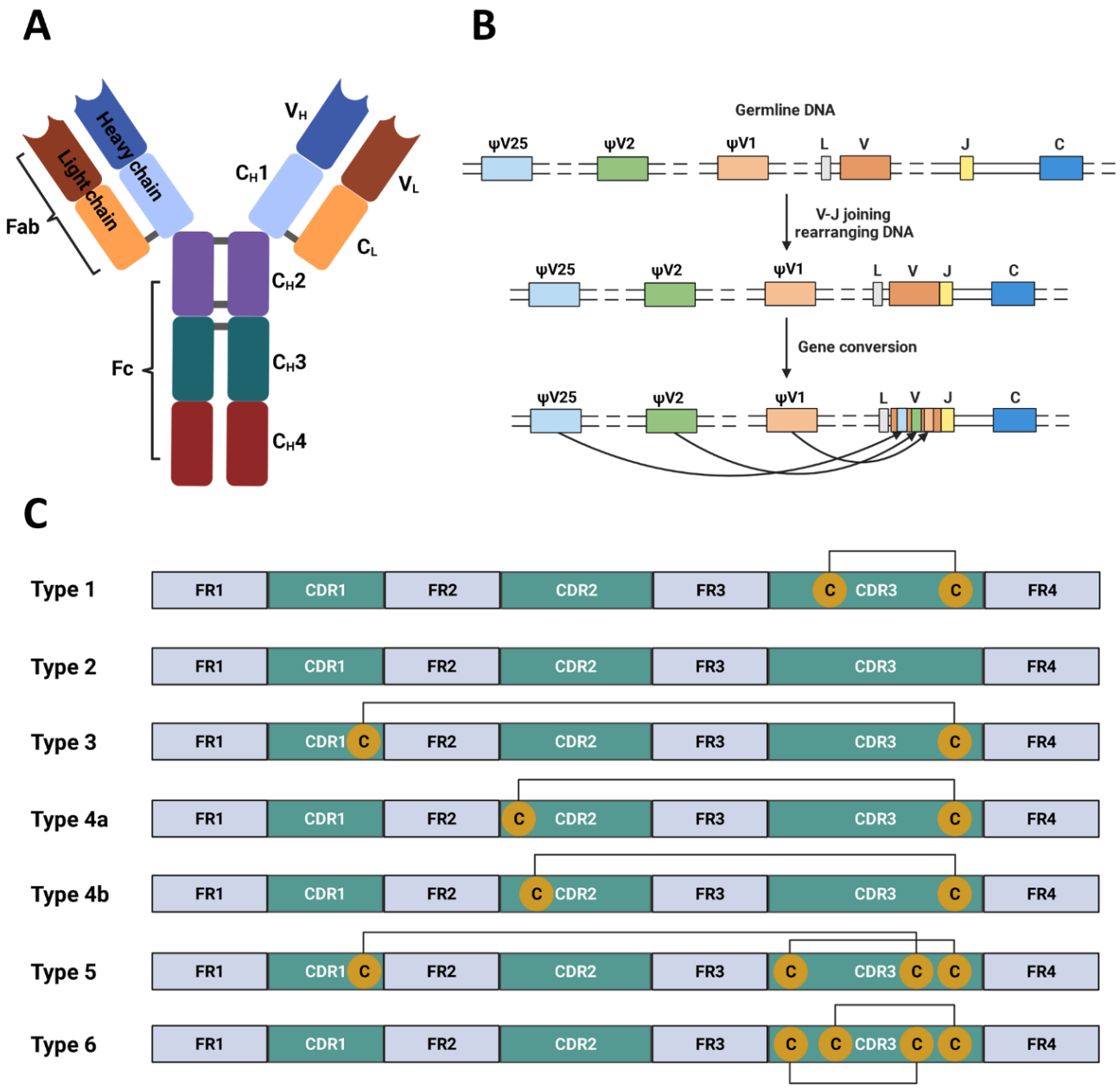

Figure 3: Chicken antibody structure and genetics. A) Schematic overview of an IgY antibody. The heavy chain is formed by one variable domain (dark blue) and four constant domains (light blue, purple, dark green, and red). The light chain comprises of one variable domain (brown) and one constant lambda domain (light brown) **B)** Overview of the genetic generation of a chicken light chain. In the first step, V- J rearrangement takes place, while subsequent homologous gene conversion is responsible to generate diversification. **C)** Different subtypes of chicken antibodies. Inter- and Intra-CDR disulfide bonds are indicated with black lines between cysteines. Subtype 1 reveals an inter-CDR3 disulfide bond, while type 2 shows no disulfide bond. Type 3 and 4 reveal an inter-CDR disulfide bind between CDR3 and CDR1 or CDR2 respectively. Type 5 shows one inter-CDR disulfide bond between CDR1 and CDR3, as well as one intra- CDR3 disulfide bond. Subtype 6 is characterized by two intra-CDR3 disulfide bonds. Created with BioRender.com.

In contrast, to the highly efficient V(D)J recombination events observed in mammalians, this process yields low diversity in avian species, due to the presence of only one functional germline-encoded V and J segment. The main mechanism to generate further diversity relies on homologous gene conversion (**Figure 3B**). In this process, the transfer of a pseudogene into the germline segment is carried out.

Repeated transfer leads to the diversification of the V segment (42, 58, 61). Overall, up to 100 heavy and 25 light chain pseudogenes are present in the avian genome (61). With V(D)J recombination as well as taking heavy and light chain pairing into consideration, diversities of up to 3 x 10^9 variants are possible.

Due to the high evolutional distance between humans and chickens, immunization with human proteins can result in a higher diversity of targeted epitopes compared to closer related species (62). Furthermore, conserved framework regions (FR) 1 and 4, enables unbiased amplification of V_H and V_L genes with one primer set (42). Different screening and display methods can be utilized to isolate high affine binders from chicken-based antibody libraries (63, 64). After selecting antibodies with favorable properties for clinical application, humanization is required to address immunogenicity issues. This can be addressed either by classical humanization approaches or recently genetically modified chickens, containing the human Ig genes (65, 66). Overall, chicken-derived antibodies reveal promising features for medical and diagnostic usage.

2.4 The IgNAR antibody derived from sharks

Cartilaginous fish are among the oldest species present on the planet. Even though their long existence, their immune system remained rather simple. In contrast to higher vertebrates, the generation of antibody diversity relies on several preexisting VH-DH-JH-CH and VL-JL-CL clusters and their subsequent RAG-mediated rearrangement within different clusters (67). This process results in three different antibody isotypes: IgM, IgW, and IgNAR (68). IgM is the most common antibody type in the blood of sharks and can be found either in monomeric or pentameric forms (69, 70). The function of the IgW isotype remains unclear, but due to the expression of up to six different heavy chain isoforms with different numbers of constant domains, recruitment of different immune cells seems likely (69, 71). The third antibody isotype immunoglobin new antigen receptor (IgNAR), consists of a heavy chain only homodimer, without a light chain (72). Furthermore, the heavy chain comprises of one variable (vNAR) and five constant domains (C1-5) (**Figure 4A**) (73). The variable domain is connected to C1 *via* a hinge-like region. Furthermore, a wide dimerization angle of C1 results in high flexibility (73). Additionally, the constant domains C1 and C3 are responsible for dimerization, while C2 and C4 reveal high resistance to chemical and thermal denaturation. Structural data of C5 are not available, since it is suspected that folding depends on additional factors (74).

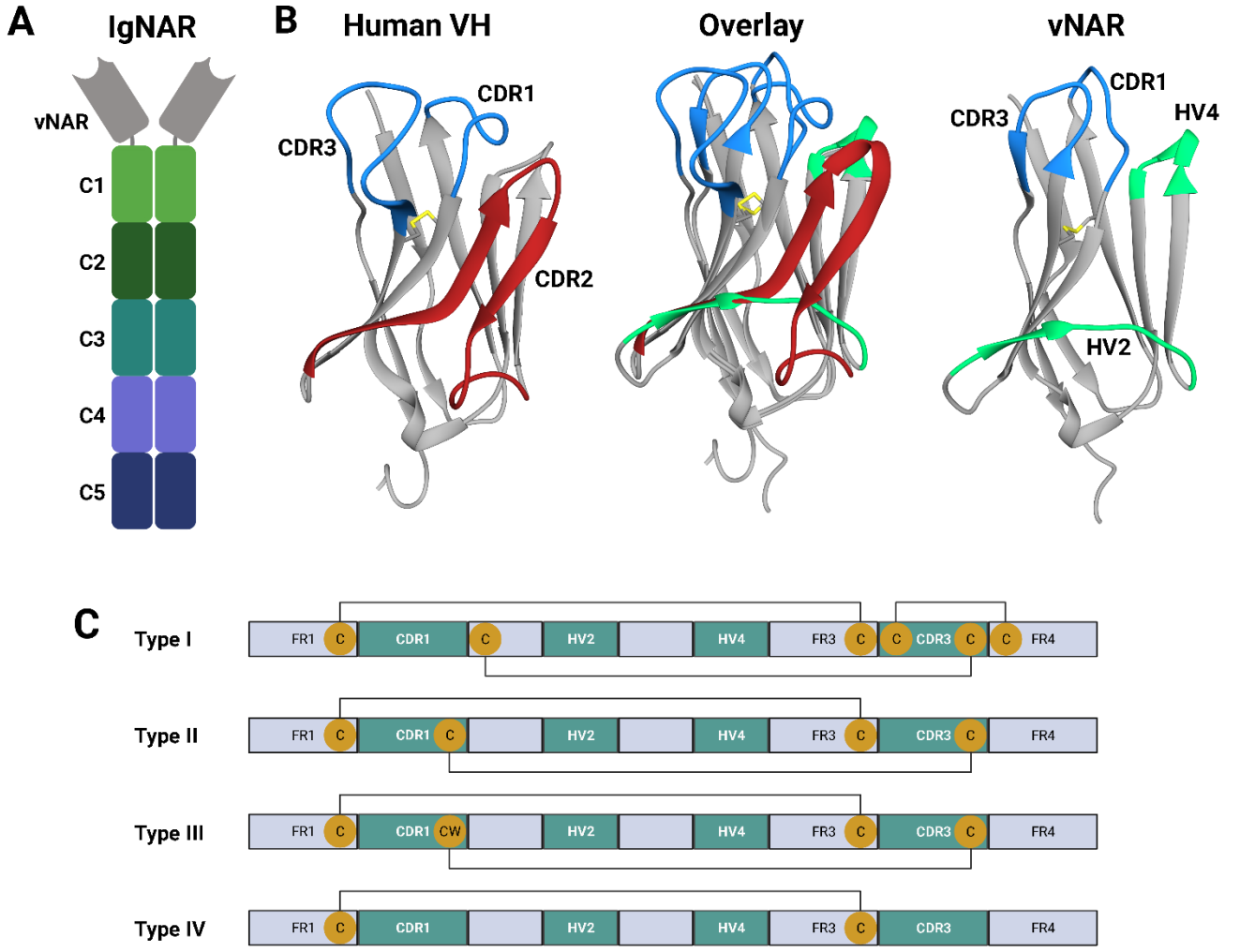

Figure 4: Schematic overview of the IgNAR antibody with a structural and genetic overview of the vNAR domain. A) Schematic overview of the IgNAR, with one variable domain (vNAR, grey) and five constant domains C1-C5 (light green, dark green, teal, light blue and dark blue). The IgNAR is classified as a heavy chain only antibody due to the lack of a light chain. **B)** Structural comparison (middle) between a human V_H (left, PDB: 7OBF) and a vNAR domain (right, PDB: 5L8L). The CDR1 and CDR3 of both proteins are colored in blue, while the framework (FR) 2 and CDR2 of the V_H are marked in red. The deletion of FR2 and the CDR2 in the vNAR results in a hypervariable loop (HV2, green). Furthermore, the vNAR reveals another hypervariable loop (HV4, green). Overall, the V_H and vNAR share large structural similarities. **C)** Overview vNAR subtypes, disulfide bonds are indicated with a black line. All vNAR subtypes reveal one canonical disulfide bond (not shown). vNAR type I shows a disulfide bond between FR2 and CDR3, as well as one inter-CDR3 disulfide bond. vNARs of type II reveal one inter-CDR1 to CDR3 disulfide bond. Type III vNARs reveal an inter-CDR1 to CDR3 disulfide bond with a conserved tryptophan within the CDR1. vNARs of type IV reveal no additional disulfide bonds. Adapted from Zielonka *et al.* (73) Created with BioRender.com.

With a molecular weight of 12 kDa, vNARs are the smallest antibody-like domains reported to date. vNARs reveal high physicochemical stability, due to the presence of up to 350 mM urea in cartilaginous fish (75). The vNAR domain reveals an Ig like structure, with the characteristic canonical disulfide bond (76). In contrast to other V_H domains, the vNAR is formed by only 8 instead of 10 beta sheets (74). The missing part in the vNAR corresponds to the CDR2 and FR2 regions (77). Connecting the remaining FR2 with the FR3 and thereby wrapping around the bottom of the vNAR is a hypervariable loop (HV4) (**Figure 4B**). Further, a hypervariable loop (HV2) and CDRs 1 and 3 are located near the N-terminus of the vNAR (78). HV2, HV4 offer additional diversity. Both regions, as well as CDR1 and CDR3 are mutated

during affinity maturation (77). The elongated CDR3 is mediating a major part of the binding and is typically 8 to 12 residues in length but can comprise up to 34 amino acids (79). Due to this elongated CDR3, vNARs can access cryptic and hidden epitopes. Furthermore, vNARs can be subdivided into four different types, based on additional non-canonical disulfide bonds (**Figure 4C**) (73). Type I is characterized by two additional disulfide bonds between FR2 and CDR3, as well as FR4 and CDR3, therefore locking CDR3 in close proximity to HV2. In type II vNARs, CDR1 and CDR3 are connected *via* an additional intra-CDR disulfide bond, forming a finger-like structure, able to access pockets, like active sites of enzymes (80). Type III vNARs reveal the same intra-CDR disulfide bond as in type II. However, very low sequence diversity, both in length and amino acid composition, is observed in CDR3, while CDR1 exhibits a conserved tryptophan residue. Furthermore, this type is highly expressed in neonates and therefore speculated to direct an immune response towards a common pathogen (81). Type IV vNARs reveal no additional non-canonical disulfide bonds. Therefore, the CDR3 reveals higher flexibility since no restrictions due to disulfide bonds occur (82). Overall, it is reported, that all vNAR types, except type III, can result in high affine binders (73). To obtain high affine binders, different approaches are suitable. Besides classic immunization, approaches using semi-synthetic and synthetic libraries resulted in high affine binders (83-85). Due to the high evolutionary distance between sharks and humans, immune tolerance is lower compared to closely related species. However, several cases of unsuccessful immunization are reported (73). Synthetic or semi-synthetic libraries often yield low-affine binders, which require affinity maturation. Affinity maturation can be carried out by error-prone PCR, CDR1 randomization, or low-fidelity RNA polymerases, resulting in subsequent screening and isolation of high-affine binders (86-88). Furthermore, by using synthetic and semi-synthetic libraries, further properties, such as histidine doping, can be integrated. The incorporation of histidine within the CDR3 and CDR1 can result in pH-dependent binders (89). Also, further randomization of HV4 or HV2 and subsequent screening towards another antigen is possible and can lead to bispecific binders (90). In all cases, the isolation of binders requires suitable display technologies. Besides phage display and ribosomal display, yeast surface display was used with great success in isolating high affine vNARs (86-88). vNARs against a variety of antigens were isolated. Besides cancer-related antigens, binders against toxins, cytokines, and viral antigens were isolated (88, 91, 92). Recently anti-idiotype vNARs directed against several therapeutic antibodies, as well as the BCR of a cancer cell line were isolated (84, 93). Furthermore, vNARs are used in diagnostic assays, due to their high physicochemical stability. Overall, vNARs represent a promising antibody scaffold.

2.5 Overview of different antibody formats

The field of antibodies represents a growing class of therapeutics. Since the approval of the first antibody, a variety of different antibody formats were developed. Based on the IgG format, bi- and trispecific antibodies were constructed. These antibodies consist of two or three different binding moieties. Therefore, different binding sites on one antigen or two different antigens can be implemented. This implementation is realized by using the knob-into-hole, SEED, charge to charge swap, or charge to steric complementarity swap technologies (94-96). These technologies enable the generation of heavy chain heterodimers each carrying a different binding moiety. If these formats comprise two or more Fab fragments, the issue of light chain mispairing arises with consequential lower expression yields of the desired bispecific antibody, due to the presence of the other possible heterodimers (97). To improve yields and simplify production, constant domain exchange and common light chain technologies were developed (98, 99). Based on the implemented binding moieties, immune cells can be directed to tumor cells, different tumor growth-promoting pathways can be blocked and higher binding specificity can be achieved (100). These highly engineered proteins can reveal several drawbacks, such as low expression yield, protein instability, and immunogenicity (100, 101). Furthermore, multispecific, large-sized molecules reveal long half-life, but a low tumor penetration (101, 102). For this reason, a variety of different antibody formats were developed. Besides Fab fragments, single chain variable fragments (scFvs) and the variable domain of camillid heavy chain only antibodies (V_HH) formats play a major role in cancer treatment and diagnostics (103-105). While these smaller fragments reveal high tumor penetration, short *in vivo* half-lives are observed (106, 107). To address this issue, several approaches were developed such as PEGylation, PASylation, and fusion of albumin binding motives (106, 108, 109). Furthermore, these smaller binding moieties are utilized to generate multi-specific binding molecules (110). One example is blinatumomab, a clinically approved bispecific T-cell engager (BiTE) consisting of two scFvs binding to CD3 and CD19 (111). The two scFvs of blinatumomab bring T cells in contact with CD19 expressing B cells and enable the elimination of malignant B cells.

Apart from antibodies using their natural binding and effector function, antibodies fused to highly potent cytotoxic payloads were generated to eliminate cancer cells. These antibody-drug conjugated (ADCs) combine the specificity and stability of an antibody with the high antitumor potency of cytotoxic drugs (112).

2.6 Antibodies and antigens classes in cancer treatment

In the past decades, monoclonal antibodies gained increasing importance in cancer therapy and are now used alongside and in combination with radiation, surgery, and chemotherapy (113). Research in cancer treatment with antibodies began with the development of the hybridoma technology (114). First antitumor effects caused by antibodies were discovered using rodent antibodies (115). These early therapeutic antibodies revealed several drawbacks in humans. Besides poor recruitment of human immune cells, these antibodies lead to anti-drug-antibodies (ADAs) (115, 116). ADAs neutralize the therapeutic antibody and rapid clearance occurs. To address and overcome immunogenicity issues, chimeric antibodies were developed, using only rodent V_H and V_L, while retaining fully human constant domains (117). Usage of human constant domains resulted in 70% human sequence, subsequent restoration of effector function, and reduction of immunogenicity (118, 119). The first approved chimeric antibody was rituximab (anti-CD20) in 1997 and up to now still remains as gold-standard in non-Hodgkin lymphoma treatment (120). However, recent studies report ADAs against rituximab during multiple sclerosis treatment, leading to incomplete B cell depletion (121). To further decrease the probability of ADAs formation, humanization of antibodies was developed (122). This technology is based on CDR grafting of a donor antibody to a fully human framework. Using this technology human sequence identity of up to 90% can be achieved (123). The first approved humanized antibody was daclizumab (anti-CD25) in 1997 (124). To obtain fully human antibodies, several strategies can be implemented. Besides screening naïve human libraries, immunization of transgenic animals carrying the human antibody repertoire represent sources for fully human antibodies (65, 125, 126). The first fully human antibody adalimumab (anti-tumor necrosis factor α) was approved in 2002. Even though massive efforts were undertaken to optimize the humanization process of antibody candidates, ADA formation is reported even in chimeric, humanized and even fully human antibodies (122, 127).

Besides reducing the immunogenicity of antibodies and increasing effector function, antibodies with immune modulating abilities were developed. These antibodies target immune checkpoint inhibitors such as CTLA-4, PD-L1, and PD-1 (128). PD-1 is present on the surface of NK, B as well as T cells and is involved in immune response down-regulation and is overexpressed in different malignancies such as lung, gastric and bladder cancer (129). In contrast, CTLA-4 expression is restricted to T cells and is involved in the early T cell activation (130). By blocking the inhibitory signaling of these immune checkpoint inhibitors, T cell mediated anti-tumor effects could be restored and have led to outstanding response rates for several antibodies (131). Important antibodies in the field of immune checkpoint inhibitors are ipilimumab (anti-CTLA-4), pembrolizumab (anti-PD-1) and atezolizumab (anti-PD-L1) (128, 132, 133).

Antibody drug conjugates (ADCs) are characterized by an antibody conjugated to a cytotoxic payload. These payloads range from radioisotopes (RACs), the fusion of cytotoxic proteins (immunotoxins) and

chemotherapeutic drugs (ADCs). ADCs comprise of three different parts, a cytotoxic payload, a covalent linker, and an antibody (134). While the antibody is responsible for drug delivery and internalization, the linker needs to release the drug specifically in the tumor cell and the drug is responsible for killing the tumor cell. Therefore, a variety of linkers and drugs were developed (135). Major challenges in this field are hydrophobicity of the drug and specific, selective and homogeneity of drug attachment (112). Conjugation methods include covalent linkage to lysine or cysteine residues as well as conjugation by enzyme and tag systems (136-138). Overall, about 80 different ADCs are in clinical development, while 12 are approved by the Food and Drug Administration (FDA). The disease indications of the approved ADCs range from breast cancer over gastric and cervical to large B cell lymphoma. Furthermore, applications in non-oncological indications, such as diabetes, cardiovascular and autoimmune disease are investigated (139).

Combinational therapy involves the combination of antibodies not only with chemotherapeutics, but also with other antibodies. These approaches rely on antibodies addressing two different antigens, or the same antigen. In the latter case, binding of different ligands to the target protein can be prevented. Therefore, different escape mechanisms can be counteracted (140). Therapies utilizing two antibodies directed against two different antigens, rely on one antibody to overcome an escape mechanism, while the other antibody enhances the therapeutic effect. In case of B cell lymphoma relapse, with B cells insensitive to rituximab treatment, several combination therapies are currently in clinical testing (141-143). One therapy approach is based on blocking the inhibitory Fc γ receptor IIb with an antibody called 6G11, while the other approach relies on CD47 blockage by the antibody magrolimab. Both combination therapies demonstrate higher efficiencies compared to treatment with only rituximab (142, 144).

In line with combination therapies, a bispecific antibody combines the specificity of two antibodies by addressing different antigens with each Fab fragment (145). One major challenge in the production of bispecific antibodies lies in the correct heterodimerization of the two light chains to their respective heavy chain. Therefore, different methods such as duomab technology, based on reduction and re-oxidation of hinge cysteines, common light chain, orthogonal Fab interface, SEED and knob-into-hole technologies were developed (146, 147). Furthermore, bispecific antibodies can be subdivided into four different approaches based on antigen selection: crosslinking of two receptors, inhibition of two receptors, blocking of two ligands, and recruitment of T cells or combinations thereof (145). Up to now, nine bispecific antibodies are currently approved by the FDA: glofitamab, epcoritamab, mosunetuzumab, teclistamab, tebentafusp, faricimab, amivantamab, emicizumab and, blinatumomab. Blinatumomab is a bispecific anti-CD19/CD3 T cell engager for treatment of B-cell acute lymphoblastic leukemia (B-ALL) (148). Emicizumab is a bispecific Factor IX/Factor X antibody for the treatment of Hemophilia A (149). Amivantamab is an anti-EGFR/c-MET bispecific antibody utilized in the treatment of non-small-cell lung cancer (150). Faricimab (anti-VEGF-A/Ang-2) was approved in 2022 by the FDA for the treatment of diabetic macular edema, wet or neovascular and age-related macular degeneration (151). Tebentafusp

is an anti-CD3/ glycoprotein 100 bispecific monoclonal TCR/scFv fusion utilized to treat uveal melanoma (152). Teclistamab is bispecific antibody directed against CD3 and BCMA for the treatment of relapsed multiple myeloma (153). Mosunetuzumab is a BiTE directed against CD20 and CD3 used in the treatment of follicular lymphoma (154). Epcoritamab is an anti-CD20 and CD3 bispecific antibody for the treatment of relapsed non-Hodgkin lymphoma (155). Epcoritamab is another anti-CD20 and CD3 bispecific antibody for the treatment of relapsed B cell lymphoma (156).

Ideal cancer associated antigens for antibody treatment are only expressed in cancer cells, but not on healthy cells. Since, the identification process remains very challenging, antibody discovery is focused on antigens either specific to a cell subtype or antigens overexpressed on cancer cells. Furthermore, the actual number of addressable antigens as well as the number of antigen positive cells with a tumor represent important criteria (157). Due to easy accessibility and frequently overexpression, membrane-associated cancer antigens play an important role in tumor imaging and antibody treatment. Furthermore, membrane bound cancer targets are associated with disease progression and prognosis (158). Up to now, the majority of antibodies are directed against membrane associated cancer targets. These targets are represented by a variety of anchoring proteins, receptors, enzymes and transporters (157). Within these different classes, anchoring protein such as cell-adhesion molecules (CAMs) and receptors are well established as cancer associated targets. Within CAMs, carcinoembryonic antigens (CEAs) and CEA related proteins (CEACAMs) as well as epithelial cell adhesion molecule (EpCAM) and E-cadherin play an important role in immune response, differentiation, cell growth, and cell adhesion (159-161). Despite their impact on disease progression only a few antibodies directing the CEACAM family are currently in clinical trials (162, 163). In contrast, catumaxomab and edrecolomab (now withdrawn) represent two approved anti-EpCAM antibodies utilized in the treatment of malignant ascites and colorectal cancer respectively (164, 165). In case of E-cadherin, no antibodies are currently investigated in clinical trials. In the class of receptors, frequent upregulation and overexpression in a variety of different cancer types is reported for the family of tyrosine kinase receptors (TKRs) (157). Members of the TKRs share a common base structure, comprising of an extracellular domain responsible for ligand binding or dimerization, a transmembrane domain and an intracellular tyrosine kinase domain for signaling (166). Within the TKR family, epidermal growth factor receptor (EGFR) and human epidermal growth factor receptor 2 (HER2) are of great importance for antibody therapy (167). Due to upregulation of EGFR in most cancer types and overexpression of HER2 in subsets of breast and stomach cancer, therapeutic antibodies such as cetuximab (anti-EGFR), matuzumab (anti-EGFR) and trastuzumab (anti-HER2) were developed (166). In case of trastuzumab, significant improved survival rates were observed for patients with metastatic breast cancer, however low response rates and resistance upon trastuzumab treatment remain major challenges (168). In case of cetuximab, response rates are similar to trastuzumab, also caused by either inherent or acquired resistance. Due to these

different resistance mechanisms, a wide usage of anti-EGFR antibodies remains not straightforward (169).

Besides membrane associated drug targets, addressing soluble targets remains challenging. There are two major challenges in addressing soluble targets. Besides potential side effects on normal physiological processes, the redundancy of receptor and ligand interaction need to be considered. If a ligand binds to several receptors or a receptor binds to several ligands, redundancy in signaling might counteract therapeutic effects of an antibody (170). Therefore, antibodies binding a ligand might have no therapeutic effect, while an antibody directed against the receptor discloses the desired effect (171). The opposite effect was shown for antibodies addressing the IL-17 receptor and ligand interaction. While the antibody brodalumab directed against the membrane attached IL-17 receptor showed no therapeutic effect in rheumatoid arthritis, the antibody ixekizumab directed against the soluble IL-17 receptor ligand (IL-17A), revealed relief in symptoms (172, 173). In contrast, side effects by disturbing receptor and ligand interaction in healthy tissue requires careful considerations. Therefore, a large number of knock-out mouse models were generated and characterized (174). Overall, 28 antibodies and antibody fragments addressing soluble targets are currently approved by the FDA. The majority of these approved drugs are utilized in the treatment of inflammation and autoimmune disorders, while only three are applied in cancer treatment (171). Bevacizumab and ranibizumab target VEGFA and are used in treatment of breast, metastatic cervical and colorectal cancer respectively (175, 176). Denosumab addresses TNFSF11 and is utilized in the treatment of breast, prostate and giant cell tumor of the bones (177).

Antibodies addressing membrane bound and soluble cancer associated antigens, play an important role in cancer treatment. However, about half of the proteome remains intracellular. Targeting intracellular antigens requires the drug to pass through the cell membrane to achieve a therapeutic effect. The major class of drugs targeting intracellular targets remains small molecules. However, lower selectivity compared to antibodies consequently leading to more off-target and side effects. To circumvent these drawbacks, several methods for delivering antibodies or antibody fragments into cells were developed. These methods can be divided into four different categories (178). Firstly, gene therapy like approaches, which utilize viruses, to insert DNA for intracellular production of the antibody (179). Secondly, encapsulating approaches to deliver antibodies or expression plasmids antibodies *via* nanoparticles or liposomes into the cell (180, 181). Thirdly, antibodies engineering can be utilized to fuse penetrating peptides to the antibody, which are responsible for intracellular delivery (182). Fourthly, antibodies which mimic T cell receptors, by binding to short peptides presented on MHC class I can address intracellular targets without the need to enter the cell (183). Up to now, no antibody utilizing one of the beforementioned methods and strategies is approved for the treatment of cancer.

The development of antibodies against a variety of different antigens resulted in a better prognosis and overall survival (184). In contrast to chemotherapy, cancer treatment with antibodies results in less severe side effects (185). However, side effects such as fever, flu-like symptoms, nausea, and skin rashes are common in antibody therapy. These side effects result in a major issue utilizing antibodies for therapy. Antigens overexpressed on cancer cells are also present in healthy tissue. For this reason, therapeutic antibodies also bind to healthy cells, leading to an immune reaction and therefore causing side effects. For this reason, choosing antigens for the development of therapeutic antibodies remains challenging. Besides addressing unique antigens present on cancer cells, a novel approach represents antibody activation within the tumor microenvironment. With this increase in specificity, side effects of antibody therapy can be reduced.

2.7 pH-dependent antibodies

Addressing cancer targets with high synthesis rates not only in the tumor but also within healthy tissues remains a challenging task. Due to antibody binding within healthy tissue, antigen internalization and subsequent degradation or side effects can occur (186). For this reason, antibodies with restricted binding to the tumor are required. Due to high metabolic rates and poor perfusion, solid tumors reveal hypoxic and acidic regions (187). Therefore, to increase specificity, pH-dependent antibodies were engineered. pH-dependent antibodies depend on the incorporation of ionizable amino acids into the CDRs. Within the ionizable amino acids Arg, Asp, Glu, His, and Lys, only histidine exhibits ionization within a physiological pH range (pK_a ~6.0) (188). Upon entering the acidic tumor microenvironment (pH 5.5-6.0) histidine is protonated and changes from a neutral to a positive charged state. Therefore, the interaction between the antibody and antigen is altered and affinity increases (189). After antigen binding, tumor growth pathways can be inhibited, or immune cells can be recruited to reduce tumor burden *via* ADCC, CDC or ADCP, while leaving healthy cells unharmed (190).

Furthermore, pH-dependent antibodies can be utilized as recycling antibodies to remove soluble antigens from circulation, which otherwise would prevent the antibody from reaching the tumor site (191). Hereby, the antibody-antigen complex is formed at physiological pH. Upon internalization of the antibody and reaching the acidic pH of the endosome, histidine residues get protonated and due to electrostatic repulsion, the antibody releases the antigen (192). While the antigen is subsequently degraded in the lysosome, the antibody is recovered by the neonatal Fc gamma receptor (FcRn) (193). By doing so, the antibody can undergo several removing cycles, compared to its non-pH-dependent counterpart. By increasing the affinity of the Fc part to the FcRn at physiological pH, antigen clearance can be enhanced (194). These so-called sweeping antibodies can undergo several removing cycles, compared to its non-pH-dependent counterpart. A similar effect can be observed, when addressing

membrane-bound antigens (191, 193). In this case, the antibody binds to the target at physiological pH and upon receptor-mediated endocytosis. In the sorting lysosome, the antibody releases the antigen, and through FcRn binding the antibody is recycled. Therefore, the antibody can undergo another cycle (193).

2.8 Anti-idiotype antibodies and the anti-idiotype network

An antibody comprises of different idiotopes and allotopes. While the allotypic differences are located within the constant regions of an antibody, the idiotopes are situated in the variable heavy and light chain domains (195). The hypervariable regions of the variable domain formed by somatic hypermutation represent a specific idiotype for each antibody (196). In contrast to the constant domains, the idiotype of an antibody can be recognized as foreign by the immune system. Therefore, the immune system is able to generate auto-anti-idiotype antibodies, which are directed against another antibody generated by the immune system, thereby forming a network of auto-antibodies (197). Anti-idiotype antibodies reveal three different modes of binding: Competing, non-competing and complex specific (**Figure 5**) (198). While complex specific anti-idiotype antibodies recognize the antibody only in presence of the antigen, antigen binding is not required in the case of the completive and non-competitive binding mode. In the non-competitive mode the anti-idiotype antibody binds to the antibody in a fashion not interfering with antigen binding. In contrast, blocking anti-idiotype entities restrict antigen binding towards the antibody, thereby creating an "internal image" by mimicking the structure of the initial epitope (199).

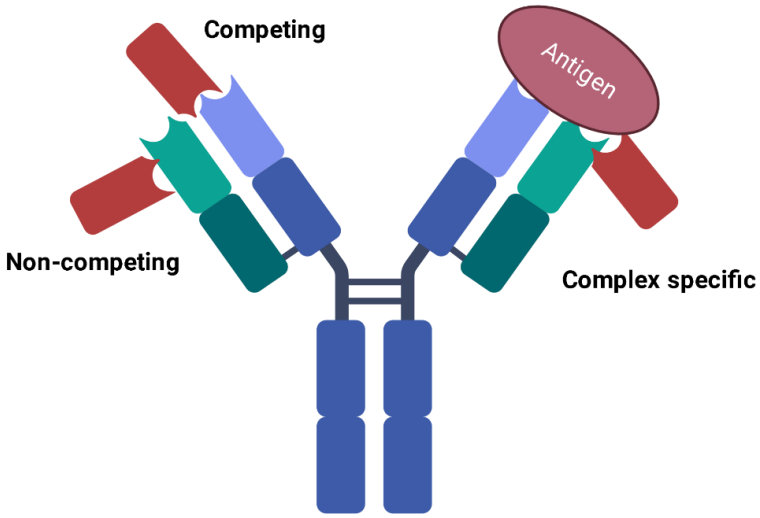

Figure 5: Overview of the three different binding modes of anti-idiotype entities. Binding of anti-idiotype entities takes place at the idiotype regions of an antibody, located in the variable region of the light and heavy chain. Since the variable regions of an antibody are responsible for antigen binding, three different binding interactions can be distinguished. Binding outside the paratope region is classified as non-competing, while binding in close proximity or at the paratope is referred to as competing. The complex specific binding is characterized by anti-idiotype entities, only recognizing the antibody-antigen complex, but not the single components.

It has been theorized, a network of anti-idiotype antibodies is present to sustain homeostasis of the immune system (200). The immune system utilizes auto-anti-idiotype antibodies to prevent overstimulation of antibody producing B- or plasma cells responsive to an antigen. After a secreted antibody reaches a certain concentration threshold, generation of an auto-anti-idiotype antibody is induced (201). If the auto-anti-idiotype also reaches the threshold, a new auto-anti-idiotype antibody is generated (202). The auto-anti-idiotype antibody blocks the interaction between the secreted antibody and its target in a reversible manner. Therefore, the immune response is subdued, but neutralization of the antigen is still possible (203). Besides their involvement in the normal immune response, dysregulation or lack of auto-anti-idiotype antibodies can lead to a series of different diseases (204). Diseases such as autoimmune thyroid diseases, systemic lupus erythematosus and type 1 diabetes display a lack of anti-idiotype antibodies (205-207). Therefore, autoimmune reactions of antibodies responsive to an autoantigen can occur. In contrast, dysregulation of the anti-idiotype network can lead to the formation of autoantibodies. The origin of these autoantibodies lies in the polyclonal antibodies present after an immune response. During the generation of subsequent auto-anti-idiotype antibodies towards the polyclonal antibodies, autoantibodies can be present (202). Further formation of anti-idiotype antibodies directed against the autoantibodies leads to additional autoantibodies.

In contrast to their relevance in diseases, anti-idiotype antibodies are utilized in several applications. These applications range from antibody purification, *in vivo* tracking of therapeutic antibodies, blocking domains in novel antibody constructs and as cancer vaccines (208-211). In case of anti-idiotype antibodies as cancer vaccines, an anti-idiotype antibody directed against the paratope region of an antibody with a disease associated antigen is administered. Thereby, the threshold for the generation of an anti-idiotype antibody is exceeded and an anti-idiotype antibody is formed. The anti-idiotype antibody directed against the antigen of the initial antibody, leads to a therapeutic effect (212).

Furthermore, anti-idiotype antibodies can be utilized to target membrane bound B and T cell receptors, identifying a specific clone in the whole repertoire. In case of B and T cell acute lymphoblastic leukemia (B and T ALL) originating from a single clone, depletion of this specific clone is possible. For the elimination different approaches were developed, such as full-length antibodies, peptide Fc fusions and ADCs (93, 212, 213). The anti-idiotype entities for these applications can be obtained by immunization of animals, generation of immune libraries and subsequent isolation of binders (214). Another form to isolate entities directed against the idiotype of an antibody is directed evolution. This approach is based on large synthetic, semi-synthetic or naïve libraries (84, 215, 216). These libraries are not restricted to antibody fragments, but can use peptides, single domain antibodies from camelids or sharks and DARPins as scaffolds for the anti-idiotype entity (84, 213, 217).

2.9 Overview of steric hinderance and affinity-based pro-antibody systems

One major goal in antibody treatment is to increase specificity to a point where the antibody only binds in the disease site and healthy tissue remains unharmed. Several concepts addressing this issue, such as pH-dependent and bispecific antibodies were developed (101, 191). Furthermore, concepts utilizing conformational switches caused by external stimuli such as light, peptides, and small molecules are investigated. Another approach is based on pro-antibodies, which are selectively activated at the disease site (218). Pro-antibodies consist of an antibody, a linker, and a masking domain. While the masking domain interferes and therefore reduces antigen binding, the linker contains a substrate peptide of a protease, overexpressed at the disease site. The linker of the pro-antibody is cleaved upon entering the disease site and the antibody retrieves antigen binding capability.

There are two different strategies for the generation of pro-antibodies, based on either affinity or steric hinderance moieties. In both cases, properties of the masking domains such as immunogenicity, applicableness, masking efficiency, and efficient release of the masking domain need to be considered (219). In the case of the steric hinderance-based approaches, a wide range of masking efficiency were found for different masking domains.

In an early approach, a 40 kDa latency-associated peptide (LAP) derived from TGF-β was fused to the N-terminus of the heavy chain of cetuximab (anti-EGFR) and infliximab (anti-TNFα) *via* an MMP-2 cleavable linker (**Figure 6A**). This masking domain resulted in about 2-fold reduction of binding, and which could be restored after MMP-2 cleavage. While blocking capability remained weak and the size of the blocking domain is rather large, wide applications are possible, low immunogenicity is predicted and the masking domain is released efficiently (220).

Another approach is based on a 2.5 kDa albumin binding peptide fused to the N-terminus of the light chain of several anti-EGFR antibodies *via* a urokinase (uPA) cleavable linker (**Figure 6B**). Upon albumin binding, EGFR binding is decreased up to 20-fold, and binding is restored after uPA cleavage. Utilizing an affinity peptide for albumin reduces the size of the expressed antibody and the antibody is blocked after administration, due to high amounts of albumin in the blood. While the blocking capacity is moderate, the peptide fused to the antibody is small and can be widely applied, while the masking domain is released efficiently (221).

The fusion of a 3.5 kDa human IgG1 hinge to the N-termini of the heavy and light chain of infliximab *via* an MMP-2/9 cleavable linker resulted in a pro-antibody with 400-fold decreased affinity (**Figure 6**C). Binding towards the antigen was fully restored after cleavage. Pharmacokinetics of the pro-antibody and infliximab revealed no differences. Furthermore, binding of anti-drug antibodies directed against infliximab was strongly reduced for the pro-antibody. This system reveals, small size of the masking domain, low immunogenicity, wide applicability, and strong binding decrease of the pro-antibody as well as efficient removal of the masking domain (222).

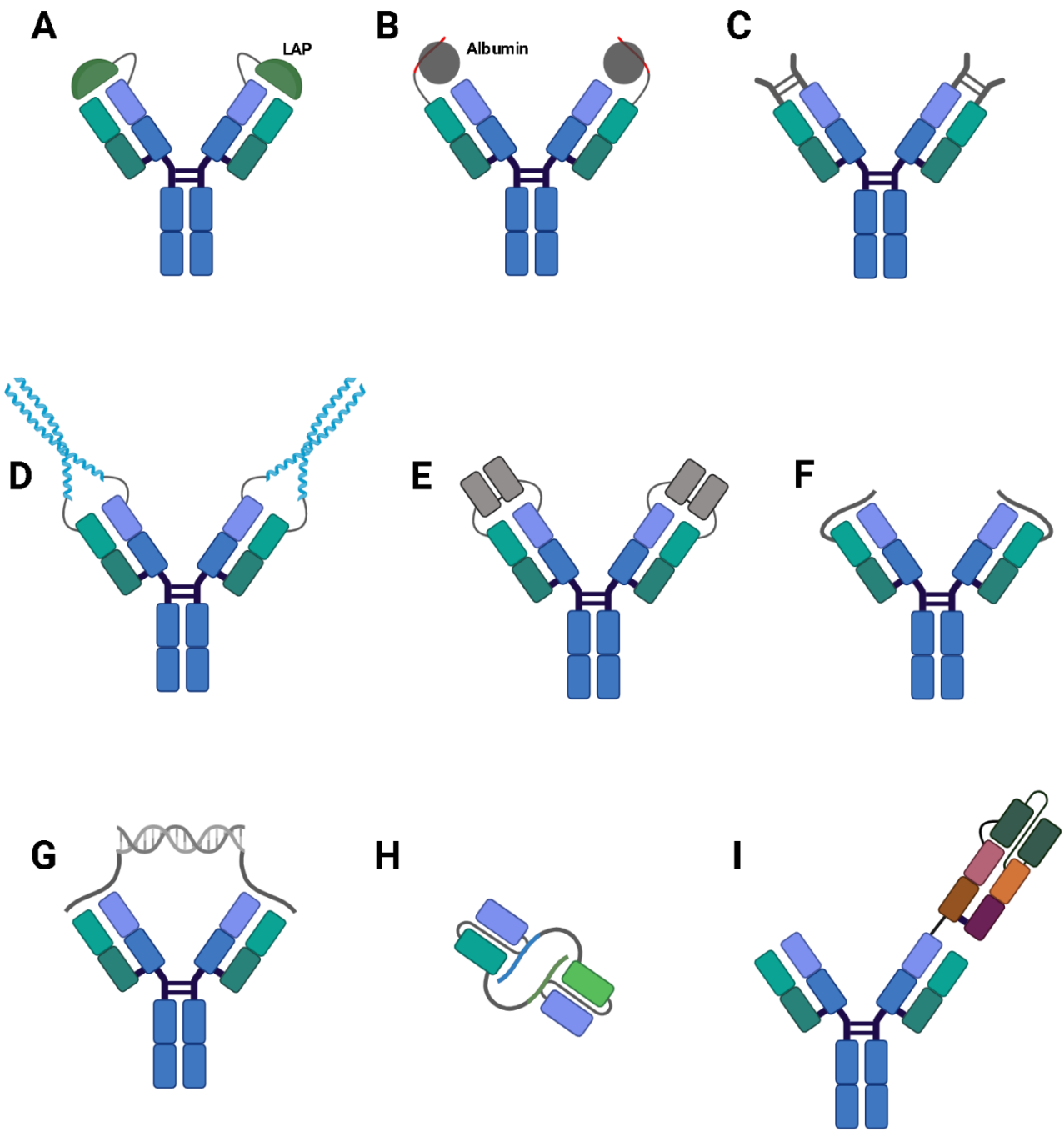

Figure 6: Overview of different pro-antibody systems. A) N-terminal heavy chain fusion of latency-associated peptide (LAP) tested with cetuximab and infliximab with 2-fold reduction in binding. **B)** N-terminal light chain fusion of an albumin binding peptide to EGFR binding antibodies. In this concept, the steric hinderance occurs after the antibody enters the bloodstream and binds to albumin. The reduction of binding is 20-fold. **C)** Fusion of an IgG1 hinge to the N-terminus of the light and heavy chain of infliximab results in 400-fold reduced binding. **D)** N-terminal fusion of a coiled-coil to the heavy and light chain to several antibodies. The steric masking of the antibodies results from the interaction between the two coils and ranges from 80- to 1000-fold reduction in binding. **E)** Fusion of a disulfide stabilized variable fragment to the N-termini of the infliximab and adalimumab light and heavy chain. The reduction of binding utilizing this steric hinderance approach is 1000-fold. **F)** Cetuximab pro-antibody with N-terminal light chain fusion of an affinity peptide. Utilizing this tailor-made peptide, a 400-fold reduction in binding was achieved. **G)** Two tailor-made anti-HIV antibody peptides connected by a DNA linker. This approach reveals an 8-fold reduction in binding. **H)** This concept requires two antibodies (cetuximab and matuzumab) and a peptide competing with antigen binding for each antibody. The peptide competing with matuzumab binding is fused to the N-terminus of the light chain of cetuximab, while the peptide competing with cetuximab binding is fused to the N-terminus of the light chain of matuzumab. This approach

leads to an 8-fold reduction in binding. **I)** N-terminal fusion of an anti-idiotype scFv to the CD3 binding Fab of a bispecific anti-CD3, anti-FLOR1 antibody. In this format, 4000-fold decrease in binding is achieved. Created with BioRender.com.

The investigation of different 5 to 9.2 kDa coiled-coil masking domains, revealed strong masking effects of parallel heterodimeric coiled-coils (**Figure 6D**). These parallel heterodimeric coiled-coils were fused *via* an MMP-2 cleavable linker to hBU12 (anti-CD19), rituximab (anti-CD20), h15H3 (anti-αVβ6), and trastuzumab (anti-Her2). Affinity of the pro-antibodies was reduced 80- to 1000-fold and after cleavage comparable to the respective parental antibody. Studies in mice with ADCs constructs containing the masking domain, revealed no loss of antibody concentration in the blood, while the parental antibody was not detected after two days. Furthermore, cleavage of the pro-antibody within the tumor tissue could be verified. While the coiled-coil domains reveal efficient release of the small-sized masking domain, and strongly decreased binding of the pro-antibody, immunogenicity risks remain due to the usage of engineered coiled-coil domains (223).

In another approach, a disulfide-stabilized variable fragment (dsFv) directed against intercellular adhesion molecule 1 (ICAM-1) was fused to the N-termini of the heavy and light chain of infliximab and adalimumab *via* an MMP-1 cleavable linker (**Figure 6E**). Thereby, a tetravalent bi-specific antibody was created. The binding of infliximab and adalimumab pro-antibodies was decreased 1000-fold, while affinities comparable to the parental antibodies were achieved after MMP-1 cleavage. Furthermore, binding of the dsFv part was comparable to the control antibody. The advantage of this system lies in the incorporation of a masking domain with an additional anti-tumor function as well as a wide range of applications, strong decrease of binding for the pro-antibody and efficient release of the masking domain. Nevertheless, the large size of the masking as well as immunogenicity risks need to be considered (224).

In contrast to pro-antibodies based on steric hinderance, the masking domains of affinity-based pro-antibodies require customization for each antibody (**Figure 6F**). In the process introduced by CytomX therapeutics, Inc., peptides derived from phage-display libraries enriched against the target antibody are fused to the N-terminus of the light chain *via* a protease cleavable linker. In the first example, a uPA cleavable cetuximab pro-antibody was constructed and revealed a 400-fold decrease in affinity compared to cetuximab. Binding after cleavage was restored to the level of cetuximab. In mouse models, the pro-antibody revealed similar anti-tumor effects as cetuximab. Furthermore, studies in non-human primates showed a longer half-life of the pro-antibody in comparison to cetuximab. Investigation of skin samples revealed accumulation of cetuximab, while binding of the pro-antibody was not detectable. Additionally, no increased immunogenicity was detected for the pro-antibody. This system discloses effective masking of cetuximab by the peptide, efficient release of the masking domain after cleavage, a small 4.4 kDa masking domain and a safe immunogenicity profile. On the other hand, the immunogenicity profile needs to be investigated for each peptide individually (225).

Other approaches based on affinity peptides rely on two peptides connected *via* a hybridized double-stranded DNA (dsDNA) linker (**Figure 6G**). In this study, the p17 (anti-HIV) antibody was mixed with an MMP-2 cleavable bivalent peptide dsDNA conjugate. The resulting pro-antibody revealed an 8-fold decreased binding, compared to the parental antibody. Removal of the masking domain resulted in similar binding properties as the parental antibody. While the masking domain in this approach discloses efficient removal and a small size, weak masking and immunogenicity issues due to the dsDNA need to be considered (226, 227).

In another study, two 28 kDa mutated EGFR III domains were connected *via* an MMP-9 cleavable linker to an matuzumab and cetuximab scFv (**Figure 6H**). In contrast to the other approaches, the matuzumab masking EGFR domain was fused to the C-terminus of the cetuximab light chain, while the cetuximab masking EGFR domain was fused to the C-terminus of the matuzumab light chain. Upon mixing both scFvs, interaction between the masking peptides and the respective antibody occurs. These cross-masked scFvs revealed an 8-fold decrease in binding, compared to the parental scFv. After MMP-9 cleavage binding affinities similar to the parental scFvs were achieved. In this approach, the efficient removal of the masking domain was demonstrated, and the immunogenicity of the masking domains is predicted to be low. However, weak masking efficiency as well as a large masking domain leave room for optimizations (228).

In another approach, a 25 kDa anti-idiotype scFv was fused to the N-terminus of the CD3 binding Fab, from an anti-CD3 and FOLR1 bispecific antibody and several cleavable linkers were investigated (**Figure 6I**). The utilized linkers contained protease cleavage sites for matriptase A, B, and C, MMP-2 and 9 as well as a linker combining the cleavage sites of matriptase A, MMP-2 and 9. Further analysis of the antibodies revealed a small impact of the different linkers on thermal stability and aggregation behavior. In cell binding experiments, pro-antibodies revealed up to 4000-fold reduction in binding, compared to the parental antibody. Binding activity after *in vitro* cleavage was fully restored. Restoration of antigen binding was also observed after incubation of the pro-antibodies with samples derived from cancer patients. Incubation of the pro-antibodies in human serum however, showed no cleavage. Analysis in non-tumor-bearing mice, however, revealed cleavage of up to 35%, depending on the linker. Investigations in tumor-bearing mice showed tumor growth inhibition in the range of the parental antibody for the pro-antibody containing the matriptase B site. The pro-antibody containing the matriptase C site, revealed weaker tumor growth inhibition, while the pro-antibody with the uncleavable linker showed no tumor growth inhibition. In this study, high masking efficiency was demonstrated, as well as effective removal of the masking domain. Furthermore, studies in mice revealed in *vivo* cleavage and tumor growth inhibition. However, the scFv remains large, compared to other masking domains and due to the usage of a mouse-scFv potential immunogenicity needs to be considered (210).

Overall, the pro-antibody field with approaches based on steric hinderance or affinity domains remains interesting for further therapy strategies. Both masking domain types reveal several advantages and disadvantages. One disadvantage of both types lies within the potential immunogenicity of the masking domain (229). While the masking domains for steric hinderance, can be chosen based on their immunogenicity profile, sequence modification of affinity-based masking domains are difficult. One advantage of the steric hinderance-based approaches relies on wide applicability of the domains, compared to the affinity-based masking domains. However, the masking efficiency of steric hinderance-based domains can vary depending on the utilized antibody (223). Therefore, insufficient masking efficiencies could only be addressed by a different linker design. In contrast, affinity-based masking domains are tailor-made for each antibody. Thereby it is possible to vary the masking efficiency based on specific requirements for the field of application of the pro-antibody (229).

2.10 Yeast surface display

With the rise of protein engineering, demands for high throughput screening methods increased. To use high throughput screening methods, linkage between protein function and corresponding genetic information needs to be guaranteed. Therefore, genotype-phenotype linking display technologies such as ribosomal, phage, mammalian, and yeast surface display were developed (230-232). Yeast surface display is based on the α-agglutinin mating factor from *saccharomyces cerevisiae*, comprising of disulfide bond connected subunits Aga1p and Ag2p (230, 233). While Aga1p is anchored on the cell surface of yeast cells and encoded on a chromosome, aga2p is encoded on a plasmid. Both genes are under the control of a galactose inducible promoter. Upon changing the carbon source in the media from glucose to galactose, protein production and surface presentation is induced (230). Surface presentation of up to 10^5 copies of the protein of interest (POI) is achieved by fusing the POI to either the C- or N-terminus of Aga2p. To confirm surface presentation, the POI is flanked by epitope tags, which can be verified by immunofluorescence staining (**Figure 7**) (230). To circumvent immunofluorescence staining, surface display can be coupled to a fluorescence protein *via* a T2A peptide (234). The T2A peptide causes ribosomal skipping, consequently creating two separate proteins from one open reading frame (ORF) (235). Therefore, the Aga2p-POI is presented on the surface and the fluorescent protein is retained in the cytoplasm (234).

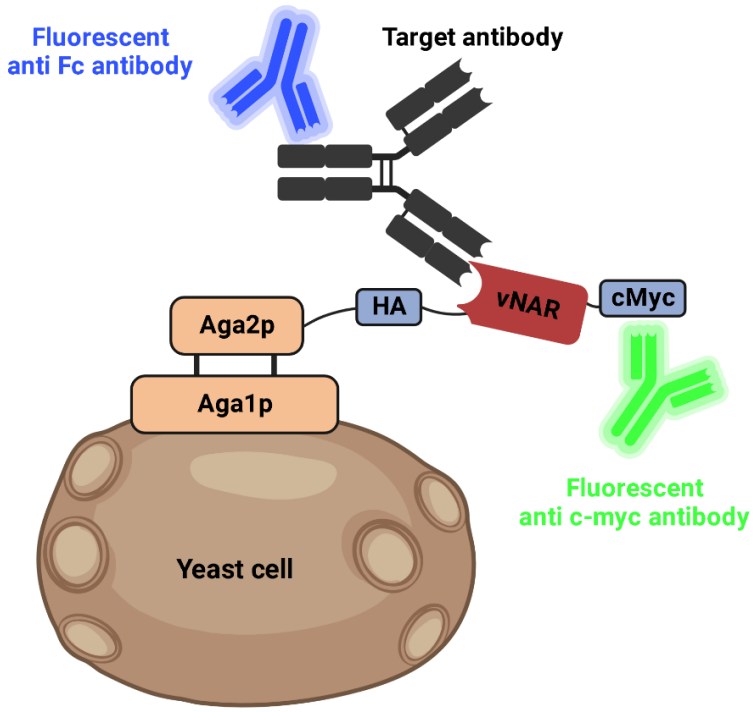

Figure 7: Schematic illustration of yeast surface display of a vNAR. Yeast surface display relies on the α-agglutinin mating factor, comprising of two disulfide bond connected subunits: Aga1p and Aga2p. While Aga1p is anchored in the cell wall, Aga2p can be fused to the vNAR, flanked by two epitope tags. Full-length surface display can be verified by immunofluorescence staining using an anti-c-Myc antibody. Binding of a target antigen can be verified by another fluorescent antibody. Created with BioRender.com.

Using the eukaryotic expression system of yeast cells, complex proteins can be displayed (236). Furthermore, gap-repair or golden gate cloning can be utilized to generate large libraries with up to 10^{10} transformants (237, 238). Library generation can be performed using error-prone-PCR, codon-based randomization, DNA-shuffling, and structure-guided design (239-242). Overall, yeast surface display was used in protein engineering of enzymes and receptors as well as antibody and alternative binding scaffold engineering (243-245). Protein engineering can be utilized in combination with fluorescence-activated cell sorting (FACS) for the enrichment of proteins with desired properties. In the case of antibody isolation, surface presentation as well as target binding, can be verified simultaneously utilizing two different fluorophores. Therefore, yeast cells exhibiting both fluorophores can be isolated from cells only revealing only one fluorophore. Isolated yeast cells can be cultivated and further enrichment can be achieved by subsequent sorting rounds (230).

2.11 Matrix metalloproteinase 9 (MMP-9)

The family of matrix metalloproteinases (MMPs) is represented by several zinc-dependent endopeptidases, playing an important role in tissue remodeling by degradation of the extracellular matrix. Based on the cleavage substrate, MMPs are subdivided into four different classes: membrane-type, collagenases, stromelysins, and gelatinases (246). Furthermore, MMPs reveal low expression and activity in normal tissue. During extracellular remodeling and inflammation MMP expression and activity is upregulated (247). Cytokines and their respective receptors can be activated by MMPs, thereby regulating inflammation and immune response (248). Therefore, MMP expression needs to be highly regulated. Regulation is controlled on transcriptional, post-transcriptional, and protein level. The transcriptional level is regulated by binding sites for specific transcription activators in the promotor region. Furthermore, mRNA half-life can increase or decrease depending on the interaction with different proteins (249). MMPs are translated as a catalytic inactive zymogen, consisting of a catalytic domain, a substrate binding domain and a propeptide. The propeptide consist of a part containing a cysteine coordinating the Zn (II) ion in the active site thereby blocking the catalytic activity and a protease cleavage site for propeptide removal. Removal of the propeptide or activation can be realized by three different mechanisms. The propeptide is cleaved off by a protease, allosteric reconformation of the propeptide, or modification of the cysteine by reactive oxygen species (250). After activation, enzyme activity can be controlled by endogenous tissue inhibitors of MMPs (TIMPs) (251).

MMP-9 is part of the gelatinase subgroup, is expressed as pro-MMP-9, and secreted in complex with TIMP-1 (252).

MMP-9 is activated by several other MMPs such as MMP-2, MMP-3, MMP-7, MMP-10, MMP-13 as well as cathepsin G and K (253). Activated MMP-9 reveals no distinct cleavage site, but rather a preferred pattern of amino acids (254). MMP-9 plays an important role in embryonic development, neurite growth, immune cell entry into tissue as well as wound healing and repair (255-258). However, overexpression of MMP-9 is associated with several diseases such as rheumatoid arthritis, aortic aneurysms, and cancer (259-261). Furthermore, MMP-9 is reported to trigger angiogenesis, cancer cell migration, and metastasis. (262-264). To counteract these negative effects on cancer progression, several inhibitors based on small molecules were developed and investigated in clinical trials. No inhibitor passed a phase III clinical trial (265). However, since MMP-9 expression in normal tissue remains low, MMP-9 overexpressed in the tumor microenvironment is utilized in several approaches to activate antibodies specifically in the tumor microenvironment (219).

2.12 Antibodies used as targets in this work

2.12.1 Matuzumab

Matuzumab is a humanized anti-epidermal growth factor receptor (EGFR) antibody, investigated in several clinical trials (NCT00113581, NCT00215644). Clinical trials were conducted in patients with non-small cell lung cancer (NSCLC), ovarian and gastric cancer, all overexpressing EGFR (266-269). EGFR is part of the ErbB receptor tyrosine kinase family and plays a major role in epithelial cell survival, proliferation, and differentiation depending on ligand-EGFR stimulation (270). During the interaction between the ligands epidermal growth factor (EGF) as well as transforming growth factor alpha (TGF-α) and EGFR, conformational changes take place and enable receptor dimerization and subsequent phosphorylation of tyrosine residues within the cytoplasmatic tail (166). Thereby different proteins are recruited and pathways such as Ras/MAPK and PI3K/AKT are activated (271). Dysregulation of these pathways due to gene mutations can lead to positive feedback loops, promoting tumor growth (272, 273). Tumor growth caused by overexpression of EGFR relies on activating mutations or gene amplification and subsequent activation of proliferation pathways (274, 275). Therefore, EGFR has been in the focus as a target for therapeutic antibodies (276). Approved antibodies such as cetuximab, as well as antibodies investigated in clinical trials like matuzumab reveal several side effects upon administration. A common side effect of anti-EGFR antibodies is skin rash, due to the presence of EGFR in epithelial tissues (269, 277).

Investigating the mode of action of matuzumab revealed two different ways contributing to the anti-tumor effect. The anti-tumor effect is induced by ADCC and a non-competitive mechanism to inhibit EGFR signaling (278). By binding to EGFR domain III, matuzumab sterically blocks the conformation required for high-affinity ligand binding and receptor dimerization (279). Thereby, the positive feedback loop of the Ras/MAPK pathway is interrupted, and proliferation is inhibited.

Several clinical trials, exploring matuzumab monotherapy as well as a combination of matuzumab and the chemotherapeutic drug paclitaxel were conducted (267). However, modest anti-tumor effects were reported and further investigations in clinical trials were halted.

2.12.2 Rituximab

Rituximab is a chimeric anti-CD20 monoclonal antibody approved by the FDA in 1997 for the treatment of follicular B cell non-Hodgkin lymphoma (NHL). Over the years, rituximab was approved for treatment of chronic lymphocytic leukemia (CLL) and auto-immune diseases such as rheumatoid arthritis (280). Furthermore, rituximab is utilized in the treatment of diffuse large B-cell lymphoma (30-40%), follicular lymphoma (about 20%), and marginal zone lymphoma (5-10%), Burkitt lymphoma (1-5%) and mantle

cell lymphoma (2-4%) (281). Mantle cell lymphoma (MCL) is classified as indolent lymphoma, which shows slow progression, in comparison to other NHLs. However, MCL clinical course is more aggressive and is considered incurable (282). Initial treatment guidance for MCL consisting of dose-intense chemotherapy or combination therapy utilizing several chemotherapeutic drugs and rituximab. Several combination therapies revealed high activity in relapsed MCL and improved overall survival (283). Still, maintenance treatment using rituximab, resulted in benefits in overall survival (284). Significant shorter overall survival is associated with high expression of MMP-9 (285, 286). Furthermore, there is evidence of an acidic tumor microenvironment in B cell lymphoma (287, 288). In rare cases, lactic acidosis has been reported (289, 290).

Administration of rituximab is approved for intravenous infusion and subcutaneous administration in the abdominal tissue, which can result in allergic reactions (291). Over a longer timeframe, side effects such as bacterial or viral infections as well as lymphopenia, toxic epidermal necrolysis, and acute tumor lysis syndrome can occur. Acute tumor lysis syndrome is a life-threatening complication resulting from the release of toxic metabolites upon massive lysis of tumor cells. Tumor cell lysis by rituximab is reported to be caused by ADCC and CDC (292). Furthermore, apoptosis can be caused upon rituximab binding to CD20 (293). CD20 is a transmembrane protein, comprising of an intracellular N- and C-terminal region and a large and small extracellular loop. Except for presence on pre and mature B cell, the details in function of CD20 is unknown. CD20 is reported to be involved in calcium influx upon B cell receptor activation. However, knock-out studies in mice revealed no negative effects on B cell development and function (294).

Resistance towards rituximab treatment can be related to several mechanisms such as downregulation of CD20, upregulation of the inhibitory receptor CD32b (inhibitory Fc γ receptor), thereby preventing rituximab binding and ADCC as well as CD55 and CD59 (membrane complement-regulator proteins) mediated blocking of CDC (295, 296).

2.12.3 BI-1206 – 6G11

BI-1206 (6G11) is a fully human, anti-inhibitory Fc γ receptor (CD32b) antibody, in clinical trials for the treatment of relapsed NHLs such as follicular lymphoma, mantle cell lymphoma, and marginal zone lymphoma (297). In current studies, 6G11 is co-administered with rituximab. In these applications (NCT03571568), 6G11 is responsible to overcome resistance mediated by overexpression of CD32b (142, 298). CD32b is an immune-checkpoint inhibitory Fc γ receptor, comprising of one extracellular, a transmembrane, and a cytoplasmatic domain. The cytoplasmatic domain contains an immunoreceptor tyrosine-based Inhibitory motif (ITIM). Upon receptor binding and signaling, phosphates hydrolyzing intermediates of activating signals are recruited (299).

CD32b is expressed on all leukocytes, except NK and T cells (300). Furthermore, CD32b plays important roles in the threshold for B and dendritic cell activation and plasma cell survival (301, 302). Besides these regulatory functions, CD32b is required for the prevention of antibody-mediated allergic reactions (300). This observation is in line with correlations between lack or low expression of CD32b and autoimmune diseases (303). Further investigations in CD32b deficient mice revealed improved activation of naïve T cells and stronger anti-tumor activity (304, 305).

Overexpression of CD32b on tumor cells is associated with worse clinical outcome and promoted internalization of therapeutic antibodies (306). Thereby, tumor responsiveness towards antibodies is lowered or lost. To regain responsiveness, binding of CD32b to the Fc of the antibody can be blocked using 6G11. 6G11 blocks CD32b in an antagonistic manner, thereby preventing intracellular signaling, restricting antibody internalization, and regaining responsiveness (142, 298). Further studies in mouse models revealed specific depletion of B cells and no cytokine storm (142). In a first dose-escalation clinical trial with refractory mantle cell lymphoma patients, resistant to rituximab treatment showed response using combination therapy of rituximab and 6G11 (307). Evaluation of 6G11 side effects at different doses is still ongoing (308).

2.12.4 Magrolimab – 5F9

Magrolimab (Hu5F9 or 5F9) is a humanized anti-CD47 antibody, currently in clinical trials for treatment of myeloid leukemia, myelodysplastic syndrome and acute myeloid leukemia (NCT05079230) (309). Furthermore, 5F9 is used in several combination therapies with chemotherapeutics or other antibodies (144, 310, 311). Thereby, 5F9 is utilized to overcome CD47-mediated resistance mechanisms. CD47 is a ubiquitous expressed transmembrane protein, comprising of a short C-terminal cytoplasmatic domain, five transmembrane domains, and an N-terminal IgV domain (312). The IgV domain is responsible for interaction with a variety of proteins such as integrins, thrombospondins, and signal regulatory protein alpha (SIRPα) (313-315). SIRPα is expressed on macrophages and dendritic cells and upon binding to CD47 results in the inhibition of phagocytosis (316). During formation of the phagocytic synapse downstream dephosphorylation of nonmuscle myosin IIA (NM2A) takes place and subsequent myosin assembly is inhibited (317). NM2A-driven cytoskeletal rearrangement is important in the formation and closure of the phagocytic cup and successive phagocytosis (318).

Overexpression of CD47 on tumor cells leads to resistance towards macrophage-mediated phagocytosis. Furthermore, overexpression is reported for several types of solid tumors with poor clinical outcome correlating with high CD47 expression (319). By blocking the CD47 SIRPα axis, using 5F9, phagocytosis is induced, however, no CDC, ADCC, or direct apoptotic activity is revealed (320). Furthermore, 40-60% receptor blocking is sufficient for full activity. This result is contrastive to findings, revealing potent

inhibition of phagocytosis at very low CD47 expression levels (317). Despite low tissue expression levels, senescent red blood cells (RBCs) reveal high levels of CD47 (321). Therefore, treatment with 5F9 leads to mild anemia and reticulocytosis (144, 320). After two to three weeks, anemia is resolved and the age distribution in the pool of RBCs is shifted towards younger RBCs, which show more resistance to CD47 blockage. Furthermore, dose-escalation studies with or without erythropoietin pre-treatment as well as several priming and maintenance dosing studies were conducted. Low priming doses (1-3 mg/kg) resulted in initial anemia, however, maintenance dosing (30 mg/kg) showed no further negative effects (320).

In a phase 1b study, 22 patients with several previous therapies for rituximab-resistant disease were treated with 5F9 in combination with rituximab. Complete response rates of 33% and 43% for rituximab-refractory diffuse large B-cell lymphoma and follicular lymphoma respectively, could be observed (144). While initial studies looked very promising, very recently magrolimab has been placed under a partial clinical hold by the FDA for its phase 3 acute myeloid leukemia (AML) studies, due to unlikelihood of a benefit of survival for patients with TP53 mutations (322).

2.12.5 T cell receptor

The T cell receptor (TCR) plays an important role in the adaptive immune system, by targeting infected cells directly or activating other immune cells, *via* interaction with MHC class I and II respectively. MHCs are loaded with short peptides for the identification of foreign antigens. To identify foreign antigens, a large diversity of TCR repertoire is essential. The TCR comprises of disulfide-connected, membrane-anchored α and β or γ and δ chains, with three CDRs per chain. The gene locus of the α chain contains 46 V and 61 J genes, while the β chain locus includes 42 V, 2 D, and 13 J genes, each with genes for constant regions (323). The γ locus comprises 8 V and 5 J genes and the δ locus is formed by 3 V, 2 D, and 3 J genes, with respective genes for constant regions (324, 325). Constant regions are added upon successful V-J or V-D-J rearrangement and N nucleotide addition. After gene rearrangement is completed, theoretical diversities of 10^{16} and 10^{18} different TCRs variants are possible for αβ and γδ TCRs respectively, thereby creating a specific idiotype for each TCR (326, 327). For both TCR types, CDR3s reveal the highest potential diversity, with longer CDR3s for the δ, shorter CDRs for γ and medium-length CDRs for α and β chain TCRs (328). Furthermore, germline-encoded CDR1 and CDR2 of αβ TCRs mediate interaction with MHC molecules, while the CDR3 is responsible for peptide binding (329). In contrast, γδ TCRs do not rely on MHC molecules for binding but can recognize antigens directly (326). T cell activation is dependent on the TCR-CD3 complex. CD3 comprises of ε, γ, δ, and ζ transmembrane subunits, each with immunoreceptor tyrosine-based activation motifs (ITAM) in the cytoplasmatic part (**Figure 8**) (330).

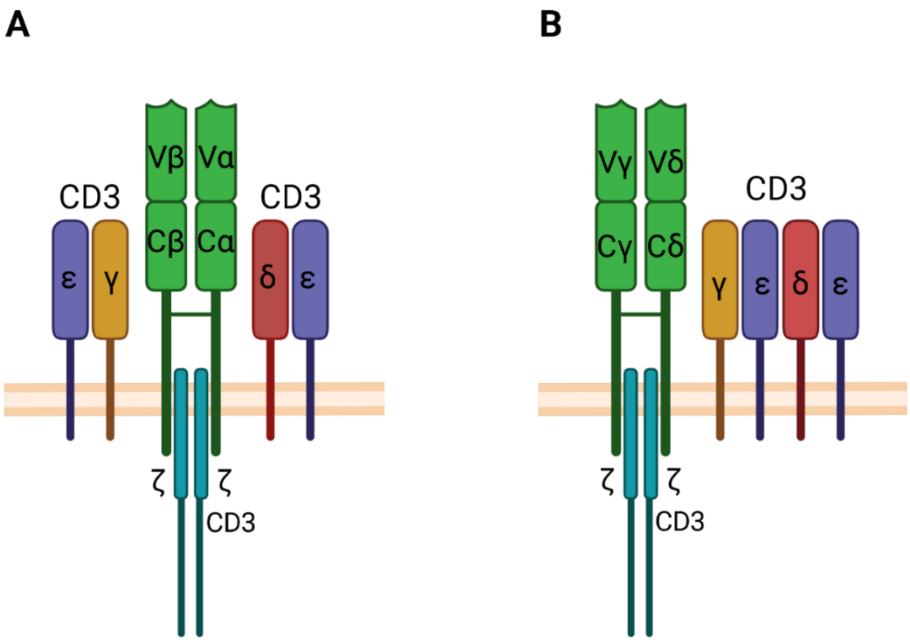

Figure 8: Schematic overview of αβ and γδ T cell receptors. A) While αβ TCRs comprise of a variable and constant domain for the α and β chain each, **B)** γδ TCRs are formed by a γ and δ chains with variable and constant domains respectively. Associated with both TCRs are CD3 subunits. While one εγ, one δε, and one ζ homodimer CD3 subunit is associated with αβ TCRs, the γδ TCR is stabilized by two εγ heterodimers and a ζ homodimer.

Despite a cytoplasmatic part, transmembrane domain, and connecting peptide, CD3 subunits ε, γ, δ reveal immunoglobulin-like extracellular domains, while the structure of CD3 ζ extracellular domain is unknown (331). The formation of CD3 subunit heterodimers stabilizes the TCR. While the αβ TCR is stabilized by one εγ and one δε (**Figure 8A**), the γδ TCR is stabilized by two εγ heterodimers (**Figure 8B**). Furthermore, a disulfide connected CD3 ζ homodimer is associated with both TCR subtypes (332). Upon binding of the antigen to the TCR, intracellular signaling occurs. Thereby, ITAMs are phosphorylated by lymphocyte-specific protein-tyrosine kinase (Lck) (333). Conformational changes in the cytoplasmatic tail of CD3 ε result in the exposure of proline-rich sequences (PRSs) and recruitment of non-catalytic region of tyrosine kinase adaptor protein (Nck). Nck on the other hand is responsible for recruitment of transcription factors and formation of an immunological synapse (334). Further interaction of CD4 or CD8 with αβ TCRs is required for further signaling, while γδ TCRs function is CD4 and CD8 independent (332).

T cell lymphomas are categorized into several subtypes and progression can range from indolent to aggressive. While indolent tumors reveal a long course of disease and resistance to standard therapy, aggressive lymphomas tend to rapid progression. In both lymphoma types prognosis remains poor (335). Furthermore, the cause of T cell lymphomas remains unknown. However, studies indicate involvement of several viruses such as HIV, Epstein-Barr-Virus (EBV), and retrovirus-like human T-cell leukemia virus (HTLV). Furthermore, T cell lymphoma can arise from overstimulated T cells, which can be found in chronic inflammatory tissues. For instance, T cells in peripheral T cell lymphomas (PTCL) are mostly

derived from $CD4^+$ αβ TCRs, however exact frequencies of αβ and γδ TCRs are unknown (336). Furthermore, T cells retain expression of chemokine and cytokine receptors and TCR signaling capacity. Therefore, involvement of TCR signaling in antigen-driven expansion in early disease phases is possible (337). General mechanisms of T cell pathogenesis are still poorly understood.

Since T cell depletion goes along with severe side effects due to their important role in immunity, treatment of T cell lymphomas remains challenging (338, 339). However, several therapy approaches can be considered. Besides small molecules, such as retinoids, standard chemotherapeutics, and histone deacetylase inhibitors, protein-based therapeutics such as immunotoxins and monoclonal antibodies are investigated for treatment (340-342). Drug testing in large randomized clinical trials is difficult, due to rarity of some T cell lymphoma subtypes. Therefore, investigating optimal treatment options remains problematic.

The A6 TCR is a well characterized TCR with studies investigating optimizing expression, crystal structures and target peptides (343-346). The TCR receptor originates from a $CD8^+$ T-cell of a human T-cell leukemia virus type1 (HTLV-1) seropositive patient diagnosed with HTLV-1-associated myelopathy/tropical spastic para-paresis (HAM/TSP) (345). Analysis of the isolated TCR revealed an αβ setup, with the variable domain formed by the Vα2.3 Jα24 and Vβ12.3 Dβ2.1 Jβ2.7 segments. The combination of these segments enables the binding towards the HTLV-1 Tax peptide (LLFGYPVYV), as well as the Tel1p peptide (MLWGYLQYV) originating from the serine/threonine-protein kinase TEL1 from *saccharomyces cerevisiae*.

2.13 Aim of the study

In recent years, efforts have been undertaken, to minimize side effects of antibody treatment. One approach in this field are antibodies which are only able to bind within the tumor tissue. This binding behavior is achieved by utilizing properties specific to tumor microenvironment such as targeting antigens only expressed on tumor cells, low pH within the tumor tissue, as well as overexpression of proteases. The aim of this work is the construction of affinity-based pro-antibodies utilizing either pH dependency or proteolytic cleavage as release mechanisms for the masking domain. The masking domains investigated in this work, comprise of either chicken-derived scFvs or shark-derived single domain antibodies (vNARs). In this work, different strategies should be employed to obtain masking domains with desired properties. In one approach, pH-dependency should be implemented in a preexisting vNAR domain directed against matuzumab. Other strategy is aimed at the identification of novel pH-dependent vNAR domains against the therapeutic antibodies magrolimab and rituximab, based on semi-synthetic vNAR libraries. Another approach should be based on a chicken immunization to address, if it is possible to obtain chicken derived scFvs which are suitable as masking domains for pro-antibodies.

The obtained shark- and chicken-derived domains should be tested for their blocking capability by biolayer interferometry or cell binding experiments. vNAR or chicken scFv domains with masking capabilities should be fused to the light chain of their respective antibody with different linkers or tested in SEED constructs with one arm carrying a Fab and the other one containing the respective masking domain. Furthermore, biophysical properties such as size, aggregation behavior, as well as melting point should be investigated for the generated constructs. Furthermore, binding behavior on cells as well as biological activity in masked and unmasked state, should be explored.

3 Material

3.1 Cell lines

3.1.1 Bacterial strains

Escherichia coli SHuffle® T7 Express (NEB)	F´ *lac, pro, lacIq / Δ(ara-leu)7697 araD139 fhuA2 lacZ::T7 gene1 Δ(phoA)PvuII phoR ahpC* galE (or U) galK λatt*::pNEB3-r1-*cDsbC* (SpecR, *lacIq*) *ΔtrxB rpsL150*(StrR) *Δgor Δ(malF)3*
Escherichia coli TOP10 (Invitrogen)	F'[lacI^{q} Tn10(tet^{R})] mcrA Δ(mrr-hsdRMS-mcrBC) φ80lacZΔM15 ΔlacX74 deoR nupG recA1 araD139 Δ(ara-leu)7697 galU galK rpsL(Str^{R}) endA1 λ^{-}

3.1.2 Yeast strains

Saccharomyces cerevisiae EBY100	[MATa::GAL-1AGA1::URA3 ura3-51 trp1 leu2Δ1 his3 Δ200 pep4::HIS3 prb1Δ1.6R can1 GAL]

3.1.3 Mammalian cell lines

Cell line	Culture medium
Expi293F™	Expi293F™ Expression medium + 1% P/S
HeLa	DMEM + 10 % (v/v) FBS + 1 % (v/v)
IM-9	RPMI-1640 + 10% (v/v) FBS + 1% (v/v) P/S
Jurkat	RPMI-1640 + 10% (v/v) FBS + 1% (v/v) P/S
Jurkat A6 TCR	RPMI-1640 + 10% (v/v) FBS + 10mM HEPES + 1% (v/v) P/S
Raji	RPMI-1640 + 20% (v/v) FBS + 1% (v/v) P/S

3.2 Plasmids

Yeast surface display plasmids	pCT
Bacterial expression plasmids	pET30
Mammalian expression plasmids	pTT5

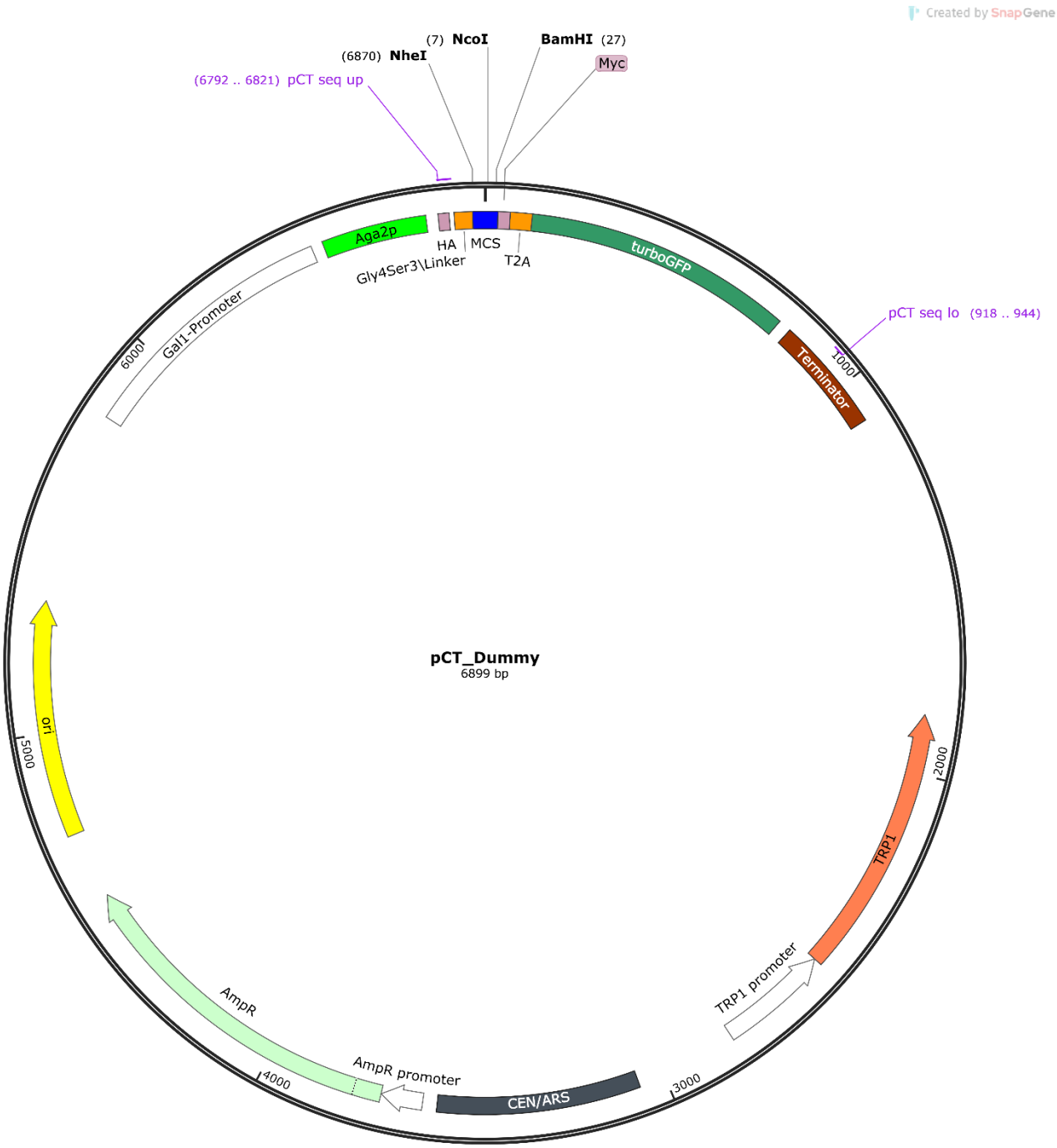

Figure 9: Graphic illustration of the pCT Dummy plasmid map. Crucial aspects are annotated. **Gal1-Promotor**: Galactose inducible promotor, **Aga2p**: A-agglutinin-binding subunit, **HA**: Peptide tag for verification of surface presentation based on human influenza hemagglutinin, **Gly4Ser3 linker**: Linker comprising of four glycine and one serine arranged in three cassettes, **MCS**: multiple cloning site containing NheI, NcoI and BamHI for linearization, **Myc**: Peptide tag for verification of surface presentation based on c-myc, **T2A**: Self-cleaving peptide caused by ribosomal skipping to obtain two separated proteins from one mRNA, **turboGFP**: Rapidly assembling green fluorescent protein (GFP) variant, **Terminator**: Terminates transcription in yeast cells, **TRP1**: Auxotrophic marker phosphoribosylanthranilate isomerase required for selection of yeast cells, **TRP1 promotor**: Enables transcription of the *trp1* gene, CEN/ARS: Origin of replication in yeast derived from a yeast centromere region, **AmpR promotor**: Enables the transcitption of the *ampr* gene, **AmpR**: Ampicillin resistance gene required for selection, **ori**: ColE1 origin of replication which enables E. coli the replication of the plasmid in high copy number. Location of sequencing primers (pCT seq up and pCT seq lo) is indicated by the purple marks. Created with SnapGene.

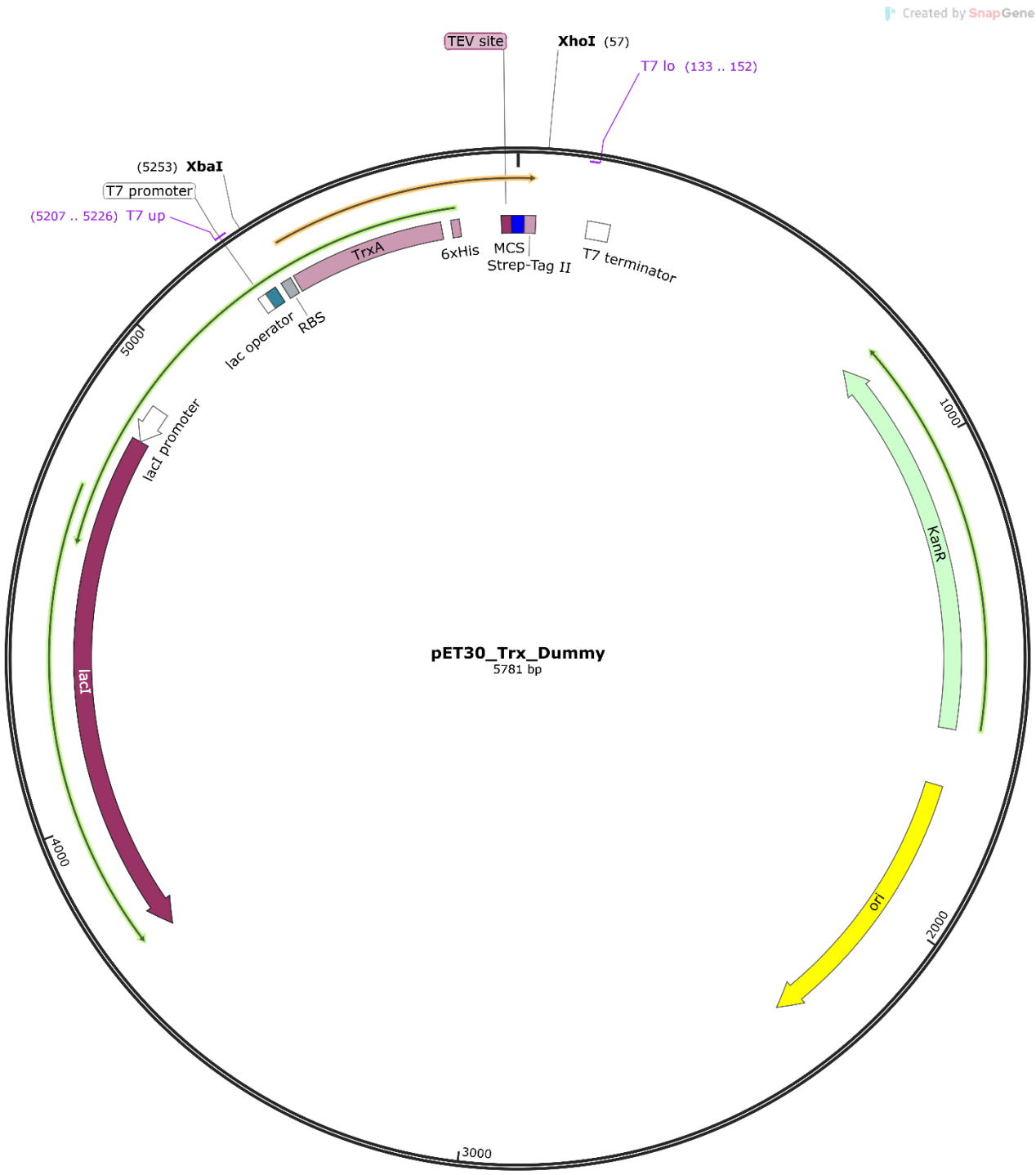

Figure 10: Graphic illustration of the pET30 Trx Dummy plasmid map. Crucial aspects are annotated: **lacI:** lac repressor which binds to the lac operator, **lacI promotor** which enables transcription of lacI, **lac operator** which is the binding site of lacI, **T7 promotor** which is responsible for mRNA formation after IPTG induction, **RBS**: Ribosome binding site which starts translation, **TrxA**: Thioredoxin which assistances in the folding process of the downstream protein, **6xHis**: Hexa-histidine purification tag, **TEV site**: TEV protease recognition site to cleave thioredoxin from the downstream protein, **MCS**: multiple cloning site containing BsaI sites for Golden Gate cloning, **Strep-TagII**: Additional purification tag, **T7 terminator**: Terminates transcription, **KanR**: Kanamycin resistance gene required for selection, **ori**: ColE1 origin of replication which enables E. coli the replication of the plasmid in high copy number. Location of sequencing primers (T7 up and T7 lo) is indicated by the purple marks. Created with SnapGene.

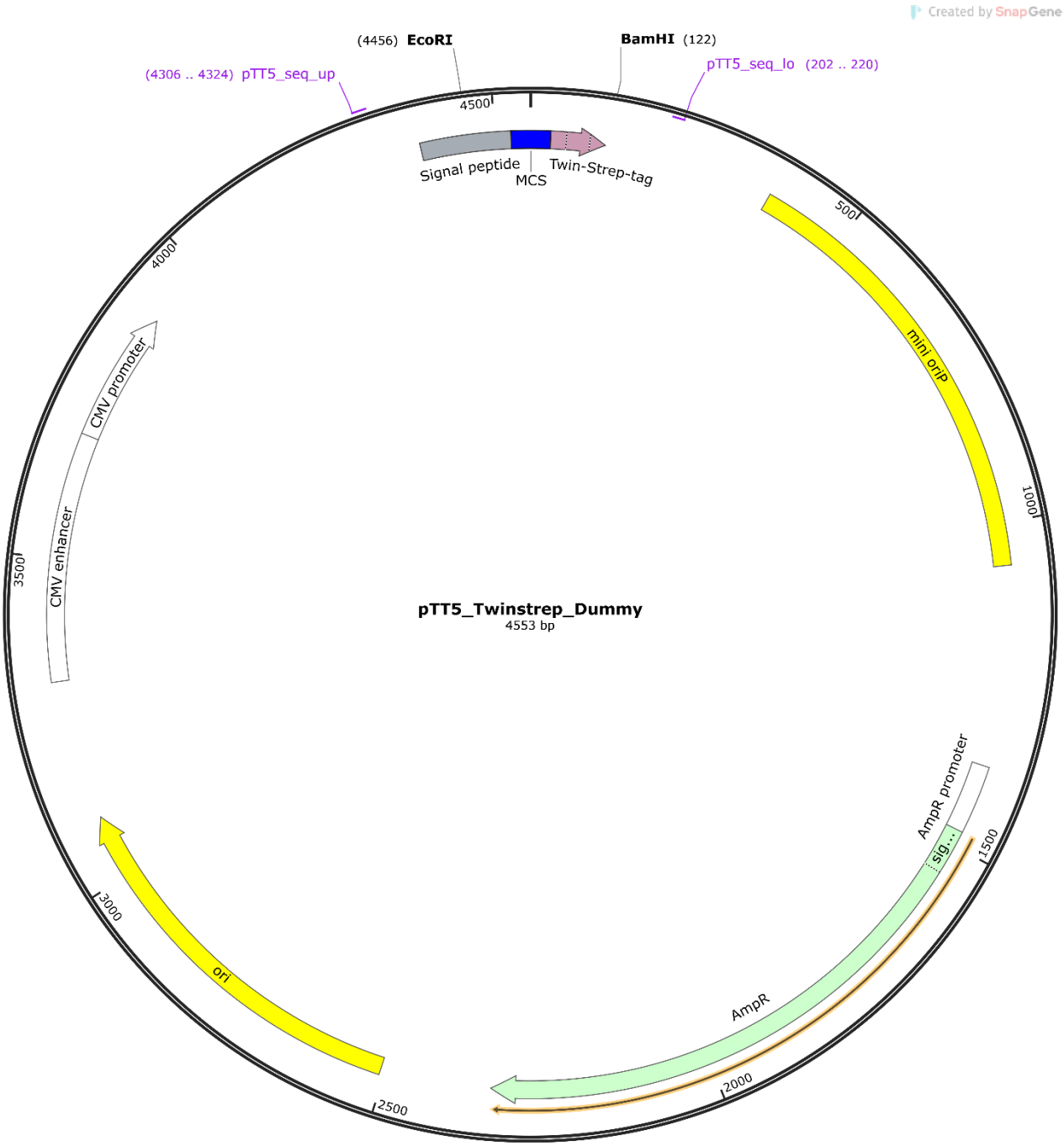

Figure 11: Graphic illustration of the pTT5 Twinstrep Dummy plasmid map. Crucial aspects are annotated. **CMV enhancer**: Human cytomegalovirus (CMV) immediate-early enhancer increases the expression of downstream genes, **CMV promotor**: Human cytomegalovirus enables the transcription of genes in human cell lines, **Signal peptide**: Peptide sequence required for the secretion of the downstream protein into the medium, **MCS**: multiple cloning site containing SapI or BsaI sites for Golden Gate cloning, **Twin-Strep-tag**: purification tag **AmpR promotor**: Enables the transcitption of the *ampr* gene, **AmpR**: Ampicillin resistance gene required for selection, **ori**: PMB1 origin of replication which enables E. coli the replication of the plasmid in high copy number. Location of sequencing primers (pCT seq up and pCT seq lo) is indicated by the purple marks. Created with SnapGene.

3.3 Enzymes and ladders

Enzyme	Supplier
1 kb Plus DNA Ladder	New England Biolabs
BamHI-HF	New England Biolabs
BsaI-HF v2	New England Biolabs
Color Prestained Protein Standard, Broad Range (10-250 kDa)	New England Biolabs
DpnI	New England Biolabs
EcoRI-HF	New England Biolabs
MMP-9	Acro Biosystems
Matriptase	Sigma-Aldrich
NcoI-HF	New England Biolabs
NheI-HF	New England Biolabs
OneTaq DNA Polymerase	New England Biolabs
Q5 High-Fidelity DNA Polymerase	New England Biolabs
SapI	New England Biolabs
T4 DNA Ligase	New England Biolabs
Trypsin-EDTA	Sigma Aldrich
uPA	Sigma-Aldrich

3.4 Antibodies

3.4.1 Target antibodies and proteins

Antibody	Supplier
5F9 – Magrolimab	In-house production
6G11	In-house production
Matuzumab	Merck KGaA, Darmstadt, Germany
Rituximab	In-house production
CD32b	Acro Biosystems

3.4.2 Antibodies and detection proteins for flow cytometry

Antibody	Supplier
Anti-human IgG Fc PE Conjugate	Thermo Fisher Scientific
Anti-mouse APC Conjugate	Thermo Fisher Scientific
Penta-His	Qiagen
Penta-His Alexa Fluor 647 Conjugate	Qiagen
Anti-c-myc FITC Conjugate	Miltenyi Biotec
Anti-c-myc biotin Conjugate	Miltenyi Biotec
Streptavidin APC Conjugate	Thermo Fisher Scientific
Streptavidin PE Conjugate	Thermo Fisher Scientific

3.4.3 Detection proteins for ELISA

Protein	Supplier
StrepTactin-HRP Conjugate	Bio-Rad Laboratories, Inc.

3.4.4 Oligonucleotides

All oligonucleotides used in this work were ordered from Sigma-Aldrich as 100 μM stocks in water. Stock solutions were diluted 1:10 in water, prior to use.

Oligonucleotides for sequencing	
pCT seq up	TACGACGTTCCAGACTACGCTCTGCAGGCT
pCT seq lo	AGTTGGTAACGGAACGAAAAATAGAAA
pTT5 seq up	CTGCGCTAAGATTGTCAGT
pTT5 seq lo	CCATATGTCCTTCCGAGTG
T7 prom up	TAATACGACTCACTATAGGG
T7 term lo	GCTAGTTATTGCTCAGCGG

Oligonucleotides for homologous recombination in yeast	
VH gr up	GGTGGTGGTGGTTCTGGTGGTGGTGGTTCTGCTAGCGCCGTGACGTTGGACG AG
VH SOE lo	TCCGCCCCCCGACCCGCCGCCGCCTGAGCCGCCTCCCCCGGAGGAGACGATGA CTTCGGT
VL SOE up	GGCGGCTCAGGCGGCGGCGGGTCGGGGGGCGGAGGGAGCGCGCTGACTCAG CCGTCCTCG

VL gr lo	CAAGTCCTCTTCAGAAATAAGCTTTTGTTCGGATCCTAGGACGGTCAGGGTTG TCCC
FR1 up	ATGGCCGCACGGCTTGAACAAACACCGACA
AMV1 His rand up	GAAGACAGTGGTACATATCACTGTGAAGCGCRTSRTCRTMWTSMTCATMWKC AKCATCAKMWKYRKMRTMATCATCMTATTGAAGGTGGCGGGACC
FR2 SOE lo	TGCGCCCTTTTTTGTGAAATACCAGTACGT
5005 bleo lo	GAGCAAAAGCTTATTTCTGAAGAGGACTTG

Oligonucleotides for Matuzumab SEED constructs	
pTT5 vNAR GG up	ATATATGCTCTTCAAGTATGGCCGCACGGCTTGAACAAACACCG AC
TILTVK Linker GG lo	ATATATGCTCTTCTTTCACCTTCTTCAAGCTTTTTCACAGTCAGA ATGGTCCCGCCACCTTC
Linker TEV GG up	ATATATGCTCTTCAGAATTTTCAGAAGCACGCGTAGAGAACCTG TACTTCCAGAGC
TEV Upper Hinge CtoS up	GAGAACCTGTACTTCCAGAGCGGAAGCGAGCCCAAGAGCAGCG ACAAGACCCACACC
SEED GA GG lo	ATATATGCTCTTCTCGCTCATCATCCGCCTGTTTCAGGCAGGGAT CCGCC
Matuzu HC GG up	ATATATGCTCTTCAAGTCAGGTGCAACTAGTGCAGTCCGGCGCC GAAG
Matuzu CH1 Hinge CtoS GG lo	ATATATGCTCTTCTGCTGCTCTTGGGCTCAACTTTCTTGTCCACC TTGGTGTTGCTGGG
SEED Hinge GG up	ATATATGCTCTTCAGAGCCCAAGAGCAGCGACAA
SEED AG GG lo	ATATATGCTCTTCTCGCTCAATGATGATGATGATGATGTTTACCC GGGGAC

Oligonucleotides for 5F9 SEED constructs	
pTT5 vNAR GG up	ATATATGCTCTTCAAGTATGGCCGCACGGCTTGAACAAACACCG AC
SEED AG GG lo	ATATATGCTCTTCTCGCTCAATGATGATGATGATGATGTTTACCC GGGGAC
SEED GA GG lo	ATATATGCTCTTCTCGCTCATCATCCGCCTGTTTCAGGCAGGGAT CCGCC
TTLTVK Linker GG lo	ATATATGCTCTTCTTTCACCTTCTTCAAGCTTTTTCACAGTCAGA GTGGTGCCCCCCCC
Linker TEV GG up	ATATATGCTCTTCAGAATTTTCAGAAGCACGCGTAGAGAACCTG TACTTCCAGAGC
TEV Upper Hinge CtoS up	GAGAACCTGTACTTCCAGAGCGGAAGCGAGCCCAAGAGCAGCG ACAAGACCCACACC
pTT5 5F9 GG Twist up	ATATATGCTCTTCGAGTCAAGTCCAACTCGTTCAATCTGGA
Matuzu CH1 Hinge CtoS GG lo	ATATATGCTCTTCTGCTGCTCTTGGGCTCAACTTTCTTGTCCACC TTGGTGTTGCTGGG

Oligonucleotides for Rituximab SEED constructs	
pTT5 vNAR GG up	ATATATGCTCTTCAAGTATGGCCGCACGGCTTGAACAAACACCGAC
SEED AG GG lo	ATATATGCTCTTCTCGCTCAATGATGATGATGATGATGTTTACCCGGGGAC
SEED GA GG lo	ATATATGCTCTTCTCGCTCATCATCCGCCTGTTTCAGGCAGGGATCCGCC
Rit HC GG up	ATATATGCTCTTCGAGTCAAGTGCAGCTGCAGCAGCC
Rit HC GG lo	ATATATGCTCTTCTGCTCACCTTCTTATCGACCTTGG
TILTVK Linker GG lo	ATATATGCTCTTCTTTCACCTTCTTCAAGCTTTTTCACAGTCAGAATGGTCCC
TPVTVK Linker GG lo	ATATATGCTCTTCTTTCACCTTCTTCAAGCTTTTTCACAGTCACAGGGGTGCC
TPVTVN Linker GG lo	ATATATGCTCTTCTTTCACCTTCTTCAAGCTTATTCACAGTCACAGGGGTCCC
TLVTVK Linker GG lo	ATATATGCTCTTCTTTCACCTTCTTCAAGCTTTTTCACAGTCACAAGGGTGCC
Hinge GG pTT5 up	ATATATGCTCTTCGAGTGAGCCCAAATCTTGTGACAAAACTCAC

Oligonucleotides for Matuzumab heavy and light chain constructs	
pTT5 vNAR GG up	ATATATGCTCTTCAAGTATGGCCGCACGGCTTGAACAAACACCGAC
TILTVK G4S lang lo	ATATATGCTCTTCACTGCCGCCACCGCCGCTACCGCCACCGCCGCTGCCAC CACCGCCTTTCACAGTCAGAATGGTCCCGCC
Mat LC G4S lang up	ATATATgctcttcaCAGCGGCGGTGGCGGTAGCGGCGGTGGCGGCAGCGGCGG TGGCGGTAGCGACATCCAGATGACACAGAGCCCTAGCAGC
Mat HC GS GG up	ATATATgctcttcaGGTAGCCAGGTGCAACTAGTGCAGTCCGGCGCCGAA
G4S up	ATATATGCTCTTCAAGCGGCGGTGGCGGTAGCGGCGGTGGCGGC AGCGGCGGTGGCGGTAGCGGCGGTGGCGGCAGCGGCGGTGGCGGTTGAA GAGCATATAT
G4S lo	ATATATGCTCTTCAACCGCCACCGCCGCTGCCGCCACCGCCGCTACCGCCA CCGCCGCTGCCGCCACCGCCGCTACCGCCACCGCCGCTTGAAGAGCATATA T
TILTVK Roche lo	ATATATGCTCTTCAGCTGCCACCACCGCCTTTCACAGTCAGAATGGTCCCGC C

Oligonucleotides for 5F9 light chain constructs	
5F9 VL Roche up	ATATATGCTCTTCATTCCTGGGCCCCGGCGGTGGCGGCAGCGGCGGT GGCGGTAGCGGTGGTGATATTGTCATGACGCAATCCCCACTC
TTLTVK Ro G4S lang lo	ATATATGCTCTTCACTGCCACCACCGCCGGGGCCCAGGAAGCCCAGG GGCATGTGCACGCTACCGCCGCCACCGCTGCCACCACCGCCTTTCAC AGTCAGAGTGGTGCCCCC
5F9 VL G4S up	ATATATGCTCTTCACAGCGGCGGTGGCGGTAGCGGCGGTGGCGGCA GCGGCGGTGGCGGTAGCGATATTGTCATGACGCAATCCCCACTC
TTLTVK G4S lo	ATATATGCTCTTCACTGCCGCCACCGCCGCTACCGCCACCGCCGCTG CCACCACCGCCTTTCACAGTCAGAGTGGTGCCCCC
5F9 VL G4S GLA up	ATATATGCTCTTCAGGCCTGGCGGGCGGTGGCGGTAGCGGCGGTGG CGGCAGCGGCGGTGGCGGTAGCGATATTGTCATGACGCAATCCCCACTC

TTLTVK G4S PLG lo	ATATATGCTCTTCAGCCCAGCGGGCTGCCGCCACCGCCGCTACCGCCAC CGCCGCTGCCACCACCGCCTTTCACAGTCAGAGTGGTGCCCCC
5F9 VL Stop lo	GCTCTTCTCGCTCTAACACTCTCCCCTGTTGAAGCTCTTTG

Oligonucleotides for Rituximab light chain constructs	
Rit VL Roche up	ATATATGCTCTTCATTCCTGGGCCCCGGCGGTGGCGGCAGCGGCGGTG GCGGTAGCGGTGGTCAAATCGTCCTGTCACAGTCCCCTG
TLVTVK Roche lo	ATATATGCTCTTCAGAAGCCCAGGGGCATGTGCACGCTACCGCCGCCA CCGCTGCCACCACCGCCTTTCACAGTCACAAGGGTGCC
Rit VL G4S up	ATATATGCTCTTCACAGCGGCGGTGGCGGTAGCGGCGGTGGCGGCAG CGGCGGTGGCGGTAGCCAAATCGTCCTGTCACAGTCCCCTG
TLVTVK G4S lo	ATATATGCTCTTCACTGCCGCCACCGCCGCTACCGCCACCGCCGCTGC CACCACCGCCTTTCACAGTCACAAGGGTGCC
MMP9 G4S GG lo	ATATATGCTCTTCACTGCCGCCACCGCCGCTACCGCCACCGCCGCTGC CACCACCGCCGGGGCCCAGGAAGCCCAGGGGCATGTG
Rit AG4S up	ATATATGGTCTCACAGTGCCGGCGGTGGCGGTAGCCAAATCGTCCTGT CACAGTCCCCTG
TLVTVK G4S lang Bsa lo	ATATATGGTCTCAGCCGCTACCGCCACCGCCGCTGCCGCCACCGCCGC TACCGCCACCGCCGCTGCCACCACCGCCTTTCACAGTCACAAGGGTGC C
G4S PLGLA Rit VL Bsa up	ATATATGGTCTCACGGCGGTGGCGGCAGCGGCGGTGGCGGTAGCCCC CTGGGCCTGGCCGGCGGTCAAATCGTCCTGTCACAGTCCCCTG
TLVTVK G4S Bsa lo	ATATATGGTCTCAGCTGCCGCCACCGCCGCTACCGCCACCGCCGCTGC CACCACCGCCTTTCACAGTCACAAGGGTGCC
Rit VL 1 PLGLA 2 up	ATATATGGTCTCACAGCGGCGGTGGCGGTAGCCCCCTGGGCCTGGCCG GCGGTGGCGGCAGCGGCGGTGGCGGTAGCCAAATCGTCCTGTCACAG TCCCCTG
Rit VL 2 PLGLA 1 up	ATATATGGTCTCACAGCGGCGGTGGCGGTAGCGGCGGTGGCGGCAGC CCCCTGGGCCTGGCCGGCGGTGGCGGTAGCCAAATCGTCCTGTCACAG TCCCCTG
Rit VL G4S lang up	atatatGGTCTCaCGGCGGTGGCGGCAGCGGCGGTGGCGGTAGCGGCGG TGGCGGTAGCCAAATCGTCCTGTCACAGTCCCCTG
Rit VL G4S PLGLA Bsa up	ATATATGGTCTCAGCAGCGGCGGTGGCGGTAGCGGCGGTGGCGGCAG CGGCGGTGGCGGTAGCCCCCTGGGCCTGGCTCAAATCGTCCTGTCACA GTCCCCTG
Kappa CL Stop BsaI lo	ATATATGGTCTCATGCCTCAACACTCACCTCTATTAAAACTTTTTGTAA C

Oligonucleotides for pET30 cloning of vNARs	
GG vNAR up	ATATATGGTCTCAATGGCCGCACGGCTTGAACAAACACCGACAA
GG LTVK vNAR lo	ATATATGGTCTCTGAGCCTTTCACAGTCAGAGTGGTGCCCCCCCCTTCA

Oligonucleotides for 6G11 scFv	
6G11 VH His GG up	ATATATGGTCTCAATGGCTCACCACCACCACCACCACGGGTCTGCTAGCG AGGTGCAGCTGCTGGAGAGC
6G11 VH Linker GG lo	ATATATGGTCTCACTTCACTACCACCGCCTTCTGATCCGCCACCCACGGTC ACCAGGGTGCCCTG

6G11 VL Linker GG up	ATATATGGTCTCAGAAGGAGGCGGTTCTGAGGGCGGAGGTCAATC AGTCCTCACTCAACCGCCT
6G11 VL Strep GG lo	ATATATGGTCTCATCATCTATTTTTCGAACTGCGGGTGGCTCCATGA TCCCAATACCGTGAGTTTTGTTCCGCC

Oligonucleotides for pET30 cloning of chicken scFvs	
scFv chick his GG up	ATATATGGTCTCAATGGCTCACCACCACCACCACCACGGGTCTGCTA GCGCCGTGACGTTGGACGAGTCCG
scFv chick SII GG lo	ATATATGGTCTCATCATCATTTTTCGAACTGCGGGTGGCTCCAAGACC CTAGGACGGTCAGGGTTGTCCCGGCC

Oligonucleotides for 6G11 light chain constructs	
Chicken VL GG up	ATATATGCTCTTCAAGTGCGCTGACTCAGCCGTCC
Chicken VL G4S lo	ATATATGCTCTTCACTGCCGCCACCGCCGCTACCGCCACCGCCGCTGCCAC CACCGCCTAGGACGGTCAGGGTTGTCCC
6G11 VL G4S up	ATATATGCTCTTCACAGCGGCGGTGGCGGTAGCGGCGGTGGCGGCA GCGGCGGTGGCGGTAGCCAATCAGTCCTCACTCAACCGCCT
Chicken VL MMP-9 lo	ATATATGCTCTTCAGAAGCCCAGGGGCATGTGCACGCTACCGCCGCC ACCGCTGCCACCACCGCCTAGGACGGTCAGGGTTGTCCC
6G11 LC MMP-9 up	ATATATGCTCTTCATTCCTGGGCCCCGGCGGTGGCGGCAGCGGCGG TGGCGGTAGCGGTGGTCAATCAGTCCTCACTCAACCGCCT
pTT5 Lambda GG lo	ATATATGCTCTTCTcgCACTATTAGCTGCACTCGGTGG

3.5 Chemicals

Chemical	**Supplier**
1,4-Dithiothreit (DTT)	Carl Roth GmbH & Co. KG
2-Mercaptoethanol	Carl Roth GmbH & Co. KG
Acetic acid	Carl Roth GmbH & Co. KG
Acrylamid/Bisacrylamid (37.5:1)	Carl Roth GmbH & Co. KG
Agar-Agar, Kobe I	Carl Roth GmbH & Co. KG
Agarose	Carl Roth GmbH & Co. KG
Ammonium persulfate (APS)	Carl Roth GmbH & Co. KG
Ammonium sulfate	Carl Roth GmbH & Co. KG
Ampicillin (sodium salt)	Carl Roth GmbH & Co. KG
Arabinose	Carl Roth GmbH & Co. KG
Bacto Casamino Acids	BD Biosciences
Bovine serum albumin (BSA)	Carl Roth GmbH & Co. KG
Calcium chloride ($CaCl_2$)	Carl Roth GmbH & Co. KG

Citric acid	Carl Roth GmbH & Co. KG
Chloramphenicol	Carl Roth GmbH & Co. KG
Coomassie Brilliant Blue G250/R250	Carl Roth GmbH & Co. KG
D-Biotin	Carl Roth GmbH & Co. KG
Dimethyl sulfoxide (DMSO)	Carl Roth GmbH & Co. KG
Dipotassium hydrogen phosphate (K_2HPO_4)	Carl Roth GmbH & Co. KG
Disodium hydrogen phosphate (Na_2HPO_4)	Carl Roth GmbH & Co. KG
D-Galactose	Carl Roth GmbH & Co. KG
D-Glucose	Carl Roth GmbH & Co. KG
D-Luciferin	Cayman Chemicals
D-Sorbitol	Carl Roth GmbH & Co. KG
Ethanol	Carl Roth GmbH & Co. KG
Ethanolamine	Sigma Aldrich
Ethylendiaminetetraacetic acid (EDTA)	Carl Roth GmbH & Co. KG
EZ-LinkTM Sulfo-NHS-LC-Biotin	Carl Roth GmbH & Co. KG
Glycerol	Carl Roth GmbH & Co. KG
Glycine	Carl Roth GmbH & Co. KG
HD GreenTM DNA stain	Carl Roth GmbH & Co. KG
Hydrochloric acid (HCl)	Carl Roth GmbH & Co. KG
Imidazole	Carl Roth GmbH & Co. KG
Isopropanol	Carl Roth GmbH & Co. KG
Isopropyl-β-D-thiogalactopyranoside (IPTG)	Carl Roth GmbH & Co. KG
Kanamycinsulfat	Carl Roth GmbH & Co. KG
Kinetics buffer	Sartorius AG
Lithium acetate	Sigma Aldrich
Magnesium sulfate ($MgSO_4$)	Carl Roth GmbH & Co. KG
Manganese chloride ($MnCl_2$)	Carl Roth GmbH & Co. KG
Meliseptol®	Carl Roth GmbH & Co. KG
MOPS	Carl Roth GmbH & Co. KG
NHS-Alexa Fluor 647	Jena Bioscience GmbH
Nickel (II) chloride	Carl Roth GmbH & Co. KG
p-Aminophenylmercuric acetate	Sigma Aldrich
Penicillin-Streptomycin (P/S)	Sigma Aldrich
Potassium acetate	Carl Roth GmbH & Co. KG

Potassium dihydrogen phosphate (KH_2PO_4)	Carl Roth GmbH & Co. KG
Potassium chloride (KCl)	Carl Roth GmbH & Co. KG
Sodium chloride (NaCl)	Carl Roth GmbH & Co. KG
Sodium dihydrogen phosphate (NaH_2PO_4)	Carl Roth GmbH & Co. KG
Sodium dihydrogen phosphate dihydrate (NaH2PO4 · 2H2O)	Carl Roth GmbH & Co. KG
Sodium dodecyl sulfate (SDS)	Carl Roth GmbH & Co. KG
Sodium hydroxide (NaOH)	Carl Roth GmbH & Co. KG
SYPRO Orange Protein Stain	Invitrogen AG
Tetramethylethylenediamine (TEMED)	Carl Roth GmbH & Co. KG
Transporter 5™ Transfection Reagent (PEI)	Carl Roth GmbH & Co. KG
Tris-(hydroxymethyl)-aminomethane (TRIS)	Carl Roth GmbH & Co. KG
Triton X-100	Sigma Aldrich
Trypan Blue Solution 0.4 %	Carl Roth GmbH & Co. KG
Tryptone/Peptone ex casein, granulated	Carl Roth GmbH & Co. KG
Yeast extract	Carl Roth GmbH & Co. KG
Yeast nitrogen base without amino acids	BD Biosciences

3.6 Buffers and solutions

Buffer/solution	Composition
Ampicillin stock solution (1000x)	100 mg/mL ampicillin (sodium salt), sterile filtered
Agarose gel loading buffer	
Buffer BXT pH 8	100 mM Tris-HCl 150 mM NaCl 1 mM EDTA 50 mM biotin
Buffer E	1M sorbitol 1mM $CaCl_2$
Buffer W	100 mM Tris-HCl 150 mM NaCl 1 mM EDTA
Coomassie Brilliant Blue staining solution	10% (v/v) acetic acid 40% (v/v) isopropanol 0.25% (w/v) Coomassie Brilliant Blue R-250 0.25% (w/v) Coomassie Brilliant Blue G-250
Chloramphenicol (1000x)	25 mg/mL ampicillin (sodium salt), sterile filtered
dNTP mixture	5 mM dATP 5 mM dCTP 5 mM dGTP

	5 mM dTTP
EDTA solution for IMAC	100 mM EDTA
IMAC A buffer	50 mM Tris-HCl, pH 7.5 150 mM NaCl 20 mM imidazole
IMAC B buffer	50 mM Tris-HCl, pH 7.5 150 mM NaCl 500 mM imidazole
Kanamycin stock solution (1000x)	50 mg/mL kanamycin, sterile-filtered
Lithium acetate / DTT buffer	100 mM lithium acetate 10 mM DTT
Luciferin substrate buffer (2x)	5 mM Tricine pH 7.8 1 mM $MgSO_4$ 0.02 mM EDTA 4 mM DDT 2% Triton-X 100 4 mM ATP 2 mM D-Luciferin
Nickel (II) chloride solution for IMAC	100 mM $NiCl_2$
Phosphate buffered saline (PBS) pH 7.4	140 mM NaCl 10 mM KCl 6.4 mM Na_2HPO_4 2 mM KH_2PO_4
Phosphate buffered saline with bovine serum albumin (PBSB) pH 7.4	140 mM NaCl 10 mM KCl 6.4 mM Na_2HPO_4 2 mM KH_2PO_4 0.1% bovine serum albumin (BSA)
Protein A elution buffer pH 3.0	100 mM glycine pH 3
Protein A neutralization buffer pH 9.0	1 M Tris-HCl
SDS-PAGE 4x running gel buffer	3 M Tris-HCl, pH 8.8 4 g/L SDS
SDS-PAGE 4x stacking gel buffer	0.5 M Tris-HCl, pH 6.8 4 g/L SDS
SDS-PAGE sample buffer (5x, reducing)	250 mM Tris-HCl, pH 8 7.5% (w/v) SDS 25% (v/v) glycerol 0.25 mg/mL bromophenol blue 12.5% (v/v) β-mercaptoethanol
SDS-PAGE Running buffer pH 8.8	50 mM Tris-HCl 190 mM glycine 1 g/L SDS
TAE buffer (50x) pH 8.0	2 M Tris-HCl 1 M acetic acid 50 mM EDTA
TN buffer pH 7.5	50 mM Tris-HCl 150 mM NaCl
TfB1 pH 5.8	30 mM potassium acetate 100 mM KCl 10 mM $CaCL_2$ 50 mM $MnCl_2$

	15% (w/v) glycerol
TfB2 pH 7	10 mM MOPS 75 mM $CaCl_2$ 10 mM KCl 15% (w/v) glycerol

3.7 Cultivation Media

3.7.1 Media for cultivation of E. coli

Medium	Components
Double concentrated Yeast Tryptone (dYT) medium	1.6 % (w/v) tryptone/peptone 1 % (w/v) yeast extract 0.5 % (w/v) NaCl
Super Broth (SB) medium	3.2 % (w/v) tryptone/peptone 2 % (w/v) yeast extract 0.5 % (w/v) NaCl 0.5 % (v/v) 1M NaOH
TYM medium	2% (w/v) tryptone/peptone 0.5% (w/v) yeast extract 0.1 M NaCl 10 mM $MgSO_4$

The preparation of agar plates was carried out, by adding 1 % (w/v) agar-agar to standard dYT medium. After sterilization *via* autoclaving (20 min at 121°C and 2 bars), the solution was cooled to approximately 60°C, the selection antibiotic added, briefly mixed, and poured into sterile petri dishes.

3.7.2 Media for cultivation of S. cerevisiae

Medium	Components
YPD medium	2 % (w/v) D-glucose (autoclaved separately) 2 % (w/v) tryptone/peptone 1 % (w/v) yeast extract
SD-W medium	2 % (w/v) D-glucose (sterile filtered) 0.5 % (w/v) ammonium sulphate (sterile filtered) 0.5 % (w/v) Bacto Casamino Acids (sterile filtered) 0.17 % (w/v) yeast nitrogen base without amino acids (sterile filtered) 0.54 % (w/v) Na_2HPO_4 (autoclaved) 0.86% (w/v) NaH_2PO_4 (autoclaved)
SG-W medium	2 % (w/v) D-galactose (sterile filtered) 0.5 % (w/v) ammonium sulphate (sterile filtered) 0.5 % (w/v) Bacto Casamino Acids (sterile filtered) 0.17 % (w/v) yeast nitrogen base without amino acids (sterile filtered) 0.54 % (w/v) Na_2HPO_4 (autoclaved) 0.86% (w/v) NaH_2PO_4 (autoclaved)

The preparation of agar plates was carried out, by adding 1 % (w/v) agar-agar to the phosphate mixture. After sterilization *via* autoclaving (20 min at 121°C and 2 bars), cooling the solution to approximately 70°C, adding the selection mix *via* sterile filtration and briefly mixing, the finished media was poured into sterile petri dishes.

3.7.3 Medium for mammalian cell culture

Medium	Supplier
Dulbecco's Modified Eagle's Medium (DMEM) - high glucose	Merck KGaA
Expi293™ Expression Medium	Thermo Fisher Scientific
Fetal bovine serum (FBS) Superior	Merck KGaA
Opti-MEM™ I reduced serum medium	Thermo Fisher Scientific
RPMI-1640 with L-glutamine and sodium bicarbonate	Merck KGaA

3.8 Kits and consumables

Kit/consumable	Supplier
Amicon® Ultra - 0.5 mL Centrifugal Filter Device (3K)	Merck KGaA
Biosensors Octet® Anti-Human IgG Fc Capture (AHC)	Satorius
Biosensors Octet® ProA	Satorius
Biosensors Octet® His1K	Satorius
Biosensors Octet® Anti-hIgG Fc capture (AHC)	Satorius
Cuvettes Semi-micro cuvette (PS)	Sarstedt AG & Co. KG
Centrifugation tube (15mL/50mL)	Sarstedt AG & Co. KG
Column HisTrap™ HP 1 mL	GE Healthcare
Column HiTrap™ Desalting 5mL	GE Healthcare
Column HiTrap™ MabSelect™ PrismA	GE Healthcare
Column HiTrap™ NHS-activated HP	GE Healthcare
Column TSKgel SuperSW3000	Tosoh Bioscience
Dialysis tubing Size No.3 - Dia20/32" - MWCO 14 kDa	Medicell Membranes Ltd
ELISA Plate Sealers	R & D Systems
ExpiFectamine™ 293 Transfection Kit	Thermo Fisher Scientific
FACS tubes 5 mL	Thermo Fisher Scientific
Gloves (latex and nitrile) Rotiprotect	Carl Roth GmbH & Co. KG

Hard-Shell® 96-Well PCR Plates, low profile, thin wall, skirted, white	Bio-Rad Laboratories, Inc.
Microseal 'B' PCR Plate Sealing Film, adhesive	Bio-Rad Laboratories, Inc.
Octet Red	FortéBio
Paper towels	Sarstedt AG & Co. KG
PCR tubes Multiply®-µStrip	Sarstedt AG & Co. KG
Petri dishes 35mm/ 60 mm	Sarstedt AG & Co. KG
Pipette filter tips 10 µL/ 20µL/ 200 µL/ 1000 µL	Biosphere®
Pipette tips 10 µL/ 20µL/ 200 µL/ 1000 µL	Sarstedt AG & Co. KG
Polycarbonate Erlenmeyer Flask with Vent Cap 50 mL	Corning
Polystyrene 96-well plate with lid, U-bottom	Thermo Fisher Scientific
Polypropylene 96-well plate flat bottom	Greiner Bio-One
PureYield™ Plasmid Midiprep System	Promega
Reaction tubes 1.5 mL/ 2 mL	Sarstedt AG & Co. KG
Serological pipettes 1 mL/ 5 mL/ 10 mL/ 25 mL	Sarstedt AG & Co. KG
SuperScript™ III Reverse Transcriptase Kit	Invitrogen by Life Technologies
Syringe filter 0.20 µm/ 0.45 µm	Sarstedt AG & Co. KG
Syringe (50 mL)	Ochs Laborfachhandel eK
Tissue culture (TC) flask T25/ T75	Sarstedt AG & Co. KG
TMB One Solution	Promega
Wizard® Plus SV Minipreps DNA Purification System	Promega
Wizard® SV Gel and PCR Clean-Up System	Promega
Zeba™ Spin Desalting Columns, 7K MWCO	Thermo Fisher Scientific
Zymoprep™ Yeast Plasmid Miniprep Kit I	Zymo Research

3.9 Equipment

Device	Supplier
ÄKTA Start	GE Healthcare
ÄKTA Pure	GE Healthcare
Autoclave LVSA 50/70	Zirbus Technologies
Balance, precision Electronic Balance AX2000	Shimadzu Europe GmbH
Balance, Precision Balance CP3202S	Sartorius AG
Cell counter TC20	Bio-Rad Laboratories, Inc.
Centrifuge accuSpin Micro 17	Thermo Fisher Scientific
Centrifuge Multifuge 3L-R	Heraeus

Centrifuge Multifuge X1R	Thermo Fisher Scientific
CLARIOstar Plus	BMG Labtech
CO_2 Incubator MCO-170AIC	Panasonic
CO_2 Incubator (shaker) New Brunswick S41i	Eppendorf
Discovery Comfort 1 mL/ 200 μL/ 20 μL	HTL Lab Solutions
CytoFlex S	Beckmann Coulter
Electrophoresis power supply EPS 601	Amersham Biosciences
Electroporation device Gene Pulser Xcell	Bio-Rad Laboratories, Inc.
FACS laser 56CLC100	CVI Melles Griot
FACS laser Cobolt Jive	Cobolt
FACS laser Sapphire 488 LP	Coherent
Fluorescence-activated cell sorter (FACS) inFlux v7 sorter #X64650000063	BD (Becton, Dickinson and Company)
Freezer (-20°C) FS12790N	BEKO
Freezer (-80 °C) VIP™ Serie Revco	Sanyo
Gel chambers Multiple gel caster	Hoefer
Gel documentation GelDoc-IT	UVP
Glassware	Schott, VWR, Merck KGaA
Heating block Thermomixer compact	Eppendorf
HPLC 1260 Infinity chromatography system	Agilent Technologies
Ice machine SP125 AS	Nordcap
Incubator (shaker) Labtherm	Adolf Kühner AG
Incubator (shaker) Thermotron High Temperature	Infors
Laminar Flow Workbench Safe 2020	Thermo Scientific
Magnetic stirrer IKAMAK RCT	IKA-Labortechnik
NanoDrop One	Thermo Fisher Scientific
PCR machine T100™	Bio-Rad Laboratories, Inc.
pH-meter pH 50 VioLab	Dostmann
Photometer BioPhotometer	Eppendorf
Pipetting controller Pipetus R standard	Hirschmann Laborgeräte
Plate centrifuge 5804 R	Eppendorf
Series 1100 HPLC system	Agilent Technologies Inc
Ultrasonic homogenizer SONOPULS HD 2070	Bandelin
Vortex Genie 2	Scientific Industries
Water bath Precision™ TSGP10	Thermo Fisher Scientific

3.10 Software

Software	Supplier
Äkta Unicorn™ Start	GE Healthcare
Äkta Unicorn™ 7	GE Healthcare
BD InfluxTM software	BD Bioscience
BioRender	Science Suite Inc.
ChimeraX	UCSF Resource for Biocomputing, Visualization, and Informatics
FlowJo (V10.7.1)	FlowJo
GraphPad PRISM	GraphPad Software Inc.
MARS data analysis software	BMG Labtech
Octet Data Acquisition and Analyis	FortéBio
SnapGene® 4.3.5	Insightful Science
VisionWorks	Analytic Jena

4 Methods

4.1 Molecular biological methods

4.1.1 Complementary DNA (cDNA) synthesis from immunized chicken

After chicken immunization, total mRNA was obtained from the immunization facility. The mRNA was washed with 70% ethanol and 70% isopropanol, before air drying the pellet. After evaporation of surplus isopropanol, the mRNA pellet was dissolved in 25 μL of RNAse free water. cDNA synthesis was performed utilizing the SuperScript III First-Strand Kit according to the manufactures protocol (**Table 1**).

Table 1: cDNA synthesis reaction mixture and temperature program for generation of cDNA.

Compound	Volume	Step in protocol	Temperature	Time
RNA	25 μL	Denature RNA	65 °C	5:00 min
Hexamer primer	5 μL	Cool 1 min on ice		
dNTPs	5 μL			
H_2O	15 μL			
Cooled reaction mix	50 μL	Primer annealing	25 °C	5:00 min
10x RT buffer	10 μL	cDNA synthesis	50 °C	60:00 min
25 mM $MgCl_2$	20 μL	Heat inactivation	85 °C	5:00 min
0.1 mM DTT	10 μL	Add 5 μL RNAse H and incubate 20:00 min at 37 °C		
RNAse Out	5 μL			
Superscript III	5 μL			

4.1.2 Polymerase chain reaction (PCR)

In this work, PCR was utilized to amplify DNA segments for subsequent cloning into expression or yeast surface display plasmids. Each PCR was performed with a specific set of primers (section 3.4.4), responsible for introducing DNA overhangs carrying either restriction sites for golden gate cloning or sequences for homologous recombination in yeast. Depending on the primer set, annealing temperature and elongation time were adjusted (NEB Tm calculator). In this work, Q5 polymerase was utilized for the amplification of all sequences cloned into expression plasmids (**Table 2**). In contrast, OneTaq polymerase was utilized for the amplification of DNA sequences utilized for homologous recombination in yeast. Furthermore, OneTaq polymerase was utilized for identifying insert bearing *E. coli* single clones. Depending on the primer set annealing temperatures and elongation times were adjusted (**Table 3**). Subsequent analysis of PCR products was carried out utilizing agarose gel electrophoresis.

Table 2: Q5 reaction mixture and temperature program for amplification of DNA segments.

Compound	Volume	PCR Step	Temperature	Time	Repetition
ddH_2O	Fill to 50 µL	Initial denaturation	98 °C	2:00 min	1x
5x Q5 reaction buffer	10 µL	Denaturation	98 °C	0:20 min	30x
dNTPs (10mM)	1 µL	Annealing	Primer dependent	0:20 min	30x
Up Primer (10 µM)	2.5 µL	Elongation	72 °C	0:30 min per kbp	30x
Lo Primer (10 µM)	2.5 µL	Final Elongation	72 °C	5:00 min	1x
Q5 polymerase	0.5 µL				
Template DNA (10ng)	1 µL				

Table 3: OneTaq reaction mixture and temperature program for amplification of DNA segments.

Compound	Volume	PCR Step	Temperature	Time	Repetition
ddH_2O	Fill to 50 µL	Initial denaturation	94 °C	2:00 min	1x
5x OneTaq reaction buffer	10 µL	Denaturation	94 °C	0:20 min	30x
dNTPs (10mM)	1 µL	Annealing	Primer dependent	0:20 min	30x
Up Primer (10 µM)	1 µL	Elongation	68 °C	1:00 min per kbp	30x
Lo Primer (10 µM)	1 µL	Final Elongation	68 °C	5:00 min	1x
Q5 polymerase	0.25 µL				
Template DNA	1 µL				

4.1.3 Golden Gate cloning

Cloning of different constructs into pTT5 or pET32 expression plasmids was carried out utilizing Golden Gate cloning. For Golden Gate reactions, plasmid and insert were mixed in a molar ratio of 3:1 (**Table 4**). Afterwards, 4 µL of the Golden Gate mixture were transformed into chemically competent E. coli cells (section 4.2.2).

Table 4: Golden Gate reaction mixture and temperature program.

Compound	Volume	Golden Gate step	Temperature	Time	Repetition
ddH_2O	Fill to 20 µL	Digestion	37 °C	2:00 min	1x
Plasmid (75ng)	1 µL	Digestion	37 °C	1:00 min	30x
Insert	Varying volume	Ligation	16 °C	1:00 min	30x
T4 ligase buffer	2 µL	Digestion	37 °C	10:00 min	1x
T4 ligase	0.5 µL	Heat inactivation	60 °C	10:00 min	1x
Restriction enzyme	1 µL				

4.1.4 Restriction enzyme digest

Restriction digests were carried out in order to analyze the insert size of plasmids prior to sequencing, prepare plasmids for homologous recombination in yeast, and remove methylated DNA. Methylated DNA was removed from PCR products by adding 1μL of DpnI to the reaction mixture and an incubation over-night at 37°C. Plasmids prepared for homologous recombination were digested with a 5-fold excess of restriction enzymes over-night at 37 °C. In contrast, plasmids analyzed for correct insert size were incubated 30 minutes at 37 °C utilizing the respective restriction enzymes. Plasmids were applied to an agarose gel, in order to confirm correct the correct insert size and complete cleavage.

4.1.5 Agarose gel electrophoresis

Agarose gel electrophoresis was utilized to analyze PCR products and restriction digests. Analysis was carried out with a gel prepared from 1 % (w/v) agarose in TAE buffer, mixed with the DNA dye HDGreen. Samples were mixed with a 6x loading dye prior to loading to the gel. Additionally, 1 kb plus DNA ladder was added to the gel. Electrophoresis was carried out for 20-30 minutes at 120 V. DNA bands were visualized using UV light.

4.1.6 DNA purification

PCR products and cleaved plasmids utilized for homologous recombination in yeast were purified utilizing the Wizard® SV Gel and PCR Clean-Up System according to the manufacturers protocol. After elution, DNA was stored at -20 °C.

4.1.7 Determination of DNA concentration

The concentration of purified DNA was determined with the NanoDrop One by measuring the absorption at 260 nm and applying the Lambert-Beer law.

4.1.8 DNA sequencing

For DNA sequencing 12 μL of plasmid (100 ng/μL) were mixed with 3 μL of sequencing primer and sent to Microsynth Seqlab GmbH (Göttingen, Germany) for sanger sequencing.

4.2 Microbiological methods

4.2.1 Cultivation of *E. coli*

E. coli cells were grown either in dYT media or on dYT agar plates supplemented with the antibiotic corresponding to the resistance gene of the utilized plasmid. Liquid cultures were grown over-night at 37 °C and 180 rpm in glass flasks containing 50 mL media. Agar plates were prepared in sterile plastic petri dishes and incubated at 37 °C over-night.

4.2.2 Generation and transformation of chemically competent TOP10 *E. coli* cells

For the generation of chemically competent *E. coli* cells, a preculture was grown in 50 mL dYT medium over-night at 37 °C and 180 rpm. The following day, the optical density at 600 nm (OD_{600}) was measured and a flask containing 250 mL TYM medium was inoculated to an OD_{600} of 0.1. The cells were grown at 37 °C and 180 rpm until an OD_{600} of 0.6-0.8 was reached. The cells were collected *via* centrifugation at 4000 rpm and 4°C, the supernatant discarded and subsequent washed with 50 mL TfB1 buffer. After washing, the cells were resuspended in 15 mL TfB 2 buffer, aliquoted to 100 μL and shock frozen in liquid nitrogen. The cells were stored at -80 °C.

Prior to the transformation of chemically competent TOP10 *E. coli* cells, an aliquot was thawed on ice and mixed with the DNA to be transformed. The cell DNA mixture was incubated for 20 minutes on ice. Transformation was carried out *via* heat shock at 42 °C for 35 seconds with subsequent incubation on ice for 5 minutes. Afterwards 1 mL of dYT was added and the cells were regenerated at 37 °C for 60 minutes.

After regeneration, the cells were either collected by centrifugation, resuspended in 100 μL media and spread on agar plated supplemented with the antibiotic corresponding to the resistance gene of the plasmid or were transferred to 50 mL media supplemented with antibiotic.

4.2.3 Plasmid isolation

For the isolation of smaller amounts of plasmid, 4 mL of dYT medium supplemented with the antibiotic corresponding to the resistance gene of the plasmid were inoculated with single clone and grown over-night. The next day, plasmid isolation was carried out utilizing the Wizard® Plus SV Minipreps DNA Purification System according to the manufacturers protocol.

For the isolation of larger amounts of plasmid, the culture volume was increased to 50 mL. Plasmid isolation was carried out utilizing the PureYield™ Plasmid Midiprep System according to the manufacturers protocol.

4.2.4 Generation and transformation of electrocompetent competent SHuffle® T7 Express E. coli cells

For the generation of electrocompetent *E. coli* cells, a preculture was grown in 50 mL dYT medium over-night at 37 °C and 180 rpm. The following day, the OD_{600} was measured and 50mL dYT medium were inoculated to an OD_{600} of 0.1. The cells were grown at 37 °C and 180 rpm until an OD_{600} of 0.6-0.8 was reached. The cells were collected *via* centrifugation at 4000 rpm and 4°C, the supernatant discarded and subsequent washed with 50 mL ice-cold distilled water. The washing step was repeated with 30 and 10 mL of ice-cold water. Afterwards, the cells were resuspended in 500 μL ice-cold water and mixed with 50 % (v/v) glycerol for storage in 100 μL aliquots at -80 °C.
Prior to transformation, the cells were thawed on ice and a 2 mm electroporation cuvette was washed extensively with distilled water and incubated on ice. Afterwards, the DNA is added to the cells and the mixture is incubated for 5 minutes on ice. Electroporation was performed at 2.5 kV, 25 μF, and 200 Ω for 5 msec. Immediately afterwards, 1 mL of prewarmed dYT medium is added to the cells. Regeneration was carried out at 37 °C for 60 minutes. After the regeneration, the cell suspension was utilized to inoculate 50 mL of dYT medium supplemented with kanamycin and chloramphenicol.

4.2.5 Protein production in *E. coli* cells

For protein production a preculture of 50 mL dYT medium containing kanamycin and chloramphenicol was inoculated with cells containing the expression plasmid and sulfhydryl oxidase (SOX) helper plasmid. The following day, the OD_{600} was measured and 250mL SB medium were inoculated to an OD_{600} of 0.1. The cells were grown at 37 °C and 180 rpm until an OD_{600} of 0.6-0.8 was reached. 1M isopropyl ß-D-1-thiogalactopyranosid (IPTG; final concentration 1mM) and 1.25 g L-arabinose (final concentration 0.5 % (w/v)) were added to the cell suspension. Subsequent incubation was carried out at 20 °C and 180 rpm over-night. The next day, cells were harvested by centrifugation (4000 rpm, 4°C, 10 minutes) and resuspended in IMAC A. Cell lysis was carried out on ice *via* sonification three times for three minutes with three minutes between each sonification cycle. Cell debris was removed by centrifugation at 14000 rpm, 4 °C for 15 minutes and subsequent sterile filtering (0.2 μm filter).

4.2.6 Cultivation of *S. cerevisiae*

S. cerevisiae cells were grown either in SD-W media or on SD-W agar plates supplemented with ampicillin and kanamycin. Liquid cultures were grown over-night at 30 °C and 180 rpm in plastic flasks containing 50 mL media. Agar plates were prepared in sterile plastic petri dishes and incubated at 30 °C over-night.

4.2.7 Generation and transformation of electrocompetent EBY100 *S. cerevisiae* cells for library generation

Electrocompetent *S. cerevisiae* cells were generated according to the protocol described in Benatuli et al. (238). Briley, 1 L of YPD medium without antibiotics was inoculated to and OD_{600} of 0.3. Cells were grown at 30°C and 180 rpm until an OD_{600} of 1.6-1.8 was reached. Afterwards, the cells were harvested by centrifugation (4000 rpm, 4 min, 4 °C) and washed twice with 50 mL ice-cold water and once with 50 mL ice-cold buffer E. After the washing step, the cell pellets were resuspended in 200 mL lithium acetate/DTT buffer and incubated for 30 minutes at 30 °C and 180 rpm. The cells were again collected *via* centrifugation and washed twice with 50 mL ice-cold buffer E. Afterwards, the cells were resuspended in 5 mL ice-cold buffer E and filled to 8 mL with ice-cold buffer E. For each electroporation 400 μL of the cell suspension were mixed with plasmid and insert DNA, transferred into an electroporation cuvette which was pre-chilled on ice and incubated for 5 minutes on ice. As a negative control, an electroporation with only cleaved plasmid DNA was prepared. Electroporation was performed at 2.5 kV, 25 μF, and 200 Ω for 5 msec. Immediately afterwards, 2 mL of a 1:1 YPD:1 M sorbitol mixture was added to the cells. Regeneration was performed for 60 minutes at 30 °C and 180 rpm. After the regeneration, the cells were again harvested by centrifugation and resuspended in 10 mL PBS. Serial 1:10 dilutions were prepared for the library and negative control (10^{-1} to 10^{-8}) and 100 μL of each dilution was plated on SD-W agar plates for determining the number of transformed cells.

4.2.8 Induction of surface presentation

Induction of yeast surface presentation was carried out by changing the medium from SD-W to SG-W. Therefore, yeast cells were harvested by centrifugation and resuspended in SG-W to attain an OD_{600} of 1. The cells were grown over-night at 30°C and 180 rpm. In contrast, single clones were grown at least 24 hours at 30°C and 180 rpm in a 3:1 SD-W:SG-D mixture.

4.2.9 Plasmid isolation

For plasmid isolation 2 mL of SD-W medium were inoculated with a single clone and grown over-night. The next day, plasmid isolation was conducted utilizing Zymoprep™ Yeast Plasmid Miniprep Kit I according to the manufacturers protocol. After plasmid isolation, freshly prepared electrocompetent *E. coli* cells were transformed with 5 μL of the plasmid solution. *E. coli* cells were plated, grown over-night and based on a single clone plasmid isolation was performed (section 4.2.3).

4.2.10 Cultivation of B-cell cell lines

B cells were cultivated in a T25 flask containing RPMI-1640 medium supplemented with 10 or 20 % (v/v) FBS and 1 % (v/v) P/S at 37 °C under humidified atmosphere containing 5 % CO_2. Cells were passaged in 1:2 – 1:10 ratios twice a week.

4.2.11 Cultivation of adherent cell lines

Adherent cells were cultivated in a T75 flask containing 10 mL of DMEM medium supplemented with 10 % (v/v) FBS and 1 % (v/v) P/S at 37 °C under humidified atmosphere containing 5 % CO_2. Passaging of cells was conducted after reaching confluency of 80-90%. Therefore, cultivation medium was removed, the cells washed with 10 mL of PBS by gentle shaking and after removal of the PBS, 1 mL of 0.05 % Trypsin-EDTA was added. Trypsinization was stopped with 9 mL of cultivation medium after cells detached from the flask. Passaging was carried out in 1:4 to 1:10 ratios and respective amounts of cultivation medium were added achieve a culture volume of 10 mL.

4.2.12 Protein expression in HEK Expi293F™ cells

HEK Expi293F™ cells were cultivated in 125 mL flask under standard conditions (37 °C, humidified atmosphere containing 8 % CO_2 and 110 rpm) in a volume of 30 mL Expi293™ Expression Medium. Cells were passaged twice a week to obtain cell densities of 0.8-5x10^6 vc/mL.

For protein production in HEK Expi293F™ cells, the cells number of a 30 mL culture was adjusted to 2.5x10^6 vc/mL. Afterwards, a mixture of 50 μg plasmid DNA in 2.5 mL 150 mM NaCl was prepared and vortexed for 5 seconds. Subsequently, 200 μL of Transporter 5™ solution were added to the mixture, mixed by vortexing for 5 seconds and incubated for 20 minutes at room temperature. Afterwards, the mixture was added dropwise and under constant shaking to the cell culture. After incubating the cells under standard conditions for 16-18 hours 825 μL of a 20 % (w/v) tryptone solution were added. Five days after transfection, the cells were harvested by centrifugation and the supernatant was utilized for protein purification.

In order to increase expression yields, Gibo™ ExpiFectamine™ 293 Transfection Kit was utilized for transfection following the manufactures protocol. Briefly, cell density of a 25.5 mL culture was adjusted to 2.5x10^6 vc/mL. Afterwards, a mixture of 30 μg of plasmid DNA and OptiMEM™ with a final volume of 1.5 mL was prepared. Simultaneous, a mixture of 80 μL ExpiFectamine™ and 1.5 mL OptiMEM™ was prepared. Both mixtures were incubated for 5 minutes. Afterwards, the ExpiFectamine™ mixture was added to the DNA mixture, mixed by vortexing for 5 seconds and incubated for 20 minutes at room temperature. Afterwards, the mixture was added dropwise and under constant shaking to the cell culture. After incubating the cells under standard conditions for 16-18 hours 150 μL of Transfection

Enhancer 1 and 1.5 mL of Transfection Enhancer 2 were added. Five days after transfection, the cells were harvested by centrifugation and the supernatant was utilized for protein purification.

4.3 Biochemical methods

4.3.1 Protein A chromatography

Purification utilizing a HiTrap™ Protein A column was carried out for antibodies and proteins carrying a human Fc. The column was connected to a Äkta™ purification system and equilibrated with 4 CV of TN buffer. Afterwards, the sterile filtered (0.2 μm filter) cell culture supernatant was loaded to the column. Washing with TN buffer was conducted until the A_{280} baseline was reached. For isocratic elution, 100 mM glycine pH 3.0 was applied to the column and the fractions were neutralized by 250 μL Tris pH 9.0. The protein containing fractions were pooled and dialyzed in TN buffer (section 4.3.4). For storage at 4 °C, 20 % (v/v) ethanol was applied to the column.

4.3.2 Immobilized metal affinity chromatography (IMAC)

Protein purification by IMAC was conducted for SEEDbodies, thioredoxin vNAR fusions and chicken scFvs. Therefore, a HiTrap™ IMAC column was connected to a Äkta™ purification system and equilibrated with 4 CV of TN buffer. Afterwards, the sterile filtered (0.2 μm filter) cell lysate or cell culture supernatant was loaded to the column. Washing with TN buffer was conducted until the A_{280} baseline was reached. For isocratic elution, buffer B was applied to the column. Protein containing fractions were pooled and in case of SEEDbodies were further purified by protein A chromatography (section 4.3.1), while thioredoxin vNAR fusions and solitary scFvs were further purified by Strep-Tactin purification (section 4.3.3). After each purification, 5 CV 100 mM EDTA was applied to the column for stripping, followed by 5 CV of 100 mM $NiCl_2$ for re-charging. For storage at 4 °C, 20 % (v/v) ethanol was applied to the column.

4.3.3 Purification *via* Strep-Tactin® system

Purification utilizing the Strep-Tactin system was performed as a secondary purification step after IMAC purification of thioredoxin vNAR fusions and solitary chicken scFvs. Therefore, the column was connected to a Äkta™ purification system and equilibrated with 2 CV of buffer W. Afterwards, the pooled fractions of the IMAC purification were loaded to the column. The column was washed with buffer W, until the A_{280} baseline was reached. The protein was eluted isocratic form the column by applying buffer E to the column. After the protein was eluted, the column was regenerated with 15 mL of 10 mM NaOH. Immediately afterwards, the column was washed with 8 CV of buffer W and stored at 4 °C. The protein containing fractions were pooled and dialyzed in TN buffer (section 4.3.4).

4.3.4 Dialysis

Dialysis was carried out after protein purification in TN buffer in a 1:1000 sample:dialysis buffer ratio. The dialysis membrane with a 14 kDa molecular weight cut-off was sealed at both ends and incubated over-night at 4°C under constant stirring in the dialysis buffer.

4.3.5 Determination of protein concentration

In order to determine protein concentration, molecular weight and molar extinction coefficient were calculated based on the protein sequence utilizing ExPAsy ProtParam (https://web.expasy.org/protparam/). NanoDrop One was utilized to measure the absorption at 280 nm.

4.3.6 Sodium dodecyl sulfate polyacrylamide gel electrophoresis (SDS-PAGE)

In order to analyze proteins after purification and dialysis, discontinuous and reducing SDS-PAGE was performed. Therefore, protein samples were mixed with 5x reducing SDS-PAGE sample buffer, incubated for 10 minutes at 98 °C and spined down. Each sample was applied to a pocket of a 5 % acrylamide stacking gel. Separation of proteins was achieved by a 15 % acrylamide separation gel. SDS-PAGE was carried out at 300V and 40 mA for 30-45 minutes. Afterwards, the gel was stained utilizing coomassie solution. Destaining was performed with 10 % (v/v) acetic acid.

4.3.7 Alexa Fluor 647 labeling of proteins

Proteins were labeled with NHS-Alexa Fluor 647 according to the manufacturers protocol. Briefly, a 5-fold molar excess of NHS-Alexa Fluor 647 was added to a protein solution and incubated for 30 minutes at room temperature. Afterwards, the reaction was stopped by incubation with 1M Tris pH 8 for 10 minutes. Surplus unreacted fluorophore was removed by a gel filtration column. Gel filtration columns utilized according to the manufacturers protocol.

4.3.8 Biotinylating of proteins

Proteins were labeled with EZ-Link™ Sulfo-NHS-Biotin according to the manufacturers protocol. Briefly, a 5-fold molar excess of EZ-Link™ Sulfo-NHS-Biotin was added to a protein solution and incubated for 30 minutes at room temperature. Afterwards, the reaction was stopped by incubation with 1M Tris pH 8 for 10 minutes. Surplus unreacted biotin was removed by a gel filtration column. Gel filtration columns utilized according to the manufacturers protocol.

4.3.9 Immobilization of proteins on HiTrap™ NHS-activated HP column

Immobilization of 6G11 on a pre-packed NHS-activated column was performed according to the manufacturers protocol. Briefly, the column was washed with 6 mL ice-cold 1 mM HCl prior to the slowly applying 1 mg of 6G11 to the column. Afterwards, the column was washed with 6 mL Buffer A (0.5 M ethanolamine, 0.5 M NaCl, pH 8.3), 6 mL Buffer B (0.1 M sodium acetate, 0.5 M NaCl, pH 4) and 6 mL Buffer A, followed by a 15-minute incubation at room temperature. Subsequently, the column was washed with 6 mL Buffer B, 6 mL Buffer A and 6 mL Buffer B, before applying 2 mL of TN buffer and storing at 4 °C.

4.3.10 MMP-9 activation

MMP-9 was activated by addition of p-Aminophenylmercuric acetate to a final concentration of 1 mM. Afterwards, the mixture is incubated over night at 37°C. Activated MMP-9 was stored at 4°C.

4.3.11 Thermal shift assay

For protein melting point analysis, 18 μL of protein solution with a concentration ranging from 0.5-1 mg/mL was mixed with 2 μL of a 1:10 dilution of SYPRO® Orange. Afterwards, the mixture was transferred into a Hard-Shell® 96-well PCR plate and sealed with a Microseal PCR plate sealing film. A temperature gradient from 20 °C to 98 °C, with a temperature increase of 0.5 °C per 30 seconds was applied with constant fluorescence monitoring.

4.3.12 NanoDSF

Protein melting point analysis utilizing Prometheus NT.48 Protein Stability Instrument (NanoTemper Technologies) was carried out by applying the protein solution to a capillary and measuring tryptophan fluorescence at 350 and 330 nm. A temperature gradient from 20 °C to 98 °C, with a temperature increase of 1°C per 60 seconds was applied with constant fluorescence monitoring.

4.3.13 Size exclusion chromatography (SEC)

In order to investigate protein aggregation, SEC measurements were performed. Therefore, 30-50 μg of protein were applied to a TSKgel SuperSW3000 column. Each run was performed in TN buffer for 20 minutes with constant monitoring of the absorption at 280 nm.

4.4 *In-vitro* assays

4.4.1 Enzyme-linked immunosorbent assay (ELISA)

Enzyme-linked immunosorbent assays were carried out to analyze binding affinites of thioredoxin vNAR fusions and solitary expressed chicken scFvs. Therefore, 100 μL of a 10 μg/mL solution of the respective antibody were added into each well of a Nunc MaxiSorp ELISA plate. The plate was sealed with an ELISA plate sealer and incubated over-night at 4 °C. The next day, the antibody solution was removed, and each well was washed three times with 200 μL of PBST. Afterwards, 200 μL of 1 % (w/v) BSA in PBSB was added in each well and incubated for 1 hour at room temperature. Subsequently, each well was washed three times and 100 μL thioredoxin vNAR fusions or solitary scFvs were added in different concentrations and incubated for 1 hour at room temperature. After three subsequent washing steps, 100 μL StrepTactin-HRP (diluted 1:10000) was added to each well and incubated for 1 hour at room temperature. Subsequently each well was washed five times and 100 μL of TMB One Solution was added and incubated until a color change was visible. The reaction was stopped immediately with 100 μL of 1 % (v/v) HCl. Absorbance at 405 nm was measured in the CLARIOstar Plus.

4.4.2 Biolayer Interferometry (BLI)

BLI measurements were carried out for affinity and epitope analysis. For determination of affinity, antibody solutions with 10 μg/mL were prepared in kinetics buffer and 200 μL were added to each well in a column of a black 96 flat bottom plate. Serial dilutions of antigens corresponding to the antibody were also prepared in kinetics buffer and added to a row on the plate. Antibodies were loaded to protein A or anti-hIgG Fc capture biosensors for 120 seconds or until a wavelength shift of 0.7 nm was reached. Association and dissociation of the antigen was carried out for 60-360 seconds. For repeated use of a biosensor within one assay, regeneration in glycine pH 1.7 and subsequent neutralization in kinetics buffer was carried out. For epitope determination, 6G11 was loaded as described above and subsequently A6G11S2B and A6G11S2NC were associated consecutively.

4.4.3 Immunostaining of yeast cells

In order to isolate binding moieties with desired properties, yeast surface display was utilized, which in turn required the verification of surface presentation and antigen binding.
In the first screening round 3-5x10^8 cells were analyzed, while in subsequent screening rounds 10 times the amount of yeast cells isolated in the last round were analyzed. Antigen concentrations were varied during the screening process, for isolation of binders with higher affinity. Prior to the staining, yeast cells were collected by centrifugation (13000 rpm, 1 min, room temperature) and washed once with 1 mL PBSB. Afterwards, the cells were incubated in PBSB containing the antigen (20 μL per 1x10^7 cells) for

30 minutes at room temperature. Subsequently, the cells were washed twice with 1 mL PBSB. Verification of antigen binding was carried out based on the tags present in the antigen and staining with appropriate secondary antibodies. Secondary antibodies were incubated for 15 minutes at 4 °C or for 30 minutes at 4°C if antibodies for verification of surface presentation were included in the staining mixture. In addition, antigens were coupled directly to NHS-Alexa Fluor 647 (section 4.3.7), thereby eliminating the need for further staining.

Libraries based on the classic yeast surface display required the staining of surface presentation in each round. Therefore, cells were first incubated with the antigen, washed twice with 1 mL PBSB and incubated with the detection antibody for the antigen and the anti-c-myc-FITC antibody.

In contrast, libraries utilizing the simplified yeast surface display required analysis of tGFP and c-myc tag correlation prior to screening. Therefore, $1x10^7$ yeast cells were collected by centrifugation and washed once with 1 mL PBSB. Afterwards, the cells were incubated for 30 minutes at 4°C with an anti-c-myc biotin antibody, washed twice with 1 mL PBSB, and incubated with streptavidin-allophycocyanin for 15 minutes on ice. After washing twice with 1 mL of PBSB the cells were resuspended in 200 μL of PBSB and analyzed by flow cytometry. If correlation between c-myc surface presentation and intracellular tGFP was ensured, the tGFP signal was utilized during the screening process as surface presentation marker.

For each screening round, a negative control was prepared in the same fashion as the sample utilized for sorting, however instead of incubation with the antigen, the cells were incubated only in PBSB.

4.4.4 Cell binding assay

Binding of antibody constructs was analyzed in cell binding assays. Therefore, 100000-250000 cells were added to each well of a 96-well U bottom plate. Cells were collected by centrifugation at 800xg for 3 minutes at 4 °C. After washing the cells prior to staining with 200 μL of PBSB, the antibody construct was added to the cells in a volume of 20 μL diluted in PBSB and incubated for 30 minutes at room temperature. After washing the cells twice with 200 μL PBSB, the secondary antibody was added and incubated for 15 minutes on ice. If the antibody was directly labeled with Alexa Fluor 647 the beforementioned step was not required. After two additional washing steps, cells were resuspended in 100 μL PBSB for flow cytometry analysis.

4.4.5 ADCC Reporter Assay

ADCC assays were performed with Raji cells as target cells and ADCC Bioassay Effector Cells from Promega as effector cells. The effector cells are based on the Jurkat cell line, which express firefly luciferase upon activation of CD16 and signal transduction *via* the NFAT pathway.

Effector cells, target cells and antibody dilutions were prepared in ADCC assay buffer. 12500 target cells were transferred into each well of a 96 flat bottom plate and mixed with 75000 effector cells for an effector-to-target ratio of 6:1. Antibody dilutions were added and incubated for 6 hours under standard conditions. Subsequently luciferase substrate buffer was added to each well, incubated for 5 minutes and luminescence was measured in the CLARIOstar Plus. For data analysis, the plate background was subtracted from each well.

5 Results and Discussion

5.1 Implementation of pH-dependency into an anti-matuzumab vNAR and investigation of inhibitory effects in different fusion proteins

Prior to this work, vNARs directed against cetuximab and matuzumab were isolated from semi-synthetic, CDR3 randomized vNAR libraries (84). The matuzumab specific vNARs revealed interference with antigen binding capabilities, however lacked pH-dependency, despite the presence of three histidines within the CDR3. In order to incorporate pH-dependency into the anti-matuzumab vNAR 1 (AMV1), a sub-library was required. This sub-library was generated by CDR3 randomization *via* PCR utilizing a degenerate primer to carry either histidine or the original amino acid at each position. This approach should ensure every possible combination of histidines in the CDR3. Additionally, this strategy should enable the isolation of binders with different degrees of pH-dependency and affinity. The library was constructed utilizing the simplified yeast surface display, based on ribosomal skipping to verify vNAR surface presentation *via* intracellular tGFP expression (234). Following library construction, the correlation between c-myc surface presentation and tGFP was verified, to utilize tGFP expression as surface presentation marker in the subsequent screening process (**Figure S 2**). After confirming the correlation, the library was incubated with 1μM matuzumab at a pH of 7.4 and sorted towards matuzumab binding (**Figure 12B**).

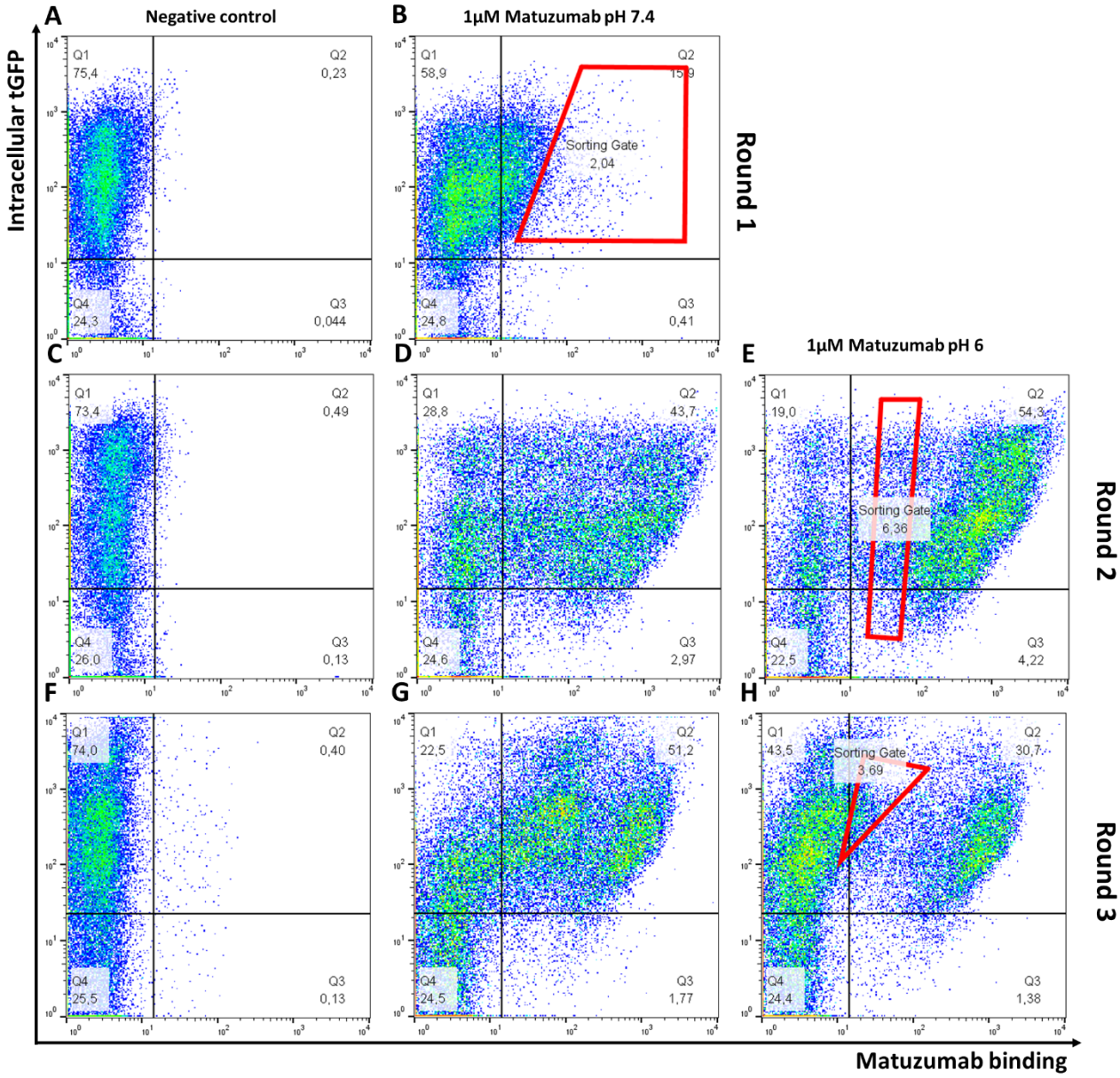

Figure 12: Overview of the screening campaign for the isolation of pH dependent anti-matuzumab vNARs (AMV1Hs), based on previous isolated, pH-insensitive single clone (AMV1). The cells depicted in the dot plots are gated on viable and single cells. Surface presentation in this screening campaign is verified by intracellular tGFP (y-axis), due to the presence of a T2A site after the vNAR. Matuzumab binding is detected *via* Alexa Flour 647 labeled Matuzumab (x-axis). Form each sample 50000 events were recorded. **A)** Negative control of the newly generated library without matuzumab. Surface presentation is evident in Q1 gate represented by 75.4% of the population. **B)** Library prior to sorting incubated with 1 µM of matuzumab. Binding towards matuzumab is shown in the Q2 gate and is represented by 15.9% of the population. Cells isolated in this screening round are displayed in the red sorting gate. **C)** Negative control of the outcome of the first screening round. Surface presentation is evident in Q1 gate represented by 73.4% of the population. **D)** Matuzumab binding after one sorting round at pH 7.4 and 1 µM matuzumab. Binding towards matuzumab is shown in the Q2 gate and is represented by 43.7% of the population. **E)** Matuzumab binding after one sorting round at pH 6.0 and 1 µM matuzumab. Binding towards matuzumab is shown in the Q2 gate and is represented by 54.3% of the population. Cells isolated in this screening round are displayed in the red sorting gate. **F)** Negative control of the outcome of the second screening round. Surface presentation is evident in Q1 gate represented by 74% of the population. **G)** Matuzumab binding after two sorting rounds at pH 7.4 and 1 µM matuzumab. Binding towards matuzumab is shown in the Q2 gate and is represented by 51.2% of the population. **H)** Matuzumab binding after two sorting rounds at pH 6.0 and 1 µM matuzumab. Binding towards matuzumab is shown in the Q2 gate and is represented by 30.7% of the population. Cells isolated in this screening round are displayed in the red sorting gate.

In contrast to the other screening campaigns in this work, significant binding towards matuzumab is evident in the initial library. However, this finding is not surprising, since the library is based on a highly affine vNAR directed against matuzumab. Hence, strong binding observed in the first screening round, the isolated variants were tested for matuzumab binding at pH 7.4 and 6.0 in the second round. (**Figure 12D** and **E**). Compared to the negative control, strong binding to matuzumab is evident in both samples. Besides a population that exhibits strong pH-independent binding, a pH-dependent population is present, indicated by the difference between the Q2 gates at pH 7.4 and 6.0. In contrast to expectations, binding at pH 6.0 is not decreased, but increased. This contrary finding could be caused by variants which lost antigen binding due to high histidine content, but in turn the high positive charge at pH 6.0 results in electrostatic interactions with matuzumab. In contrast, the strong pH-independent binding in both samples is likely caused by variants carrying sequences similar to the original AMV1 sequence. In order to isolate binders with lower affinity at pH 6.0, a negative selection round at pH 6.0 was performed. Due to the presence of variants not interacting with matuzumab at pH 7.4 and 6.0, the sorting gate was positioned between the pH-independent and non-responsive population. The cells obtained from this sorting round were again examined for pH-dependent binding behavior (**Figure 12G** and **H**). Like in the previous round, a pH-independent, pH-dependent and non-binding population could be observed. In contrast to the last round, the pH-dependent population exhibits stronger binding at pH 7.4 and reduced binding at pH 6.0. Since the desired binding behavior could be observed, sorting was performed for single clone analysis (**Figure 13**).

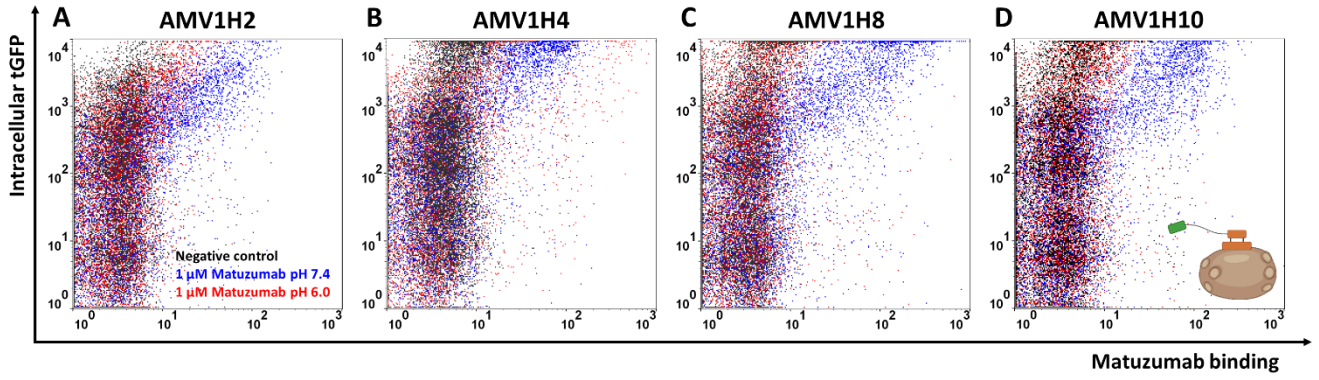

Figure 13: Single clone analysis of four pH-dependent anti-matuzumab (AMV1H) clones isolated after the third screening round. The surface presentation is shown on the y-axis, indicated by intracellular tGFP, while matuzumab binding on the x-axis is verified by Alexa Fluor 647 labeled Matuzumab. The cells depicted in the dot plots are gated on viable and single cells. **A)** Single clone analysis of pH-dependent anti-Matuzumab vNAR clone 2 (AMV1H2). The negative of cells incubated only in PBS is shown in black, while samples incubated with 1µM matuzumab ab pH 7.4 and 6.0 are shown in blue and red respectively. **B-D)** Binding analysis of AMV1H4, AMV1H8 and AMV1H10 with the negative control depicted in black and incubation with 1µM matuzumab at pH 7.4 and 6.0 shown in blue and red respectively. Form each sample 50,000 events were recorded.

Overall, ten single clones were tested towards pH-dependent matuzumab binding. AMV1H2 and AMV1H4 revealed weak binding at pH 7.4 and binding comparable to the negative control at pH 6.0. In

comparison, AMV1H8 and AMV1H10 revealed stronger binding at pH 7.4, while binding at pH 6.0 decreased to negative control level.

The four clones were chosen for sequence analysis and overall, three unique sequences were obtained (**Table S 2**). All analyzed sequences reveal a higher frequency of histidines within the CDR3 compared to the parental variant. Surprisingly, additional mutations in the CDR1 as well as HV2 region could be observed. Since the library is based on a single variant with defined CDR1 and HV2 sequences, these regions are not expected to be mutated. In this case, an accumulation of spontaneous mutations during PCR amplification or replication in yeast seems unlikely. More likely this finding is caused, by a contamination with another vNAR sequence during the PCR amplification during preparation for library generation. Nevertheless, all single clones reveal pH-dependent binding towards matuzumab. Since clone 2 (AMV1H2) revealed the weakest binding during single clone analysis and the CDR3 of clone 8 (AMV1H8) comprises almost entirely of histidine, clone 10 (AMV1H10) was chosen for further characterization. Therefore, AMV1H10 and the parental AMV1 were expressed as one-armed SEEDs (**Figure S 3**). In order to verify pH-dependent binding properties of the expressed AMV1H10, the affinity was measured at pH 7.4 and 6.0 *via* BLI (**Figure 14**). The calculated affinities towards matuzumab at pH 7.4 and 6.0 were 282 nM and 651 nM respectively. Even though the affinity at pH 6.0 is only decreased 2.3-fold, the dissociation rate is faster compared to pH 7.4 (**Figure 14**).

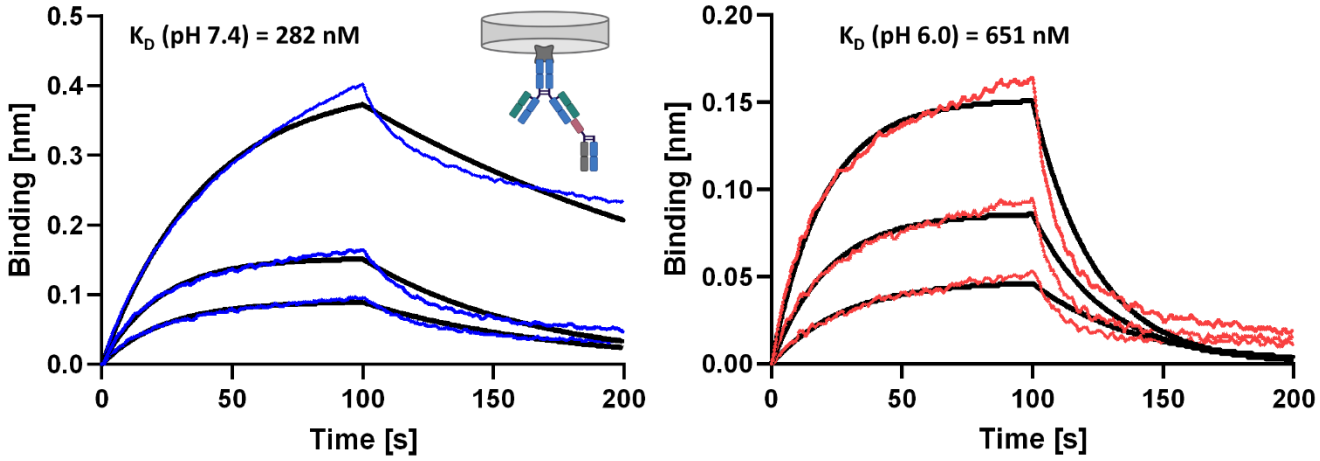

Figure 14: Binding kinetics of AMV1H10 one armed SEED at pH 7.4 and pH 6.0. The binding in nanometer (nm) is shown on the y-axis, while the time in seconds (s) is depicted on the x-axis. Binding curves at pH 7.4 and pH 6.0 are visualized by blue and red lines respectively, while the fits to determine the dissociation constant (K_D) are shown in black.

Furthermore, the affinity is decreased about 300-fold compared to the parental non-pH-responsive AMV1. In order to investigate the inhibitory effect on matuzumab binding both vNARs were co-incubated at different concentrations with matuzumab 30 minutes prior to applying the mixture to the HeLa cells. (**Figure 15**).

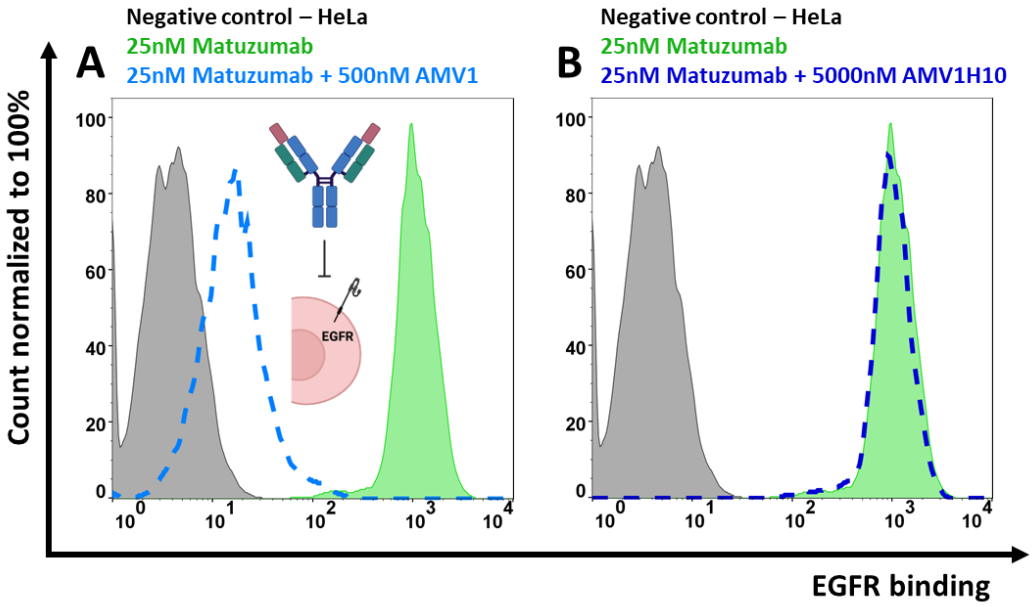

Figure 15: Inhibitory impact of the parental AMV1 and the pH-dependent AMV1H10 on matuzumab binding in co-incubation experiments on HeLa cells. The normalized count is shown on the y-axis, while matuzumab mediated EGFR binding is depicted on the x-axis. Matuzumab binding is detected by Alexa Fluor 647. **A)** Analysis of blocking capacity of AMV1. The negative control of HeLa cells incubated only in PBS is shown in grey. The positive control consists of HeLa cells incubated with 25nM of matuzumab (green) and shifts about three orders of magnitude compared to the negative control. Co-incubated matuzumab with a 20-fold excess of AMV1 is represented by the dashed blue line, with a shift decreased about two orders of magnitude compared to the positive control. **B)** Investigation in the blocking capacity of AMV1H10. The negative control is shown in grey, whereas the positive control is shown in green. Preincubated matuzumab and AMVH10 present in a 2000-fold excess is displayed by the dark blue dashed line with an identical shift as the negative control. Form each sample 10,000 events were recorded.

In case of AMV1, a 200-fold excess of the vNAR reduces matuzumab binding significantly (**Figure 15A**). In contrast, even a 2000-fold excess of AMV1H10 is not able to decrease matuzumab binding (**Figure 15B**). This finding could be either explained by the decreased affinity or an epitope drift during the screening process. An epitope drift could be tested in BLI experiments, by loading matuzumab to the biosensor and subsequent successive association of both vNARs. Further analyzing the inhibitory effect of both vNARs on matuzumab, different constructs were developed and tested in parallel. Overall, both vNARs were tested in a SEED format, with one arm comprising of the vNAR and the other arm comprising of the matuzumab Fab and by fusion to the heavy or light chain of matuzumab with different linkers. All constructs should provide a close proximity of the matuzumab Fab to the vNARs and therefore subsequent higher local concentration of the epitope. Consequently, the reduced affinity of AMV1H10 might be compensated. In case of the SEED constructs a linker was added to the hinge region, to bring the Fab and vNAR into closer proximity. The linker consists of a flexible part which originates from a linker utilized in scFvs and a TEV protease recognition sequence. All constructs were expressed in HEK Expi293 cells, purified and analyzed by SDS-PAGE (**Figure S 3**).

Before exploring cell binding properties of the different constructs, potential pH-dependency of matuzumab was investigated (**Figure 18A**). No difference was observed between both conditions.

Therefore, only the matuzumab binding signal at pH 7.4 is shown as positive control during cell binding assays.

In case of the SEED constructs, the first cysteine in the hinge region was substituted by serine, in order to increase the flexibility of both SEED arms. Furthermore, a linker was added in between the vNAR and hinge, for further enhancement of flexibility. Evaluation of the inhibitory effect of AMV1 and AM1H10 SEED constructs was carried out by BLI and cell binding assays (**Figure S 4**, **Figure 16**). BLI assays indicated no binding of AMV1 SEED at pH 7.4, while weak binding of AM1H10 SEED was observed. However, AMV1H10 SEED binding towards EGFR was restored at pH 6.0. Encouraged by these results, a cell binding assay on HeLa cells was performed (**Figure 16**).

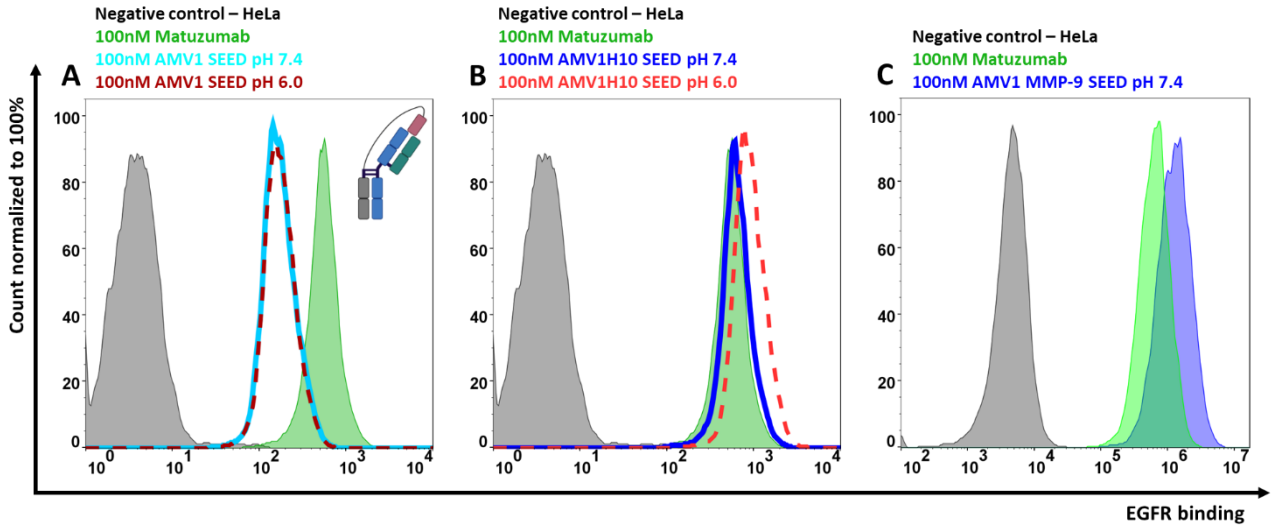

Figure 16: Analysis of binding properties of AMV1 and AMV1H10 matuzumab SEED constructs on HeLa cells. The normalized count is depicted in the y-axis, whereas EGFR binding is shown on the x-axis. The SEED constructs as well as matuzumab were labeled with Alexa Fluor 647 prior to the staining. **A)** Binding analysis of AMV1 matuzumab SEED at pH 7.4 and 6.0. The negative control is shown in grey, while the positive control is depicted in green. The positive control reveals a shift of two orders of magnitude compared to the negative control. AMV1 matuzumab SEED incubated at pH 7.4 and 6.0 are displayed by the light blue and dashed dark red line respectively. Both constructs display an about 5-fold decrease in binding compared to the positive control. **B)** Binding properties of AMV1H10 matuzumab SEED at pH 7.4 and 6.0. The negative control is depicted in grey, whereas the positive control is displayed in green. Binding of AMV1H10 matuzumab SEED at pH 7.4 and 6.0 is shown by the blue and dashed red line respectively. Binding of AMV1H10 SEED at pH 7.4 is in the same range as matuzumab, binding at pH 6.0 is slightly increased. **C)** Binding analysis of the MMP9 cleavable AMV1 SEED construct. The negative control is depicted in grey, the positive control in green and binding of the SEED at pH 7.4 in blue. Binding of AMV1 MMP-9 SEED is increased about 2-fold compared to the positive control.

AMV1 SEED revealed non-pH-dependent binding behavior and a small, but significant decrease in binding, compared to the matuzumab positive control (**Figure 16A**). This finding could also be caused by the differences in valency of matuzumab and the SEED construct. Since matuzumab is a bivalent antibody and the one arm of the SEED construct is formed by the vNAR, differences in cell binding could occur. However, binding of AMV1H10 SEED at pH 7.4 is not decreased compared to matuzumab binding and at pH 6.0 is even slightly increased (**Figure 16B**). Therefore, matuzumab is a suitable positive control for the SEED constructs. Despite this consideration, the lack of inhibitory behavior of AMV1H10

SEED at pH 7.4 is probably not related to an improper linker, since AMV1 SEED reveals a decrease in cell binding. However, since AMV1 SEED reveals less strong restriction of binding, as could be expected by co-incubation experiments, the initial linker was substituted by a longer linker containing an MMP-9 site (**Figure 16C**). However, the linker change did not result the desired effect, but instead nullified the inhibitory effect of AMV1. Besides analysis of inhibitory effects, unspecific binding was investigated, as AMV1H10 SEED revealed increased binding at pH 6.0 on HeLa cells. Therefore, binding of AMV1 and AMV1H10 SEEDs were tested on EGFR negative IM9 cells at pH 7.4 and 6.0 (**Figure 17**).

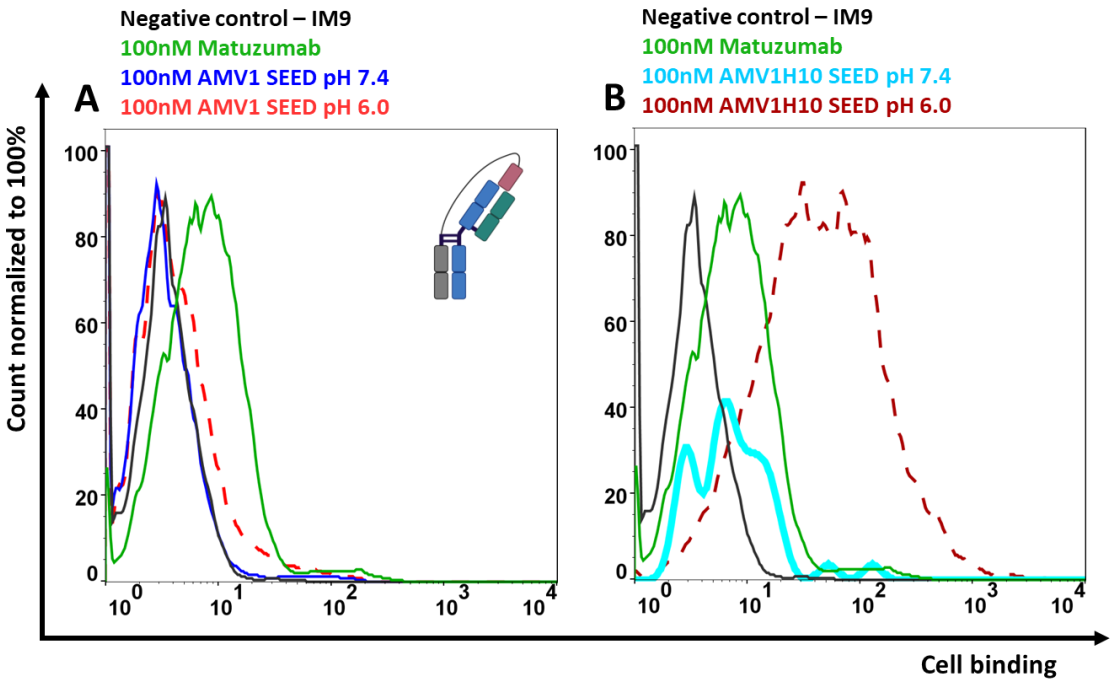

Figure 17: Off-target binding analysis of AMV1 and AMV1H10 matuzumab SEEDs on EGFR negative IM9 cells. The y-axis depicts the normalized count, while the x-axis shows off-target binding. **A)** Off-target binding analysis of AMV1 matuzumab SEED. IM9 cells incubated only with PBS serve as negative control, indicated by the black line. IM9 cells incubated with matuzumab as well as AMV1 matuzumab SEED at pH 7.4 and 6.0 are displayed by the green, blue, and dashed red lines. While matuzumab displays a binding signal about 2-fold increased to the negative control, AMV1 SEED binding at pH 7.4 and 6.0 is in the range of the negative control. **B)** Investigation of the off-target effect by the AMV1H10 matuzumab SEED at pH 7.4 and 6.0. The negative control is shown in black, while the sample incubated with matuzumab is shown in green. IM9 cells incubated with AMV1H10 matuzumab SEED at pH 7.4 are displayed in light blue, whereas the sample incubated at pH 6.0 is depicted by the dark red dashed line. Binding of AMV1H10 SEED at pH 7.4 is comparable to matuzumab, while at pH 6.0 binding is increased about one order of magnitude compared to the negative control.

Matuzumab was utilized as control antibody, but contrary to expectations revealed a weak binding signal. Both SEED constructs revealed a signal comparable to the negative control and matuzumab at pH 7.4. Upon switching the pH to 6.0, the signal of AMV1 SEED ranges between matuzumab and the negative control, while AMV1H10 SEED displays significant binding. Binding of AMV1H10 SEED at pH 6.0 is probably caused by electrostatic interactions between the negatively charged cell surface and the up to eight positively charged histidines within the CDR3. Since AMV1H10 SEED revealed no restricted binding, independent from the condition and furthermore displayed off-target binding under acid

conditions, only AMV1 SEED was chosen for the implementation of an MMP-9 cleavable linker. The implemented MMP-9 cleavable linker consists of an MMP-9 cleavable sequence, flanked by flexible glycine serine linkers. In comparison to the previous linker, the length of the MMP-9 cleavable linker was increased, in order to accommodate for potential rigidity of the MMP-9 cleavage site. Furthermore, increased length and flexibility might be beneficial for AMV1 binding and consequently restriction of matuzumab binding. However, cell binding analysis of the construct with the MMP-9 cleavable linker revealed a complete abolishment of the inhibitory effect of AMV1 (**Figure 16C**).

Since all SEED constructs did not meet the requirements for conditional inhibition and restauration of binding, no further experiments were conducted. However, linker optimization for the AMV1 SEED construct might result in a variant with desired inhibition and restoration of binding upon protease cleavage.

In case of the light and heavy chain constructs, flexible glycine-serine linkers were utilized to fuse the vNARs to the matuzumab chains. Fusion of AMV1H10 to the heavy chain of matuzumab revealed no differences in binding between matuzumab and the fusion construct under neutral and acidic conditions (**Figure 18**).

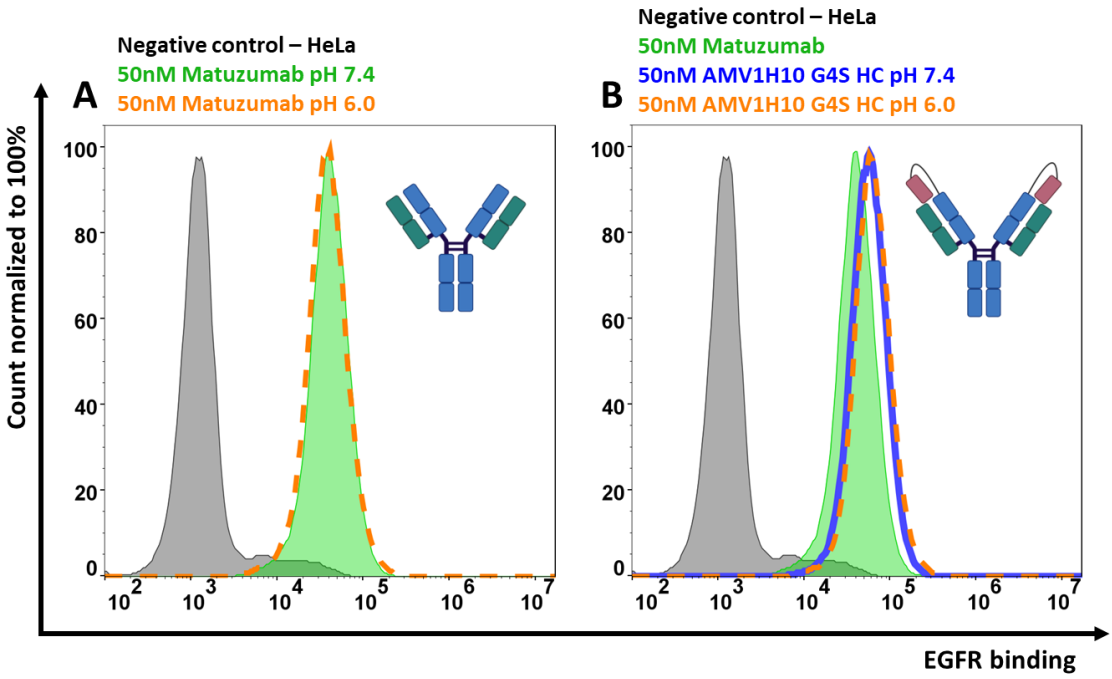

Figure 18: Binding analysis of the AMV1 heavy chain fusion on HeLa cells. A) Investigation of the influence of pH towards matuzumab binding on HeLa cells. The negative control is depicted in grey, matuzumab binding is shown in green and orange for pH 7.4 and 6.0 respectively. Binding of matuzumab is increased about 1.5 orders of magnitude compared to the negative control. No difference is observed between the samples incubated at pH 7.4 and 6.0. **B)** Binding of matuzumab with AMV1 fused to the N-terminus of the heavy chain *via* a flexible glycine serine linker. The negative control is shown in grey, while the positive control is depicted in green. Binding of the heavy chain fusion at pH 7.4 is represented by the blue line, while binding at pH 6.0 is illustrated by the dashed orange line. Binding of the heavy chain fusion is in the range of matuzumab binding for both pH conditions.

This finding is not surprising, since co-incubation as well as the AMV1 SEED construct exhibited no inhibitory effect of AMV1H10 on matuzumab binding. However, maybe the AMV1H10 epitope is blocked by the linker, or the linker lacks flexibility or length to enable an interaction between AMV1H10 and matuzumab. Since the glycine serine linker implemented in this construct is reported to offer high flexibility, linker inflexibility is probably not responsible for this effect. In contrast, the length of 35 amino acids might be either too short or long to enable an interaction between the vNAR and matuzumab. Furthermore, AMV1H10 might addresses an epitope near the N-terminus of the matuzumab heavy chain and therefore the AMV1H10 epitope is sterically blocked by the linker. In order to investigate this hypothesis, AMV1H10 as well as was AMV1 was fused to the light chain of matuzumab (**Figure 19**).

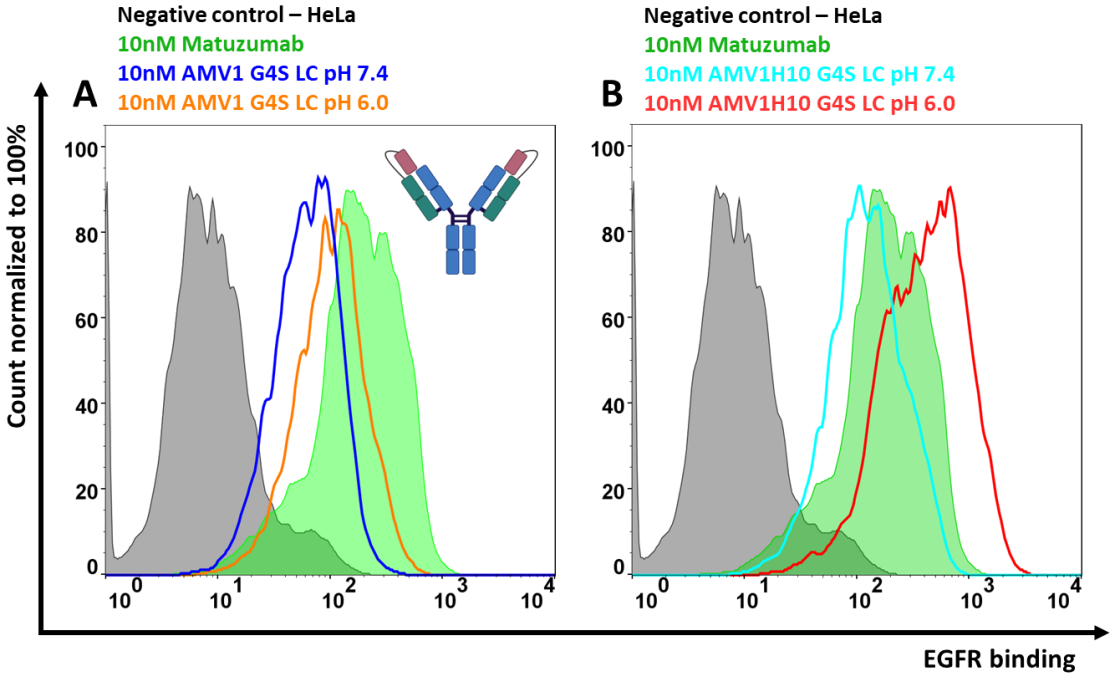

Figure 19: Binding analysis of AMV1 and AMV1H10 fused to the N-terminus of the matuzumab light chain fusions *via* a flexible non-cleavable glycine serine linker on HeLa cells. The normalized count is shown on the y-axis, whereas EGFR binding is depicted on the x-axis. Prior to the cell staining, all constructs were labeled with Alexa Fluor 647 for detection of binding. **A)** Binding analysis of AMV1 fused to the N-terminus of the matuzumab light chain fusion at pH 7.4 and 6.0. The negative control is shown in grey, while the positive control is depicted in green. Incubation of the AMV1 light chain fusion at pH 7.4 and 6.0 are displayed by the blue and orange line respectively. **B)** Analysis of AMV1H10 fused to the N-terminus of the matuzumab light chain a pH 7.4 and pH 6.0. The positive control is shown in green, whereas the negative control is depicted in grey. AMV1H10 light chain fusions incubated at pH 7.4 and 6.0 are shown in light blue and red respectively.

In comparison to the heavy chain fusion, binding behavior of the light chain fusion constructs differs from the positive control. The AMV1 light chain fusion construct revealed a small decrease in binding under neutral and acidic conditions (**Figure 19A**). However, the decrease in binding is not as strong as in case of the SEED construct and as indicted by the co-incubation experiment. In contrast, the AMV1H10

light chain fusion revealed a slight decrease in binding under neutral conditions, while binding is increased under acidic conditions (**Figure 19B**). Increased binding is probably caused by electrostatic interactions as previously discussed.

Overall, the approach of incorporating pH-dependency in an existing anti-matuzumab vNAR resulted in four unique single clones. One single clone was chosen for further characterization and revealed strongly decreased binding compared to the parental vNAR. The aforementioned experiments suggest that the pH-dependent variant is unsuitable as an inhibitory domain to prevent matuzumab binding, due to a lack of affinity and cell binding under acidic conditions. In contrast, the parental vNAR revealed a strong inhibitory effect in co-incubation experiments and in a lesser degree in SEED constructs. Since efficient inhibition of binding by the vNAR is not possible due to insufficient linker properties, further investigation in this direction could solve this issue.

5.2 Isolation of anti-CD47 antibody 5F9 binding vNARs and investigation of masking properties in different antibody based constructs

In comparison to the matuzumab screening campaign, which was based on a preexisting binder, screening against anti-CD47 antibody 5F9 was carried out utilizing histidine doped vNAR libraries. These semi-synthetic libraries originate from vNAR framework regions of three bamboo sharks and randomized CDR3 sequences. CDR3 sequences consist of either 12, 14, 16, or 18 randomized amino acids. While cysteine was excluded, to prevent formation of disulfide bonds, histidine was included with a frequency of 2–3 histidines per CDR3. Due to the presence of histidines and their ability to be protonated at mild acidic pH levels, isolation of pH-dependent vNARs from this library was shown before (89).
The isolation of vNARs against 5F9 was achieved by five subsequent screening rounds (**Figure 20**).

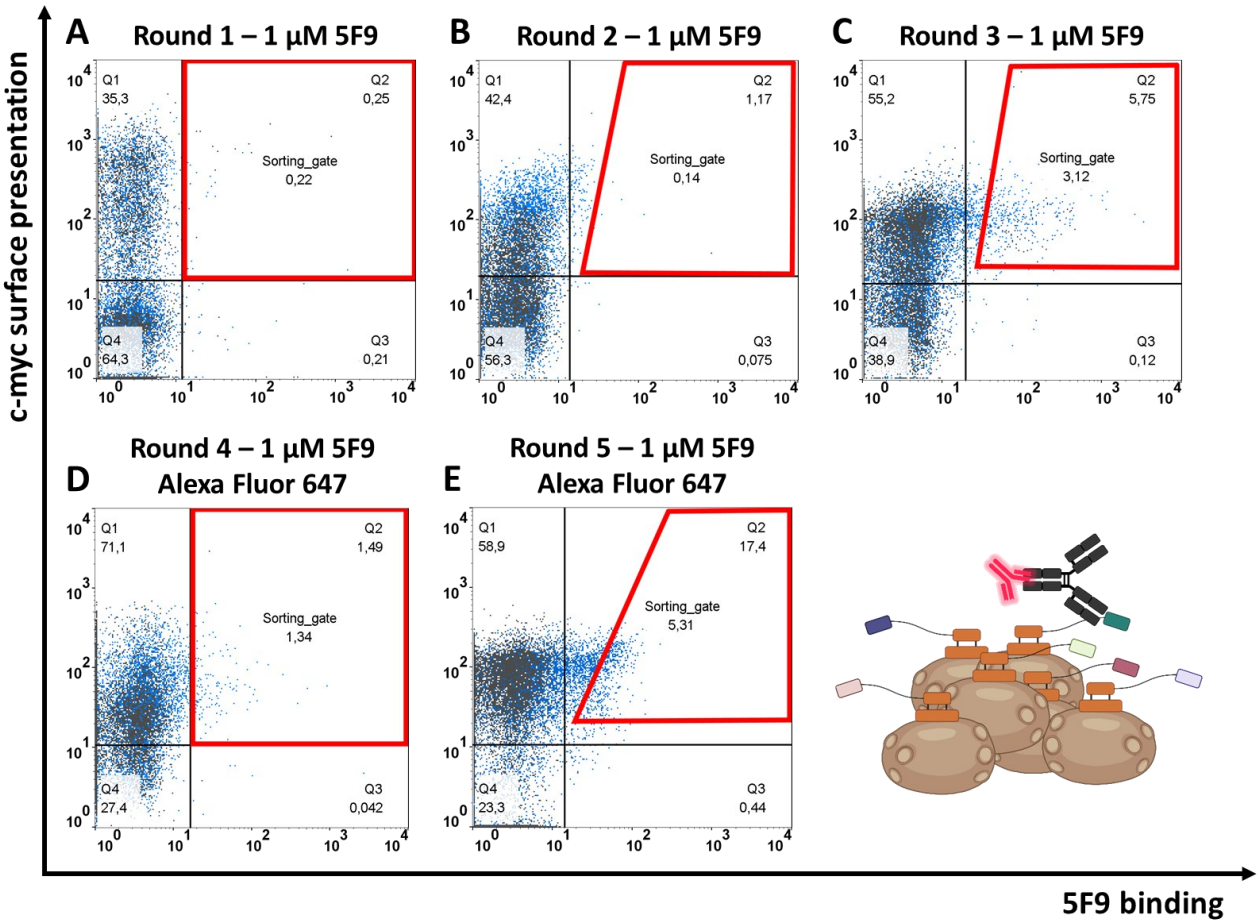

Figure 20: Screening campaign of histidine-doped vNAR yeast libraries with CDR3 lengths of 12, 14, 16, or 18 amino acids towards pH-dependent 5F9 binding vNARs. The y-axis of the dot plots correlates with surface presentation verified by anti-myc FITC, while the x-axis depicts 5F9 binding verified either by staining with anti-human Fc PE or directly labeled 5F9 with Alexa Fluor 647. The cells depicted in the dot plots are gated on viable and single cells. **A)** Round 1 of the screening campaign. Surface presentation is verified by anti-c-myc FITC and represented by 35.3% of the population in the Q1 gate, while 5F9 binding is detected *via* anti-human Fc PE, displayed by 0.22% of the population int Q2 gate. The negative control is shown in grey, whereas the sample incubated with 1µM of 5F9 is displayed in blue. Yeast cells isolated in the first round are depicted in the red sorting gate. **B)** Sorting round 2 for isolation of 5F9 binding vNARs at a concentration of 1 µM 5F9. Surface presentation (42.4%, Q1 gate) as well as target binding (1.17% Q2 gate) are detected as in round 1. Yeast cells isolated in the second round are depicted

in the red sorting gate. **C)** Round 3 of sorting for vNARs directed against 5F9 with an 5F9 concentration of 1 µM. Target binding (5.75%, Q2 gate) and surface presentation (55.2%, Q1 gate) are verified as in rounds 1 and 2. Binding in the sample incubated with 5F9 as well as in the negative control is evident. Yeast cells isolated in the third round are depicted in the red sorting gate. **D)** Sorting round 4, with surface presentation verified with anti-c-myc FITC (71.1%, Q1 gate) and target binding with 1 µM of Alexa Fluor 647 labeled 5F9 (1.34%, gate Q2). Yeast cells isolated in the fourth round are depicted in the red sorting gate. **E)** Round 5 of isolating 5F9 binding vNARs at an 5F9 concentration of 1 µM. Surface presentation (58.9%, Q1 gate) and 5F9 binding (17.4%, Q2 gate) are detected as in round 4. Yeast cells isolated in the fifth round are depicted in the red sorting gate. Form each sample 50000 events were recorded.

In rounds one and two, no enrichment of 5F9 binding vNARs could be observed (**Figure 20A** and **B**). In round three, enrichment of 5F9 binding vNARs was detected. However, binding towards the detection antibody was also observed. To circumvent this issue, screening utilizing alternating detection antibodies can be conducted. Therefore, subsequent screening rounds were conducted using Alexa Fluor 647 labeled 5F9 (**Figure 20C** and **D**). In round four, target binding was not improved compared to round three (**Figure 20**D). This finding could be caused by change of the detection fluorophore from PE to Alexa Fluor 647 and therefore different quantum yields. Furthermore, a detection antibody bound by a vNAR on the yeast cell surface could bind to the Fc part of 5F9, which in turn could be bound again by another detection antibody, thereby increasing the binding signal. Sorting was carried out anyway and the outcome of round 4 reveals an 5F9 binding population (**Figure 20E**), which was plated on SD-W agar plates to obtain single clones for FACS and sequence analysis. Sequencing of eight single clones resulted in two unique clones, with one dominant clone found in seven out of the eight analyzed sequences (**Table S 3**). Both single clones exhibit a 14 amino acid long CDR3. While the dominant clone reveals five histidines in the CDR3, the other clone contains four histidines. Besides a higher frequency in histidines than the library average, both clones share histidine residues at positions eight and 13 in the CDR3. Moreover, the dominant clone reveals three methionines with in the CDR3, while the less frequent clone presents a HKHKH motif, which suggests the possibility of proton transfer between the histidine and lysine residues. After sequence analysis, pH-dependency of both single clones on the surface of yeast cells was investigated (**Figure 21**).

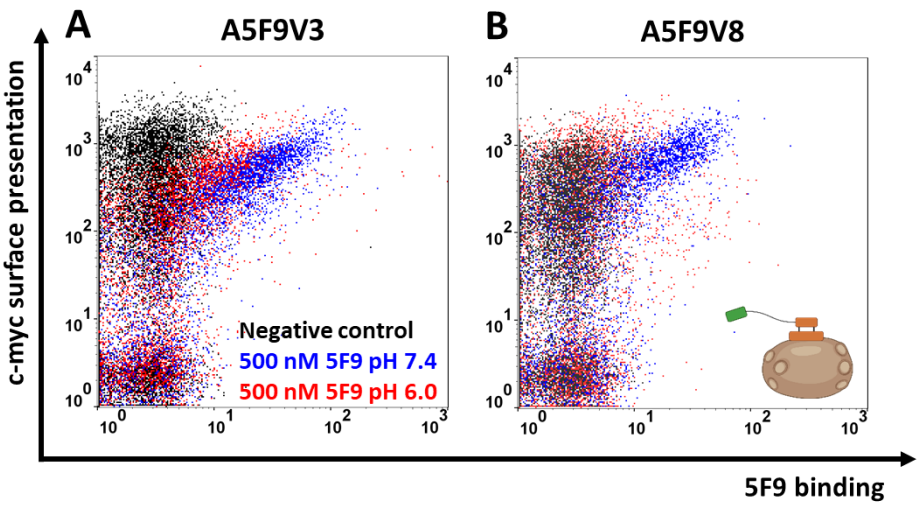

Figure 21: Yeast single clone analysis of anti-5F9 vNARs (A5F9V). Surface presentation is shown on the y-axis *via* anti-c-myc-FITC antibody and target binding on the x-axis utilizing Alexa Fluor 647 labeled 5F9. The cells depicted in the dot plots are gated on viable and single cells. Both single clones were incubated with 5F9 at pH 7.4 and pH 6.0. The negative control, incubated without the target antibody is shown in black, while incubation at pH 7.4 and 6.0 are depicted in blue and red respectively. **A)** Binding of A5F9V3 on the yeast surface under different conditions. Stronger binding at pH 7.4 compared to pH 6.0 is evident, with an about 5-fold decrease in binding at pH 6.0. **B)** Binding of A5F9V8 on the yeast surface under different conditions. A5F9V8 binding is weaker compared to A5F9V3 binding. Binding at pH 7.4 is stronger compared to pH 6.0, with an about 5-fold decrease in binding at pH 6.0.

5F9 binding at pH 7.4 was evident for both clones, with A5F9V3 revealing a stronger binding signal compared to A5F9V8 (**Figure 21**, blue). Binding analysis of the clones showed decreased binding at pH 6.0 in both cases (**Figure 21**, red). While binding of A5F9V3 at pH 6.0 was still detectable, the binding signal of A5F9V8 was similar to the negative control incubated without target (**Figure 21B**, black). Since both single clones revealed pH-dependent binding, reformatting in pET30 for expression in *E. coli* was performed. After expression and purification, the correct size was verified *via* SDS-PAGE (**Figure S 5**). Afterwards vNAR thioredoxin fusions were tested for inhibition of 5F9 binding in co-incubation experiments (**Figure 22**).

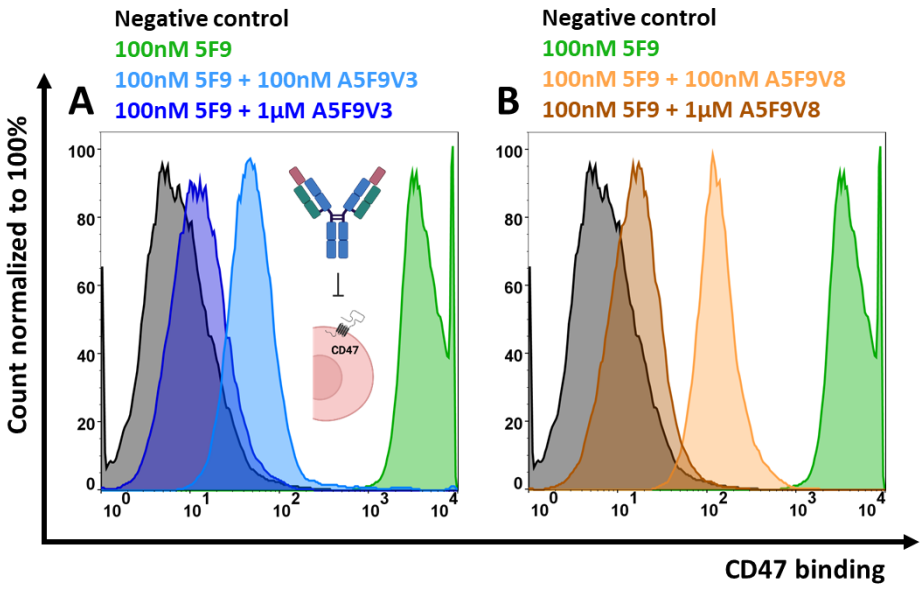

Figure 22: Analysis of blocking properties of A5F9V3 and A5F9V8 in co-incubation experiments on Daudi cells. Cell count is shown on the y-axis, while CD47 binding of 5F9 is shown on the x-axis. The negative control is displayed in black, while the positive control is shown in green. Positive control binding is increased three orders of magnitude compared to the negative control. **A)** Co-incubation of A5F9V3 with 5F9. Incubation of 5F9 and A5F9V3 in a 2:1 ratio (light blue) results in two orders of magnitude decrease in binding compared to the positive control. By changing the 5F9 to A5F9V3 ratio to 1:5 (dark blue), the binding signal is decreased to the level of the negative control. **B)** Co-incubation of A5F9V8 with 5F9. Incubation of 5F9 and A5F9V8 in a 2:1 ratio (orange) results in one orders of magnitude decrease in binding compared to the positive control. By changing the 5F9 to A5F9V8 ratio to 1:5 (brown), the binding signal is decreased to the level of the negative control.

Therefore, a fixed concentration of 5F9 and different concentrations of respective vNAR thioredoxin fusions were pre-incubated 30 minutes prior to applying the mixture to Daudi cells expressing CD47 (**Figure 22**). Both vNARs inhibit 5F9 binding equally efficient at high concentrations of 1μM (**Figure 22A** dark blue, **Figure 22B** brown), with only a small shift compared to the negative control. In contrast, at a lower concentration of 100nM, A5F9V3 reveals stronger inhibition (**Figure 22A** light blue), compared to A5F9V8 **Figure 22B** orange). The different effectiveness in inhibiting 5F9 binding of the two vNARs could be associated to addressing different epitopes, differences in protein stability or affinities towards 5F9. Therefore, affinity measurements as well as melting point analysis were carried out. Melting point analysis revealed comparable melting points with 56°C and 55°C for A5F9V3 and A5F9V8, respectively. Since melting points of both proteins are similar, protein stability probably does not cause differences in inhibiting 5F9 binding. Therefore, BLI experiments were performed, to investigate potential differences in affinities (**Figure S 7**). Affinities were calculated to be in the single digit nanomolar range for both vNARs at pH 7.4. Further analysis at a more acidic pH of 6.0 revealed faster dissociation for both vNARs and therefore affinity decreased to 49 nM and 35 nM for A5F9V3 and A5F9V8 respectively. Consequently, weaker blocking of A5F9V8 cannot be accounted to lower affinities at neutral and acidic conditions. While affinity and protein stability could be addressed with BLI and determination of the melting point with thermal shift assay, structural data could not be obtained. However, CDR3 sequences of both clones reveal different arrangements of hydrophobic and hydrophilic

amino acids. Therefore, different epitopes for both vNARs remains a possibility. To investigate this hypothesis, BLI based epitope binning experiments could be carried out in the future. Additionally, the inhibitory effect might not be attributed to the vNARs themselves, but rather to the N-terminally fused thioredoxin. If the vNARs address an epitope which is not located in the paratope region of 5F9, inhibition by vNARs is possible. However, if binding occurs in an orientation which enables the thioredoxin to sterically block the interaction of 5F9 and CD47, reduced binding is observed. In order to address this possibility, the thioredoxin should be separated from the vNAR utilizing the TEV cleavage site between the thioredoxin and vNAR. Subsequent Streptactin purification removes the thioredoxin and the solitary vNAR is obtained.

After confirming blocking properties of both vNARs and pH-dependency not only on yeast cells, but also in BLI experiments, both vNARs were fused to the N-terminus of the light and heavy chain of 5F9 *via* a variety of different linkers (**Table S 1**). The linkers consist of either a flexible glycine-serine linkers or MMP-9 cleavable linkers, with different MMP-9 recognitions sequences. While the different light chain fusions were expressible, heavy chain fusions could not be expressed in Expi HEK cells (**Figure S 5B**). The different light chain fusions of both vNARs were tested towards binding on cells, to verify which linker enables the vNARs to interfere with antigen binding. Binding was tested under neutral conditions (**Figure 23** blue peaks) as well as acidic conditions (**Figure 23** red peaks).

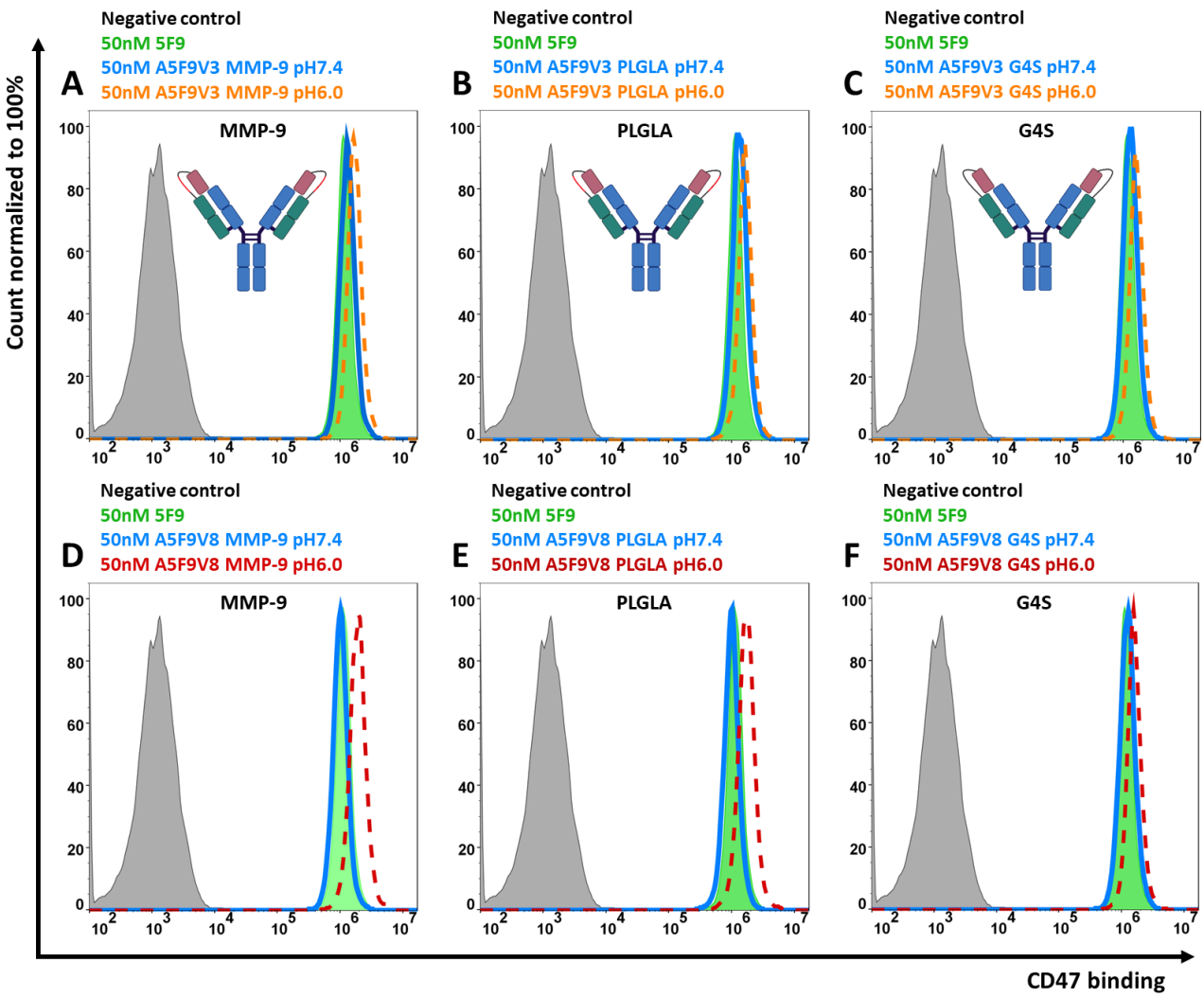

Figure 23: Overlay cell binding analysis of A5F9V3 and A5F9V8 light chain fusions with different linkers on Daudi cells. CD47 binding is shown on the x-axis, while cell count is displayed on the y-axis. The negative control is depicted in black, while the positive control is shown in green, displaying a shift three orders of magnitude compared to the negative control. **A)** Incubation of A5F9V3 fused to the light chain of 5F9 *via* the MMP-9 linker. Binding under neutral conditions is displayed in blue, while binding under acidic conditions is represented by the orange dashed line. Binding under both conditions is comparable to the positive control. **B)** Incubation of A5F9V3 fused to the light chain of 5F9 *via* the PLGLA linker. Binding under neutral conditions is shown in blue, while binding under acidic conditions is shown by the orange dashed line. Binding under both conditions is comparable to the positive control. **C)** Incubation of A5F9V3 fused to the light chain of 5F9 *via* the G4S linker. Binding under neutral conditions is displayed in blue, while binding under acidic conditions is depicted by the orange dashed line. Binding under both conditions is comparable to the positive control. **D)** Incubation of A5F9V8 fused to the light chain of 5F9 *via* the MMP-9 linker. Binding under neutral conditions is displayed in blue, while binding under acidic conditions is represented by the dark red dashed line. Binding under neutral conditions is comparable to the positive control, binding at pH 6.0 is increased about 2-fold. **E)** Incubation of A5F9V8 fused to the light chain of 5F9 *via* the PLGLA linker. Binding under neutral conditions is shown in blue, while binding under acidic conditions is displayed by the dark red dashed line. Binding under neutral conditions is comparable to the positive control, binding at pH 6.0 is increased about 2-fold. **F)** Incubation of A5F9V8 fused to the light chain of 5F9 *via* the G4S linker. Binding under neutral conditions is depicted in blue, while binding under acidic conditions is represented by the dark red dashed line. Binding under both conditions is comparable to the positive control.

Analysis of all light chain fusions revealed binding at pH 7.4 and 6.0 comparable to the positive control, independent of vNAR and linker. This surprising finding contradicts results obtained by the co-incubation experiments, which indicated an inhibitory effect of the vNARs towards the 5F9 interaction with CD47.

While some influence of the employed linkers on blocking efficiency was expected due to different flexibilities, observing no inhibitory effect of the vNARs was not expected. Since all light chain fusions lack a blocking effect of the vNAR, a systematic error might have occurred. One reason for this result might be misfolding of the vNAR by the mammalian expression system. Furthermore, none of the linkers might be able to achieve the required conformation to allow binding towards the 5F9 paratope. Therefore, presumable differences in vNAR epitopes, based on major differences in the CDR3 sequences, might be incorrect assumptions. Nevertheless, epitopes may overlap to a certain extent and therefore placing the linker on the light chain might mask the epitope of the vNARs and therefore binding is not possible. In case of insufficient linker properties as well as blocking the vNAR epitope with the linker, unbound vNAR could be detected with BLI experiments utilizing 5F9 for association. Furthermore, changing the linker position from the light to the heavy chain should give insights, whether the linker on the light chain blocks the vNAR epitope. However, heavy chain fusions were not expressible and therefore, other constructs are required to investigate vNAR blocking capacities. Therefore, parallel to the light and heavy chain fusions, the SEED technology was utilized to achieve a heterodimer of the 5F9 Fab on one arm and the vNAR on the other arm. The linker between the vNAR and the hinge region is the same as in the matuzumab constructs. The cysteine to serine mutation to increase flexibility of the construct was introduced as well. Since the SEED construct contains only one Fab fragment and steric effects of the vNAR needed to be considered, a control SEED with an unrelated vNAR was utilized as positive control for the SEED experiments. The unrelated vNAR is directed against EpCAM, which is not present on B cells. During cell binding experiments, binding behavior at pH 7.4 and 6.0 was tested (**Figure 24**).

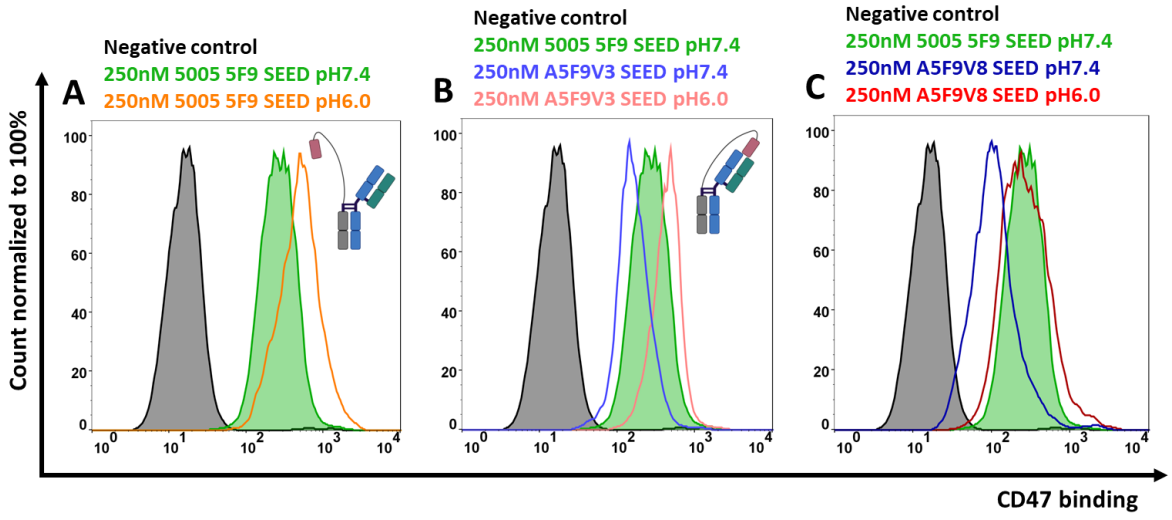

Figure 24: Cell binding analysis of 5005 5F9 SEED, A5F9V3 SEED, and A5F9V8 SEED constructs on Daudi cells. CD47 binding is shown on the x-axis, while cell count is depicted on the y-axis. The negative control in all plots is shown black. **A)** Binding of the 5005 5F9 SEED is displayed in green and orange for incubation at pH 7.4 and 6.0 respectively. Binding at pH 7.4 is increase about one order of magnitude compared to the negative control. Additional, binding at pH 6.0 is increased about 2-fold compared to pH 7.4. **B)** Binding of A5F9V3 SEED incubated at pH 7.4 and 6.0 are visualized in light blue and light red respectively. While A5F9V3 SEED under neutral conditions reveals a slight decrease in binding compared to the positive control, binding at pH 6.0

is slightly increased. **C)** Binding of A5F9V8 SEED incubated at pH 7.4 and 6.0 are visualized in dark blue and dark red respectively. While A5F9V8 SEED under neutral conditions reveals a 2-fold decrease in binding compared to the positive control, binding at pH 6.0 is comparable to the positive control.

Analysis of the positive control revealed a slight increase in binding when incubated at pH 6.0 (**Figure 24A**, red). The increase in cell binding at pH 6.0 could be caused by the presence of protonated and therefore positively charged histidines in the CDR3 of the control vNAR. The positively charged histidines can interact *via* electrostatic interaction with the negatively charged cell surface and therefore contribute to cell binding. Cell binding of the A5F9V3 SEED is slightly decreased at pH 7.4 compared to the positive control (**Figure 24**B, light blue) and slightly increased at pH 6.0 (**Figure 24B**, light red). The increase of binding at pH 6.0 is probably also caused by the positively charged histidines. In contrast the reduction of cell binding at pH 7.4 might indicate a blocking effect of the vNAR. However, the difference between the positive control and construct remains behind expectations based on the co-incubation experiments. In case of the A5F9V8 SEED binding at pH 7.4 reveals a stronger reduction in binding compared to the A5F9V3 SEED (**Figure 24C**, dark blue). Furthermore, binding is restored to the level of the positive control at pH 6.0 **Figure 24C**, dark red). Nevertheless, blocking is not reached to an extent suggested by the co-incubation experiments. As in the case of the light chain fusions, the vNARs might be prevented from binding and thereby inhibiting 5F9 binding by either misfolding or disadvantageous linker length or flexibility. Since the vNARs were not able to block 5F9 binding in neither the light chain fusions nor the SEED constructs, different approaches for further investigations can be considered. In a first step, misfolding of both vNARs during mammalian expression should be investigated. Therefore, both vNARs should be produced in mammalian cells and afterwards melting points as well as affinities should be determined. By comparing the properties of vNARs expressed in mammalian or *E. coli* cells, differences between the expression systems as well as the potential impact on light chain fusions can be identified. If these data should result in no major differences between both expression systems, structural information based on x-ray crystallography of 5F9 in complex with both vNARs should be obtained. These data should give insights in the interaction between the vNARs and 5F9 and therefore could give an approach for linker improvement. Furthermore, yeast surface display in combination with golden gate could be utilized in the development of a suitable linker. Therefore, the vNAR should be fused to the 5F9 heavy or light chain *via* library of different linkers. The linker library could be implemented *via* golden gate cloning with hybridized primers coding for a variety of different linkers. For library format, a Fab display should be utilized, in order to investigate the effects of the linker as close as possible to the final construct.

In summary, two pH-dependent vNARs directed against 5F9 were obtained after five consecutive screening rounds. Binding of both variants decreased under acidic conditions. The isolated vNARs revealed pH-dependent binding properties on the surface of yeast as well as thioredoxin fusion.

Furthermore, the solitary proteins revealed an inhibitory effect on 5F9 in cell binding experiments. However, this inhibitory effect was not observed in SEED constructs or light chain fusions.

5.3 Isolation of vNARs directed against rituximab and analysis of the masking effects as well as restoration of binding after protease cleavage or pH switch

For the isolation of pH-dependent vNARs directed against rituximab, the same histidine-doped libraries as in the 5F9 screening campaign were utilized. Overall, four sorting rounds were required for the enrichment of vNAR directed against rituximab (**Figure 25**).

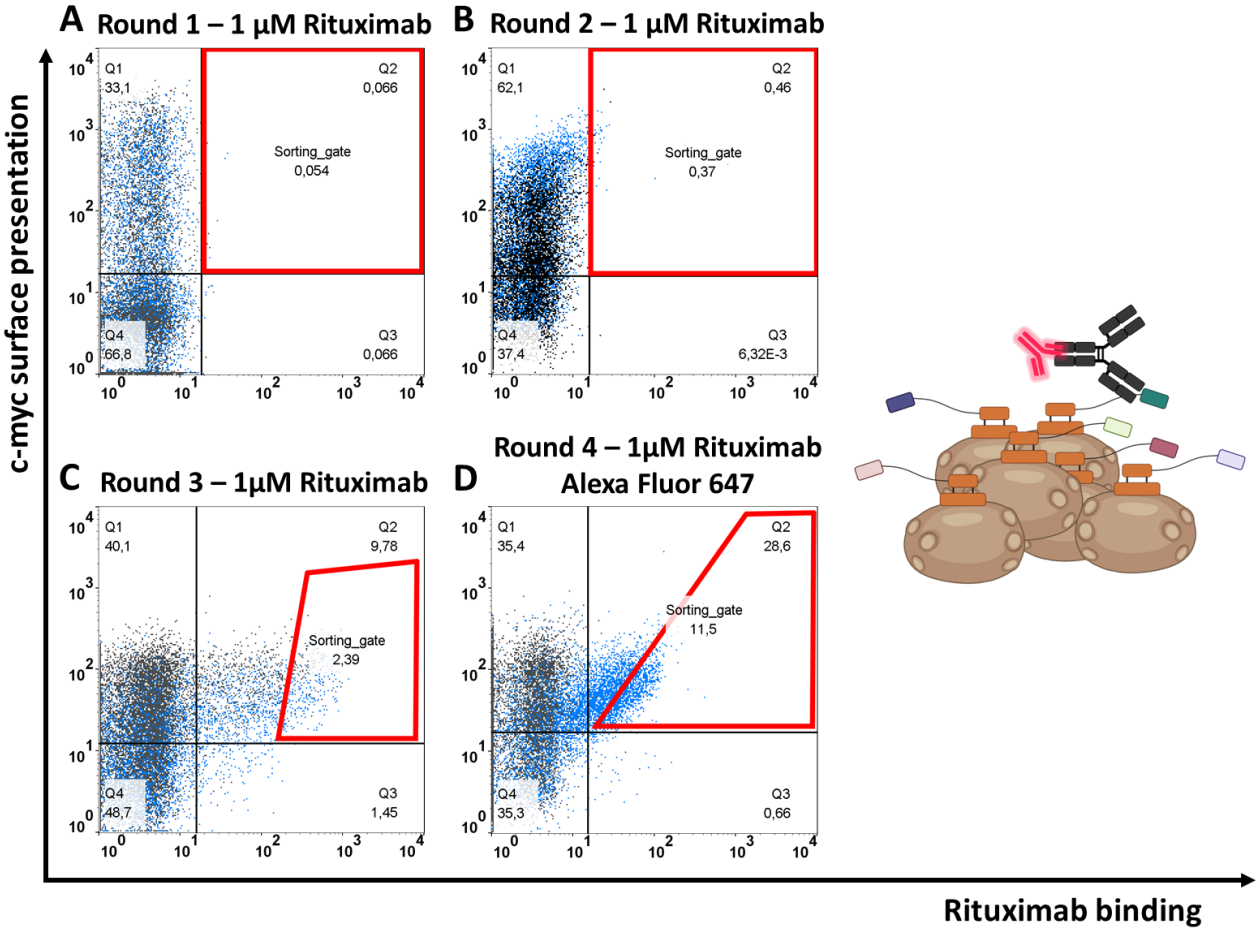

Figure 25: Screening campaign for the isolation of pH-dependent anti-rituximab vNARs utilizing histidine-doped vNAR yeast libraries with CDR3 lengths of 12, 14, 16, or 18 amino acids. vNAR surface presentation verified by anti-myc FITC is shown on the y-axis, while binding towards rituximab verified by anti-human Fc PE or directly labeled rituximab with Alexa Fluor 647 is displayed on the x-axis. The cells depicted in the dot plots are gated on viable and single cells. During all four screening rounds, the anti-c-myc FITC antibody was utilized to verify surface presentation. The negative control is shown in grey, while the samples incubated with 1 µM of rituximab are depicted in blue. Form each sample 50000 events were recorded. **A)** First screening round for the isolation of vNARs directed against rituximab. Surface presentation of the library is 33.1% as indicated by the Q1 gate. Rituximab binding is represented by 0.066% of the population in the Q2 gate. Cells isolated during this screening round are shown in the red sorting gate. **B)** Second screening round with a surface presentation of 62.1% (Q1 gate) and a rituximab binding of 0.46% (Q2 gate). Cells isolated during this screening round are depicted in the red sorting gate. **C)** Third sorting round with surface presentation of 49.88% (Q1 and Q2 gate). Surface presentation is calculated from the Q1 and Q2 gate, since binding towards the detection antibody is evident. Binding towards rituximab is 9.78% (Q2 gate). Cells isolated during this screening round are displayed in the red sorting gate. D) Surface presentation of the fourth screening round is 35.4% (Q1 gate).

Binding of rituximab was verified by directly Alexa Fluor 647 labeled rituximab (26.6%, Q2 gate). The cells isolated in each round are depicted in the red sorting gate.

During the first and second screening round, no enrichment towards rituximab binding is observed (**Figure 25A** and **B**). In round three, enrichment of vNAR directed against rituximab is observed, however also binding towards the detection antibody is visible (**Figure 25C**). Therefore, rituximab was coupled to Alexa Fluor 647 and utilized in the subsequent screening round. The outcome of round three resulted in a population which depicts a decreased binding signal compared to previous round, however the number of rituximab binding cells in increased. This finding could either be explained by the differences in the quantum yield of the utilized fluorophores or multiple anti-human Fc PE detection antibodies of the polyclonal mixture binding to the Fc part of rituximab. Nevertheless, the binding population was isolated and for ten single clones sequence analysis was carried out (**Table S 4**). Overall, four unique sequences were obtained. Two variants were found only once (ARV1 and ARV9), while one variant was found twice (ARV2 and ARV8) and one variant five times (ARV4, ARV5, ARV6, ARV7 and ARV10). The CDR3 length of the variants is either 14 or 16 amino acids with no variants exhibiting 12 or 18 amino acids. Additionally, the number of histidines varies greatly between the variants with ARV1 only containing one histidine, while ARV8 revealed three histidines, ARV6 displayed four histidines and ARV9 containing six histidines. Furthermore, all variants except ARV9 exhibit hydrophobic amino acids in the center of the CDR3, flanked by hydrophilic amino acids. In contrast, the CDR3 of ARV9 displays a hydrophilic core consisting of an HHHPH motif. Furthermore, the N-terminal part of the CDR3 comprises of a hydrophobic part containing three leucine resides. In contrast, the C-terminal part comprises of hydrophilic residues and a tryptophane at the end. Based on the results obtained from the sequencing data, ARV1 should display the least amount of pH-dependency, while ARV2, ARV6 and ARV9 should reveal an increase in pH-dependency. Analysis of these variants on the surface of yeast cells confirmed these expectations (**Figure 26**).

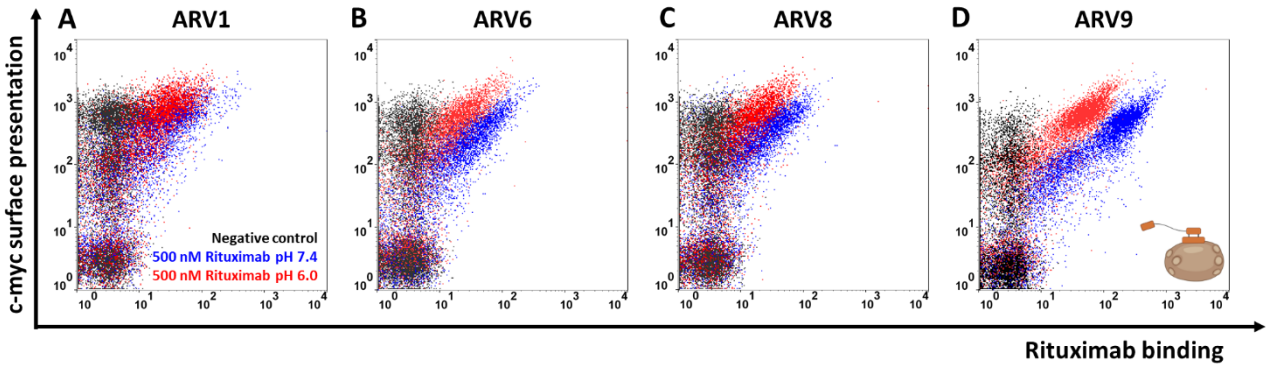

Figure 26: Yeast single clone analysis of anti-rituximab (ARV) vNARs. Surface presentation is shown on the y-axis *via* anti-c-myc-FITC antibody and target binding on the x-axis utilizing Alexa Fluor 647 labeled rituximab. The cells depicted in the dot plots are gated on viable and single cells. The single clones were incubated with rituximab at pH 7.4 and pH 6.0. The negative control, incubated without the target antibody is shown in black, while incubation at pH 7.4 and 6.0 are depicted in blue and red respectively. **A)** Binding of ARV1 on the yeast surface. Binding at pH 7.4 is slightly increased compared to binding at pH 6.0. **B)**

Binding of ARV6 on the surface of yeast. ARV6 binding at pH 7.4 is about 5-fold increased to binding at pH 6.0. **C)** Binding of ARV8 on the yeast surface. Binding at pH 7.4 is increased about 5-fold compared to binding at pH 6.0. **D)** Binding of ARV9 on the surface of yeast. ARV9 binding at pH 7.4 is about 10-fold increased compared to binding at pH 6.0.

ARV1 displays insignificant pH-dependency as well as the weakest binding of all analyzed clones, while ARV6 and ARV8 exhibit moderate binding and pH-dependency. ARV9 shows the highest pH-dependency and binding of all analyzed clones.

Expression of all variants as thioredoxin fusions in *E. coli* resulted in little to no protein (data not shown). Therefore, the four variants were directly tested in a SEED construct in order to investigate expression, the inhibitory effect of each vNAR and pH-dependency of each construct on CD20 expressing IM9 cells (**Figure 27**).

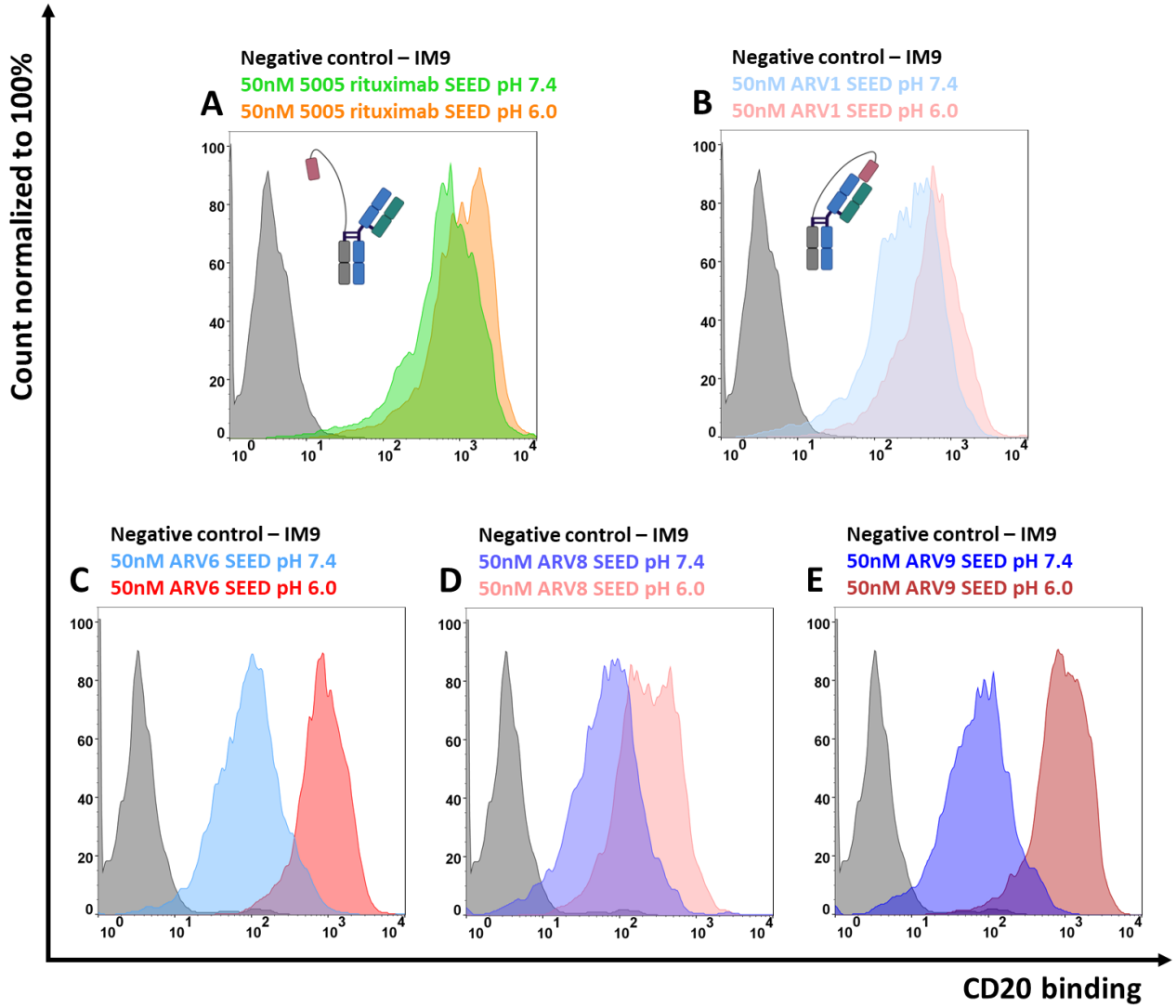

Figure 27: Cell binding analysis of 5005 rituximab SEED, ARV1, ARV6, ARV8, and ARV9 SEED constructs on IM-9 cells. CD20 binding is shown on the x-axis, while normalized cell count is depicted on the y-axis. The negative control in all plots is shown black. **A)** Binding of 5005 rituximab SEED under neutral (pH 7.4) and acidic (pH 6.0) conditions is displayed in green and orange respectively. Binding at both conditions is about three orders of magnitude increased compared to the negative control. Binding

under acidic conditions is slightly increased compared to the neutral condition. **B)** Binding of ARV1 SEED under neutral and acidic conditions is depicted in light blue and light red respectively. Binding at both conditions is about three orders of magnitude increased compared to the negative control. Binding under acidic conditions is slightly increased compared to the neutral condition. **C)** Binding of ARV6 SEED under neutral and acidic conditions is depicted in blue and red respectively. Binding under neutral conditions is about two orders of magnitude increased compared to the negative control. In contrast, binding under acidic conditions reveals an increase of about one order of magnitude compared to the neutral condition. **D)** Binding of ARV8 SEED under neutral and acidic conditions is depicted in dark blue and light red respectively. Binding under neutral conditions is about two orders of magnitude increased compared to the negative control. In contrast, binding under acidic conditions reveals an increase of about 5-fold compared to the neutral condition. **E)** Binding of ARV9 SEED under neutral and acidic conditions is depicted in dark blue and dark red respectively. Binding under neutral conditions is about two orders of magnitude increased compared to the negative control. In contrast, binding under acidic conditions reveals an increase of about one order of magnitude compared to the neutral condition.

As a control, a SEED construct was generated with one arm consisting of the rituximab Fab, while the other arm comprising of an unrelated vNAR directed against EpCAM (**Figure 27A**). In this construct, the vNAR does not contribute to binding nor inhibits rituximab binding. Cell binding on IM9 cells under neutral and acidic conditions was measured independent to the other SEED constructs. Therefore, a direct comparison with the data from the other measurement is not possible, however the data indicate where the maximum binding without an inhibitory effect of a vNAR should be expected. In terms of pH-dependency, the control construct containing an unrelated vNAR reveals only a small difference with a slight increase in binding under acidic conditions. For the other constructs, expression was possible, and a wide range of pH-dependencies is observable. ARV1 SEED revealed the least pH-dependency and the least reduction in binding under neutral conditions (**Figure 27B**). In contrast, ARV6 SEED showed a decrease of one order of magnitude in binding under neutral conditions and upon changing into acidic conditions the binding is restored (**Figure 27C**). In the case of ARV8 SEED the binding under neutral conditions is comparable to ARV6 SEED, however upon changing to acidic conditions the binding was not entirely restored (**Figure 27D**). ARV9 SEED reveals a binding behavior similar to ARV6 SEED, but binding under acidic conditions seems to be slightly increased (**Figure 27E**). These results indicate a significant inhibitory effect of ARV6, ARV8 and ARV9 on rituximab binding under neutral conditions. In contrast, ARV1 reveals only a slight impact on rituximab binding. Furthermore, ARV6, ARV8 and ARV9 SEEDs display pH-dependent restoration of binding upon changing to acidic conditions. Consequently, ARV6, ARV8 and ARV9 might be suitable affinity-based masking domains for conditioned restoration of binding under acidic conditions. For further characterization, off-target cell binding on Hela cells was investigated for all constructs under neutral and acidic conditions (**Figure S 9**). Overall, all constructs revealed binding under neutral conditions comparable to the negative control, while binding under acidic conditions is observable. However, binding at acidic conditions differs between the constructs. While the 5005 rituximab SEED, ARV1 and ARV9 SEED revealed only a modest binding signal, ARV6 and ARV8 SEED showed increased binding. Binding of the constructs is probably caused by electrostatic interactions between the negatively charged cell surface and the positively charged histidines in the CDR3s of the vNARs. While this hypothesis explains the general finding of all SEEDs interacting with the

cell surface, it does not provide an explanation for the weak binding of ARV9 SEED compared to ARV6 and ARV8 SEED. Based on the sequencing data and the frequency of histidines within the CDR3, ARV9 SEED should display the strongest binding since six histidines are present in the CDR3 of ARV9. Also, ARV6 and ARV8 SEED should exhibit a similar degree of binding, since both vNARs carry three and four histidines respectively. In case of ARV1, which carries only one histidine in the CDR3 modest to no binding under acidic conditions would be expected. Since expectation and observation differ for ARV6, ARV8 and ARV9 SEED, the observed effects are not only caused by electrostatic interaction. Another explanation could be that proton delocalization between two or more histidines is responsible for a decrease of the overall positive charge of the CDR3. If this hypothesis was true, ARV6 and ARV9 should exhibit a decrease in charge due to three histidines in direct proximity. However, in this case ARV9 should still exhibit stronger electrostatic binding than ARV6. Furthermore, ARV6 should reveal a decreased binding compared to ARV8, since ARV8 only displays two histidines in direct proximity. Consequently, other factors need to be considered, such as three-dimensional orientation of the amino acids of the CDR3. If histidine residues interact with other amino acids in the CDR3, mild acidic conditions might be insufficient to protonate this histidines. Consequently, it could be predicted that the CDR3 of ARV9 forms a three-dimensional structure which renders some of the histidines inaccessible for protonation, while the CDR3 of ARV6 does not exhibit such behavior. Independent of the effect responsible for the differences in off-target cell binding, all constructs were analyzed *via* analytical size exclusion chromatography (**Figure S 10**). ARV1 and ARV9 SEED as well as 5005 rituximab SEED display one dominant peak in the range of nine to ten minutes, with minor peaks shifted to higher time points. In contrast, ARV6 and ARV8 SEED reveal not one dominant peak, but instead several peaks in the range of nine to 12 minutes. The shift towards longer retention times for the minor peaks indicates the presence of impurities within the sample, fragmentation of the protein or different protein conformations with decisive changes in the overall protein structure. The SDS-PAGE of all SEED constructs revealed additional bands, which could explain the minor peaks in the SEC profile of 5005 rituximab SEED and ARV1 SEED. However, the drastically different SEC profiles of ARV6 and ARV8 cannot be explained by these minor impurities. Furthermore, a partly denaturation of the vNARs due to low stability could cause the changes in the SEC profile. However, denaturation would lead to an increase in the hydrodynamic radius und therefore shorter retention times. Since ARV9 revealed the strongest pH-dependency, while revealing the least amount of off target binding at pH 6.0 and a promising SEC profile, ARV9 was chosen for further characterization. Therefore, ARV9 was expressed as one-armed SEED (**Figure S 8A**) in order to determine the ability to inhibit rituximab binding to CD20 (**Figure 28**).

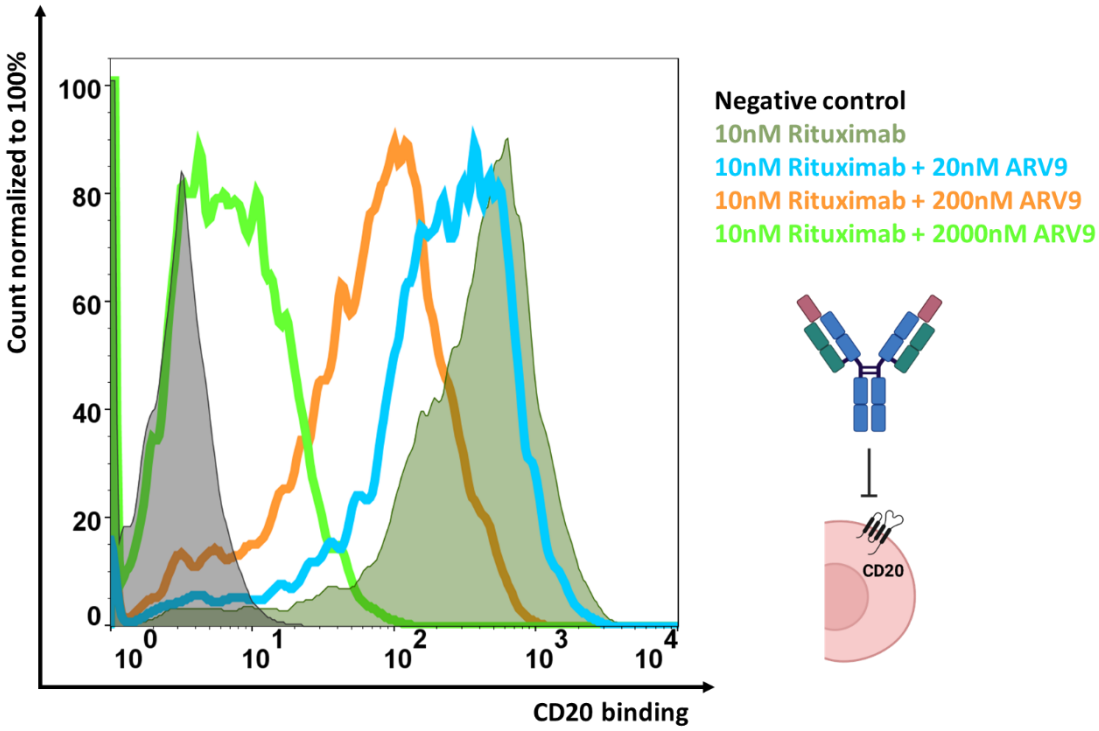

Figure 28: Analysis of blocking properties of ARV9 in co-incubation experiments on Daudi cells. Cell count is shown on the y-axis, while CD20 binding of rituximab is shown on the x-axis. The negative control is displayed in black, while the positive control is shown in dark green. Positive control binding is increased two and a half orders of magnitude compared to the negative control. Incubation of rituximab and ARV9 in a 1:1 ratio (light blue) results in slight decrease in binding compared to the positive control. By changing the rituximab to ARV9 ratio to 1:10 (orange), the binding signal is decreased about one order of magnitude compared to the positive control, while a 1:100 ratio leads to a binding signal comparable to the negative control.

Therefore, a constant concentration of rituximab was preincubated with different ARV9 concentrations prior to applying the mixture to Daudi cells. Cell binding analysis revealed a concentration-dependent inhibition of rituximab binding. While a 1:1 ratio of rituximab paratope per ARV9 has little impact on rituximab binding, a 1:100 ratio results in one order of magnitude decrease in cell binding compared to the sample of rituximab without ARV9. At high ratios of 1:100 rituximab binding is decreased to the level of the negative control. Since strong inhibition of binding is only detectable at higher ARV9 concentrations, the vNAR might address an epitope directly at the rituximab paratope. Since the affinity of rituximab is reported to be 8 nM, the vNAR might exhibit a lower affinity and therefore, is not able to interfere with rituximab binding at lower concentrations. Therefore, the affinity of ARV9 to rituximab was determined *via* BLI (**Figure S 11**). Based on BLI measurements the K_D of ARV9 for rituximab binding was determined to be 18.4 nM at pH 7.4 and 30.7 nM at pH 6.0. Surprisingly the difference in affinity between pH 7.4 and 6.0 is only 1.7-fold, despite the presence of six histidines in the CDR3 of ARV9. The reduction of the affinity is caused by a faster dissociation under acidic conditions since the association remains unchanged (**Figure S 11C**). Since the affinity of ARV9 towards rituximab is in the same range as rituximab binding to CD20, the small effect on rituximab binding at a 1:1 ratio with ARV9 is probably not affinity driven. However, a discrepancy in the on and off rate between rituximab and ARV9 could

cause the observed behavior. If the off rate of ARV9 is faster than the on rate of rituximab, as soon as ARV9 dissociates from rituximab, rituximab can bind to CD20. Since on and off rates are not reported for rituximab, confirming this hypothesis is not possible and for further insight in the interaction co-crystallization of ARV9 and rituximab could be performed.

In order to further investigate the inhibitory properties of ARV9 also in respect to the pH-dependency of the inhibitory effect, an EC_{50} determination of ARV9 SEED on Daudi cells was carried out (**Figure 29**).

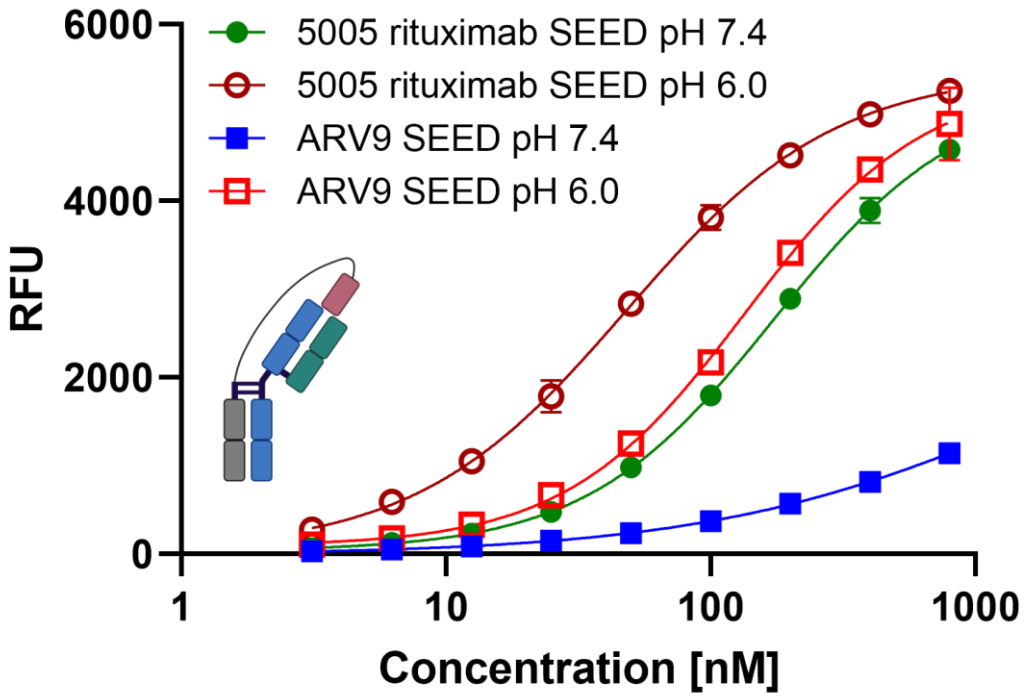

Figure 29: EC_{50} determination of ARV9 and 5005 rituximab SEED under neutral and acidic conditions. Relative fluorescence units are depicted on the y-axis, while the concentration in nanomolar is shown on the logarithmic x-axis. Binding of 5005 rituximab SEED at pH 7.4 is indicated by the green dots and line, while binding at pH 6.0 is shown by the dark red dots and line. Binding of ARV9 SEED at pH 7.4 is depicted by the blue rectangle and line, while binding at pH 6.0 is indicated by the red rectangles and line. EC_{50}s are depicted in the same color as the construct and condition.

Binding of the ARV9 SEED under neutral conditions is decreased and an EC_{50} value could not be determined. This finding is surprising, since ARV9 revealed only weak inhibition in a 1:1 ratio with the rituximab paratope. Therefore, the strong decrease in binding is probably caused by additional effects. One effect could be associated with the close proximity of ARV9 to rituximab due to the SEED format. Thereby the local concentration is increased, and an interaction is more likely. Furthermore, due to the substitution of one rituximab Fab, the affinity of the remaining Fab is decreased due to the loss of the avidity effect. Thereby further increasing the inhibitory effect of ARV9. Upon switch to acidic conditions, binding of ARV9 SEED is restored to the range of 5005 rituximab SEED binding under neutral conditions with EC_{50}s of 135.2 and 173 nM respectively. By comparing the obtained EC_{50} values with the literature,

a 20-fold decrease in binding is observed. Therefore, it can be assumed that rituximab relies heavily on the avidity effect for high affine cell binding. Surprisingly, cell binding of 5005 rituximab SEED under acidic conditions reveals an EC_{50} of 47.9 nM, which is 3.6-fold increase in affinity compared to the neutral condition. This effect could be caused by the vNAR, since under acidic conditions binding of the 5005 rituximab SEED was evident on HeLa cells. In order to test this hypothesis, a SEED with an vNAR without any charged amino acids in the CDRs or without any vNAR would be required. Despite the increased binding of 5005 rituximab SEED under acidic conditions, further characterization in form of an ADCC assay was performed. Therefore, a proof of principle ADCC assay at pH 7.4 and 6.0 utilizing cetuximab was performed (**Figure S 12**). While the signals at pH 7.4 were in the expected range, no signal was obtained in the samples at pH 6.0, indicating that the ADCC reporter assay was deemed non-functional at acidic pH.

A 20-fold difference of masked rituximab was observed between pH 7.4 and 6.0. Based on these promising results, another format was investigated where the vNAR was fused to the N-terminus of the rituximab light chain. The advantage of the light chain fusions is the preservation of the two Fab fragments and therefore no loss of affinity, furthermore recognitions sites of disease associated proteases can be incorporated into the linker sequences connecting the light chain with the vNAR. As a proof of principle protease MMP-9 was chosen. ARV9 was connected with four different linkers containing MMP-9 recognition sequences (**Table S 1**) to the light chain of rituximab. One linker is obtained from Geiger *et al.* (210), which utilizes a long MMP-9 recognition sequence (VHMPLGFLGP). The other three linkers contain a shortened MMP-9 recognition sequence (PLGLA) with different distances between the recognition site and the light chain. Since MMP-9 requires the recognition sequence exposed in a loop, but the amino acids remaining after cleavage could negatively influence binding behavior, the PLGLA motif was placed with a distance of two, five or ten amino acids away from the beginning of the light chain.

The constructs containing the different linker sequences were expressed in Expi HEK cells (**Figure S 8E** and **F**). After expression, all constructs were treated with MMP-9 to investigate cleavage efficiency (**Figure S 8G** and **H**). While ARV9 MMP-9 G4S revealed full cleavage without any remaining light chain fusion, ARV9 PLGLA and ARV9 PLGLA2 revealed a small band of remaining fusion protein. In contrast, ARV9 G4S PLGLA displayed little to no cleavage. This indicates that a distance of two amino acids between the V_L domain and the recognition sequence are not sufficient to ensure effective cleavage. Nevertheless, all constructs in the cleaved and non-cleaved state were tested in cell binding experiments (**Figure 30**).

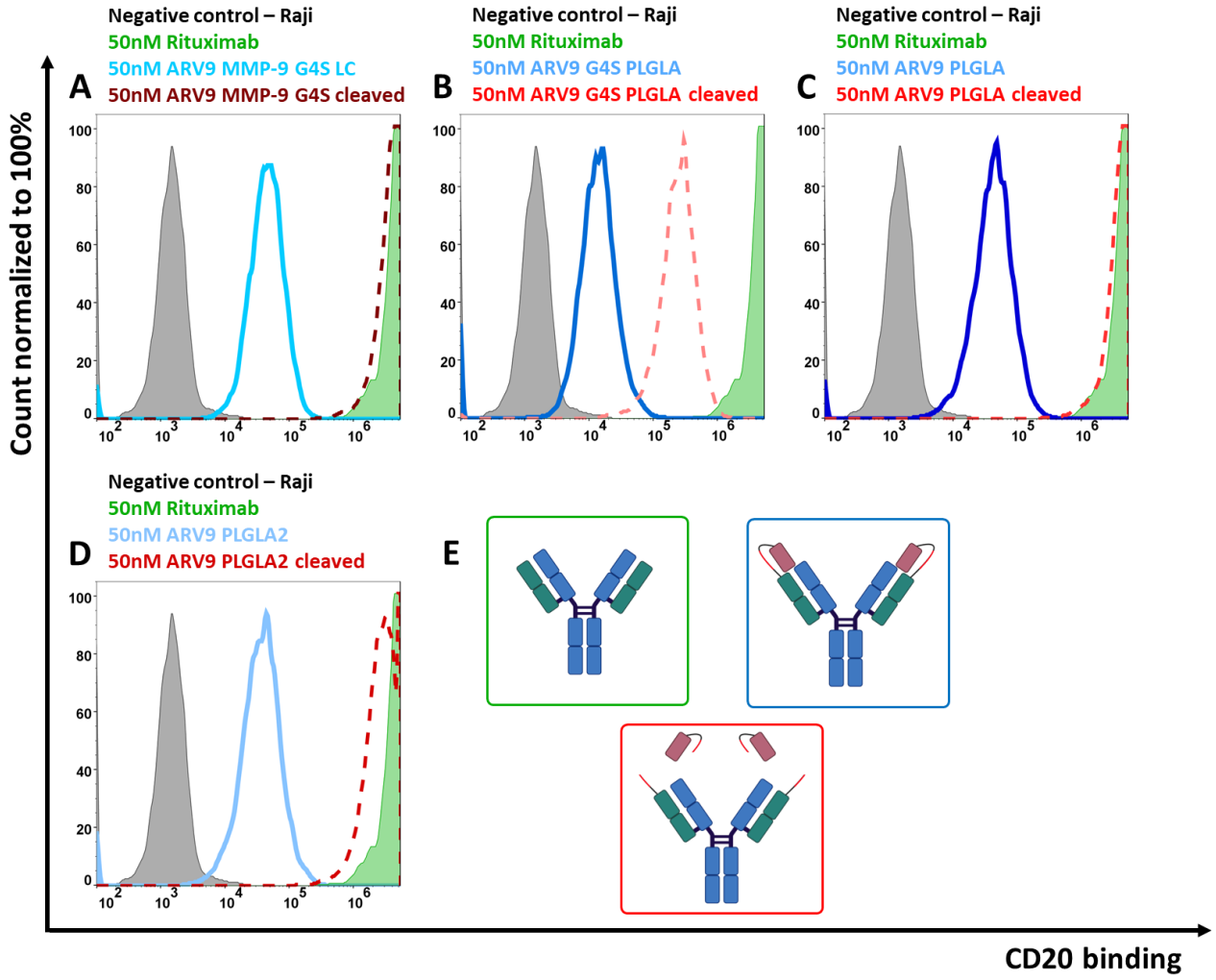

Figure 30: Cell binding of ARV9 fused to the light chain of rituximab *via* different MMP-9 cleavable linkers in a cleaved and non-cleaved form. Binding of the construct to CD20 on Raji cells in shown on the x-axis, while the count normalized to 100% is displayed on the y-axis. The negative control only incubated with anti-human-Fc-PE is shown in grey, while the sample incubated with rituximab is depicted in green. **A)** Cell binding of ARV9 connected to the rituximab light chain *via* the MMP-9 G4S linker. The sample with the non-cleaved linker is depicted in light blue, while the construct after MMP-9 cleavage is displayed by the dark red dashed line. Binding is fully restored after MMP-9 cleavage. The difference in binding for the samples with or without MMP-9 treatment is about two orders of magnitude. **B)** Cell binding of ARV9 connected to the rituximab light chain *via* the G4S PLGLA linker. The sample with the non-cleaved linker is depicted in blue, while the construct after MMP-9 cleavage is displayed by the light red dashed line. Binding is not fully restored upon MMP-9 cleavage. The difference in binding for the samples with or without MMP-9 treatment is about one and a half orders of magnitude. **C)** Cell binding of ARV9 connected to the rituximab light chain *via* PLGLA linker. The sample with the non-cleaved linker is depicted in blue, while the construct after MMP-9 cleavage is displayed by the red dashed line. Binding is fully restored upon MMP-9 cleavage. The difference in binding for the samples with or without MMP-9 treatment is about two orders of magnitude. **D)** Cell binding of ARV9 connected to the rituximab light chain *via* PLGLA2 linker. The sample with the non-cleaved linker is depicted in light blue, while the construct after MMP-9 cleavage is displayed by the red dashed line. Binding is fully restored upon MMP-9 cleavage. The difference in binding for the samples with or without MMP-9 treatment is about two orders of magnitude. **E)** A schematic illustration of the constructs for rituximab (green box) as well as the cleaved (red box) and non-cleaved (blue box) constructs. The non-cleaved state for each construct is shown in a scale of blue, while the cleaved state is shown in a scale of red.

As expected based on previous experiments, all light chain fusions revealed a decrease in binding compared to the positive control. While ARV9 MMP-9 G4S, ARV9 PLGLA and ARV PLGLA2 display a similar degree of reduction in binding, ARV9 G4S PLGLA displays an even higher reduction (**Figure**

30B). This finding might indicate a negative effect of the MMP-9 sites on linker flexibility. However, the PLGLA G4S linker seems unsuitable due to insufficient MMP-9 cleavage (**Figure S 8F**) and therefore retention of the masking effect which was observed in cell binding assays. In contrast, ARV9 PLGLA2 reveals near full restoration of binding, while ARV9 MMP-9 G4S and ARV9 PLGLA reveal full restoration of binding upon MMP-9 cleavage. This finding is surprising, since results of ARV9 PLGLA2 indicate that more amino acids on the N-terminus of the light chain negatively influences binding. Therefore, ARV9 PLGLA was chosen for further investigation, since the cleavage site is closer to the N-terminus of the light chain. SEC analysis of ARV9 PLGLA and rituximab revealed a single peak for both proteins and a small decrease in the retention time for ARV9 PLGLA. The decrease in retention time indicates an increase in protein size for ARV9 PLGLA, due to the presence of vNARs on the light chains (**Figure S 13**). Furthermore, this result indicates binding of the vNAR to a rituximab Fab within the same antibody. Additionally, cell binding analysis of ARV9 PLGLA for determination of EC_{50} was carried out (**Figure 31**).

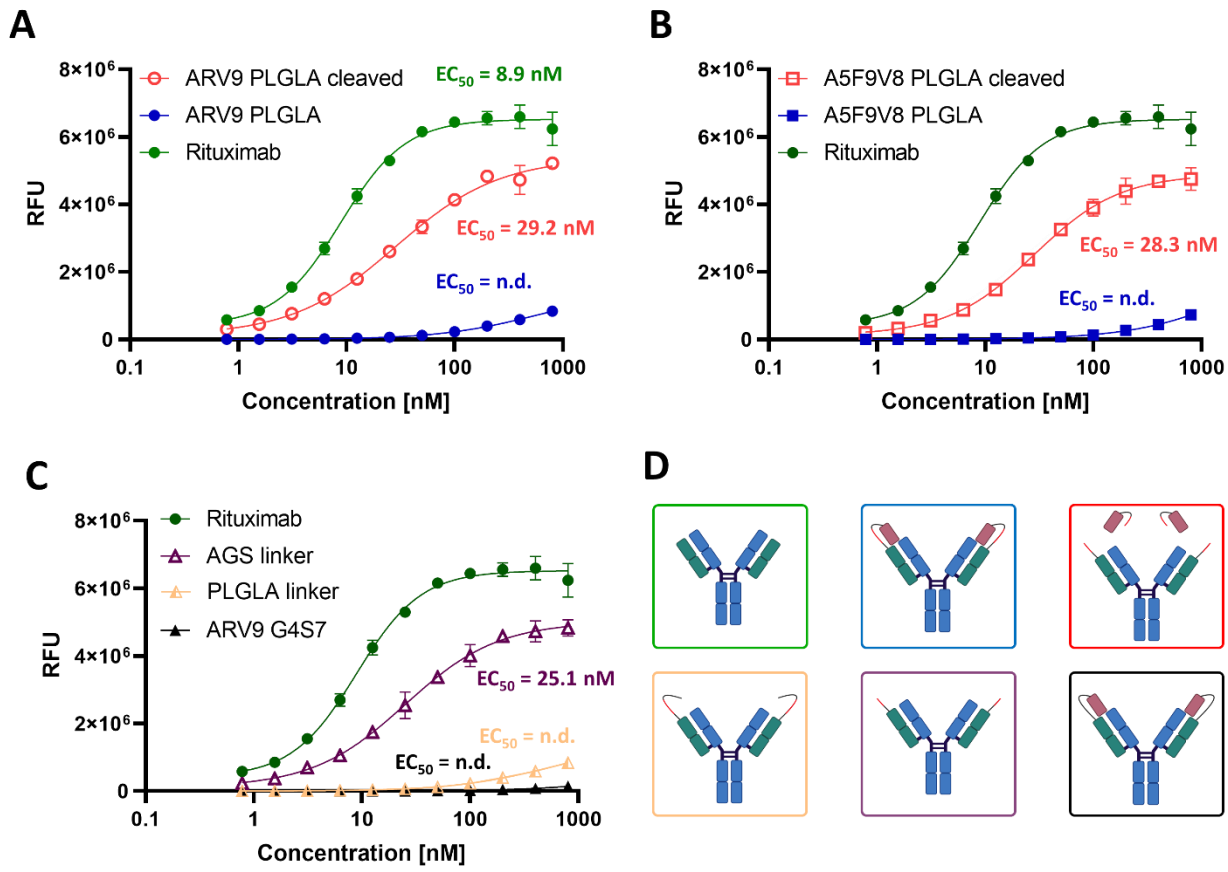

Figure 31: EC_{50} determination of different rituximab light chain fusions. Relative fluorescence units are depicted on the y-axis, while the concentration in nanomolar is shown on the logarithmic x-axis. The EC_{50} for each construct is shown in the same color as the respective binding curve. Binding curves were calculated utilizing the variable slope four-parameter fit. **A)** Binding curves of rituximab, as well as ARV9 PLGLA in the cleaved and non-cleaved state. The positive control is represented by rituximab is displayed by the green curve. ARV9 PLGLA in the non-cleaved state and after MMP-9 cleavage are shown in blue and red respectively. Rituximab as well as cleaved ARV9 PLGLA sample display a sigmoidal curve, while before cleavage ARV9 PLGLA

displays a slight increase in the binding signal at higher concentrations. **B)** Binding curves of an unrelated vNAR (A5F9V8) fused to the light chain of rituximab *via* the PLGLA linker in the cleaved and non-cleaved stare as well as rituximab. The positive control is represented by rituximab is displayed by the green curve. A5F9V8 PLGLA in the non-cleaved state and after MMP-9 cleavage are shown in blue and red respectively. Rituximab as well as cleaved A5F9V8 PLGLA sample display a sigmoidal curve, while before cleavage ARV9 PLGLA displays a slight increase in the binding signal at higher concentrations. **C)** Binding curves of different control constructs as well as rituximab as positive control (green curve). For the AGS control, the six amino acids remaining after cleavage were fused to the light chain of rituximab and are displayed by the purple curve. The PLGLA linker control contains the full length PLGLA linker N-terminally of the rituximab light chain and is shown in light orange. For the ARV9 G4S7 control ARV9 was fused to the light chain of rituximab *via* a non-cleavable glycine-serine linker which is represented by the black curve. **D)** Schematic depiction of the different constructs utilized in for EC_{50} determination. The colored boxes represent the colors of the different binding curves. Rituximab is shown in the green box, while non-cleaved and MMP-9 cleaved constructs are displayed in the blue and red box respectively. The controls containing the linker pre and post cleavage as well as ARV9 fused to the rituximab light chain by a non-cleavable linker are shown in the light orange, purple and black boxes.

An EC50 determination of ARV9 PLGLA was not possible since the binding was strongly reduced and the EC50 was not reached even at high concentrations of 800 nM (**Figure 31A**, blue curve). The binding of ARV9 PLGLA is about 1500-fold decreased compared to rituximab. The EC_{50} of rituximab was determined at 8.9 nM (**Figure 31A**, green curve) and is comparable to the EC_{50} value found in the literature (347). After MMP-9 cleavage of ARV9 PLGLA and removal of the vNAR (**Figure S 8J**) an EC_{50} of 29.2 nM was calculated (**Figure 31A**, red curve). The EC_{50} of the cleaved variant is decreased about 3-fold compared to the EC_{50} of rituximab. Furthermore, the amount of surface bound antibody is also decreased, which is represented by the amplitude of the RFU. These findings lead to the assumption that either traces of ARV9, which were not detectable by SDS-PAGE were present or an effect of the remaining linker fragment is responsible for the decrease of EC_{50} and surface bound antibody. Therefore, different controls were cloned and investigated. Firstly, the five remaining amino acids were fused to the light chain of rituximab (**Figure S 8L**). The EC_{50} of the AGS control was determined at 25.1 nM, which is comparable to the ARV9 PLGLA construct post cleavage and purification (**Figure 31C**, purple curve). Therefore, the decrease in EC_{50} and surface bound antibody can be attributed to the remaining five amino acids after MMP-9 cleavage. In consequence, the remaining amino acids either cause a slight alteration of the rituximab light chain structure as an allosteric antagonist or interfere directly with antigen binding. Since the analysis for changes in protein structure requires X-ray crystallography, further addressing this question was out of scope for this work. However, additional controls were generated to investigate, if the inhibitory effect in the ARV9 PLGLA construct can be attributed to an interaction of ARV9 with rituximab or a steric effect of the vNAR. Therefore, an unrelated vNAR directed against 5F9 (A5F9V8) was fused to the light chain of rituximab utilizing the PLGLA linker (**Figure S 8I**, **Figure 31B**). EC_{50} analysis of this construct revealed an inhibitory effect of the A5F9V8 similar to ARV9 with an about 500-fold EC_{50} decrease. After MMP-9 cleavage and removal of the vNAR, the EC50 was determined at 28.3 nM, which is also similar to the ARV9 PLGLA construct post cleavage and purification. This finding is highly surprising, since the previously isolated anti-idiotype vNARs revealed a high specificity. In order to investigate if the inhibitory effect is caused by the vNAR or the linker, two linker

controls were generated and tested (**Figure 31C**). The first control is represented by the PLGLA linker fused to the light chain of rituximab (**Figure S 8L**). EC_{50} determination of this construct revealed 1430-fold decrease in binding (**Figure 31C**, light orange curve), similar to the ARV9 PLGLA and A5F9V8 PLGLA constructs. Therefore, it can be concluded that the inhibitory effect on rituximab binding is not only caused by the fusion of ARV9 or A5F9V8, but the fusion of the PLGLA linker makes great a great contribution to rituximab masking. One possible explanation for this effect might be similarities of the epitope addressed by rituximab and the sequence of the PLGLA linker (348). The core epitope of rituximab in CD20 comprises of the NPSE motif, which tolerates little to no amino acid substitutions (**Figure 32A**).

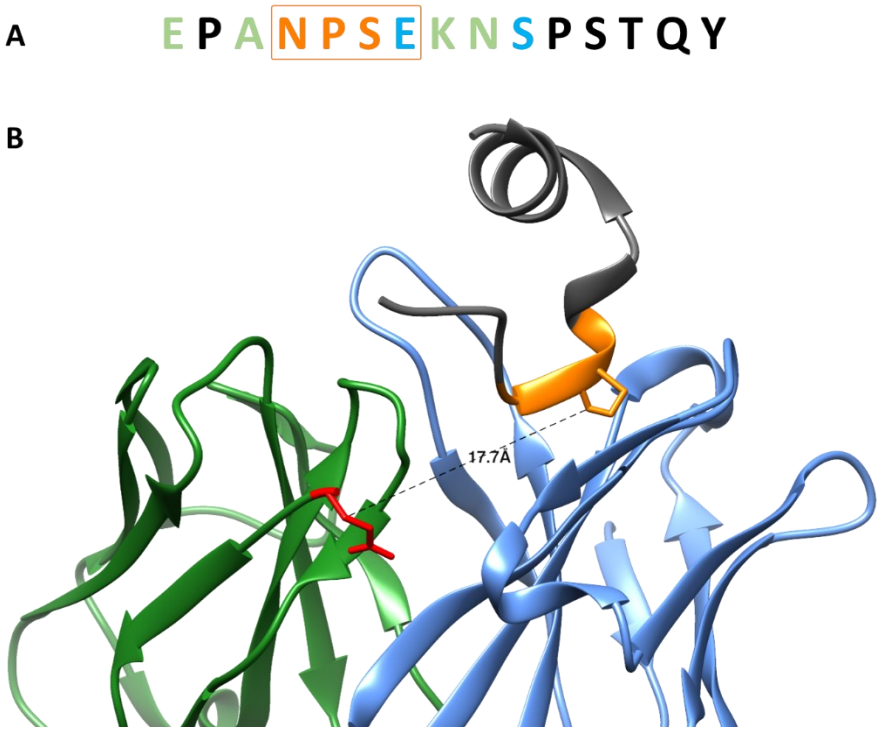

Figure 32: Analysis of the rituximab epitope and crystal structure to obtain insights in the masking of the PLGLA linker. A) Rituximab epitope with the core epitope highlighted by the orange box. Amino acid positions marked in green tolerate a wide variety of different exchanges (348). Positions marked in light blue tolerate substitutions to amino acids of similar properties. Amino acid positions marked in orange tolerate no substitutions. Positions marked in black have not been investigated so far. Adapted from Klein et al (348). **B)** Crystal structure of the rituximab Fab with a CD20 peptide (PDB: 2OSL). The V_L domain is shown in green, while the V_H is depicted in light blue. The CD20 peptide is displayed in black, with the core epitope shown in orange. The distance between the N-terminus of the light chain (marked in red) and the proline of the core epitope was determined to be 17.7 Å. Created with ChimeraX.

Therefore, it is unlikely that binding of the PLGLA linker occurs in a similar fashion as the core epitope. In contrast to the core epitope, a large part of the remaining epitope tolerates different kinds of amino acid substitutions. Therefore, it could be possible, that the PLGLA motif surrounded by the flexible glycine-serine segments is able to interact with the CDRs of the rituximab V_H. However, interaction between the PLGLA motif and the rituximab V_H CDRs is only possible, if the glycine-serine linker between

the N-terminus of the rituximab light chain and the PLGLA spans over the correct distance. Therefore, the distance between the N-terminus of the proline in the core epitope was measured based on a crystal structure of rituximab binding to a CD20 peptide (**Figure 32B**). The calculated distance between the N-terminus of the rituximab light chain and the proline of the core epitope is 17.7 Å. The length of the glycine-serine linker connecting the light chain to the PLGLA motif was calculated to be 19 Å (349). Therefore, the linker could be able to span the distance from the light chain to the CDRs of the heavy chain and thereby negatively interfere with rituximab binding to CD20.

Due to the notable finding that the masking effect is already seen with placement of the PLGLA linker sequence to the N-terminus of the rituximab light chain further characterization of the ARV9 PLGLA construct was performed. In analytical SEC analysis, the ARV9 PLGLA construct revealed one dominant peak with a slightly increased retention time compared to rituximab (**Figure S 13**). Furthermore, the melting point of ARV9 PLGLA (**Figure S 14A**) as well as A5F9V8 PLGLA (**Figure S 14B**) in the cleaved and uncleaved state were determined. Additionally, melting points of the AGS, ARV9 G4S7 and rituximab were determined (**Figure S 14C**). The melting point of all constructs were above 62 °C, indicating high stability. In addition to the characterization of protein aggregation behavior and stability, an ADCC reporter assay of ARV9 PLGLA in the uncleaved as well as cleaved and purified state was performed (**Figure S 15**). The ADCC reporter assay revealed no signal for the uncleaved ARV9 PLGLA construct, while activity was restored upon MMP-9 cleavage and removal of the vNAR. However, activity decreased about 1000-fold compared to rituximab. This strong reduction in activity was not expected since the difference in EC_{50} of rituximab and the cleaved and purified ARV9 PLGLA is only 3-fold. Therefore, another unknown effect might be responsible for the strong decrease in ADCC activity.

Overall, the screening campaign against rituximab resulted in four unique single clones, displaying different degrees of pH-dependency. ARV9 was chosen for further characterization due to strongest binding on yeast cells and highest pH-dependency. The inhibitory effect of ARV9 on rituximab binding to CD20 was confirmed in cell binding experiments. The generated SEED construct revealed restricted binding under neutral conditions, but upon switching to acidic conditions binding was restored. Different light chain fusions containing MMP-9 cleavable linkers revealed also restricted binding, which was restored upon MMP-9 cleavage. However, the remaining linker amino acids after cleavage revealed an inhibitory effect on rituximab binding and activity. Additionally, it was confirmed that the inhibitory effect of the PLGLA construct was caused by the PLGLA linker itself. As consequence, in this experimental setting not only Rituximab blocking vNARs were identified but serendipitously also a short peptide sequence (GGGGSGGGGSGGGGSGGGGSGGGGSPLGLAGGGGS) that, when amended to the Rituximab N-Terminus abolished target binding of the therapeutic antibody that could be restored upon its removal by MMP9 cleavage.

5.4 Screening and characterization of binding behavior for vNARs directed against the A6 T cell receptor

This proof of principle study was performed in collaboration with Katrin Schoenfeld and addresses the isolation of anti-idiotype-like vNARs directed against the T-cell receptor of the A6 cell line. To this end, the well characterized A6 TCR was chosen, due to the availability of a stabilized version with an optimized expression protocol (343). The A6 TCR cell line was lastly reported in the 1980s and is unobtainable. Therefore, a cell line was recreated based on the Jurkat cells by Philipp Wendel (Universitätsklinikum Frankfurt) utilizing CRISPR Cas9 mediated knockout of the Jurkat TCR and subsequent knock in of the A6 TCR. The knockout and knock in were verified by DNA sequencing and FACS-based analysis of TCR expression.

The screening campaign for the isolation of vNARs directed against the A6 TCR was carried out utilizing the histidine-doped vNAR libraries over four subsequent sorting rounds (**Figure 33**).

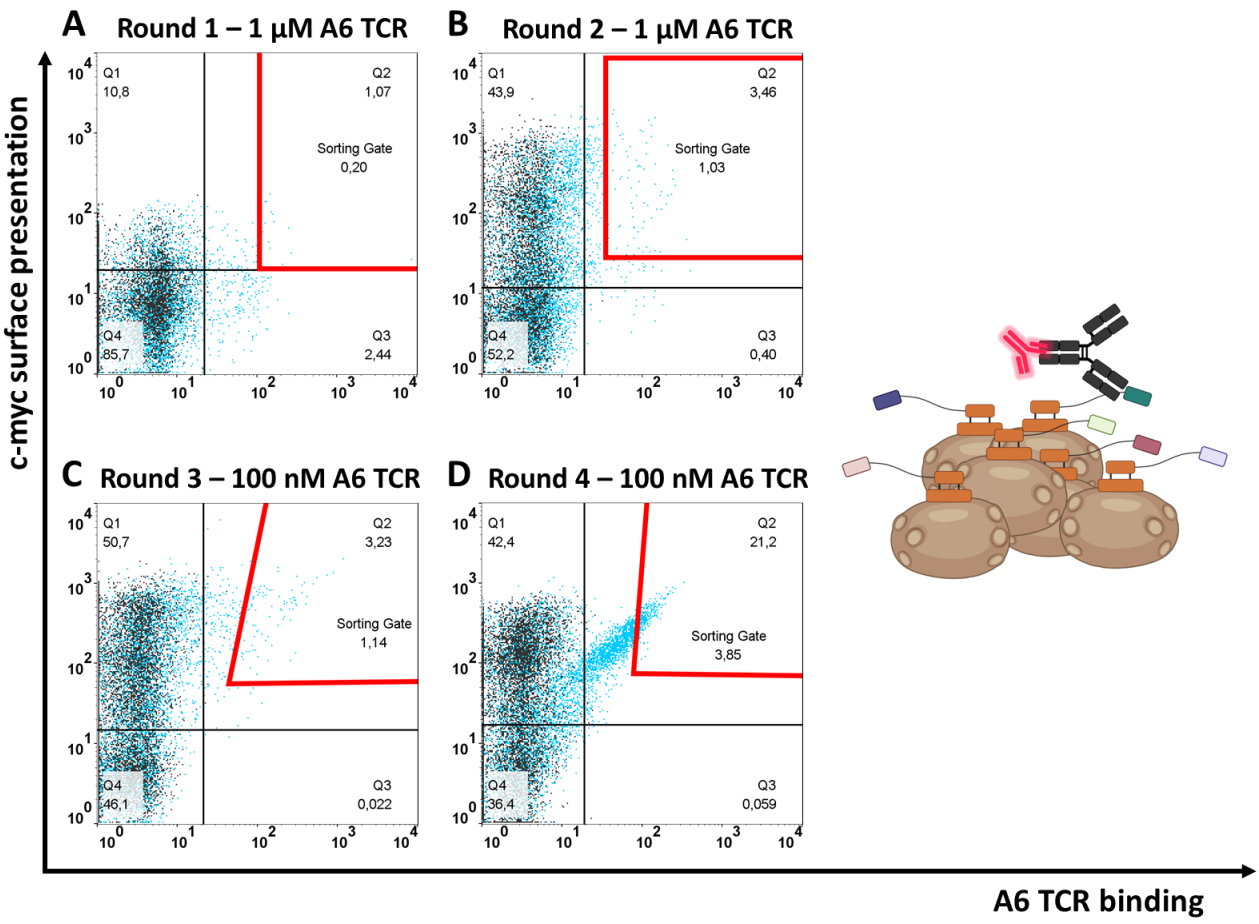

Figure 33: Screening campaign for the isolation of anti-A6 TCR vNARs utilizing histidine-doped vNAR yeast libraries with CDR3 lengths of 12, 14, 16, or 18 amino acids. vNAR surface presentation verified by anti-myc FITC is shown on the y-axis, while A6 TCR binding is displayed on the x-axis, verified by Alexa Fluor 647 labeled A6 TCR. The cells depicted in the dot plots are gated on viable and single cells. The negative control is shown in grey, while the sample incubated with Alexa Fluor 647 labeled A6 TCR is depicted in light blue. **A)** The first screening round reveals low surface presentation of 10.8% in the Q1 gate and target

binding at 1 µM of 1.07% in the Q2 gate. Cells isolated during this screening round are depicted in the red sorting gate. **B)** In the second screening round surface presentation is increased compared to the first screening round with 43.9% of the population located in the Q1 gate. Additionally, target binding at 1 µM A6 TCR is also increased to 3.46% in the Q2 gate. Cells isolated during this screening round are displayed in the red sorting gate. **C)** The third screening round reveals 50.7% of surface presentation, represented by the population in the Q1 gate. Target binding at a decreased A6 TCR concentration of 100 nM is represented by 3.23% of the population in the Q2 gate. Cells isolated during this screening round are shown in the red sorting gate. **D)** In the fourth screening round surface presentation is revealed by 42.4% of the population located in the Q1 gate. A6 TCR binding at 100 nM is increased compared to the last sorting round to 21.2% in the Q2 gate. Cells isolated during this screening round are displayed in the red sorting gate.

In the first round, the cells were incubated with 1 μM of Alexa Fluor 647 labeled A6 TCR (**Figure 33A**). A subpopulation of the yeast cells reveals binding towards the TCR. Since binding is visible not only in gate Q2, but also in Q3, it can be concluded that non-specific binding is responsible for the shift of the subpopulation. This binding behavior could be explained by a subpopulation which displays shortened vNAR variants or vNARs with very hydrophobic CDR3s interacting with partly denatured TCR molecules or the TCR is binding to a protein expressed only in a specific cell cycle. Therefore, the sorting strategy was adjusted and only cells displaying strong TCR binding were isolated. In the subsequent second screening round the cells were once more incubated with 1 μM of TCR (**Figure 33B**). A clear shift of the vNAR presenting population is evident in gate Q2, while non-specific binding in Q3 gate is greatly reduced compared to first round. Since non-specific binding is reduced in this screening round, TCR binding to a cell-cycle specific protein seems unlikely. In contrast, depletion of shortened vNAR variants as well as vNARs with hydrophobic CDR3s is more likely. In the outcome of sorting round two, depletion of all non-specific binders is observed, as well as an enrichment of binding variants (**Figure 33C**). Analysis of the fourth screening round revealed a strong enrichment of the binding population (**Figure 33D**). Therefore, subsequent single clone analysis was carried out (**Figure 34**).

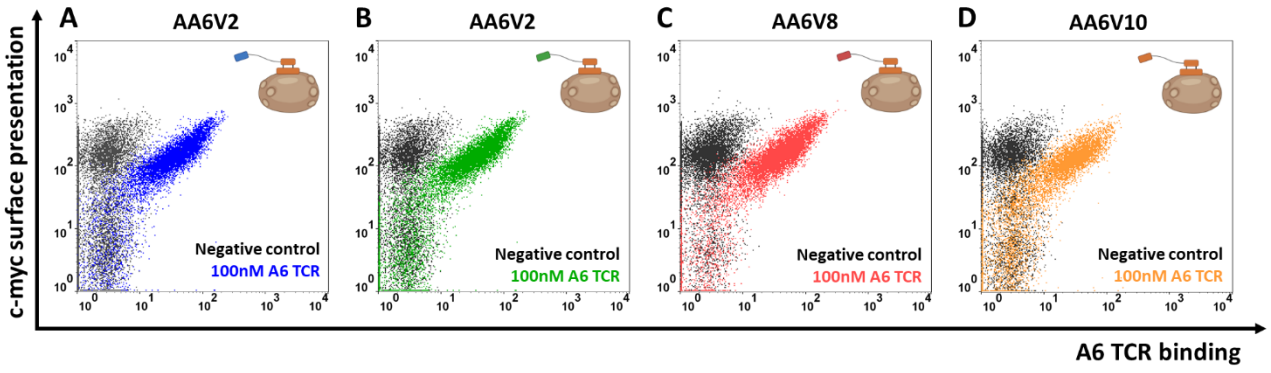

Figure 34: Yeast single clone analysis of anti-A6 TCR vNARs (AA6Vs). Surface presentation is shown on the y-axis *via* anti-c-myc-FITC antibody and target binding on the x-axis utilizing Alexa Fluor 647 labeled A6 TCR. The cells depicted in the dot plots are gated on viable and single cells. The negative control, incubated without the target is shown in black. **A-D)** Samples incubated with 100 nM of Alexa Fluor 647 labeled A6 TCR are displayed in blue, green, red and orange.

All analyzed single clones revealed strong TCR binding with minor differences among each other. Based on the binding analysis it could be speculated that one dominant clone is present in the population, however sequence analysis revealed four unique sequences (**Table S 5**). Sequence analysis of AA6V1 revealed an E86I point mutation in vNAR framework, which might contribute to binding, since the two epitopes of the A6 TCR (LLFGYPVYV and MLWGYLQYV) are primarily formed by hydrophobic amino acids. Furthermore, the CDR3 of AA6V1 exhibits 12 amino acids with one cysteine present, despite the fact that cysteine in the CDR3 was exclude during library design. Therefore, potential intermolecular disulfide bonds could lead to dimer formation and an altered binding behavior compared to monomeric vNARs. AA6V2 reveals 16 amino acids in the CDR3 with seven histidines, of which six are in groups of two and the rest of the CDR mostly formed by charged amino acids. In contrast, AA6V9 displays two tryptophans at the beginning and two phenylalanines at the end of the CDR3, while the middle part is formed by hydrophilic amino acids. AA6V10 reveals a 16 amino acid long CDR3 with three tryptophane residues of which two are located next to each other (**Table S 5**). Furthermore, the CDR3 of AA6V10 displays the closest match to the known A6 TCR epitopes of the analyzed four vNARs in terms of amino acid composition. All four constructs were expressed as thioredoxin fusions in *E. coli* and purified *via* IMAC and Streptactin chromatography (**Figure S 16A**). Afterwards, all constructs were tested in cell binding assays on Jurkat wild type (wt) and Jurkat A6 TCR cells (**Figure 35**).

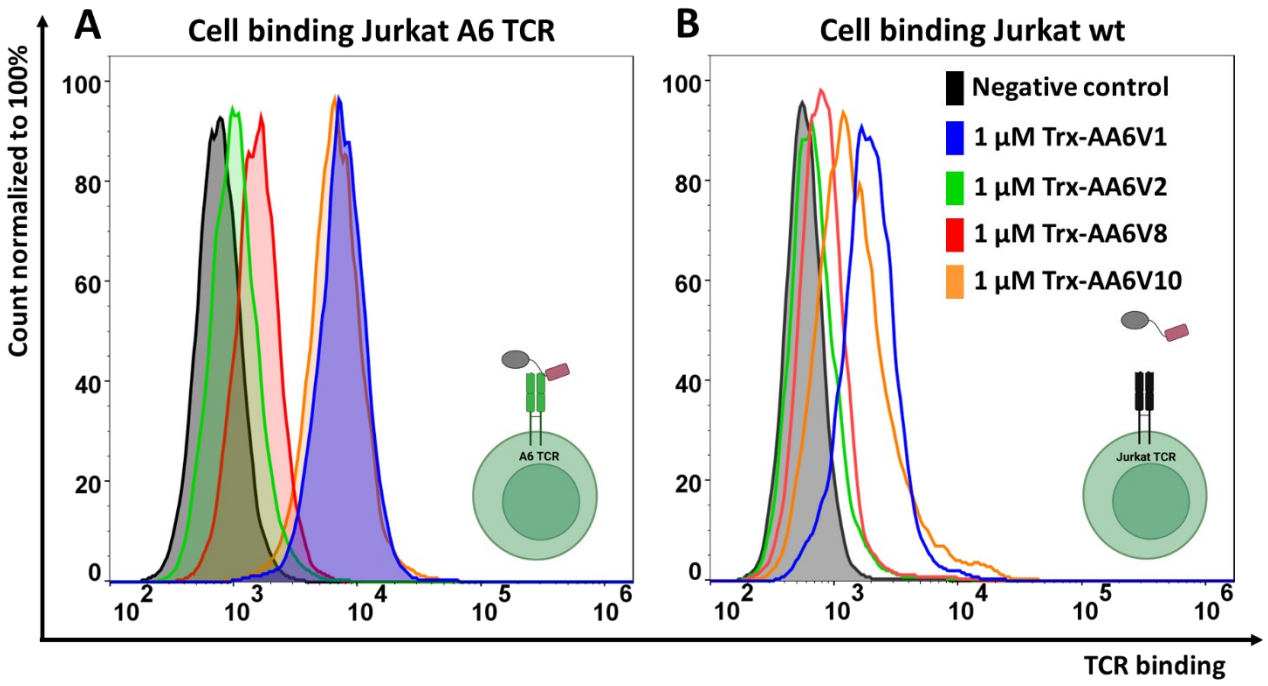

Figure 35: Cell binding analysis of anti-A6 TCR vNAR thioredoxin fusions on Jurkat A6 TCR and Jurkat wt cell lines. A) Binding of AA6V1, AA6V2, AA6V8 and AA6V10 on Jurkat A6 TCR cell line. Binding was verified with an anti-penta His Alexa Fluor 647 antibody and is depicted in blue, green, red and orange respectively, while the negative control is displayed in black. AA6V1 and AA6V10 reveal an increased binding of one order of magnitude compared to the negative control. In contrast, AA6V2 and AA6V8 display a 1.5- and 2-fold increase in cell binding respectively, **B)** Binding of AA6V1, AA6V2, AA6V8 and AA6V10 on Jurkat

wt cells. Binding is depicted in blue, green, red and orange respectively, while the negative control is displayed in black. AA6V1 and AA6V10 reveal a 5- and 2-fold increase in binding signal compared to the negative control. Binding increase of AA6V8 is about 1.5-fold, while AA6V2 displays binding in the range of the negative control.

Cell binding on Jurkat A6 TCR cells is evident for AA6V1 and AA6V10, whereas AA6V2 and AA6V8 display only a weak shift compared to the negative control (**Figure 35A**). This finding is surprising, since all vNARs demonstrated a comparable binding signal on the yeast surface. Since the expression machinery of *E. coli* differs from *S. cerevisiae*, the structure of the purified proteins could be altered or in case of AA6V1 formation of the disulfide bonds could be incorrect. Another factor impacting the binding properties of the vNARs is overall protein stability. Therefore, the melting point of all constructs was determined (**Figure S 16B**). The melting point of AA6V1 was determined to be 50 °C, while the melting point of AA6V2 is 58 °C. AA6V8 and AA6V10 displayed a melting point of 58.5 °C. Since the melting points of two vNARs with the weak binding is similar and even higher compared to the ones exhibiting strong binding, it is unlikely, protein instability causes the differences in binding behavior. Furthermore, the protein structure of the A6 TCR could be different on the Jurkat surface due to the presence of the extra- and intracellular segments of CD3. Furthermore, binding analysis of all constructs on the Jurakt wt negative control cell line revealed a weak shift for all constructs (**Figure 35B**). Binding of for AA6V2 and AA6V8 lies within the range of the negative control, while AA6V1 and AA6V10 reveal increased binding. By comparing binding between both Jurkat cell lines, binding of AA6V2 and AA6V8 to the Jurkat A6 TCR cell line might be caused by non-specific interactions. Binding of AA6V1 is evident for both cell lines. Therefore, it can be assumed, that binding does not occur in an anti-idiotype-like fashion, but rather that the epitope is located on constant regions of the alpha or beta chain. In contrast, AA6V10 binding towards the Jurkat A6 TCR cell line is evident, while only weak binding is visible for the Jurkat wt cell line. The binding on the Jurkat wt cell line is probably caused by the hydrophobic CDR3 and therefore subsequent interaction with hydrophobic sites on the cell surface. Since AA6V10 revealed anti-idiotype-like binding behavior further characterization was performed *via* BLI and EC_{50} determination (**Figure 36**).

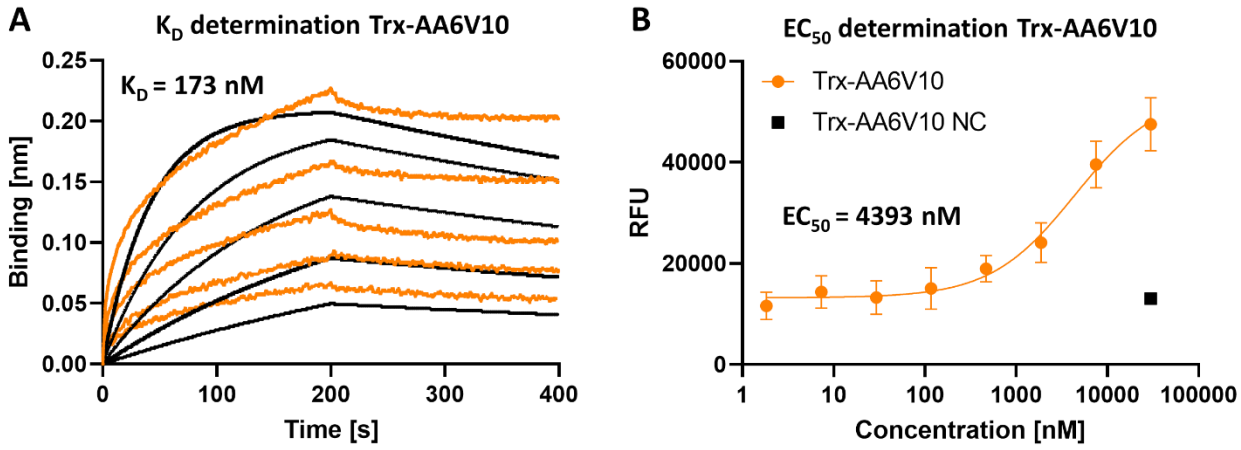

Figure 36: Determination of AA6V10 affinity *via* a cell binding assay and BLI. A) K_D Determination of the AA6V10 thioredoxin fusion. The time in seconds is shown on the x-axis, while binding in nanometer is displayed on the y-axis. The A6 TCR was biotinylated and loaded to streptavidin biosensors. Trx-AA6V10 was associated in different concentrations to the A6 TCR covered biosensor. The biosensor raw data are depicted in orange, while the fits for affinity determination are shown in black. An increase in binding is evident during the association step in the first 200 seconds. While a plateau is not reached in the association step, a plateau is reached about 100 seconds after beginning the dissociation step. **B)** Determination of the EC_{50} by a cell binding assay with the Jurkat A6 TCR cell line. The concentration (Start at 30 µM, 1:4 dilution) on a logarithmic scale is depicted on the x-axis, while the relative fluorescence units are shown on the y-axis. The orange dots indicate each data point, while the orange line represents the variable slope four-parameter fit utilized for EC_{50} determination. The black rectangle represents the highest concentration applied to Jurkat wt cells.

The determination of the K_D by BLI resulted in an affinity of 173 nM (**Figure 36A**). Due to the poor fit of the biding curves, affinity could not be determined in a reliable fashion. Despite this fact, the affinity should be in the correct order of magnitude and therefore is low, compared to the other anti-idiotype binding moieties described in this work. In the cell binding assay, AA6V10 does not bind to Jurkat wt cells even at high concentrations of 30 μM (**Figure 36B**, black rectangle). Furthermore, the cell binding assays revealed an EC_{50} value of 4393 nM for the Jurkat A6 TCR cell line. With an on-cell affinity in the micromolar large, AA6V10 seems not to be of high potency.

Overall, the screening of the histidine-doped vNAR libraries resulted in four unique single clones, which could be all expressed and purified. Only two of these clones displayed significant cell binding to the Jurkat A6 TCR cell line. One of these clones (AA6V1) exhibited binding towards the Jurkat wt cell line, therefore probably addressing an epitope on the constant domains of the TCR. In contrast, the other clone (AA6V10) binds specific to the Jurkat A6 TCR cell line. However, affinity determined by BLI and cell binding assays is in the high nanomolar to low micromolar range and therefore inferior in terms of affinity to most of the anti-idiotype moieties described in this work. In order to address this issue in upcoming experiments, increasing the valency by fusing up to four vNARs to a Fc, thereby increasing the avidity effect should be conducted. Furthermore, these multivalent constructs could be analyzed on potential proliferation inhibition or induction of apoptosis *via* clustering of the TCR. Additionally, antibody drug conjugates could be constructed and tested on cytotoxic effect. In contrast to different

antibody formats, the vNAR could be implemented as chimeric antigen receptor (CAR) in immune cell such as T- and NK-cells. The advantage of CAR constructs is the increase of avidity due to a high copy number of binding moieties on the cell surface as well as the utilization of the natural cytotoxic mechanisms to eliminate target cells.

In summary, the screening of vNAR libraries towards A6 TCR binding resulted in four unique single clones. Cell binding experiments revealed that three single clones addressed targets on the constant domains of an TCR. For the remaining single clone affinities were determined in BLI and cell binding experiments. Both determined affinities are moderate compared to other binding domains described in this work.

5.5 Isolation of anti-idiotypic chicken-derived scFvs directed against 6G11 and generation of masked light chain fusions displaying conditional activation upon MMP-9 digestion

In contrast to the other projects in this work, where shark-derived vNAR domains were used as potential antibody masking domains, this approach in collaboration with Dominic Happel was aimed at the isolation of anti-idiotypic chicken scFvs directed against 6G11. In order to obtain anti-idiotypic chicken scFvs, a chicken was immunized with a scFv of a therapeutic antibody. The antibody chosen for this approach was 6G11, which is currently in clinical trials. The 6G11 sequences were obtained from a patent and the scFv was generated by linking the V_H and V_L of 6G11 *via* a glycine-serine linker (350). Immunization, titer determination (**Figure S 17**), spleen and mRNA isolation were carried out at the service provider Davids Biotech. Upon receival of the mRNA, cDNA synthesis was carried out and V_H and V_L genes were amplified and fused together by PCR. The yeast library was generated, utilizing the amplified scFv sequences and a plasmid containing the T2A and tGFP sequences for the simplified yeast surface display. Prior to screening, the correlation of intracellular tGFP and c-myc surface presentation was investigated (**Figure S 18**). After confirming tGFP and c-myc surface presentation, the first screening round was carried out utilizing 1 μM of 6G11 containing the Fc silencing PGLALA mutations (from here on referred as 6G11, since all following constructs carry the PGLALA mutation) (**Figure 37A**).

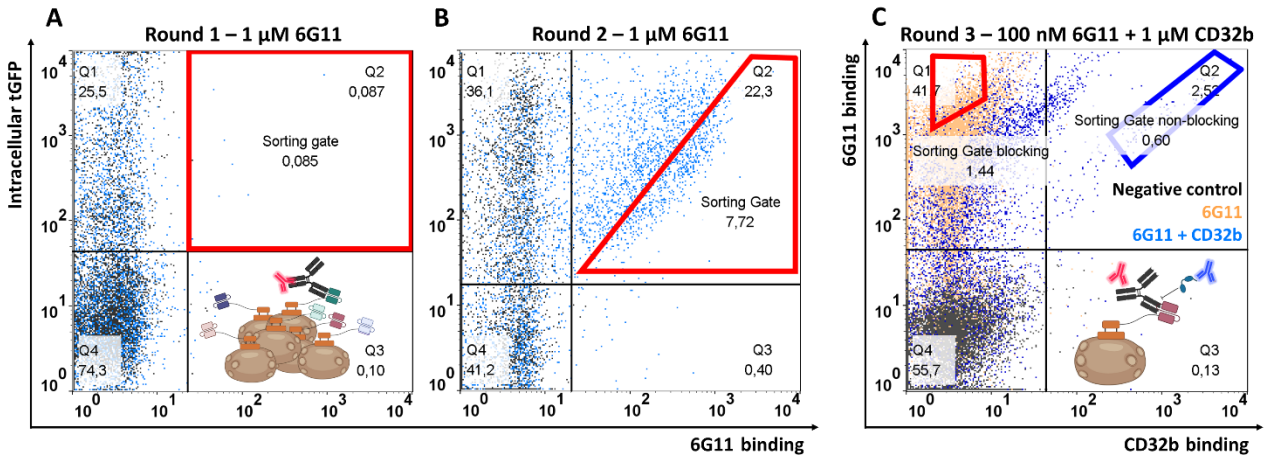

Figure 37: Dot plots of chicken scFv library screening towards 6G11 binding. The cells depicted in the dot plots are gated on viable and single cells. **A)** Screening round 1 towards 6G11 binding. Chicken scFv surface presentation is depicted on the y-axis indicated by intracellular tGFP expression, while antigen binding (anti-human Fc PE) is shown on the x-axis. The negative control is depicted in grey, whereas cells incubated with 1 µM 6G11 are shown in blue. Surface presentation of the initial library is 25.5% (Q1 gate), while binding towards 6G11 is 0.087% (Q2 gate). The cells isolated during this round are displayed in the red sorting gate. **B)** Round 2 of screening towards 6G11. Surface presentation is shown on the y-axis (tGFP expression) and 6G11 (DyeLight647) binding on the x-axis. The negative control is depicted in grey, while the cells shown in blue are incubated with 1 µM 6G11. Surface presentation of the initial after one screening round is 36.1% (Q1 gate), while binding towards 6G11 is strongly increased to 22.3% (Q2 gate), compared to round 1. The isolated cells are shown in the red sorting gate. **C)** Round 3 of screening towards blocking and non-blocking anti-6G11 chicken scFvs. The cells displayed in the dot plot are gated on viable, single, and surface presenting cells. 6G11 binding (anti-human Fc PE) is shown on the y-axis, while CD32b binding (anti-penta His Alexa Fluor 647) is depicted on the x-axis. The negative control (anti-human Fc PE and anti-penta His Alexa Fluor 647) is shown in grey, while cells incubated with 100 nM 6G11 (41.7%) are depicted in light orange and cells co-incubated with 100 nM 6G11 and 1 µM CD32b are shown in dark blue. For the sample incubated with 6G11 and CD32b only a small population (2.52%) reveals binding towards the 6G11-CD32b complex, while the majority of the variants interferes with the 6G11 and CD32b interaction. Sorting gates for the isolation of 6G11-CD32b inhibiting scFvs is shown in red, while the sorting gate for the isolation of variants not interfering with 6G11 and CD32b binding is shown in blue.

As expected, binding towards 6G11 is weakly detected in the library prior to sorting. However, after the first screening round variants binding to 6G11 are strongly increased (**Figure 37B**). Another sorting round towards 6G11 binding was carried out to ensure the absence of variants not binding to 6G11 for the isolation of scFv interfering in the 6G11 and CD32b interaction. For the isolation of scFv interfering and not interfering in the 6G11 and CD32b interaction an adjustment in the gating strategy was required. The cells shown in **Figure 37C** were not only gated on viable and single cells, but also on surface presentation. The sample incubated with 6G11 and CD32b reveals only a small population binding to the 6G11-CD32b complex, while the majority of the variants interferes in the 6G11-CD32 interaction. Besides the variants allowing weak CD32b binding, some variants blocking the 6G11-CD32b interaction completely. These variants (**Figure 37C**, red gate) as well as variants not interfering in the 6G11-CD32b binding (**Figure 37C**, blue gate) were enriched in the third screening round. Sequence analysis of single clones obtained from both screening approaches revealed the presence of one dominant single clone for each approach (**Table S 6**). Sequence analysis of the V_H and V_L domains revealed only minor variations in the CDRs of V_L domain. CDR length for both V_L domains is identical, while the amino acids within the

CDRs display similar characteristics. In contrast, the CDRs of the V_H domains reveal greater sequence diversity. Additionally, the characteristics of the amino acids within the CDRs differ widely. Most notably, the CDR2 of A6G11S2NC comprises of five aspartic acid residues in a row.

The two obtained single clones isolated under two conditions were tested for their capabilities to block the 6G11-CD32b interaction (**Figure 38**).

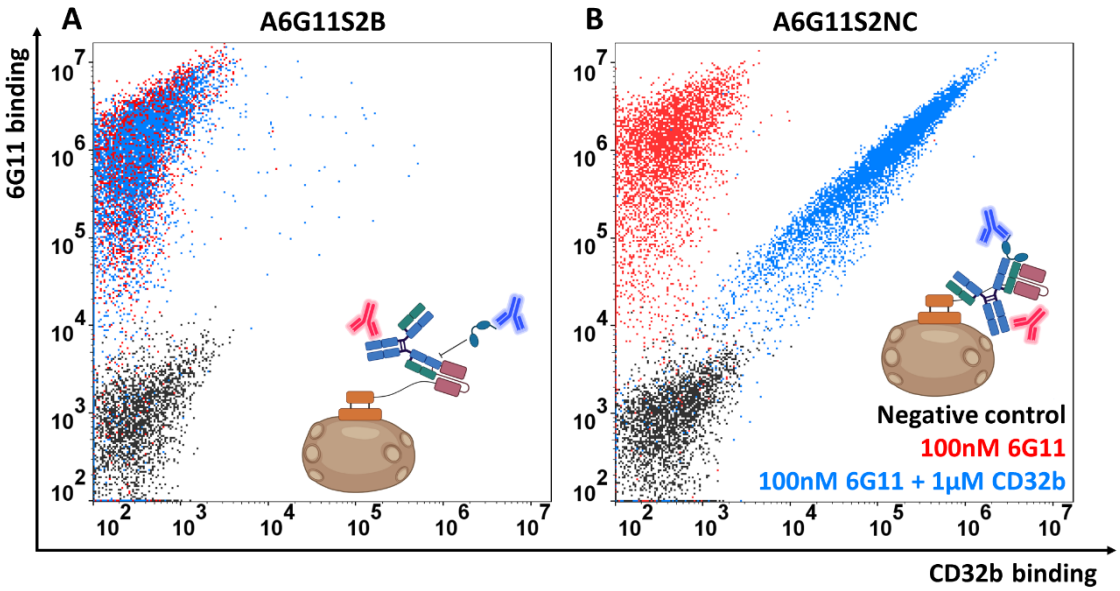

Figure 38: Dot plots of yeast single clone analysis for chicken scFv variants interfering and non-interfering in the 6G11-CD32b interaction. 6G11 binding is depicted on the y-axis, while CD32b binding is shown on the x-axis. The cells depicted in the dot plots are gated on viable and single cells. **A)** Anti-6G11 scFv clone 2 (A6G11S2B) obtained from the third sorting round for scFv interfering in the 6G11 and CD32b interaction. The negative control (anti-human Fc PE and anti-penta his Alexa Fluor 647) is shown in grey, while the sample incubated with 100nM 6G11 is displayed in red, whereas cells co-incubated with 100 nM 6G11 and 1 µM CD32b are depicted in blue. **B)** Anti-6G11 scFv clone 2 (A6G11S2NC) obtained from the third sorting round for scFv not interfering in the 6G11 and CD32b interaction. The negative control (anti-human Fc PE and anti-penta his Alexa Fluor 647) is shown in grey, while the sample incubated with 100nM 6G11 is displayed in red, whereas cells co-incubated with 100 nM 6G11 and 1 µM CD32b are depicted in blue.

The single clone isolated from the population interfering with the 6G11-CD32b interaction blocks the interaction between 6G11 and CD32b entirely, since no binding towards CD32b was detected (**Figure 38A**). In contrast, the clone obtained from the approach not affecting the 6G11-CD32b interaction shows simultaneous binding of 6G11 and CD32b (**Figure 38B**). For further investigating binding properties, both clones were expressed in *E. coli*. Firstly, the binding of both variants towards 6G11 was investigated *via* ELISA (**Figure S 19**). Both variants display an EC_{50} in the low nanomolar range, with A6G11S2NC (EC_{50} = 3.8 nM) revealing a 7.5-fold lower EC_{50} compared to A6G11S2B (EC_{50} = 28.7 nM). The EC_{50} of A6G11S2B is in the same range as the interaction of 6G11 with CD32b (K_D = 26.4 nM). Despite the fact that both affinities are in the same range, A6G11S2B displays significant interference in the 6G11-CD32b interaction. This blocking effect could be attributed to either very fast association of the scFv to 6G11 or

a very slow dissociation. Therefore, BLI analysis of A6G11S2B was performed (**Figure 39A**). The analysis revealed a very fast association of A6G11S2B to 6G11, while the dissociation occurs moderately fast. Therefore, the inhibitory effect of A6G11S2B is probably caused by a fast association, as soon as 6G11 releases CD32b. In contrast, the association of A6G11S2NC is slower compared to A6G11S2B. This difference can be attributed to the screening process, since A6G11S2NC was not required to interfere in the 6G11-CD32b binding and therefore does not require a fast association rate. Analysis of the dissociation exhibits no major differences between the two scFvs. For further analysis, specificity of both scFvs were conducted *via* a BLI experiments in presence of different antibodies (**Figure 39B** and **C**).

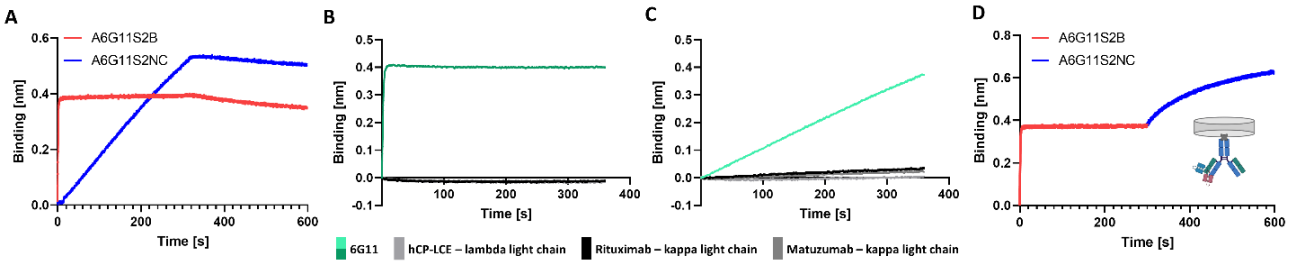

Figure 39: Epitope mapping and specificity analysis of A6G11S2B and A6G11S2NC *via* BLI. The time in seconds is shown on the x-axis, while binding in nanometer is displayed on the y-axis. **A)** Analysis of A6G11S2B and A6G11S2NC binding properties towards 6G11. Binding curve of A6G11S2B is depicted in red, while A6G11S2NC is shown in blue. 6G11 was loaded to a protein A tip and association as well as dissociation of A6G11S2B and A6G11S2NC were measured. A6G11S2B reveals a very fast association towards 6G11, while the dissociation is moderate fast. In contrast, association of A6G11S2NC is slower compared to A6G11S2B, however a higher binding signal is achieved. Dissociation of A6G11S2NC is slightly slower compared to A6G11S2B. **B)** Specificity analysis of A6G11S2B. Different antibodies were loaded to a protein A biosensor and subsequent incubation in a well containing A6G11S2B. 6G11 represents the positive control (green; 0.4 nm increase of binding), while hCP-LCE and matuzumab represent controls for lambda and kappa light chain binding respectively. With rituximab potential binding to murine fragments is tested. No binding towards hCP-LCE, matuzumab and rituximab is observable. **C)** Specificity analysis of A6G11S2NC. Different antibodies were loaded to a protein A biosensor and subsequent incubation in a well containing A6G11S2NC. 6G11 represents the positive control (light green; 0.4 nm increase of binding), while hCP-LCE and matuzumab represent controls for lambda and kappa light chain binding respectively. With rituximab potential binding to murine fragments is tested. No binding towards hCP-LCE, matuzumab and rituximab is observable. **D)** Epitope mapping of A6G11S2B and A6G11S2NC scFvs. 6G11 was loaded to a protein A biosensor and A6G11S2B and A6G11S2NC were associated successively. The binding signal marked in red represents association of A6G11S2B (about 0.4 nm increase of binding), while subsequent binding of A6G11S2NC is displayed in blue (about 0.2 nm increase of binding).

The BLI analysis revealed high specificity of A6G11S2B and A6G11S2NC towards 6G11 since no binding towards antibodies containing a lambda or kappa light chain as well as murine V_H/V_L domains is observed. The findings for A6G11S2B are not surprising, since A6G11S2B interferes with 6G11 binding and therefore the epitope is required to be located at the CDRs. In contrast, A6G11S2NC does not interfere with 6G11 binding and therefore, the epitope could be located in the framework regions of 6G11. Consequently, off-target binding of A6G11S2NC could be possible. However, the epitope of A6G11S2NC could be located in a CDR, which has a small or no impact on the interaction between 6G11 and CD32b. This hypothesis could be addressed by co-crystallization of both scFvs with 6G11. However, crystallization is a laborious method and therefore a BLI-based epitope mapping was chosen to analyze the epitopes *via* subsequent association of A6G11S2B and A6G11S2NC to 6G11 (**Figure 39D**). If the

epitopes addressed by the scFvs overlap, association of the only one scFv is possible or in case of minor overlaps, binding of the second scFv would be decreased. If the scFvs address different epitopes, association of both scFvs is feasible. Based on the data obtained from the subsequent association of both scFvs, addressing of two different epitopes seems the most likely option.

Since A6G11S2B revealed an inhibitory effect on the 6G11-CD32b interaction, the scFv was fused to the light chain of 6G11 utilizing an MMP-9 cleavable linker described in Geiger *et al.* (210). In order to evaluate the effect of a scFv fused to the 6G11 light chain which does not interfere with the 6G11-CD32b interaction, A6G11S2NC was as well fused to the 6G11 light chain *via* the MMP-9 cleavable linker. Light chain fusions were expressed in Expi HEK cells and purified *via* protein A chromatography. After the purification, the stability of the constructs was tested in the presence of different proteases (**Figure S 20**). 6G11, A6G11S2B fused to the light chain of 6G11 (S2B MMP-9) as well as A6G11S2NC fused to the light chain of 6G11 (S2NC MMP-9) were incubated over night with either no protease, MMP-9, matriptase or uPA, since both proteases are overexpressed in several cancers. As expected, 6G11 was not cleaved by any protease (**Figure S 20A)**. In the case of S2B MMP-9 and S2NC MMP-9, only MMP-9 was able to cleave the constructs (**Figure S 20B and C)**. The other proteases had no effect on the constructs. Next, EC_{50} determination of 6G11 and the fusion constructs on CD32b expressing Raji cells was carried out (**Figure 40**). The EC_{50} determined for 6G11 on Raji cells is comparable to the EC_{50} found in the literature (**Figure 40A**, green) (142). The EC_{50} of S2B MMP-9 in the uncleared state could not be determined since no binding is observed (**Figure 40A**, dark blue). The binding of S2B MMP-9 is decreased about 2700-fold compared to 6G11. This finding is surprising, since the affinity of 6G11 to CD32b and A6G11S2B to 6G11 are in the same concentration range. Therefore, some binding of the construct would be expected. One explanation for this finding could be the close proximity of A6G11S2B to 6G11, due to linking the scFv to the light chain. Furthermore, the linker seems not to interfere with A6G11S2B binding towards 6G11. Therefore, binding of A6G11S2B to the CDRs of the V_H domain of 6G11 could be hypothesized. Independent from the exact epitope, S2B MMP-9 binding towards CD32b is restored upon MMP-9 cleavage (**Figure 40A**, dark red). However, the calculated EC_{50} of the cleaved construct is about 65-fold decreased in comparison to 6G11. Furthermore, the absolute binding signal of the cleaved S2B MMP-9 construct is higher than 6G11. This finding could be explained by alterations in the 6G11 structure after binding caused by the remaining amino acids at the N-terminus of the light chain after MMP-9 cleavage, which somehow enables more 6G11 molecules to bind to the cell surface. The findings of decreased EC_{50} and an increased number of antibodies on the cell surface could be attributed to the remaining A6G11S2B in the cleavage mix, the MMP-9 digestion conditions or to the remaining amino acids after MMP-9 cleavage. In order to investigate the hypothesis of an effect of the remaining amino acids after MMP-9 cleavage, data obtained from S2NC MMP-9 might give an insight.

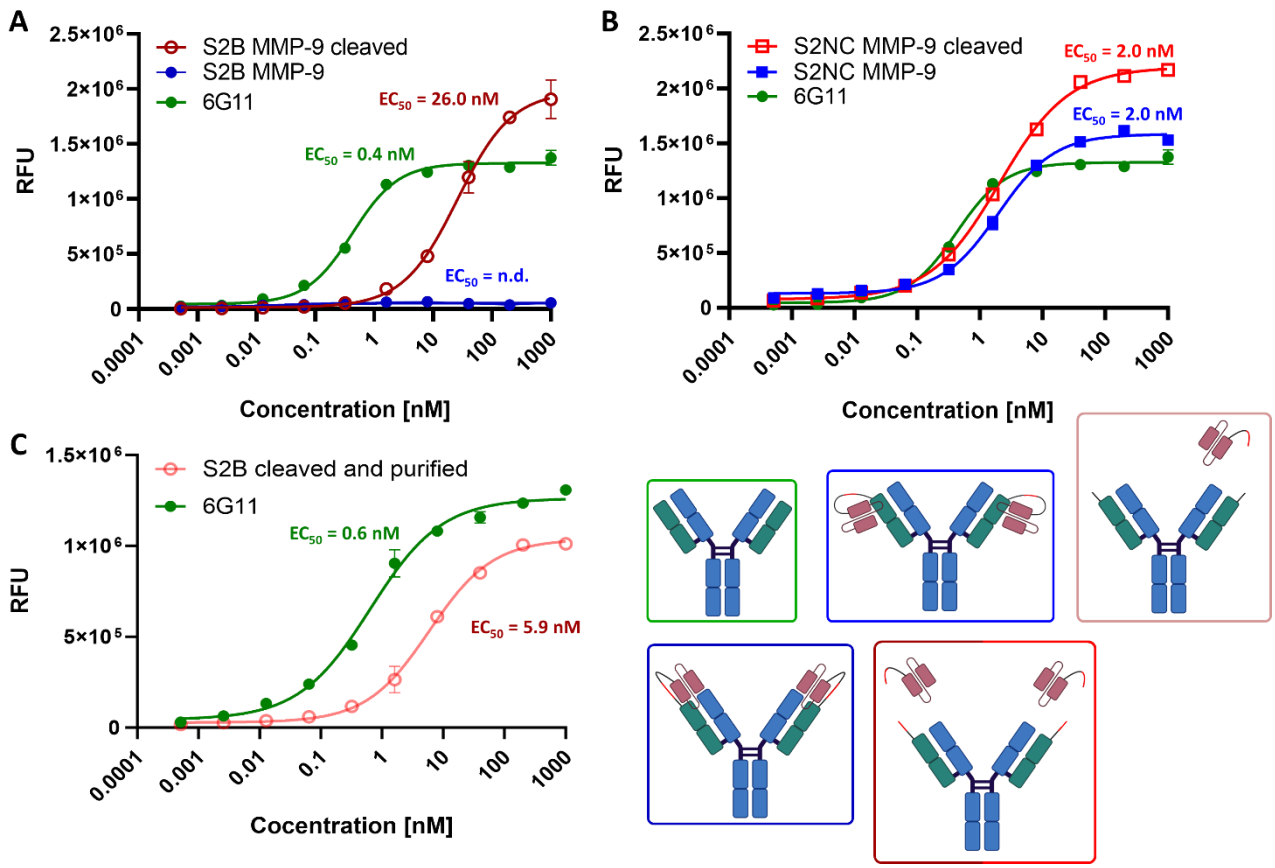

Figure 40: EC_{50} determination of anti-6G11 chicken scFv fused to the light chain of 6G11 *via* an MMP-9 cleavable linker. The concentration is shown on the x-axis, while RFU are depicted on the y-axis. EC50s and a schematic overview of the analyzed construct are displayed in the respective color of the binding curve. For each construct data points obtained from flow cytometry measurements and the line representing the fit for EC_{50} determination are shown in the same color. **A)** Binding curves of A6G11S2B light chain fusion prior and post MMP-9 cleavage. The positive control is represented by unmodified 6G11, shown in green. A6G11S2B fused to the light chain of 6G11 *via* the MMP-9 cleavable linker is shown in dark blue. Binding after cleavage with MMP-9 is depicted in dark red. 6G11 reveals a sigmoidal curve and reaches plateaus in at concentrations <0.01 nM and >10 nM with a calculated EC_{50} of 0.4 nM. S2B MMP-9 reveals no binding and therefore, no EC_{50} could be determined. Upon MMP-9 cleavage, binding is restored with a plateau reached for concentration <1 nM, the upper plateau is presumedly reached at 1000 nM with a calculated EC_{50} of 26 nM. **B)** Binding curves of A6G11S2NC light chain fusion prior and post MMP-9 cleavage. The positive control is represented by unmodified 6G11, shown in green. A6G11S2NC fused to the light chain of 6G11 *via* the MMP-9 cleavable linker is shown in blue. Binding after cleavage with MMP-9 is depicted in red. S2NC MMP-9 reveals plateaus at concentrations <0.01 nM and >10 nM with a calculated EC_{50} of 2 nM. Upon MMP-9 cleavage the plateaus and EC_{50} remains unchanged. **C)** Binding curves of A6G11S2B light chain fusion post MMP-9 cleavage and removal of the A6G11S2B scFv via an 6G11-based purification column. The positive control is represented by unmodified 6G11, shown in green. Binding after cleavage with MMP-9 and removal of the vNAR is depicted in light red. 6G11 reveals a sigmoidal curve and reaches plateaus in at concentrations <0.001 nM and >10 nM with a calculated EC_{50} of 0.7 nM. After MMP-9 cleavage and scFv removal, binding is evident with plateaus reached for concentration <0.1 nM and >100 nM with a calculated EC_{50} of 6.9 nM.

In fact, the binding signal for the S2NC MMP-9 light chain fusion exhibits an increase in absolute binding signal upon MMP-9 cleavage. The effect is even stronger compared to the MMP-9 digested S2B MMP-9 light chain fusion. Therefore, no final conclusion could be obtained from the acquired data. For further investigation, additional controls would be required. The focus should be on a construct which only carries the amino acids after MMP-9 cleavage on the N-terminus of the light chain. This construct could furthermore address the question if the MMP-9 cleavage conditions play a role in this phenomenon.

Further analysis of the S2NC MMP-9 construct prior to MMP-9 prior and post MMP-9 cleavage revealed an identical EC50 for both conditions which is 5-fold reduced compared to 6G11. Therefore, it can be concluded that the fusion of A6G11S2NC has no effect on the EC_{50}, since the amino acids after MMP-9 digestion reveal the same influence on the EC_{50}.

In order to address the decreased EC_{50} of the S2B MMP-9 light chain fusion after MMP-9 cleavage, an 6G11-based affinity column was constructed, to remove A6G11S2B from the cleavage mixture. After applying the cleavage mixture two times to the column, a decrease intensity for the A6G11S2B band in the SDS-PAGE could be observed (**Figure S 20D**). EC_{50} determination of the S2B MMP-9 post MMP-9 digestion and purification revealed an about 10-fold decrease compared to 6G11. Additionally, a decrease in cell surface bound antibody is observed. This finding suggests that the MMP-9 cleavage conditions are responsible for the increase in surface bound antibody.

In addition to EC_{50} determination on cells, the K_D of all constructs were determined *via* BLI (**Figure 41**).

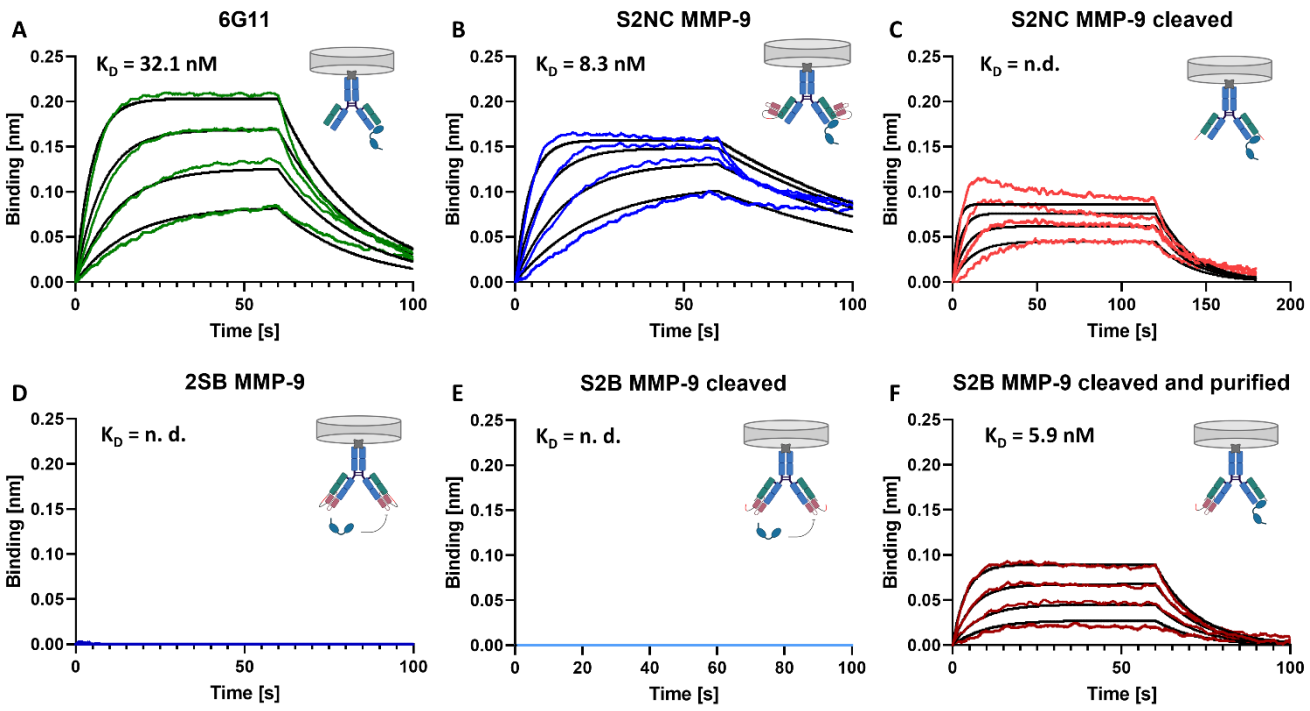

Figure 41: Affinity determination of different 6G11 constructs *via* BLI. Binding in nanometers is shown on the y-axis, while the time in seconds is displayed on the x-axis. The K_D and a schematic depiction of the analyzed antibody is shown for each construct. **A)** K_D determination of 6G11. The biosensor raw data are displayed in green, while the fits for affinity calculation are depicted in black. The fits correlate well with the measured data. **B)** K_D determination of S2NC MMP-9. The biosensor raw data are displayed in blue, while the fits for affinity calculation are depicted in black. The fits correlate well for the association, while the correlation for the dissociation is moderate. **C)** K_D determination of S2NC MMP-9 after MMP-9 cleavage. The biosensor raw data are displayed in red, while the fits for affinity calculation are depicted in black. The correlation between the measured data and the fit for the association are poor, while the fits correlate well for the dissociation. **D)** K_D determination of S2B MMP-9. The binding signal is depicted in dark blue. Since no binding signal was obtained, the K_D could not be calculated. **E)** K_D determination of S2B MMP-9 post MMP-9 cleavage. The binding signal is depicted in light blue. Since no binding signal was obtained, the K_D could not be calculated. **F)** K_D determination of S2B MMP-9 post MMP-9 cleavage and removal of the scFv. The biosensor raw data are displayed in dark red, while the fits for affinity calculation are depicted in black. The fits correlate well with the measured data.

The increase in binding for all analyzed variants is in the range of 0.2 to 0.05 nanometers, since the extracellular receptor domain of CD32b exhibits a calculated mass of only 21.8 kDa. Therefore, all measurements are prone to small changes in concentrations and measurement inaccuracies.

The calculated affinity of 32.1 nM for 6G11 binding to CD32b is in the same range as the affinity described in the literature (142). The affinity of S2NC MMP-9 prior to MMP-9 cleavage was calculated to be 8.3 nM (**Figure 41B**). Although the values are in the same range as the affinity of 6G11, the increase in affinity can be attributed to discrepancies between the measured data and the fit which is utilized to calculate the affinity. While the association of the construct correlates well with the fit, the dissociation does not. The dissociation is in fact faster than the fits suggests. Thereby, the affinity is biased towards a higher affinity. In case of the MMP-9 cleaved S2NC MMP-9 light chain fusion (**Figure 41C**), the fit for the association step is highly inaccurate and does not allow the calculation of a K_D value. In contrast, the dissociation matches well with the fit. Analysis of S2B MMP-9 prior to MMP-9 cleavage resulted as expected in no binding signal and therefore no K_D could be determined (**Figure 41D**). The S2B MMP-9 light chain fusion after MMP-9 cleavage revealed no binding towards CD32b (**Figure 41E**). This finding is surprising, since binding of this construct was observed in the cell binding experiment. One explanation for this finding could be a simultaneous dissociation of A6G11S2B and association of CD32b. The size of both proteins is in a similar range and 28.1 kDa for CD32b and 26.6 kDa for A6G11S2B. Whether this hypothesis is correct or not, an affinity determination is not possible based on these data. The removal of about half of the scFv restores the binding capacity (**Figure 41F**). The calculated affinity is about 5-fold increased compared to 6G11. Furthermore, in this case the measured data and the corresponding fits correlate with the fits. Therefore, the increased affinity can-not be explained by a discrepancy between measured data and the fits.

In summary, a yeast library based on the immunization of a chicken with the 6G11 scFv was constructed and binders interfering and not interfering with the 6G11-CD32b interaction could be isolated during the screening process. The isolated scFv could be solitary expressed in *E. coli* and revealed high affinity to 6G11. Fusing the A6G11S2B to the light chain of 6G11 *via* an MMP-9 cleavable linker, a masked 6G11 was obtained with a 2700-fold decreased binding compared to the unmasked 6G11. Binding could be restored after MMP-9 cleavage, however not to the range of the unmasked 6G11. Binding in the range of 6G11 could only be obtained after removal of about half of the scFv by an 6G11-based purification column, even than binding is about 10-fold decreased. Analysis of the A6G11S2NC light chain fusion revealed a 5-fold reduction in binding caused by the fusion of an scFv to the light chain of 6G11 as well as by the amino acids remaining after MMP-9 cleavage. Further analysis of all constructs *via* BLI revealed the same binding trends for most of the constructs. The only difference was displayed by the S2B MMP-9 light chain fusion after MMP-9 cleavage where no binding was observed.

6 Conclusion and outlook

Since the introduction of therapeutic antibodies in the late 1990s, this class of molecules has been improved for the treatment of cancer and a wide range of other diseases. One major goal in the antibody field is the identification of tumor specific antigens. This task is very challenging and the vast majority of cases, antigens overexpressed in tumors are chosen as targets (157). One major drawback of this strategy is that the antigen overexpressed in the tumor is often also present in the healthy tissue, resulting in a narrow therapeutic window. In order to address this downside, different antibody formats have been investigated. Besides increasing the selectivity of an antibody by addressing two or more overexpressed tumor antigens in the form of bi- and multispecific antibodies, immune modulatory antibodies have been developed (110, 145). These class of antibodies, addresses immune checkpoint inhibitors and enable the immune system to overcome the immunosuppressive tumor microenvironment. Furthermore, characteristics of the tumor microenvironment were utilized to develop antibodies with restricted binding. One example is the class of pH-dependent antibodies, which reveal an increased affinity towards the target upon entering the acidic tumor microenvironment (189). Another class of antibodies that has been studied more recently can be activated by proteases. These antibodies require a linker which is cleavable by a disease associated protease and a masking domain. The masking domain can either comprise of a bulky protein or structure which inhibit interaction with the antigen by steric hinderance or a tailor-made affinity-based masking domain which directly interacts with the paratope of the antibody (218). In this work, different affinity-based masking domains based on vNARs and chicken scFvs have been isolated and investigated.

One approach in this work was aimed on introducing pH-dependency in an existing anti-matuzumab vNAR, which blocked the matuzumab-EGFR interaction. The introduction of pH-dependency utilizing yeast surface display and FACS resulted in several variants exhibiting pH-dependency. However, affinity of all variants was decreased and in-depth analysis of one clone revealed the complete loss of the inhibitory effect towards the matuzumab-EGFR interaction, based on co-incubation experiments of the vNAR and matuzumab. Furthermore, construction of SEED constructs as well as light and heavy chain fusions utilizing a protease cleavable linker and a flexible glycine-serine linker were not able to restore the masking effect. Furthermore, also the parental, pH-independent vNAR was not able to exhibit the degree of masking, which was observed in co-incubation experiments, which indicates that fine-tuning of linker sequence, length and flexibility would be required.

Another approach was aimed at isolating pH-dependent vNARs from histidine-doped yeast libraries directed against 5F9 and rituximab. The isolation of pH-dependent vNARs directed against both antibodies was successful. Several clones were obtained in both screening campaigns, which were also expressible in either *E. coli* or mammalian Expi cells. The analysis of the expressed variants revealed high affinity towards their respective antibody as well as a blocking effect on the antibody-target interaction

in co-incubation experiments. Different approaches were investigated to transfer the masking properties in an antibody fusion format. While the construction of SEED antibodies resulted in a masking of rituximab by the vNAR, both vNARs directed against 5F9 were unable to interfere with CD47 binding. Construction of light chain fusions with an implemented protease cleavable linker were not able to restore the masking effect of the vNARs directed against 5F9. In contrast, the vNAR directed against rituximab tested with different MMP-9 cleavable linkers was able to inhibit rituximab binding in all cases. Furthermore, rituximab binding could be restored upon MMP-9 cleavage for most of the linkers. In-depth analysis of one linker revealed an inhibitory effect of the remaining amino acids after MMP-9 cleavage and removal of the vNAR. The observed effect was small in binding experiments, however ADCC assays revealed a 1000-fold decrease in activity. Moreover, analysis of different controls revealed, that the masking effect is attributed to the linker and not to the vNAR.

In third proof of principle project, vNAR libraries were screened towards binders directed against the A6 TCR. Since treatment options for T cell lymphomas are limited and therapy approaches based on anti-idiotype like binders could be implemented in future treatment if the T cell lymphoma originates from a single T cell clone. The screening process resulted in several unique single clones which all displayed binding towards the Jurkat cell line carrying the A6 TCR. While three clones exhibited also binding towards the Jurkat wild type cell line, one clone exhibited specific binding. Characterization of this clone revealed moderate affinities in BLI and cell binding experiments.

The last project of this work was aimed at the isolation of chicken scFv directed against 6G11 from a yeast library which is based on sequences obtained from an immunization campaign of a chicken with 6G11 scFv. Incorporation of CD32b into the screening process enabled the isolation scFvs interfering and not interfering with 6G11 and CD32b interaction. BLI analysis revealed high specificity of both scFvs towards 6G11. Fusion of the scFvs interfering with the 6G11 and CD32b interaction *via* an MMP-9 cleavable linker to the light chain of 6G11, resulted in a masked 6G11 with a 2700-fold decreased affinity towards CD32b. Upon MMP-9 cleavage 6G11 binding was restored, but not to the full extent. Partly removal of the scFv resulted in restoration of binding comparable to the control light chain fusion with the scFv not interfering with the 6G11-CD32b interaction.

Overall, the isolation of anti-idiotype binders was successful for all approaches. Based on the data generated in this work, further proceedings for the individual follow-up approaches can be given. In case of the implementation of pH-dependency into matuzumab, a new library should be constructed. Instead of testing histidine incorporation at every position at the same time, the CDR3 could be divided into four parts and each part by itself could be investigated in histidine incorporation. Furthermore, during the screening process the matuzumab concentration should be lowered after the first sorting round in order to obtain high affine binders.

One major issue during this work was finding the correct linker for each vNAR. This issue could be solved by a linker library approach. Thereby, a vNAR displaying inhibitory properties towards the antibody-target interaction could be fused to the heavy and light chain of the antibody in a Fab display approach. For the fusion different linkers could be introduced either by golden gate cloning or PCR. PCR based linker attachment would be required for each new library, while the golden gate-based approach would only require the attachment of the endonuclease recognition sequence. The different linker variants can be provided by short double stranded oligonucleotides and containing the linker sequence as well as endonuclease recognition sequences. However, screening of a new library would be necessary for each vNAR-antibody pair. Alternatively, the linker library could be introduced *via* the aforementioned golden gate approach, in a plasmid for expression in Expi cells. Plasmids without an insert can be removed by digestion with the enzyme utilized for golden gate cloning and a plasmid safe DNase, which only degrades cleaved plasmids. The mixture can be utilized in for transfection and a variety of different constructs should be expressed simultaneously. After purification, the mixture can be applied to column coated with the target of the antibody under neutral pH conditions. Thereby, variants with restricted antigen binding can be collected in the flow through. Variants with restored binding upon MMP-9 cleavage can be isolated by applying the digestion mixture to the same column, thereby remove non-cleaved variants. The variants isolated by this method can be proteolytically digested and analyzed *via* mass spectrometry (351). Thereby, linkers which demonstrate the desired behavior can be identified. One major drawback of this method would be the presence of multiple linkers within the same antibody and presumably low expression yields of the individual constructs. Therefore, it could be possible that not enough material is obtained after purification process for analysis *via* mass spectrometry. However, if enough material is obtained and different linker variants have been obtained, each of the linker variants should be individually characterized in detail in respect to cleavage efficiency, degree of inhibiting antigen binding, impact on protein stability and aggregation.

In the project based on the chicken scFvs, further characterization of the different constructs should be performed. Besides melting point analysis, analytical SEC should be performed in order to gain insight into protein stability and aggregation behavior. In addition, the functionality of the constructs should be evaluated by analyzing the phosphorylation status of CD32b in co-incubation experiments with rituximab on Raji cells. Furthermore, humanization of the scFv should be conducted in order to reduce immunogenicity as well as generate variants with different binding affinities towards 6G11. Based on the variants with different affinities, masking domains with high interference in the 6G11-CD32b interaction as well as better restoration of binding upon MMP-9 cleavage could be isolated. Furthermore, pH-dependency could be implemented by histidine doping the CDRs based in the procedure described by Bogen et. al. (352). In this case, full restoration of binding under acidic conditions could be achieved, without removing the scFv.

7 References

1. Medzhitov R, Janeway CA, Jr. Decoding the patterns of self and nonself by the innate immune system. Science. 2002;296(5566):298-300.
2. Iwasaki A, Medzhitov R. Regulation of adaptive immunity by the innate immune system. Science. 2010;327(5963):291-5.
3. Akira S, Hemmi H. Recognition of pathogen-associated molecular patterns by TLR family. Immunol Lett. 2003;85(2):85-95.
4. Elinav E, Strowig T, Henao-Mejia J, Flavell RA. Regulation of the antimicrobial response by NLR proteins. Immunity. 2011;34(5):665-79.
5. Rehwinkel J, Gack MU. RIG-I-like receptors: their regulation and roles in RNA sensing. Nat Rev Immunol. 2020;20(9):537-51.
6. Briard B, Place DE, Kanneganti TD. DNA Sensing in the Innate Immune Response. Physiology (Bethesda). 2020;35(2):112-24.
7. Henning LN, Azad AK, Parsa KV, Crowther JE, Tridandapani S, Schlesinger LS. Pulmonary surfactant protein A regulates TLR expression and activity in human macrophages. J Immunol. 2008;180(12):7847-58.
8. Noh JY, Yoon SR, Kim TD, Choi I, Jung H. Toll-Like Receptors in Natural Killer Cells and Their Application for Immunotherapy. J Immunol Res. 2020;2020:2045860.
9. Hayashi F, Means TK, Luster AD. Toll-like receptors stimulate human neutrophil function. Blood. 2003;102(7):2660-9.
10. de Saint-Vis B, Fugier-Vivier I, Massacrier C, Gaillard C, Vanbervliet B, Ait-Yahia S, et al. The cytokine profile expressed by human dendritic cells is dependent on cell subtype and mode of activation. J Immunol. 1998;160(4):1666-76.
11. Perussia B. The Cytokine Profile of Resting and Activated NK Cells. Methods. 1996;9(2):370-8.
12. Aderem A, Underhill DM. Mechanisms of phagocytosis in macrophages. Annu Rev Immunol. 1999;17:593-623.
13. Smyth MJ, Cretney E, Kelly JM, Westwood JA, Street SE, Yagita H, et al. Activation of NK cell cytotoxicity. Mol Immunol. 2005;42(4):501-10.
14. Koutsakos M, McWilliam HEG, Aktepe TE, Fritzlar S, Illing PT, Mifsud NA, et al. Downregulation of MHC Class I Expression by Influenza A and B Viruses. Front Immunol. 2019;10:1158.
15. Orange JS. Formation and function of the lytic NK-cell immunological synapse. Nat Rev Immunol. 2008;8(9):713-25.
16. Trapani JA. Target cell apoptosis induced by cytotoxic T cells and natural killer cells involves synergy between the pore-forming protein, perforin, and the serine protease, granzyme B. Aust N Z J Med. 1995;25(6):793-9.
17. Bluman EM, Bartynski KJ, Avalos BR, Caligiuri MA. Human natural killer cells produce abundant macrophage inflammatory protein-1 alpha in response to monocyte-derived cytokines. J Clin Invest. 1996;97(12):2722-7.
18. Uribe-Querol E, Rosales C. Phagocytosis: Our Current Understanding of a Universal Biological Process. Front Immunol. 2020;11:1066.
19. Jain A, Pasare C. Innate Control of Adaptive Immunity: Beyond the Three-Signal Paradigm. J Immunol. 2017;198(10):3791-800.
20. Janeway CA Jr, Travers P, Walport M, al. e. Immunobiology : the immune system in health and disease. New York: Garland Publishing; 2001.
21. Hennecke J, Wiley DC. T cell receptor-MHC interactions up close. Cell. 2001;104(1):1-4.
22. Wooldridge L, van den Berg HA, Glick M, Gostick E, Laugel B, Hutchinson SL, et al. Interaction between the CD8 coreceptor and major histocompatibility complex class I stabilizes T cell receptor-antigen complexes at the cell surface. J Biol Chem. 2005;280(30):27491-501.
23. Harty JT, Tvinnereim AR, White DW. CD8+ T cell effector mechanisms in resistance to infection. Annu Rev Immunol. 2000;18:275-308.

24. Haabeth OA, Tveita AA, Fauskanger M, Schjesvold F, Lorvik KB, Hofgaard PO, et al. How Do CD4(+) T Cells Detect and Eliminate Tumor Cells That Either Lack or Express MHC Class II Molecules? Front Immunol. 2014;5:174.
25. Mellman I, Steinman RM. Dendritic cells: specialized and regulated antigen processing machines. Cell. 2001;106(3):255-8.
26. Glatzova D, Cebecauer M. Dual Role of CD4 in Peripheral T Lymphocytes. Front Immunol. 2019;10:618.
27. Schmitz J, Assenmacher M, Radbruch A. Regulation of T helper cell cytokine expression: functional dichotomy of antigen-presenting cells. Eur J Immunol. 1993;23(1):191-9.
28. Geginat J, Paroni M, Maglie S, Alfen JS, Kastirr I, Gruarin P, et al. Plasticity of human CD4 T cell subsets. Front Immunol. 2014;5:630.
29. Horikawa K, Takatsu K. Interleukin-5 regulates genes involved in B-cell terminal maturation. Immunology. 2006;118(4):497-508.
30. Clark MR, Massenburg D, Siemasko K, Hou P, Zhang M. B-cell antigen receptor signaling requirements for targeting antigen to the MHC class II presentation pathway. Curr Opin Immunol. 2004;16(3):382-7.
31. Parker DC. T cell-dependent B cell activation. Annu Rev Immunol. 1993;11:331-60.
32. Anelli T, van Anken E. Missing links in antibody assembly control. Int J Cell Biol. 2013;2013:606703.
33. Wabl M, Steinberg C. Affinity maturation and class switching. Curr Opin Immunol. 1996;8(1):89-92.
34. Akkaya M, Kwak K, Pierce SK. B cell memory: building two walls of protection against pathogens. Nat Rev Immunol. 2020;20(4):229-38.
35. Lo Nigro C, Macagno M, Sangiolo D, Bertolaccini L, Aglietta M, Merlano MC. NK-mediated antibody-dependent cell-mediated cytotoxicity in solid tumors: biological evidence and clinical perspectives. Ann Transl Med. 2019;7(5):105.
36. Ehrnthaller C, Ignatius A, Gebhard F, Huber-Lang M. New insights of an old defense system: structure, function, and clinical relevance of the complement system. Mol Med. 2011;17(3-4):317-29.
37. Tay MZ, Wiehe K, Pollara J. Antibody-Dependent Cellular Phagocytosis in Antiviral Immune Responses. Front Immunol. 2019;10:332.
38. Zhao Q, Maynard CL. Mucus, commensals, and the immune system. Gut Microbes. 2022;14(1):2041342.
39. Fitzsimmons CM, Falcone FH, Dunne DW. Helminth Allergens, Parasite-Specific IgE, and Its Protective Role in Human Immunity. Front Immunol. 2014;5:61.
40. Vidarsson G, Dekkers G, Rispens T. IgG subclasses and allotypes: from structure to effector functions. Front Immunol. 2014;5:520.
41. Schroeder HW, Jr., Cavacini L. Structure and function of immunoglobulins. J Allergy Clin Immunol. 2010;125(2 Suppl 2):S41-52.
42. Finlay WJ, Almagro JC. Natural and man-made V-gene repertoires for antibody discovery. Front Immunol. 2012;3:342.
43. Van Oss CJ. Hydrophobic, hydrophilic and other interactions in epitope-paratope binding. Mol Immunol. 1995;32(3):199-211.
44. Teplyakov A, Obmolova G, Malia TJ, Luo J, Muzammil S, Sweet R, et al. Structural diversity in a human antibody germline library. MAbs. 2016;8(6):1045-63.
45. Ravetch JV, Bolland S. IgG Fc receptors. Annu Rev Immunol. 2001;19:275-90.
46. Ben Mkaddem S, Benhamou M, Monteiro RC. Understanding Fc Receptor Involvement in Inflammatory Diseases: From Mechanisms to New Therapeutic Tools. Front Immunol. 2019;10:811.
47. Roopenian DC, Akilesh S. FcRn: the neonatal Fc receptor comes of age. Nat Rev Immunol. 2007;7(9):715-25.
48. Kubota T, Niwa R, Satoh M, Akinaga S, Shitara K, Hanai N. Engineered therapeutic antibodies with improved effector functions. Cancer Sci. 2009;100(9):1566-72.
49. Quast I, Keller CW, Maurer MA, Giddens JP, Tackenberg B, Wang LX, et al. Sialylation of IgG Fc domain impairs complement-dependent cytotoxicity. J Clin Invest. 2015;125(11):4160-70.

50. Roth DB. V(D)J Recombination: Mechanism, Errors, and Fidelity. Microbiol Spectr. 2014;2(6).
51. Neuberger MS, Di Noia JM, Beale RC, Williams GT, Yang Z, Rada C. Somatic hypermutation at A.T pairs: polymerase error versus dUTP incorporation. Nat Rev Immunol. 2005;5(2):171-8.
52. Muramatsu M, Kinoshita K, Fagarasan S, Yamada S, Shinkai Y, Honjo T. Class switch recombination and hypermutation require activation-induced cytidine deaminase (AID), a potential RNA editing enzyme. Cell. 2000;102(5):553-63.
53. Bork P, Holm L, Sander C. The immunoglobulin fold. Structural classification, sequence patterns and common core. J Mol Biol. 1994;242(4):309-20.
54. Chiu ML, Goulet DR, Teplyakov A, Gilliland GL. Antibody Structure and Function: The Basis for Engineering Therapeutics. Antibodies (Basel). 2019;8(4).
55. Pettinello R, Dooley H. The immunoglobulins of cold-blooded vertebrates. Biomolecules. 2014;4(4):1045-69.
56. Zhang X, Calvert RA, Sutton BJ, Dore KA. IgY: a key isotype in antibody evolution. Biol Rev Camb Philos Soc. 2017;92(4):2144-56.
57. Warr GW, Magor KE, Higgins DA. IgY: clues to the origins of modern antibodies. Immunol Today. 1995;16(8):392-8.
58. Parvari R, Avivi A, Lentner F, Ziv E, Tel-Or S, Burstein Y, et al. Chicken immunoglobulin gamma-heavy chains: limited VH gene repertoire, combinatorial diversification by D gene segments and evolution of the heavy chain locus. EMBO J. 1988;7(3):739-44.
59. Grant JA, Sanders B, Hood L. Partial amino acid sequences of chicken and turkey immunoglobulin light chains. Homology with mammalian lambda chains. Biochemistry. 1971;10(16):3123-32.
60. Wu L, Oficjalska K, Lambert M, Fennell BJ, Darmanin-Sheehan A, Ni Shuilleabhain D, et al. Fundamental characteristics of the immunoglobulin VH repertoire of chickens in comparison with those of humans, mice, and camelids. J Immunol. 2012;188(1):322-33.
61. Reynaud CA, Anquez V, Grimal H, Weill JC. A hyperconversion mechanism generates the chicken light chain preimmune repertoire. Cell. 1987;48(3):379-88.
62. Ching KH, Collarini EJ, Abdiche YN, Bedinger D, Pedersen D, Izquierdo S, et al. Chickens with humanized immunoglobulin genes generate antibodies with high affinity and broad epitope coverage to conserved targets. MAbs. 2018;10(1):71-80.
63. Yamanaka HI, Inoue T, Ikeda-Tanaka O. Chicken monoclonal antibody isolated by a phage display system. J Immunol. 1996;157(3):1156-62.
64. Bogen JP, Carrara SC, Fiebig D, Grzeschik J, Hock B, Kolmar H. Expeditious Generation of Biparatopic Common Light Chain Antibodies via Chicken Immunization and Yeast Display Screening. Front Immunol. 2020;11:606878.
65. Ching KH, Berg K, Reynolds K, Pedersen D, Macias A, Abdiche YN, et al. Common light chain chickens produce human antibodies of high affinity and broad epitope coverage for the engineering of bispecifics. MAbs. 2021;13(1):1862451.
66. Nishibori N, Horiuchi H, Furusawa S, Matsuda H. Humanization of chicken monoclonal antibody using phage-display system. Mol Immunol. 2006;43(6):634-42.
67. Rumfelt LL, Avila D, Diaz M, Bartl S, McKinney EC, Flajnik MF. A shark antibody heavy chain encoded by a nonsomatically rearranged VDJ is preferentially expressed in early development and is convergent with mammalian IgG. Proc Natl Acad Sci U S A. 2001;98(4):1775-80.
68. Smith LE, Crouch K, Cao W, Muller MR, Wu L, Steven J, et al. Characterization of the immunoglobulin repertoire of the spiny dogfish (Squalus acanthias). Dev Comp Immunol. 2012;36(4):665-79.
69. Lee V, Huang JL, Lui MF, Malecek K, Ohta Y, Mooers A, et al. The evolution of multiple isotypic IgM heavy chain genes in the shark. J Immunol. 2008;180(11):7461-70.
70. Small PA, Jr., Klapper DG, Clem LW. Half-lives, body distribution and lack of interconversion of serum 19S and 7S IgM of sharks. J Immunol. 1970;105(1):29-37.
71. Hsu E. Assembly and Expression of Shark Ig Genes. J Immunol. 2016;196(9):3517-23.

72. Greenberg AS, Avila D, Hughes M, Hughes A, McKinney EC, Flajnik MF. A new antigen receptor gene family that undergoes rearrangement and extensive somatic diversification in sharks. Nature. 1995;374(6518):168-73.
73. Zielonka S, Empting M, Grzeschik J, Konning D, Barelle CJ, Kolmar H. Structural insights and biomedical potential of IgNAR scaffolds from sharks. MAbs. 2015;7(1):15-25.
74. Feige MJ, Grawert MA, Marcinowski M, Hennig J, Behnke J, Auslander D, et al. The structural analysis of shark IgNAR antibodies reveals evolutionary principles of immunoglobulins. Proc Natl Acad Sci U S A. 2014;111(22):8155-60.
75. Yancey PH, Clark ME, Hand SC, Bowlus RD, Somero GN. Living with water stress: evolution of osmolyte systems. Science. 1982;217(4566):1214-22.
76. Stanfield RL, Dooley H, Flajnik MF, Wilson IA. Crystal structure of a shark single-domain antibody V region in complex with lysozyme. Science. 2004;305(5691):1770-3.
77. Dooley H, Flajnik MF. Antibody repertoire development in cartilaginous fish. Dev Comp Immunol. 2006;30(1-2):43-56.
78. Kovaleva M, Ferguson L, Steven J, Porter A, Barelle C. Shark variable new antigen receptor biologics - a novel technology platform for therapeutic drug development. Expert Opin Biol Ther. 2014;14(10):1527-39.
79. Feng M, Bian H, Wu X, Fu T, Fu Y, Hong J, et al. Construction and next-generation sequencing analysis of a large phage-displayed VNAR single-domain antibody library from six naive nurse sharks. Antib Ther. 2019;2(1):1-11.
80. Streltsov VA, Carmichael JA, Nuttall SD. Structure of a shark IgNAR antibody variable domain and modeling of an early-developmental isotype. Protein Sci. 2005;14(11):2901-9.
81. Diaz M, Stanfield RL, Greenberg AS, Flajnik MF. Structural analysis, selection, and ontogeny of the shark new antigen receptor (IgNAR): identification of a new locus preferentially expressed in early development. Immunogenetics. 2002;54(7):501-12.
82. Kovalenko OV, Olland A, Piche-Nicholas N, Godbole A, King D, Svenson K, et al. Atypical antigen recognition mode of a shark immunoglobulin new antigen receptor (IgNAR) variable domain characterized by humanization and structural analysis. J Biol Chem. 2013;288(24):17408-19.
83. Dooley H, Flajnik MF, Porter AJ. Selection and characterization of naturally occurring single-domain (IgNAR) antibody fragments from immunized sharks by phage display. Mol Immunol. 2003;40(1):25-33.
84. Konning D, Rhiel L, Empting M, Grzeschik J, Sellmann C, Schroter C, et al. Semi-synthetic vNAR libraries screened against therapeutic antibodies primarily deliver anti-idiotypic binders. Sci Rep. 2017;7(1):9676.
85. Cabanillas-Bernal O, Duenas S, Ayala-Avila M, Rucavado A, Escalante T, Licea-Navarro AF. Synthetic libraries of shark vNAR domains with different cysteine numbers within the CDR3. PLoS One. 2019;14(6):e0213394.
86. Nuttall SD, Humberstone KS, Krishnan UV, Carmichael JA, Doughty L, Hattarki M, et al. Selection and affinity maturation of IgNAR variable domains targeting Plasmodium falciparum AMA1. Proteins. 2004;55(1):187-97.
87. Kopsidas G, Roberts AS, Coia G, Streltsov VA, Nuttall SD. In vitro improvement of a shark IgNAR antibody by Qbeta replicase mutation and ribosome display mimics in vivo affinity maturation. Immunol Lett. 2006;107(2):163-8.
88. Zielonka S, Weber N, Becker S, Doerner A, Christmann A, Christmann C, et al. Shark Attack: high affinity binding proteins derived from shark vNAR domains by stepwise in vitro affinity maturation. J Biotechnol. 2014;191:236-45.
89. Konning D, Hinz S, Grzeschik J, Schroter C, Krah S, Zielonka S, et al. Construction of Histidine-Enriched Shark IgNAR Variable Domain Antibody Libraries for the Isolation of pH-Sensitive vNAR Fragments. Methods Mol Biol. 2018;1827:109-27.
90. Zielonka S, Empting M, Konning D, Grzeschik J, Krah S, Becker S, et al. The Shark Strikes Twice: Hypervariable Loop 2 of Shark IgNAR Antibody Variable Domains and Its Potential to Function as an Autonomous Paratope. Mar Biotechnol (NY). 2015;17(4):386-92.

91. Liu JL, Anderson GP, Delehanty JB, Baumann R, Hayhurst A, Goldman ER. Selection of cholera toxin specific IgNAR single-domain antibodies from a naive shark library. Mol Immunol. 2007;44(7):1775-83.
92. Ohtani M, Hikima J, Jung TS, Kondo H, Hirono I, Takeyama H, et al. Variable domain antibodies specific for viral hemorrhagic septicemia virus (VHSV) selected from a randomized IgNAR phage display library. Fish Shellfish Immunol. 2013;34(2):724-8.
93. Macarron Palacios A, Grzeschik J, Deweid L, Krah S, Zielonka S, Rosner T, et al. Specific Targeting of Lymphoma Cells Using Semisynthetic Anti-Idiotype Shark Antibodies. Front Immunol. 2020;11:560244.
94. Davis JH, Aperlo C, Li Y, Kurosawa E, Lan Y, Lo KM, et al. SEEDbodies: fusion proteins based on strand-exchange engineered domain (SEED) CH3 heterodimers in an Fc analogue platform for asymmetric binders or immunofusions and bispecific antibodies. Protein Eng Des Sel. 2010;23(4):195-202.
95. Ridgway JB, Presta LG, Carter P. 'Knobs-into-holes' engineering of antibody CH3 domains for heavy chain heterodimerization. Protein Eng. 1996;9(7):617-21.
96. Ha JH, Kim JE, Kim YS. Immunoglobulin Fc Heterodimer Platform Technology: From Design to Applications in Therapeutic Antibodies and Proteins. Front Immunol. 2016;7:394.
97. Wang C, Vemulapalli B, Cao M, Gadre D, Wang J, Hunter A, et al. A systematic approach for analysis and characterization of mispairing in bispecific antibodies with asymmetric architecture. MAbs. 2018;10(8):1226-35.
98. Dietrich S, Gross AW, Becker S, Hock B, Stadlmayr G, Ruker F, et al. Constant domain-exchanged Fab enables specific light chain pairing in heterodimeric bispecific SEED-antibodies. Biochim Biophys Acta Proteins Proteom. 2020;1868(1):140250.
99. Bogen JP, Storka J, Yanakieva D, Fiebig D, Grzeschik J, Hock B, et al. Isolation of Common Light Chain Antibodies from Immunized Chickens Using Yeast Biopanning and Fluorescence-Activated Cell Sorting. Biotechnol J. 2021;16(3):e2000240.
100. Dhimolea E, Reichert JM. World Bispecific Antibody Summit, September 27-28, 2011, Boston, MA. MAbs. 2012;4(1):4-13.
101. Fan G, Wang Z, Hao M, Li J. Bispecific antibodies and their applications. J Hematol Oncol. 2015;8:130.
102. Thurber GM, Schmidt MM, Wittrup KD. Antibody tumor penetration: transport opposed by systemic and antigen-mediated clearance. Adv Drug Deliv Rev. 2008;60(12):1421-34.
103. Chen X, Ding G, Gao Q, Sun J, Zhang Q, Du L, et al. A human anti-c-Met Fab fragment conjugated with doxorubicin as targeted chemotherapy for hepatocellular carcinoma. PLoS One. 2013;8(5):e63093.
104. Hu Y, Liu C, Muyldermans S. Nanobody-Based Delivery Systems for Diagnosis and Targeted Tumor Therapy. Front Immunol. 2017;8:1442.
105. Cheng WW, Allen TM. The use of single chain Fv as targeting agents for immunoliposomes: an update on immunoliposomal drugs for cancer treatment. Expert Opin Drug Deliv. 2010;7(4):461-78.
106. Chapman AP, Antoniw P, Spitali M, West S, Stephens S, King DJ. Therapeutic antibody fragments with prolonged in vivo half-lives. Nat Biotechnol. 1999;17(8):780-3.
107. van Lith SAM, Huizing FJ, Franssen GM, Hoeben BAW, Lok J, Doulkeridou S, et al. Novel VHH-Based Tracers with Variable Plasma Half-Lives for Imaging of CAIX-Expressing Hypoxic Tumor Cells. Mol Pharm. 2022.
108. Schlapschy M, Binder U, Borger C, Theobald I, Wachinger K, Kisling S, et al. PASylation: a biological alternative to PEGylation for extending the plasma half-life of pharmaceutically active proteins. Protein Eng Des Sel. 2013;26(8):489-501.
109. van Faassen H, Ryan S, Henry KA, Raphael S, Yang Q, Rossotti MA, et al. Serum albumin-binding VH Hs with variable pH sensitivities enable tailored half-life extension of biologics. FASEB J. 2020;34(6):8155-71.
110. Hudson PJ, Kortt AA. High avidity scFv multimers; diabodies and triabodies. J Immunol Methods. 1999;231(1-2):177-89.
111. Wu J, Fu J, Zhang M, Liu D. Blinatumomab: a bispecific T cell engager (BiTE) antibody against CD19/CD3 for refractory acute lymphoid leukemia. J Hematol Oncol. 2015;8:104.

112. Beck A, Goetsch L, Dumontet C, Corvaia N. Strategies and challenges for the next generation of antibody-drug conjugates. Nat Rev Drug Discov. 2017;16(5):315-37.
113. Zahavi D, Weiner L. Monoclonal Antibodies in Cancer Therapy. Antibodies (Basel). 2020;9(3).
114. Schwaber J, Cohen EP. Human x mouse somatic cell hybrid clone secreting immunoglobulins of both parental types. Nature. 1973;244(5416):444-7.
115. Vaickus L, Foon KA. Overview of monoclonal antibodies in the diagnosis and therapy of cancer. Cancer Invest. 1991;9(2):195-209.
116. Kipps TJ, Parham P, Punt J, Herzenberg LA. Importance of immunoglobulin isotype in human antibody-dependent, cell-mediated cytotoxicity directed by murine monoclonal antibodies. J Exp Med. 1985;161(1):1-17.
117. Boulianne GL, Hozumi N, Shulman MJ. Production of functional chimaeric mouse/human antibody. Nature. 1984;312(5995):643-6.
118. Liu AY, Robinson RR, Hellstrom KE, Murray ED, Jr., Chang CP, Hellstrom I. Chimeric mouse-human IgG1 antibody that can mediate lysis of cancer cells. Proc Natl Acad Sci U S A. 1987;84(10):3439-43.
119. Hwang WY, Foote J. Immunogenicity of engineered antibodies. Methods. 2005;36(1):3-10.
120. Casan JML, Wong J, Northcott MJ, Opat S. Anti-CD20 monoclonal antibodies: reviewing a revolution. Hum Vaccin Immunother. 2018;14(12):2820-41.
121. Faustini F, Parodis I, Dunn N, Ryner M, Fogdell-Hahn A, Gunnarsson I. AB0512 Occurrence and consequences of anti-drug antibodies to rituximab in systemic lupus erythematosus. Annals of the Rheumatic Diseases. 2018;77(Suppl 2):1414-5.
122. Harding FA, Stickler MM, Razo J, DuBridge RB. The immunogenicity of humanized and fully human antibodies: residual immunogenicity resides in the CDR regions. MAbs. 2010;2(3):256-65.
123. Safdari Y, Farajnia S, Asgharzadeh M, Khalili M. Antibody humanization methods - a review and update. Biotechnol Genet Eng Rev. 2013;29:175-86.
124. Tsurushita N, Hinton PR, Kumar S. Design of humanized antibodies: from anti-Tac to Zenapax. Methods. 2005;36(1):69-83.
125. Vaughan TJ, Williams AJ, Pritchard K, Osbourn JK, Pope AR, Earnshaw JC, et al. Human antibodies with sub-nanomolar affinities isolated from a large non-immunized phage display library. Nat Biotechnol. 1996;14(3):309-14.
126. Osborn MJ, Ma B, Avis S, Binnie A, Dilley J, Yang X, et al. High-affinity IgG antibodies develop naturally in Ig-knockout rats carrying germline human IgH/Igkappa/Iglambda loci bearing the rat CH region. J Immunol. 2013;190(4):1481-90.
127. Getts DR, Getts MT, McCarthy DP, Chastain EM, Miller SD. Have we overestimated the benefit of human(ized) antibodies? MAbs. 2010;2(6):682-94.
128. Postow MA, Callahan MK, Wolchok JD. Immune Checkpoint Blockade in Cancer Therapy. J Clin Oncol. 2015;33(17):1974-82.
129. Wang X, Teng F, Kong L, Yu J. PD-L1 expression in human cancers and its association with clinical outcomes. Onco Targets Ther. 2016;9:5023-39.
130. Buchbinder EI, Desai A. CTLA-4 and PD-1 Pathways: Similarities, Differences, and Implications of Their Inhibition. Am J Clin Oncol. 2016;39(1):98-106.
131. Lao Y, Shen D, Zhang W, He R, Jiang M. Immune Checkpoint Inhibitors in Cancer Therapy-How to Overcome Drug Resistance? Cancers (Basel). 2022;14(15).
132. Dang TO, Ogunniyi A, Barbee MS, Drilon A. Pembrolizumab for the treatment of PD-L1 positive advanced or metastatic non-small cell lung cancer. Expert Rev Anticancer Ther. 2016;16(1):13-20.
133. Markham A. Atezolizumab: First Global Approval. Drugs. 2016;76(12):1227-32.
134. Khongorzul P, Ling CJ, Khan FU, Ihsan AU, Zhang J. Antibody–Drug Conjugates: A Comprehensive Review. Molecular Cancer Research. 2020;18(1):3-19.
135. Sheyi R, de la Torre BG, Albericio F. Linkers: An Assurance for Controlled Delivery of Antibody-Drug Conjugate. Pharmaceutics. 2022;14(2).
136. Wang L, Amphlett G, Blattler WA, Lambert JM, Zhang W. Structural characterization of the maytansinoid-monoclonal antibody immunoconjugate, huN901-DM1, by mass spectrometry. Protein Sci. 2005;14(9):2436-46.

137. Schneider H, Deweid L, Avrutina O, Kolmar H. Recent progress in transglutaminase-mediated assembly of antibody-drug conjugates. Anal Biochem. 2020;595:113615.
138. Baalmann M, Neises L, Bitsch S, Schneider H, Deweid L, Werther P, et al. A Bioorthogonal Click Chemistry Toolbox for Targeted Synthesis of Branched and Well-Defined Protein-Protein Conjugates. Angew Chem Int Ed Engl. 2020;59(31):12885-93.
139. McPherson MJ, Hobson AD. Pushing the Envelope: Advancement of ADCs Outside of Oncology. Methods Mol Biol. 2020;2078:23-36.
140. Baselga J, Swain SM. CLEOPATRA: a phase III evaluation of pertuzumab and trastuzumab for HER2-positive metastatic breast cancer. Clin Breast Cancer. 2010;10(6):489-91.
141. Leonard JP, Coleman M, Ketas J, Ashe M, Fiore JM, Furman RR, et al. Combination antibody therapy with epratuzumab and rituximab in relapsed or refractory non-Hodgkin's lymphoma. J Clin Oncol. 2005;23(22):5044-51.
142. Roghanian A, Teige I, Martensson L, Cox KL, Kovacek M, Ljungars A, et al. Antagonistic human FcgammaRIIB (CD32B) antibodies have anti-tumor activity and overcome resistance to antibody therapy in vivo. Cancer Cell. 2015;27(4):473-88.
143. Maute RL, Chen JY, Marjon KD, Duan J, Choi T, Chao M, et al. Translational Study of Cell Surface Proteins in Non-Hodgkin Lymphoma Patients Treated with the First-in-Class Anti-CD47 Antibody Magrolimab (5F9) in Combination with Rituximab. Blood. 2019;134:5229.
144. Advani R, Flinn I, Popplewell L, Forero A, Bartlett NL, Ghosh N, et al. CD47 Blockade by Hu5F9-G4 and Rituximab in Non-Hodgkin's Lymphoma. N Engl J Med. 2018;379(18):1711-21.
145. Krishnamurthy A, Jimeno A. Bispecific antibodies for cancer therapy: A review. Pharmacol Ther. 2018;185:122-34.
146. Krah S, Sellmann C, Rhiel L, Schroter C, Dickgiesser S, Beck J, et al. Engineering bispecific antibodies with defined chain pairing. N Biotechnol. 2017;39(Pt B):167-73.
147. Sustmann C, Dickopf S, Regula JT, Kettenberger H, Molhoj M, Gassner C, et al. DuoMab: a novel CrossMab-based IgG-derived antibody format for enhanced antibody-dependent cell-mediated cytotoxicity. MAbs. 2019;11(8):1402-14.
148. Przepiorka D, Ko CW, Deisseroth A, Yancey CL, Candau-Chacon R, Chiu HJ, et al. FDA Approval: Blinatumomab. Clin Cancer Res. 2015;21(18):4035-9.
149. Franchini M, Marano G, Pati I, Candura F, Profili S, Veropalumbo E, et al. Emicizumab for the treatment of haemophilia A: a narrative review. Blood Transfus. 2019;17(3):223-8.
150. Syed YY. Amivantamab: First Approval. Drugs. 2021;81(11):1349-53.
151. Shirley M. Faricimab: First Approval. Drugs. 2022;82(7):825-30.
152. Chen LN, Carvajal RD. Tebentafusp for the treatment of HLA-A*02:01-positive adult patients with unresectable or metastatic uveal melanoma. Expert Rev Anticancer Ther. 2022;22(10):1017-27.
153. Granger K, Gaffney KJ, Davis JA. Newly approved and forthcoming T-cell-redirecting bispecific antibodies for the treatment of relapsed/refractory multiple myeloma. J Oncol Pharm Pract. 2023;29(3):722-6.
154. Bispecific Antibody Takes Down FL. Cancer Discov. 2022;12(2):280.
155. Hutchings M, Mous R, Clausen MR, Johnson P, Linton KM, Chamuleau MED, et al. Dose escalation of subcutaneous epcoritamab in patients with relapsed or refractory B-cell non-Hodgkin lymphoma: an open-label, phase 1/2 study. Lancet. 2021;398(10306):1157-69.
156. Hutchings M, Morschhauser F, Iacoboni G, Carlo-Stella C, Offner FC, Sureda A, et al. Glofitamab, a Novel, Bivalent CD20-Targeting T-Cell-Engaging Bispecific Antibody, Induces Durable Complete Remissions in Relapsed or Refractory B-Cell Lymphoma: A Phase I Trial. J Clin Oncol. 2021;39(18):1959-70.
157. Boonstra MC, de Geus SW, Prevoo HA, Hawinkels LJ, van de Velde CJ, Kuppen PJ, et al. Selecting Targets for Tumor Imaging: An Overview of Cancer-Associated Membrane Proteins. Biomark Cancer. 2016;8:119-33.
158. Nicholson RI, Gee JM, Harper ME. EGFR and cancer prognosis. Eur J Cancer. 2001;37 Suppl 4:S9-15.
159. Kelleher M, Singh R, O'Driscoll CM, Melgar S. Carcinoembryonic antigen (CEACAM) family members and Inflammatory Bowel Disease. Cytokine Growth Factor Rev. 2019;47:21-31.

160. Huang L, Yang Y, Yang F, Liu S, Zhu Z, Lei Z, et al. Functions of EpCAM in physiological processes and diseases (Review). Int J Mol Med. 2018;42(4):1771-85.
161. Kaszak I, Witkowska-Pilaszewicz O, Niewiadomska Z, Dworecka-Kaszak B, Ngosa Toka F, Jurka P. Role of Cadherins in Cancer-A Review. Int J Mol Sci. 2020;21(20).
162. Gazzah A, Bedard PL, Hierro C, Kang YK, Abdul Razak A, Ryu MH, et al. Safety, pharmacokinetics, and antitumor activity of the anti-CEACAM5-DM4 antibody-drug conjugate tusamitamab ravtansine (SAR408701) in patients with advanced solid tumors: first-in-human dose-escalation study. Ann Oncol. 2022;33(4):416-25.
163. Dotan E, Cohen SJ, Starodub AN, Lieu CH, Messersmith WA, Simpson PS, et al. Phase I/II Trial of Labetuzumab Govitecan (Anti-CEACAM5/SN-38 Antibody-Drug Conjugate) in Patients With Refractory or Relapsing Metastatic Colorectal Cancer. J Clin Oncol. 2017;35(29):3338-46.
164. Linke R, Klein A, Seimetz D. Catumaxomab: clinical development and future directions. MAbs. 2010;2(2):129-36.
165. Reichert JM. Marketed therapeutic antibodies compendium. MAbs. 2012;4(3):413-5.
166. Kovacs E, Zorn JA, Huang Y, Barros T, Kuriyan J. A structural perspective on the regulation of the epidermal growth factor receptor. Annu Rev Biochem. 2015;84:739-64.
167. Hsu JL, Hung MC. The role of HER2, EGFR, and other receptor tyrosine kinases in breast cancer. Cancer Metastasis Rev. 2016;35(4):575-88.
168. Nahta R, Esteva FJ. Trastuzumab: triumphs and tribulations. Oncogene. 2007;26(25):3637-43.
169. Wykosky J, Fenton T, Furnari F, Cavenee WK. Therapeutic targeting of epidermal growth factor receptor in human cancer: successes and limitations. Chin J Cancer. 2011;30(1):5-12.
170. Kim JW, Cochran JR. Targeting ligand-receptor interactions for development of cancer therapeutics. Curr Opin Chem Biol. 2017;38:62-9.
171. Attwood MM, Jonsson J, Rask-Andersen M, Schioth HB. Soluble ligands as drug targets. Nat Rev Drug Discov. 2020;19(10):695-710.
172. Genovese MC, Greenwald M, Cho CS, Berman A, Jin L, Cameron GS, et al. A phase II randomized study of subcutaneous ixekizumab, an anti-interleukin-17 monoclonal antibody, in rheumatoid arthritis patients who were naive to biologic agents or had an inadequate response to tumor necrosis factor inhibitors. Arthritis Rheumatol. 2014;66(7):1693-704.
173. Martin DA, Churchill M, Flores-Suarez L, Cardiel MH, Wallace D, Martin R, et al. A phase Ib multiple ascending dose study evaluating safety, pharmacokinetics, and early clinical response of brodalumab, a human anti-IL-17R antibody, in methotrexate-resistant rheumatoid arthritis. Arthritis Res Ther. 2013;15(5):R164.
174. Dickinson ME, Flenniken AM, Ji X, Teboul L, Wong MD, White JK, et al. High-throughput discovery of novel developmental phenotypes. Nature. 2016;537(7621):508-14.
175. Taira K, Okazaki S, Akiyoshi K, Machida H, Ikeya T, Kimura A, et al. Short bevacizumab infusion as an effective and safe treatment for colorectal cancer. Mol Clin Oncol. 2022;17(3):139.
176. Saif MW. Anti-VEGF agents in metastatic colorectal cancer (mCRC): are they all alike? Cancer Manag Res. 2013;5:103-15.
177. Jamshidi K, Gharehdaghi M, Hajialiloo SS, Mirkazemi M, Ghaffarzadehgan K, Izanloo A. Denosumab in Patients with Giant Cell Tumor and Its Recurrence: A Systematic Review. Arch Bone Jt Surg. 2018;6(4):260-8.
178. Trenevska I, Li D, Banham AH. Therapeutic Antibodies against Intracellular Tumor Antigens. Front Immunol. 2017;8:1001.
179. Marasco WA, Haseltine WA, Chen SY. Design, intracellular expression, and activity of a human anti-human immunodeficiency virus type 1 gp120 single-chain antibody. Proc Natl Acad Sci U S A. 1993;90(16):7889-93.
180. Chatin B, Mevel M, Devalliere J, Dallet L, Haudebourg T, Peuziat P, et al. Liposome-based Formulation for Intracellular Delivery of Functional Proteins. Mol Ther Nucleic Acids. 2015;4:e244.
181. Peer D, Karp JM, Hong S, Farokhzad OC, Margalit R, Langer R. Nanocarriers as an emerging platform for cancer therapy. Nat Nanotechnol. 2007;2(12):751-60.

182. Jain M, Chauhan SC, Singh AP, Venkatraman G, Colcher D, Batra SK. Penetratin improves tumor retention of single-chain antibodies: a novel step toward optimization of radioimmunotherapy of solid tumors. Cancer Res. 2005;65(17):7840-6.
183. Weidanz JA, Hawkins O, Verma B, Hildebrand WH. TCR-like biomolecules target peptide/MHC Class I complexes on the surface of infected and cancerous cells. Int Rev Immunol. 2011;30(5-6):328-40.
184. Adams GP, Weiner LM. Monoclonal antibody therapy of cancer. Nat Biotechnol. 2005;23(9):1147-57.
185. Scott AM, Wolchok JD, Old LJ. Antibody therapy of cancer. Nat Rev Cancer. 2012;12(4):278-87.
186. Tabrizi MA, Tseng CM, Roskos LK. Elimination mechanisms of therapeutic monoclonal antibodies. Drug Discov Today. 2006;11(1-2):81-8.
187. Zhang X, Lin Y, Gillies RJ. Tumor pH and its measurement. J Nucl Med. 2010;51(8):1167-70.
188. Tripathy DB, Mishra A, Clark J, Farmer T. Synthesis, chemistry, physicochemical properties and industrial applications of amino acid surfactants: A review. Comptes Rendus Chimie. 2018;21(2):112-30.
189. Lee PS, MacDonald KG, Massi E, Chew PV, Bee C, Perkins P, et al. Improved therapeutic index of an acidic pH-selective antibody. MAbs. 2022;14(1):2024642.
190. Weiner LM, Murray JC, Shuptrine CW. Antibody-based immunotherapy of cancer. Cell. 2012;148(6):1081-4.
191. Igawa T, Ishii S, Tachibana T, Maeda A, Higuchi Y, Shimaoka S, et al. Antibody recycling by engineered pH-dependent antigen binding improves the duration of antigen neutralization. Nat Biotechnol. 2010;28(11):1203-7.
192. Igawa T, Haraya K, Hattori K. Sweeping antibody as a novel therapeutic antibody modality capable of eliminating soluble antigens from circulation. Immunol Rev. 2016;270(1):132-51.
193. Igawa T, Mimoto F, Hattori K. pH-dependent antigen-binding antibodies as a novel therapeutic modality. Biochim Biophys Acta. 2014;1844(11):1943-50.
194. Igawa T, Maeda A, Haraya K, Tachibana T, Iwayanagi Y, Mimoto F, et al. Engineered monoclonal antibody with novel antigen-sweeping activity in vivo. PLoS One. 2013;8(5):e63236.
195. Novotny J, Handschumacher M, Haber E. Location of antigenic epitopes on antibody molecules. J Mol Biol. 1986;189(4):715-21.
196. Wells JV, Fudenberg HH, Givol D. Localization of idiotypic antigenic determinants in the Fv region of murine myeloma protein MOPC-315. Proc Natl Acad Sci U S A. 1973;70(5):1585-7.
197. Rodkey LS. Studies of idiotypic antibodies. Production and characterization of autoantiidiotypic antisera. J Exp Med. 1974;139(3):712-20.
198. Wallmann J, Pali-Scholl I, Jensen-Jarolim E. Anti-ids in allergy: timeliness of a classic concept. World Allergy Organ J. 2010;3(6):195-201.
199. Thanavala YM, Bond A, Hay FC, Roitt IM. Immunofluorescent technique for the detection of monoclonal internal image anti-idiotypic antibodies of hepatitis B surface antigen. J Immunol Methods. 1985;83(2):227-32.
200. Pan SY, Chia YC, Yee HR, Fang Cheng AY, Anjum CE, Kenisi Y, et al. Immunomodulatory potential of anti-idiotypic antibodies for the treatment of autoimmune diseases. Future Sci OA. 2020;7(2):FSO648.
201. Cosenza H. Detection of anti-idiotype reactive cells in the response to phosphorylcholine. Eur J Immunol. 1976;6(2):114-6.
202. Shoenfeld Y. The idiotypic network in autoimmunity: antibodies that bind antibodies that bind antibodies. Nat Med. 2004;10(1):17-8.
203. Kluskens L, Kohler H. Regulation of immune response by autogenous antibody against receptor. Proc Natl Acad Sci U S A. 1974;71(12):5083-7.
204. Hampe CS. Protective role of anti-idiotypic antibodies in autoimmunity--lessons for type 1 diabetes. Autoimmunity. 2012;45(4):320-31.
205. Williams WM, Isenberg DA. Naturally occurring anti-idiotypic antibodies reactive with anti-DNA antibodies in systemic lupus erythematosus. Lupus. 1998;7(3):164-75.

206. Tada H, Izumi Y, Watanabe Y, Takano T, Fukata S, Kuma K, et al. Blocking type anti-tSH receptor antibodies detected by radioreceptor assay in Graves' disease. Endocr J. 2001;48(6):703-10.
207. Oak S, Gilliam LK, Landin-Olsson M, Torn C, Kockum I, Pennington CR, et al. The lack of anti-idiotypic antibodies, not the presence of the corresponding autoantibodies to glutamate decarboxylase, defines type 1 diabetes. Proc Natl Acad Sci U S A. 2008;105(14):5471-6.
208. Godar M, Morello V, Sadi A, Hultberg A, De Jonge N, Basilico C, et al. Dual anti-idiotypic purification of a novel, native-format biparatopic anti-MET antibody with improved in vitro and in vivo efficacy. Sci Rep. 2016;6:31621.
209. Lim SY, Chan CE, Lisowska MM, Hanson BJ, MacAry PA. The Molecular Engineering of an Anti-Idiotypic Antibody for Pharmacokinetic Analysis of a Fully Human Anti-Infective. PLoS One. 2015;10(12):e0145381.
210. Geiger M, Stubenrauch KG, Sam J, Richter WF, Jordan G, Eckmann J, et al. Protease-activation using anti-idiotypic masks enables tumor specificity of a folate receptor 1-T cell bispecific antibody. Nat Commun. 2020;11(1):3196.
211. de Cerio AL, Zabalegui N, Rodriguez-Calvillo M, Inoges S, Bendandi M. Anti-idiotype antibodies in cancer treatment. Oncogene. 2007;26(25):3594-602.
212. Miller RA, Maloney DG, Warnke R, Levy R. Treatment of B-cell lymphoma with monoclonal anti-idiotype antibody. N Engl J Med. 1982;306(9):517-22.
213. Torchia J, Weiskopf K, Levy R. Targeting lymphoma with precision using semisynthetic anti-idiotype peptibodies. Proc Natl Acad Sci U S A. 2016;113(19):5376-81.
214. Baker JR, Jr., Lukes YG, Burman KD. Production, isolation, and characterization of rabbit anti-idiotypic antibodies directed against human antithyrotrophin receptor antibodies. J Clin Invest. 1984;74(2):488-95.
215. Leivo J, Vehniainen M, Lamminmaki U. Phage Display Selection of an Anti-Idiotype-Antibody with Broad-Specificity to Deoxynivalenol Mycotoxins. Toxins (Basel). 2020;13(1).
216. Shu M, Xu Y, Wang D, Liu X, Li Y, He Q, et al. Anti-idiotypic nanobody: A strategy for development of sensitive and green immunoassay for Fumonisin B(1). Talanta. 2015;143:388-93.
217. Vogel M, Keller-Gautschi E, Baumann MJ, Amstutz P, Ruf C, Kricek F, et al. Designed ankyrin repeat proteins as anti-idiotypic-binding molecules. Ann N Y Acad Sci. 2007;1109:9-18.
218. Lucchi R, Bentanachs J, Oller-Salvia B. The Masking Game: Design of Activatable Antibodies and Mimetics for Selective Therapeutics and Cell Control. ACS Cent Sci. 2021;7(5):724-38.
219. Lin WW, Lu YC, Chuang CH, Cheng TL. Ab locks for improving the selectivity and safety of antibody drugs. J Biomed Sci. 2020;27(1):76.
220. Chen IJ, Chuang CH, Hsieh YC, Lu YC, Lin WW, Huang CC, et al. Selective antibody activation through protease-activated pro-antibodies that mask binding sites with inhibitory domains. Sci Rep. 2017;7(1):11587.
221. Lowman HB, Liu S, inventors; Cytomx Therapeutics Inc, assignee. Activatable antibodies having non-binding steric moieties and methods of using the same. US2018.
222. Lu YC, Chuang CH, Chuang KH, Chen IJ, Huang BC, Lee WH, et al. Specific activation of pro-Infliximab enhances selectivity and safety of rheumatoid arthritis therapy. PLoS Biol. 2019;17(6):e3000286.
223. Trang VH, Zhang X, Yumul RC, Zeng W, Stone IJ, Wo SW, et al. A coiled-coil masking domain for selective activation of therapeutic antibodies. Nat Biotechnol. 2019;37(7):761-5.
224. Onuoha SC, Ferrari M, Sblattero D, Pitzalis C. Rational design of antirheumatic prodrugs specific for sites of inflammation. Arthritis Rheumatol. 2015;67(10):2661-72.
225. Desnoyers LR, Vasiljeva O, Richardson JH, Yang A, Menendez EE, Liang TW, et al. Tumor-specific activation of an EGFR-targeting probody enhances therapeutic index. Sci Transl Med. 2013;5(207):207ra144.
226. Janssen BMG, Lempens EHM, Olijve LLC, Voets IK, van Dongen JLJ, de Greef TFA, et al. Reversible blocking of antibodies using bivalent peptide–DNA conjugates allows protease-activatable targeting. Chemical Science. 2013;4(4):1442-50.

227. Patel SJ, Jindal R, King KR, Tilles AW, Yarmush ML. The inflammatory response to double stranded DNA in endothelial cells is mediated by NFkappaB and TNFalpha. PLoS One. 2011;6(5):e19910.
228. Donaldson JM, Kari C, Fragoso RC, Rodeck U, Williams JC. Design and development of masked therapeutic antibodies to limit off-target effects: application to anti-EGFR antibodies. Cancer Biol Ther. 2009;8(22):2147-52.
229. Orozco CT, Bersellini M, Irving LM, Howard WW, Hargreaves D, Devine PWA, et al. Mechanistic insights into the rational design of masked antibodies. MAbs. 2022;14(1):2095701.
230. Boder ET, Wittrup KD. Yeast surface display for screening combinatorial polypeptide libraries. Nat Biotechnol. 1997;15(6):553-7.
231. Mattheakis LC, Bhatt RR, Dower WJ. An in vitro polysome display system for identifying ligands from very large peptide libraries. Proc Natl Acad Sci U S A. 1994;91(19):9022-6.
232. McCafferty J, Griffiths AD, Winter G, Chiswell DJ. Phage antibodies: filamentous phage displaying antibody variable domains. Nature. 1990;348(6301):552-4.
233. Cappellaro C, Hauser K, Mrsa V, Watzele M, Watzele G, Gruber C, et al. Saccharomyces cerevisiae a- and alpha-agglutinin: characterization of their molecular interaction. EMBO J. 1991;10(13):4081-8.
234. Grzeschik J, Hinz SC, Konning D, Pirzer T, Becker S, Zielonka S, et al. A simplified procedure for antibody engineering by yeast surface display: Coupling display levels and target binding by ribosomal skipping. Biotechnol J. 2017;12(2).
235. Szymczak AL, Workman CJ, Wang Y, Vignali KM, Dilioglou S, Vanin EF, et al. Correction of multi-gene deficiency in vivo using a single 'self-cleaving' 2A peptide-based retroviral vector. Nat Biotechnol. 2004;22(5):589-94.
236. Heinzelman P, Greenhalgh JC, Romero PA. Yeast surface display-based identification of ACE2 mutations that modulate SARS-CoV-2 spike binding across multiple mammalian species. Protein Eng Des Sel. 2022;35.
237. Rosowski S, Becker S, Toleikis L, Valldorf B, Grzeschik J, Demir D, et al. A novel one-step approach for the construction of yeast surface display Fab antibody libraries. Microb Cell Fact. 2018;17(1):3.
238. Benatuil L, Perez JM, Belk J, Hsieh CM. An improved yeast transformation method for the generation of very large human antibody libraries. Protein Eng Des Sel. 2010;23(4):155-9.
239. Traxlmayr MW, Faissner M, Stadlmayr G, Hasenhindl C, Antes B, Ruker F, et al. Directed evolution of stabilized IgG1-Fc scaffolds by application of strong heat shock to libraries displayed on yeast. Biochim Biophys Acta. 2012;1824(4):542-9.
240. Lipovsek D, Lippow SM, Hackel BJ, Gregson MW, Cheng P, Kapila A, et al. Evolution of an interloop disulfide bond in high-affinity antibody mimics based on fibronectin type III domain and selected by yeast surface display: molecular convergence with single-domain camelid and shark antibodies. J Mol Biol. 2007;368(4):1024-41.
241. Konning D, Zielonka S, Sellmann C, Schroter C, Grzeschik J, Becker S, et al. Isolation of a pH-Sensitive IgNAR Variable Domain from a Yeast-Displayed, Histidine-Doped Master Library. Mar Biotechnol (NY). 2016;18(2):161-7.
242. Schroter C, Gunther R, Rhiel L, Becker S, Toleikis L, Doerner A, et al. A generic approach to engineer antibody pH-switches using combinatorial histidine scanning libraries and yeast display. MAbs. 2015;7(1):138-51.
243. Konning D, Kolmar H. Beyond antibody engineering: directed evolution of alternative binding scaffolds and enzymes using yeast surface display. Microb Cell Fact. 2018;17(1):32.
244. Pepper LR, Cho YK, Boder ET, Shusta EV. A decade of yeast surface display technology: where are we now? Comb Chem High Throughput Screen. 2008;11(2):127-34.
245. Bacon K, Burroughs M, Blain A, Menegatti S, Rao BM. Screening Yeast Display Libraries against Magnetized Yeast Cell Targets Enables Efficient Isolation of Membrane Protein Binders. ACS Comb Sci. 2019;21(12):817-32.
246. Johnson LL, Dyer R, Hupe DJ. Matrix metalloproteinases. Curr Opin Chem Biol. 1998;2(4):466-71.

247. Parks WC, Wilson CL, Lopez-Boado YS. Matrix metalloproteinases as modulators of inflammation and innate immunity. Nat Rev Immunol. 2004;4(8):617-29.
248. Van Lint P, Libert C. Chemokine and cytokine processing by matrix metalloproteinases and its effect on leukocyte migration and inflammation. J Leukoc Biol. 2007;82(6):1375-81.
249. Yan C, Boyd DD. Regulation of matrix metalloproteinase gene expression. J Cell Physiol. 2007;211(1):19-26.
250. Ra HJ, Parks WC. Control of matrix metalloproteinase catalytic activity. Matrix Biol. 2007;26(8):587-96.
251. Brew K, Dinakarpandian D, Nagase H. Tissue inhibitors of metalloproteinases: evolution, structure and function. Biochim Biophys Acta. 2000;1477(1-2):267-83.
252. Roderfeld M, Graf J, Giese B, Salguero-Palacios R, Tschuschner A, Muller-Newen G, et al. Latent MMP-9 is bound to TIMP-1 before secretion. Biol Chem. 2007;388(11):1227-34.
253. Christensen J, Shastri VP. Matrix-metalloproteinase-9 is cleaved and activated by cathepsin K. BMC Res Notes. 2015;8:322.
254. Kridel SJ, Chen E, Kotra LP, Howard EW, Mobashery S, Smith JW. Substrate hydrolysis by matrix metalloproteinase-9. J Biol Chem. 2001;276(23):20572-8.
255. Buisson AC, Zahm JM, Polette M, Pierrot D, Bellon G, Puchelle E, et al. Gelatinase B is involved in the in vitro wound repair of human respiratory epithelium. J Cell Physiol. 1996;166(2):413-26.
256. Delclaux C, Delacourt C, D'Ortho MP, Boyer V, Lafuma C, Harf A. Role of gelatinase B and elastase in human polymorphonuclear neutrophil migration across basement membrane. Am J Respir Cell Mol Biol. 1996;14(3):288-95.
257. Gu J, Han CH, Hu FF, Wang YB, Cao YJ. The correlation analysis of human embryonic MMP-9 secretion and embryo quality. Eur Rev Med Pharmacol Sci. 2015;19(13):2354-8.
258. Shubayev VI, Myers RR. Matrix metalloproteinase-9 promotes nerve growth factor-induced neurite elongation but not new sprout formation in vitro. J Neurosci Res. 2004;77(2):229-39.
259. Gruber BL, Sorbi D, French DL, Marchese MJ, Nuovo GJ, Kew RR, et al. Markedly elevated serum MMP-9 (gelatinase B) levels in rheumatoid arthritis: a potentially useful laboratory marker. Clin Immunol Immunopathol. 1996;78(2):161-71.
260. Newman KM, Ogata Y, Malon AM, Irizarry E, Gandhi RH, Nagase H, et al. Identification of matrix metalloproteinases 3 (stromelysin-1) and 9 (gelatinase B) in abdominal aortic aneurysm. Arterioscler Thromb. 1994;14(8):1315-20.
261. Joseph C, Alsaleem M, Orah N, Narasimha PL, Miligy IM, Kurozumi S, et al. Elevated MMP9 expression in breast cancer is a predictor of shorter patient survival. Breast Cancer Res Treat. 2020;182(2):267-82.
262. Bergers G, Brekken R, McMahon G, Vu TH, Itoh T, Tamaki K, et al. Matrix metalloproteinase-9 triggers the angiogenic switch during carcinogenesis. Nat Cell Biol. 2000;2(10):737-44.
263. Hiratsuka S, Nakamura K, Iwai S, Murakami M, Itoh T, Kijima H, et al. MMP9 induction by vascular endothelial growth factor receptor-1 is involved in lung-specific metastasis. Cancer Cell. 2002;2(4):289-300.
264. Rolli M, Fransvea E, Pilch J, Saven A, Felding-Habermann B. Activated integrin alphavbeta3 cooperates with metalloproteinase MMP-9 in regulating migration of metastatic breast cancer cells. Proc Natl Acad Sci U S A. 2003;100(16):9482-7.
265. Das S, Amin SA, Jha T. Inhibitors of gelatinases (MMP-2 and MMP-9) for the management of hematological malignancies. Eur J Med Chem. 2021;223:113623.
266. Rao S, Starling N, Cunningham D, Sumpter K, Gilligan D, Ruhstaller T, et al. Matuzumab plus epirubicin, cisplatin and capecitabine (ECX) compared with epirubicin, cisplatin and capecitabine alone as first-line treatment in patients with advanced oesophago-gastric cancer: a randomised, multicentre open-label phase II study. Ann Oncol. 2010;21(11):2213-9.
267. Schiller JH, von Pawel J, Schutt P, Ansari RH, Thomas M, Saleh M, et al. Pemetrexed with or without matuzumab as second-line treatment for patients with stage IIIB/IV non-small cell lung cancer. J Thorac Oncol. 2010;5(12):1977-85.

268. Seiden MV, Burris HA, Matulonis U, Hall JB, Armstrong DK, Speyer J, et al. A phase II trial of EMD72000 (matuzumab), a humanized anti-EGFR monoclonal antibody, in patients with platinum-resistant ovarian and primary peritoneal malignancies. Gynecol Oncol. 2007;104(3):727-31.
269. Kollmannsberger C, Schittenhelm M, Honecker F, Tillner J, Weber D, Oechsle K, et al. A phase I study of the humanized monoclonal anti-epidermal growth factor receptor (EGFR) antibody EMD 72000 (matuzumab) in combination with paclitaxel in patients with EGFR-positive advanced non-small-cell lung cancer (NSCLC). Ann Oncol. 2006;17(6):1007-13.
270. Lindsey S, Langhans SA. Epidermal growth factor signaling in transformed cells. Int Rev Cell Mol Biol. 2015;314:1-41.
271. Lemmon MA, Schlessinger J. Cell signaling by receptor tyrosine kinases. Cell. 2010;141(7):1117-34.
272. Arteaga CL, Engelman JA. ERBB receptors: from oncogene discovery to basic science to mechanism-based cancer therapeutics. Cancer Cell. 2014;25(3):282-303.
273. Avraham R, Yarden Y. Feedback regulation of EGFR signalling: decision making by early and delayed loops. Nat Rev Mol Cell Biol. 2011;12(2):104-17.
274. Shigematsu H, Gazdar AF. Somatic mutations of epidermal growth factor receptor signaling pathway in lung cancers. Int J Cancer. 2006;118(2):257-62.
275. Bhargava R, Gerald WL, Li AR, Pan Q, Lal P, Ladanyi M, et al. EGFR gene amplification in breast cancer: correlation with epidermal growth factor receptor mRNA and protein expression and HER-2 status and absence of EGFR-activating mutations. Mod Pathol. 2005;18(8):1027-33.
276. Cai WQ, Zeng LS, Wang LF, Wang YY, Cheng JT, Zhang Y, et al. The Latest Battles Between EGFR Monoclonal Antibodies and Resistant Tumor Cells. Front Oncol. 2020;10:1249.
277. Roe E, Garcia Muret MP, Marcuello E, Capdevila J, Pallares C, Alomar A. Description and management of cutaneous side effects during cetuximab or erlotinib treatments: a prospective study of 30 patients. J Am Acad Dermatol. 2006;55(3):429-37.
278. Meira DD, Nobrega I, de Almeida VH, Mororo JS, Cardoso AM, Silva RLA, et al. Different antiproliferative effects of matuzumab and cetuximab in A431 cells are associated with persistent activity of the MAPK pathway. Eur J Cancer. 2009;45(7):1265-73.
279. Schmiedel J, Blaukat A, Li S, Knochel T, Ferguson KM. Matuzumab binding to EGFR prevents the conformational rearrangement required for dimerization. Cancer Cell. 2008;13(4):365-73.
280. Delate T, Hansen ML, Gutierrez AC, Le KN. Indications for Rituximab Use in an Integrated Health Care Delivery System. J Manag Care Spec Pharm. 2020;26(7):832-8.
281. Pierpont TM, Limper CB, Richards KL. Past, Present, and Future of Rituximab-The World's First Oncology Monoclonal Antibody Therapy. Front Oncol. 2018;8:163.
282. Rosenwald A, Wright G, Wiestner A, Chan WC, Connors JM, Campo E, et al. The proliferation gene expression signature is a quantitative integrator of oncogenic events that predicts survival in mantle cell lymphoma. Cancer Cell. 2003;3(2):185-97.
283. Dreyling M, Aurer I, Cortelazzo S, Hermine O, Hess G, Jerkeman M, et al. Treatment for patients with relapsed/refractory mantle cell lymphoma: European-based recommendations. Leuk Lymphoma. 2018;59(8):1814-28.
284. Le Gouill S, Thieblemont C, Oberic L, Moreau A, Bouabdallah K, Dartigeas C, et al. Rituximab after Autologous Stem-Cell Transplantation in Mantle-Cell Lymphoma. N Engl J Med. 2017;377(13):1250-60.
285. Yan W, Yang Y, Yang W, Wei M. Discovery and Design of Peptides as MMP9 Inhibitors through Structure-Based Molecular Docking for Targeted Mantle Cell Lymphoma Therapy. Anticancer Agents Med Chem. 2021;21(12):1551-63.
286. Yan W, Li SX, Wei M, Gao H. Identification of MMP9 as a novel key gene in mantle cell lymphoma based on bioinformatic analysis and design of cyclic peptides as MMP9 inhibitors based on molecular docking. Oncol Rep. 2018;40(5):2515-24.
287. Cai X, Yu X, Qin W, Wang T, Jia Z, Xiao R, et al. Preparation and anti-Raji lymphoma efficacy of a novel pH sensitive and magnetic targeting nanoparticles drug delivery system. Bioorg Chem. 2020;94:103375.

288. De Milito A, Iessi E, Logozzi M, Lozupone F, Spada M, Marino ML, et al. Proton pump inhibitors induce apoptosis of human B-cell tumors through a caspase-independent mechanism involving reactive oxygen species. Cancer Res. 2007;67(11):5408-17.
289. Chan KH, Prabhakar L, Al-Radideh O, Okwesili B, Are G, Shaaban H. A Rare Case of Severe Lactic Acidosis in a Patient With Mantle Cell Lymphoma. J Investig Med High Impact Case Rep. 2021;9:23247096211034040.
290. Ohtsubo K, Imamura R, Seki R, Ohshima K, Hashiguchi M, Yakushiji K, et al. Blastoid variant of mantle cell lymphoma with lactic acidosis: a case report. Int J Hematol. 2004;80(5):428-31.
291. Yelvington BJ. Subcutaneous Rituximab in Follicular Lymphoma, Chronic Lymphocytic Leukemia, and Diffuse Large B-Cell Lymphoma. J Adv Pract Oncol. 2018;9(5):530-4.
292. Reff ME, Carner K, Chambers KS, Chinn PC, Leonard JE, Raab R, et al. Depletion of B cells in vivo by a chimeric mouse human monoclonal antibody to CD20. Blood. 1994;83(2):435-45.
293. Pedersen IM, Buhl AM, Klausen P, Geisler CH, Jurlander J. The chimeric anti-CD20 antibody rituximab induces apoptosis in B-cell chronic lymphocytic leukemia cells through a p38 mitogen activated protein-kinase-dependent mechanism. Blood. 2002;99(4):1314-9.
294. Uchida J, Lee Y, Hasegawa M, Liang Y, Bradney A, Oliver JA, et al. Mouse CD20 expression and function. Int Immunol. 2004;16(1):119-29.
295. Fishelson Z, Donin N, Zell S, Schultz S, Kirschfink M. Obstacles to cancer immunotherapy: expression of membrane complement regulatory proteins (mCRPs) in tumors. Mol Immunol. 2003;40(2-4):109-23.
296. Rankin CT, Veri MC, Gorlatov S, Tuaillon N, Burke S, Huang L, et al. CD32B, the human inhibitory Fc-gamma receptor IIB, as a target for monoclonal antibody therapy of B-cell lymphoma. Blood. 2006;108(7):2384-91.
297. orphanet. Research and trials 2022 [Available from: https://www.orpha.net/consor/cgi-bin/ResearchTrials_ClinicalTrials.php?lng=EN&data_id=3823&type_list=researchtrials_from_substancetradename_shd&MISSING%20CONTENT=BI-1206&Typ=Sub&search=ResearchTrials_ClinicalTrials_SubstanceTradename&data_type=Product&title=BI-1206&diseaseType=Drug&ResearchTrials_ResearchTrials_ClinicalTrials_ClinicalTrialPhase=&ResearchTrials_ResearchTrials_ClinicalTrials_GeographicType=null&ResearchTrials_ResearchTrials_ClinicalTrials_country=NN&diseaseGroup=.] Last access: 08. September 2022
298. Jiang VC, Liu Y, Jordan A, Leeming A, McIntosh J, Huang S, et al. Targeting FcgammaRIIB by antagonistic antibody BI-1206 improves the efficacy of rituximab-based therapies in aggressive mantle cell lymphoma. J Hematol Oncol. 2022;15(1):42.
299. Ono M, Bolland S, Tempst P, Ravetch JV. Role of the inositol phosphatase SHIP in negative regulation of the immune system by the receptor Fc(gamma)RIIB. Nature. 1996;383(6597):263-6.
300. Nimmerjahn F, Ravetch JV. Fcgamma receptors as regulators of immune responses. Nat Rev Immunol. 2008;8(1):34-47.
301. Xiang Z, Cutler AJ, Brownlie RJ, Fairfax K, Lawlor KE, Severinson E, et al. FcgammaRIIb controls bone marrow plasma cell persistence and apoptosis. Nat Immunol. 2007;8(4):419-29.
302. Karnell JL, Dimasi N, Karnell FG, 3rd, Fleming R, Kuta E, Wilson M, et al. CD19 and CD32b differentially regulate human B cell responsiveness. J Immunol. 2014;192(4):1480-90.
303. Su K, Li X, Edberg JC, Wu J, Ferguson P, Kimberly RP. A promoter haplotype of the immunoreceptor tyrosine-based inhibitory motif-bearing FcgammaRIIb alters receptor expression and associates with autoimmunity. II. Differential binding of GATA4 and Yin-Yang1 transcription factors and correlated receptor expression and function. J Immunol. 2004;172(11):7192-9.
304. Clynes RA, Towers TL, Presta LG, Ravetch JV. Inhibitory Fc receptors modulate in vivo cytotoxicity against tumor targets. Nat Med. 2000;6(4):443-6.
305. van Montfoort N, t Hoen PA, Mangsbo SM, Camps MG, Boross P, Melief CJ, et al. Fcgamma receptor IIb strongly regulates Fcgamma receptor-facilitated T cell activation by dendritic cells. J Immunol. 2012;189(1):92-101.

306. Lim SH, Vaughan AT, Ashton-Key M, Williams EL, Dixon SV, Chan HT, et al. Fc gamma receptor IIb on target B cells promotes rituximab internalization and reduces clinical efficacy. Blood. 2011;118(9):2530-40.
307. Karlsson I, Gertsson S, Kilany S, Borggren M, Abrisqueta P, Carneiro A, et al. Phase 1/2a Clinical Trial of BI-1206, a Monoclonal Antibody to Fc γ riib, in Combination with Rituximab in Subjects with Indolent B-Cell Non-Hodgkin Lymphoma That Has Relapsed or Is Refractory to Rituximab. Blood. 2021;138:1354.
308. U. S. National Library of Medicine. BI-1206 and an Anti-CD20 Antibody in Patients With CD32b Positive B-cell Lymphoma or Leukaemia: U. S. National Library of Medicine; 2022 [Available from: https://clinicaltrials.gov/ct2/show/results/NCT02933320.] Last access: 09. September 2022
309. orphanet. Phase 1/2a Clinical Trial of BI-1206, a Monoclonal Antibody to CD32b (Fc gamma RIIB), in Combination with Rituximab in Subjects with Indolent B-Cell Non-Hodgkin Lymphoma That has Relapsed or is Refractory to Rituximab - ES 2022 [Available from: https://www.orpha.net/consor/cgi-bin/ResearchTrials_ClinicalTrials.php?lng=EN&data_id=3823&type_list=researchtrials_from_substancetradename_shd&MISSING%20CONTENT=BI-1206&Typ=Sub&search=ResearchTrials_ClinicalTrials_SubstanceTradename&data_type=Product&title=BI-1206&diseaseType=Drug&ResearchTrials_ResearchTrials_ClinicalTrials_ClinicalTrialPhase=&ResearchTrials_ResearchTrials_ClinicalTrials_GeographicType=null&ResearchTrials_ResearchTrials_ClinicalTrials_country=NN&diseaseGroup=.] Last access: 03. September 2022
310. Daver N, Jonas BA, Medeiros BC, Patil U, Yan M. Phase 1b, open-label study evaluating the safety and pharmacokinetics of atezolizumab (anti-PD-L1 antibody) administered in combination with Hu5F9-G4 to patients with relapsed and/or refractory acute myeloid leukemia. Leuk Lymphoma. 2022:1-4.
311. Daver NG, Vyas P, Kambhampati S, Malki MMA, Larson RA, Asch AS, et al. Tolerability and efficacy of the first-in-class anti-CD47 antibody magrolimab combined with azacitidine in frontline TP53m AML patients: Phase 1b results. Journal of Clinical Oncology. 2022;40(16_suppl):7020-.
312. Fenalti G, Villanueva N, Griffith M, Pagarigan B, Lakkaraju SK, Huang RY, et al. Structure of the human marker of self 5-transmembrane receptor CD47. Nat Commun. 2021;12(1):5218.
313. Shinohara M, Ohyama N, Murata Y, Okazawa H, Ohnishi H, Ishikawa O, et al. CD47 regulation of epithelial cell spreading and migration, and its signal transduction. Cancer Sci. 2006;97(9):889-95.
314. Kaur S, Martin-Manso G, Pendrak ML, Garfield SH, Isenberg JS, Roberts DD. Thrombospondin-1 inhibits VEGF receptor-2 signaling by disrupting its association with CD47. J Biol Chem. 2010;285(50):38923-32.
315. Seiffert M, Brossart P, Cant C, Cella M, Colonna M, Brugger W, et al. Signal-regulatory protein alpha (SIRPalpha) but not SIRPbeta is involved in T-cell activation, binds to CD47 with high affinity, and is expressed on immature CD34(+)CD38(-) hematopoietic cells. Blood. 2001;97(9):2741-9.
316. Oldenborg PA, Gresham HD, Lindberg FP. CD47-signal regulatory protein alpha (SIRPalpha) regulates Fcgamma and complement receptor-mediated phagocytosis. J Exp Med. 2001;193(7):855-62.
317. Tsai RK, Discher DE. Inhibition of "self" engulfment through deactivation of myosin-II at the phagocytic synapse between human cells. J Cell Biol. 2008;180(5):989-1003.
318. Barger SR, Gauthier NC, Krendel M. Squeezing in a Meal: Myosin Functions in Phagocytosis. Trends Cell Biol. 2020;30(2):157-67.
319. Willingham SB, Volkmer JP, Gentles AJ, Sahoo D, Dalerba P, Mitra SS, et al. The CD47-signal regulatory protein alpha (SIRPa) interaction is a therapeutic target for human solid tumors. Proc Natl Acad Sci U S A. 2012;109(17):6662-7.
320. Liu J, Wang L, Zhao F, Tseng S, Narayanan C, Shura L, et al. Pre-Clinical Development of a Humanized Anti-CD47 Antibody with Anti-Cancer Therapeutic Potential. PLoS One. 2015;10(9):e0137345.
321. Oldenborg PA, Zheleznyak A, Fang YF, Lagenaur CF, Gresham HD, Lindberg FP. Role of CD47 as a marker of self on red blood cells. Science. 2000;288(5473):2051-4.
322. Gilead. Gilead Statement on the Discontinuation of Magrolimab Study in AML with TP53 Mutations: Gilead,; 2023 [Available from: https://www.gilead.com/news-and-press/company-

statements/gilead-statement-on-the-discontinuation-of-magrolimab-study-in-aml-with-tp53-mutations.] Last eccess: 28. October 2023
323. Arstila TP, Casrouge A, Baron V, Even J, Kanellopoulos J, Kourilsky P. A direct estimate of the human alphabeta T cell receptor diversity. Science. 1999;286(5441):958-61.
324. Lefranc MP, Chuchana P, Dariavach P, Nguyen C, Huck S, Brockly F, et al. Molecular mapping of the human T cell receptor gamma (TRG) genes and linkage of the variable and constant regions. Eur J Immunol. 1989;19(6):989-94.
325. Hata S, Clabby M, Devlin P, Spits H, De Vries JE, Krangel MS. Diversity and organization of human T cell receptor delta variable gene segments. J Exp Med. 1989;169(1):41-57.
326. Chien YH, Bonneville M. Gamma delta T cell receptors. Cell Mol Life Sci. 2006;63(18):2089-94.
327. Yague J, White J, Coleclough C, Kappler J, Palmer E, Marrack P. The T cell receptor: the alpha and beta chains define idiotype, and antigen and MHC specificity. Cell. 1985;42(1):81-7.
328. Rock EP, Sibbald PR, Davis MM, Chien YH. CDR3 length in antigen-specific immune receptors. J Exp Med. 1994;179(1):323-8.
329. Garcia KC, Adams JJ, Feng D, Ely LK. The molecular basis of TCR germline bias for MHC is surprisingly simple. Nat Immunol. 2009;10(2):143-7.
330. Call ME, Wucherpfennig KW. The T cell receptor: critical role of the membrane environment in receptor assembly and function. Annu Rev Immunol. 2005;23:101-25.
331. Kuhns MS, Davis MM, Garcia KC. Deconstructing the form and function of the TCR/CD3 complex. Immunity. 2006;24(2):133-9.
332. Morath A, Schamel WW. alphabeta and gammadelta T cell receptors: Similar but different. J Leukoc Biol. 2020;107(6):1045-55.
333. Love PE, Hayes SM. ITAM-mediated signaling by the T-cell antigen receptor. Cold Spring Harb Perspect Biol. 2010;2(6):a002485.
334. Gil D, Schamel WW, Montoya M, Sanchez-Madrid F, Alarcon B. Recruitment of Nck by CD3 epsilon reveals a ligand-induced conformational change essential for T cell receptor signaling and synapse formation. Cell. 2002;109(7):901-12.
335. Weisenburger DD, Savage KJ, Harris NL, Gascoyne RD, Jaffe ES, MacLennan KA, et al. Peripheral T-cell lymphoma, not otherwise specified: a report of 340 cases from the International Peripheral T-cell Lymphoma Project. Blood. 2011;117(12):3402-8.
336. Belhadj K, Reyes F, Farcet JP, Tilly H, Bastard C, Angonin R, et al. Hepatosplenic gammadelta T-cell lymphoma is a rare clinicopathologic entity with poor outcome: report on a series of 21 patients. Blood. 2003;102(13):4261-9.
337. Warner K, Weit N, Crispatzu G, Admirand J, Jones D, Herling M. T-cell receptor signaling in peripheral T-cell lymphoma - a review of patterns of alterations in a central growth regulatory pathway. Curr Hematol Malig Rep. 2013;8(3):163-72.
338. Edgar JD. T cell immunodeficiency. J Clin Pathol. 2008;61(9):988-93.
339. Foss FM, Zinzani PL, Vose JM, Gascoyne RD, Rosen ST, Tobinai K. Peripheral T-cell lymphoma. Blood. 2011;117(25):6756-67.
340. Zhang C, Duvic M. Treatment of cutaneous T-cell lymphoma with retinoids. Dermatol Ther. 2006;19(5):264-71.
341. Gallamini A, Zaja F, Patti C, Billio A, Specchia MR, Tucci A, et al. Alemtuzumab (Campath-1H) and CHOP chemotherapy as first-line treatment of peripheral T-cell lymphoma: results of a GITIL (Gruppo Italiano Terapie Innovative nei Linfomi) prospective multicenter trial. Blood. 2007;110(7):2316-23.
342. Izykowska K, Rassek K, Korsak D, Przybylski GK. Novel targeted therapies of T cell lymphomas. J Hematol Oncol. 2020;13(1):176.
343. Sadio F, Stadlmayr G, Stadlbauer K, Graf M, Scharrer A, Ruker F, et al. Stabilization of soluble high-affinity T-cell receptor with de novo disulfide bonds. FEBS Lett. 2020;594(3):477-90.
344. Ding YH, Baker BM, Garboczi DN, Biddison WE, Wiley DC. Four A6-TCR/peptide/HLA-A2 structures that generate very different T cell signals are nearly identical. Immunity. 1999;11(1):45-56.

345. Utz U, Banks D, Jacobson S, Biddison WE. Analysis of the T-cell receptor repertoire of human T-cell leukemia virus type 1 (HTLV-1) Tax-specific CD8+ cytotoxic T lymphocytes from patients with HTLV-1-associated disease: evidence for oligoclonal expansion. J Virol. 1996;70(2):843-51.
346. Hausmann S, Biddison WE, Smith KJ, Ding YH, Garboczi DN, Utz U, et al. Peptide recognition by two HLA-A2/Tax11-19-specific T cell clones in relationship to their MHC/peptide/TCR crystal structures. J Immunol. 1999;162(9):5389-97.
347. Pescovitz MD. Rituximab, an anti-cd20 monoclonal antibody: history and mechanism of action. Am J Transplant. 2006;6(5 Pt 1):859-66.
348. Klein C, Lammens A, Schafer W, Georges G, Schwaiger M, Mossner E, et al. Epitope interactions of monoclonal antibodies targeting CD20 and their relationship to functional properties. MAbs. 2013;5(1):22-33.
349. Huston JS, Levinson D, Mudgett-Hunter M, Tai MS, Novotny J, Margolies MN, et al. Protein engineering of antibody binding sites: recovery of specific activity in an anti-digoxin single-chain Fv analogue produced in Escherichia coli. Proc Natl Acad Sci U S A. 1988;85(16):5879-83.
350. FRENDÉUS B. TI, MÅRTENSSONL., Cragg M., Roghanian A., inventor MEDICAMENTS, USES AND METHODS. Worldwide 2015 US15/311,016.
351. Ladwig PM, Barnidge DR, Willrich MAV. Mass Spectrometry Approaches for Identification and Quantitation of Therapeutic Monoclonal Antibodies in the Clinical Laboratory. Clin Vaccine Immunol. 2017;24(5).
352. Bogen JP, Hinz SC, Grzeschik J, Ebenig A, Krah S, Zielonka S, et al. Dual Function pH Responsive Bispecific Antibodies for Tumor Targeting and Antigen Depletion in Plasma. Front Immunol. 2019;10:1892.

8 Appendix

8.1 Supplementary figures and tables

Table S 1: Amino acid sequences of the different linkers. MMP-9 cleavage sites within the linkers are underlined.

Linker name	Amino acid sequence
MMP-9	GGGGSGGGGSVHMPLGFLGPGGGGSGGGGSGGGGSGGGGSGGGGSGGGGS
PLGLA	GGGGSGGGGSGGGGSGGGGSGGGGSPLGLAGGGGS
PLGLA2	GGGGSGGGGSGGGGSGGGGSPLGLAGGGGSGGGGS
G4S PLGLA	GGGGSGGGGSGGGGSGGGGSGGGGSGGGGSPLGLAGG
G4S7	GGGGSGGGGSGGGGSGGGGSGGGGSGGGGSGGGGS
AGS	AGGGGS

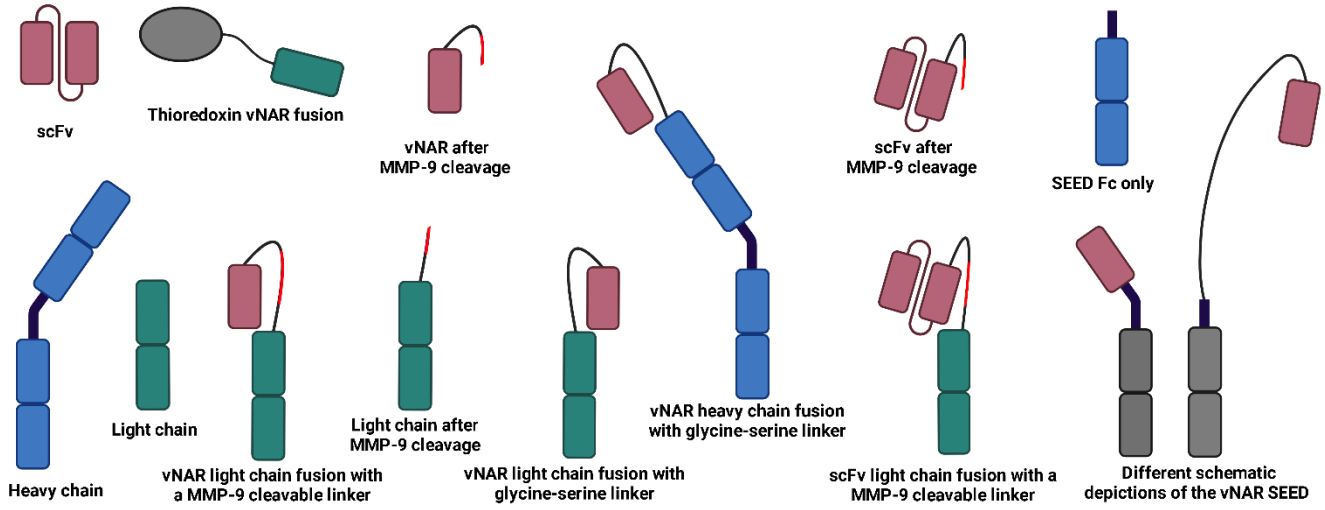

Figure S 1: Overview and description of the different schematic depictions utilized to illustrate the SDS-PAGES.

8.2 Supplementary figures and tables for the matuzumab project

Table S 2: Amino acid sequence alignment of AMV1 and the pH-dependent single clones AMV1H2, AMV1H5, AMV1H8 and AMV1H10. Positions with high consensus are shown in red, whereas positions in blue represent low consensus. Positions indicated in black, reveal no consensus.

Clone	Sequence
AMV1	MAARLEQTPTTTTKEAGESLTINCVLKGSAYALGNTYWYFTKKGATKKASLSTGGRYSDTKNTASKSFSLLISDLRVEDSGTYHCEARGRIAHMQHQMWSNHPIEGGGTILTVK
AMV1H2	MAARLEQTPTTTTKEAGESLTINCVLKGSRYGLGNTYWYFTKKGATKKARLSTGGRYSDTKNTASKSFSLRISDLRVEDSGTYHCEAHGRHAHIQHQHRSNHHIEGGGTTLTVK
AMV1H5	MAARLEQTPTTTTKEAGESLTINCVLKGSAYGLGKTYWYFTKKGATRQAILSTGGRYSDTKNTASKSFSLRISDLRVEDSGTYHCEARGRHAHMHHQLHSHHPIEGGGTILTVK
AMV1H8	MAARLEQTPTTTTKEAGESLTINCVLKGSRYGLGNTYWYFTKKGATKKARLSTGGRYSDTKNTASKSFSLRISDLRVEDSGTYHCEAHGHHHIQHQKYSHHHIEGGGTILTVK
AMV1H10	MAARLEQTPTTTTKEAGESLTINCVLKGSAYGLGKTYWYFTKKGATRQAILSTGGRYSDTKNTASKSFSLRISDLRVEDSGTYHCEARGRHAHMHHQLHSHHPIEGGGTILTVK

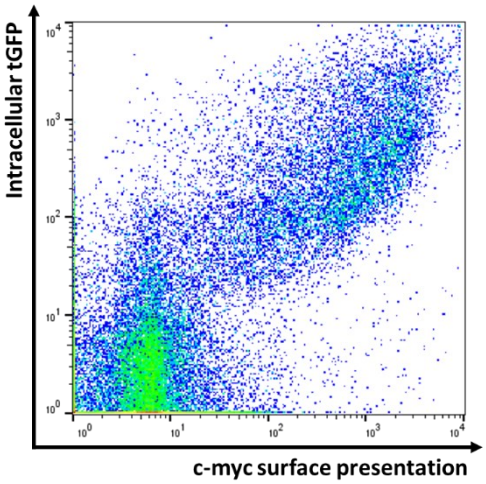

Figure S 2: Analysis of correlation between intracellular tGFP and c-myc surface presentation. The cells depicted in the dot plots are gated on viable and single cells. The intracellular tGFP is shown in the y-axis, while c-myc surface presentation is depicted on the x-axis. C-myc surface presentation is verified by an anti-c-myc antibody coupled to biotin and subsequent staining with SAPC.

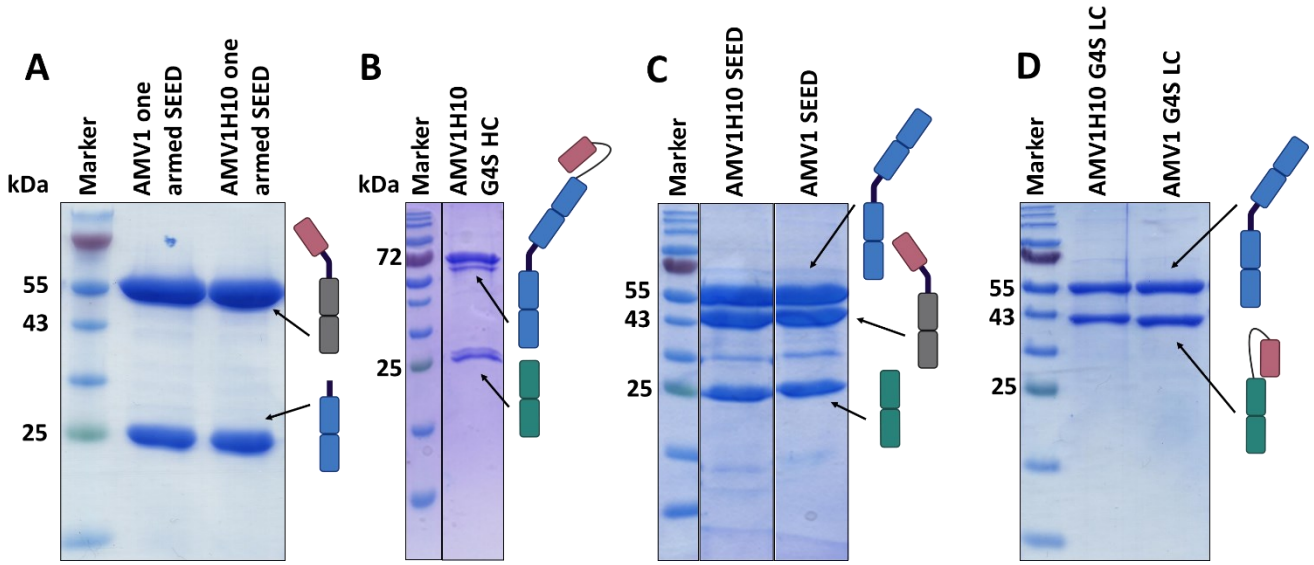

Figure S 3: Reducing SDS-PAGE of different AMV1 and AMV1H10 constructs. A) Analysis of AMV1 and AMV1H10 one armed SEED in HEK Expi293F™ cells. In both cases a band at 55 and 25 kDa is visible, while several weaker bands with low intensity between both bands are present. The expected size of the AMV1 and AMV1H10 arm is 42 kDa, while the size of the constant SEED domain is 27.3 kDa. **B)** Analysis of AMV1H10 fused to the heavy chain of matuzumab *via* a glycine-serine linker (Expected size heavy chain: 64.5 kDa, light chain: 23.4 kDa). Double bands are evident at around 72 and 25 kDa. **C)** Analysis of AMV1H10 and AMV1 SEEDs. Overall, four bands are evident for both constructs at 55, 43, 34 and 25 kDa. The expected size for the matuzumab SEED chain is 50.9 kDa, while the calculated size for the light chain is 23.4 kDa and the size of the AMV1H10 and AMV1 domains is 42 kDa. **D)** Analysis of AMV1H10 and AMV1 fused to the light chain of matuzumab *via* a glycine-serine linker. Two bands are visible for both constructs, one in the range of 55 kDa, while the other is in the range of 34 and 43 kDa. The calculated size for the heavy chain is 49.8 kDa, while the size of the light chains was calculated to be 37.8 kDa.

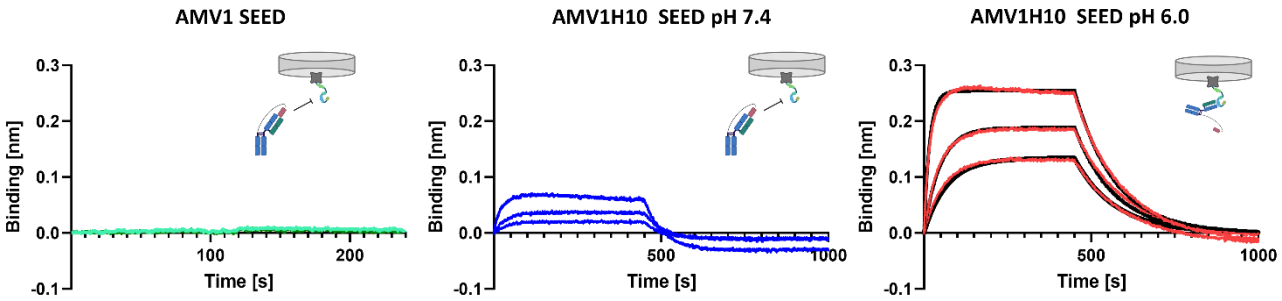

Figure S 4: Binding kinetics of AMV1 SEED at pH 7.4 and AMV1H10 SEED at pH 7.4 and 6.0. The binding in nanometer (nm) is shown on the y-axis, while the time in seconds (s) is depicted on the x-axis. Binding curves of AMV1 SEED at pH 7.4 are shown by the green curves, while binding of AMV1H10 SEED at pH 7.4 and 6.0 are visualized by blue and red lines respectively.

8.3 Supplementary figures and tables for the 5F9 project

Table S 3: Amino acid sequence alignment of anti-5F9 vNARs (A5F9V) derived from eight yeast single clones. Clones with identical amino acid sequences share the same color in the first column. Positions with high amino acid consensus are shown in red, low consensus is displayed in blue and neutral positions are depicted in black.

Clone	Sequence
A5F9V3	MAARLEQTPTTTTKEAGESLTINCVLKGSGYGLGITYWYFTKKGATKKASLSTGGRYSDTKDTASKSFSLRISDLRVEDSGTYHCEAHNMMYMNHHWRHHIIEGGGTTLTVK
A5F9V4	MAARLEQTPTTTTKEAGESLTINCVLKGSGYGLGITYWYFTKKGATKKASLSTGGRYSDTKDTASKSFSLRISDLRVEDSGTYHCEAHNMMYMNHHWRHHIIEGGGTTLTVK
A5F9V5	MAARLEQTPTTTTKEAGESLTINCVLKGSGYGLGITYWYFTKKGATKKASLSTGGRYSDTKDTASKSFSLRISDLRVEDSGTYHCEAHNMMYMNHHWRHHIIEGGGTTLTVK
A5F9V6	MAARLEQTPTTTTKEAGESLTINCVLKGSGYGLGITYWYFTKKGATKKASLSTGGRYSDTKDTASKSFSLRISDLRVEDSGTYHCEAHNMMYMNHHWRHHIIEGGGTTLTVK
A5F9V7	MAARLEQTPTTTTKEAGESLTINCVLKGSGYGLGITYWYFTKKGATKKASLSTGGRYSDTKDTASKSFSLRISDLRVEDSGTYHCEAHNMMYMNHHWRHHIIEGGGTTLTVK
A5F9V8	MAARLEQTPTTTTKEAGESLTINCVLKGSRYVLGITYWYFTKKGATKKARLSTGGRYSDTKNTASKSFSLRISDLRVEDSGTYHCEAEWLHKHKHDDPRHMIEGGGTTLTVK
A5F9V9	MAARLEQTPTTTTKEAGESLTINCVLKGSGYGLGITYWYFTKKGATKKASLSTGGRYSDTKDTASKSFSLRISDLRVEDSGTYHCEAHNMMYMNHHWRHHIIEGGGTTLTVK
A5F9V10	MAARLEQTPTTTTKEAGESLTINCVLKGSGYGLGITYWYFTKKGATKKASLSTGGRYSDTKDTASKSFSLRISDLRVEDSGTYHCEAHNMMYMNHHWRHHIIEGGGTTLTVK

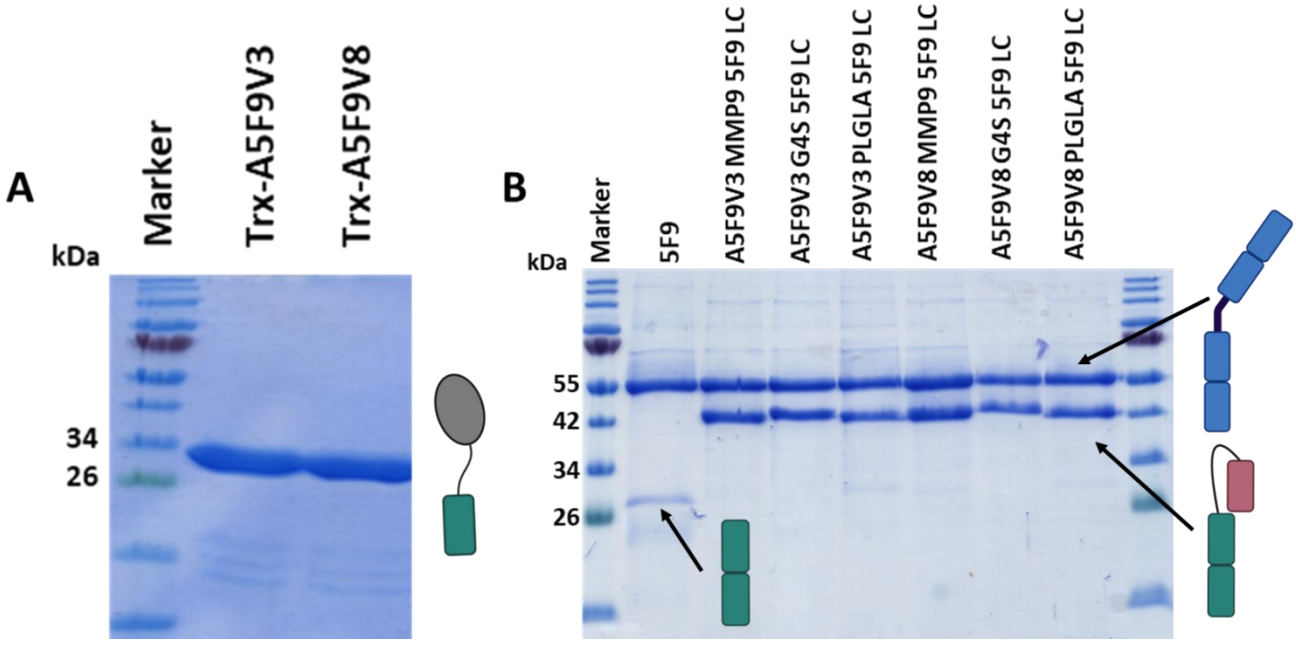

Figure S 5: Reducing SDS-PAGE of different A5F9V3 and A5F9V8 constructs. A) Analysis of A5F9V3 and A5F9V8 thioredoxin fusion proteins expressed in *E. coli*. In both cases, one band with high intensity between 26 and 34 kDa is visible, while three weaker bands with lower molecular weight are present. The expected molecular weight is 30.8 kDa for Trx-A5F9V3 and 30.9 kDa for Trx-A5F9V8. **B)** Analysis of different A5F9V3 and A5F9V8 light chain fusions expressed in HEK Expi293F™ cells. For all constructs a band in the range of 55 kDa is visible. In case of 5F9, a weaker band is visible between 26 and 34 kDa. All other constructs reveal a second band in the range of 42 kDa. The expected sizes for the different constructs are 49 kDa for the 5F9

heavy chain which remains constant for all constructs, 24 kDa for the 5F9 light chain, 38.8 kDa for the A5F9V3 MMP-9 5F9 light chain, 38.2 kDa for the A5F9V3 G4S 5F9 light chain, 39.9 kDa for the A5F9V3 PLGLA 5F9 light chain, 38.9 kDa for the A5F9V8 MMP-9 5F9 light chain, 38.3 kDa for the A5F9V8 G4S 5F9 light chain and, 40 kDa for the A5F9V8 PLGLA 5F9 light chain.

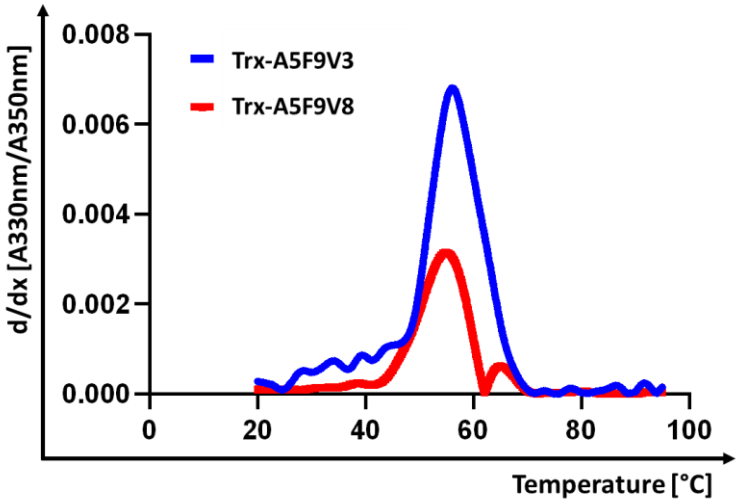

Figure S 6: Melting point analysis by nano differential scanning fluorimetry for Trx-A5F9V3 and Trx-A5F9V8. The derivation of A330nm/A350nm is depicted on the y-axis, while the temperature is shown on the x-axis. The melting curve of Trx-A5F9V3 and A5F9V8 are depicted in blue and red respectively.

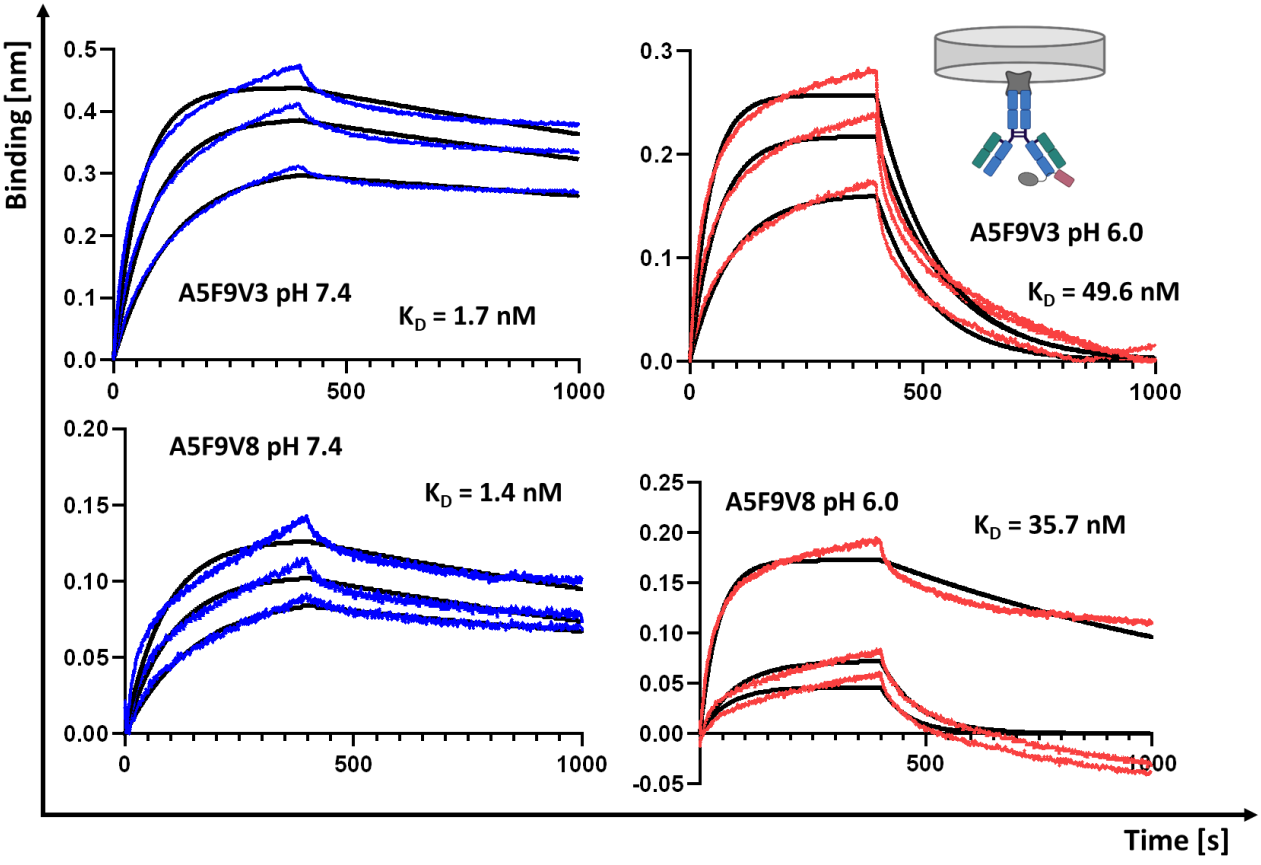

Figure S 7: Binding kinetics of A5F9V3 and A5F9V8 at pH 7.4 and 6.0. The binding in nanometer (nm) is shown on the y-axis, while the time in seconds (s) is depicted on the x-axis. Binding curves at pH 7.4 and pH 6.0 are visualized by blue and red lines respectively, while the fits to determine the dissociation constant (K_D) are shown in black.

8.4 Supplementary figures and tables for the rituximab project

Table S 4: Amino acid sequence alignment of anti-rituximab vNARs (ARV) derived from nine yeast single clones. Clones with identical amino acid sequences share the same color in the first column. Positions with high amino acid consensus are shown in red, low consensus is displayed in blue and neutral positions are depicted in black.

Clone	Sequence
ARV1	MAARLEQTPTTTTKEAGESLTINCVLKGSGYGLGNTYWYFTKKGATKKASLSTGGRYSDTKNTASKSFSLRISDLRVEDSGTYHCEAWQR-EHAQAWISIYN--IEGGGTILTVK
ARV2	MAARLEQTPTTTTKEAGESLTINCVLKGSGYGLGSTYWYFTKKGATKKASLSTGGRYSDTKNTASKSFSLRISDLRVEDSGTYHCEAEQQ-FAAHHWHSMYKVQIEGGGTPVTVK
ARV4	MAARLEQTPTTTTKEAGESLTINCVLKGSAYALGTTYWYFTKKGATKKASLSTGGRYSDTKNTASKSFSLRISDLRVEDSGTYHCEANQS-HFALAWHHHFDADIEGGGTPVTVN
ARV5	MAARLEQTPTTTTKEAGESLTINCVLKGSAYALGTTYWYFTKKGATKKASLSTGGRYSDTKNTASKSFSLRISDLRVEDSGTYHCEANQS-HFALAWHHHFDADIEGGGTPVTVN
ARV6	MAARLEQTPTTTTKEAGESLTINCVLKGSAYALGTTYWYFTKKGATKKASLSTGGRYSDTKNTASKSFSLRISDLRVEDSGTYHCEANQS-HFALAWHHHFDADIEGGGTPVTVN
ARV7	MAARLEQTPTTTTKEAGESLTINCVLKGSAYALGTTYWYFTKKGATKKASLSTGGRYSDTKNTASKSFSLRISDLRVEDSGTYHCEANQS-HFALAWHHHFDADIEGGGTPVTVN
ARV8	MAARLEQTPTTTTKEAGESLTINCVLKGSGYGLGSTYWYFTKKGATKKASLSTGGRYSDTKNTASKSFSLRISDLRVEDSGTYHCEAEQQ-FAAHHWHSMYKVQIEGGGTPVTVK
ARV9	MAARLEQTPTTTTKEAGESLTINCVLKGSNYGLGRTYWYFTKKGATKKASLSTGGRYSDTKNTASKSFSLRISDLRVEDSGTYHCEANLLLHHHPHYHGHW---IEGGGTLVTVK
ARV10	MAARLEQTPTTTTKEAGESLTINCVLKGSAYALGTTYWYFTKKGATKKASLSTGGRYSDTKNTASKSFSLRISDLRVEDSGTYHCEANQS-HFALAWHHHFDADIEGGGTPVTVN

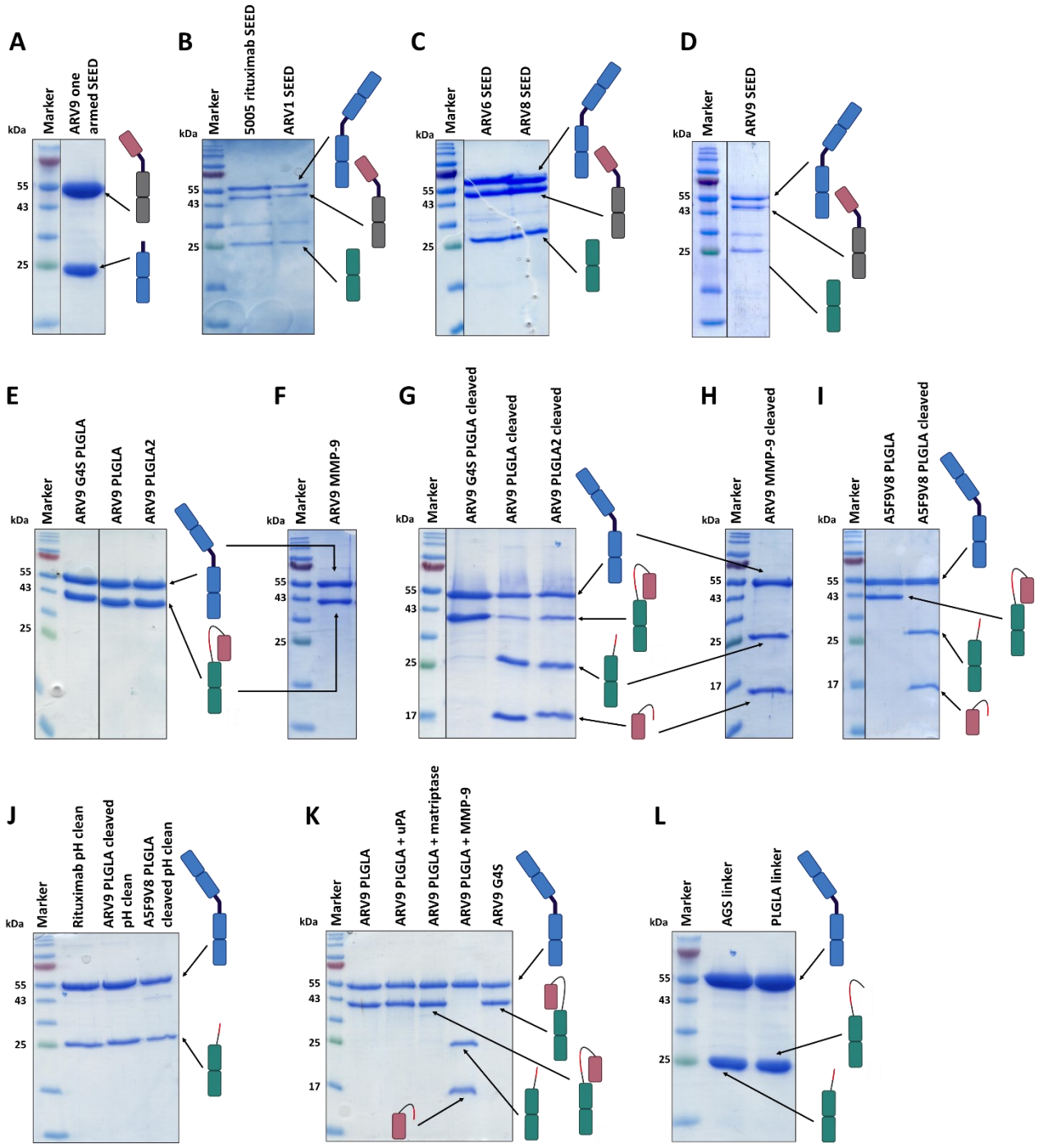

Figure S 8: Reducing SDS-PAGE of different rituximab constructs expressed in Expi HEK cells. A) Rituximab one armed SEED with bands visible at about 55 and 25 kDa with bands of less intensity in a ladder like fashion in between. The calculated size of the chains is 41.9 kDA for the ARV9 SEED and 27.3 kDa for the heavy chain only portion. **B-D)** Rituximab, 5005 and ARV SEED constructs. For 5005, ARV1, ARV6 and ARV8 SEED constructs bands with high intensity are detectible at about 55, 43 and 25 kDa. Furthermore, bands with less intensity are evident at 43 kDa. The calculated mass of the different parts are 50 kDa for the rituximab SEED, 23.1 kDa for the rituximab light chain and 41.7, 41.8, 41.9, 42, and 41.9 kDa for the 5005, ARV1, ARV6, ARV8 and ARV9 SEED portion. **E)** ARV9 fused to the rituximab light chain via different MMP-9 cleavable linkers. For all constructs a band at 55 and 43 kDa is evident. The calculated mass is 49.3 kDa for the rituximab heavy chain, 37.8 kDa for the ARV9 G4S PLGLA, ARV9 PLGLA and PLGLA2 light chain fusion. **F)** ARV9 MMP-9 light chain fusion with bands evident at 55 and 43 kDa. The calculated mass for the heavy chain is 49.4 kDa and 39 kDa for the light chain. **G)** Analysis of ARV9 rituximab light chain fusions after MMP-9 cleavage. For ARV9 G4S PLGLA a band at 55 and 43 kDa is visible, while AVR9 PLGLA and ARV9 PLGLA2 reveal bands at 55, 43, 25 and 17 kDa. The calculated size is 49.3 kDa for the rituximab heavy chain, 23.4 kDa for the rituximab light chain after cleavage of the ARV9 G4S PLGLA construct and 13.8 kDa for the vNAR of the previously mentioned construct. The calculated mass for the rituximab light chain of the ARV9 PLGLA and ARV9 PLGLA2 constructs after cleavage is 23.4 and

23.8 kDa respectively, while the mass of the vNARs is 14.4 and 14.1 respectively. **H)** ARV9 MMP-9 after MMP-9 cleavage. Three bands are visible at 55, 25 and 17 kDa. The calculated masses are 49.3 KDa for the rituximab heavy chain, 25.3 kDa for the rituximab light chain and 13.8 kDa for the vNAR. **I)** Fusion of an unrelated vNAR (A5F9V8) to the light chain of rituximab. A band at 55 and 43k Da is visible before MMP-9 cleavage, while after cleavage bands at 55 kDa, 25 kDa and 17 kDa are evident. The calculated mass is 49.3 kDa for the rituximab heavy chain and 38 kDa for the A5F9V8 rituximab light chain fusion. The calculated masses after cleavage are 23.4 kDa for the rituximab light chain and 14.6 kDa for the vNAR. **J)** Verification of vNAR removal *via* protein A purification and extensive washing with PBS pH 6.0. For all three samples, bands at 55 and 25 kDa are evident. The calculated mass is 49.3 kDa for the rituximab heavy chain, 23.1 kDa for the unmodified rituximab light chain and 23.4 kDa for the light chains after cleavage. **K)** Analysis of ARV9 PLGLA protease stability upon incubation without a protease, with uPA, matriptase and MMP-9 as well as non-cleaved ARV9 G4S7. For ARV9 PLGLA without protease, incubated with uPA, matriptase and ARV9 G4S7 bands at 55 and 43 kDa are evident. ARV9 PLGLA treated with MMP-9 exhibits bands at 55, 25 and 17 kDa. The masses for the ARV9 PLGLA before and cleavage are mentioned above. The calculated mass for the ARV9 G4S7 light chain is 37.7 kDa. **L)** AGS and PLGLA linker fused to the light chain of rituximab. For both samples bands at 55 and 25 kDa are evident. The calculated mass for the rituximab heavy chain is 49.3 kDa, while the size of the light chain is 23.5 kDa for the AGS linker control and 25.5 kDa for the PLGLA linker control.

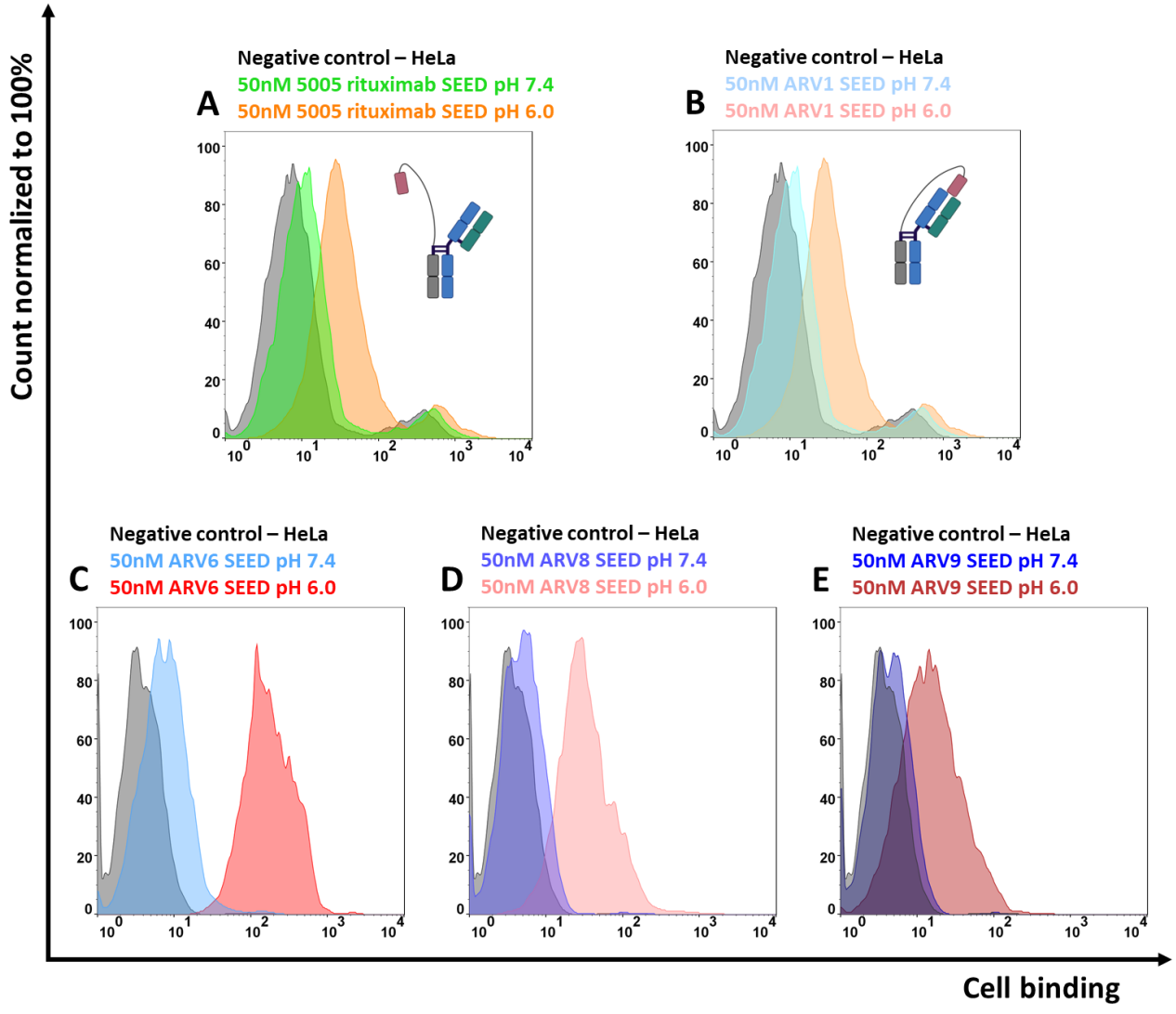

Figure S 9: Off-target cell binding of rituximab SEED constructs on CD20 negative HeLa cells. Cell binding is shown in the x-axis, while the normalized count is depicted on the y-axis. The negative control in all graphs is shown in black. **A)** Off-target cell binding of the 5005 rituximab SEED construct under neutral (green) and acidic (orange) conditions. **B)** Off-target cell binding of the ARV1 rituximab SEED construct under neutral (cyan) and acidic (light orange) conditions. **C)** Off-target cell binding of the ARV6 rituximab SEED construct under neutral (light blue) and acidic (red) conditions. **D)** Off-target cell binding of the ARV8 rituximab SEED construct under neutral (blue) and acidic (light red) conditions. **E)** Off-target cell binding of the ARV9 rituximab SEED construct under neutral (dark blue) and acidic (dark red) conditions.

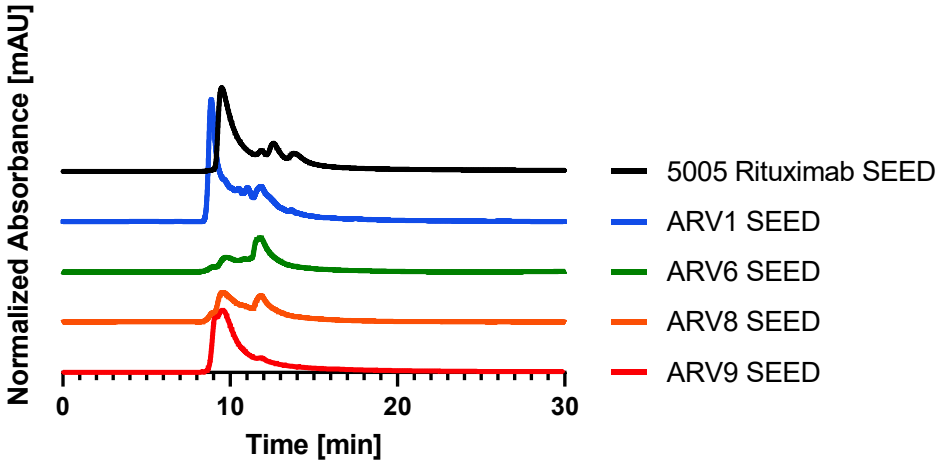

Figure S 10: Analytical size exclusion chromatography of rituximab SEED constructs. The time in minutes is shown on the x-axis, while the normalized absorbance is displayed on the y-axis. The different constructs are depicted in different colors.

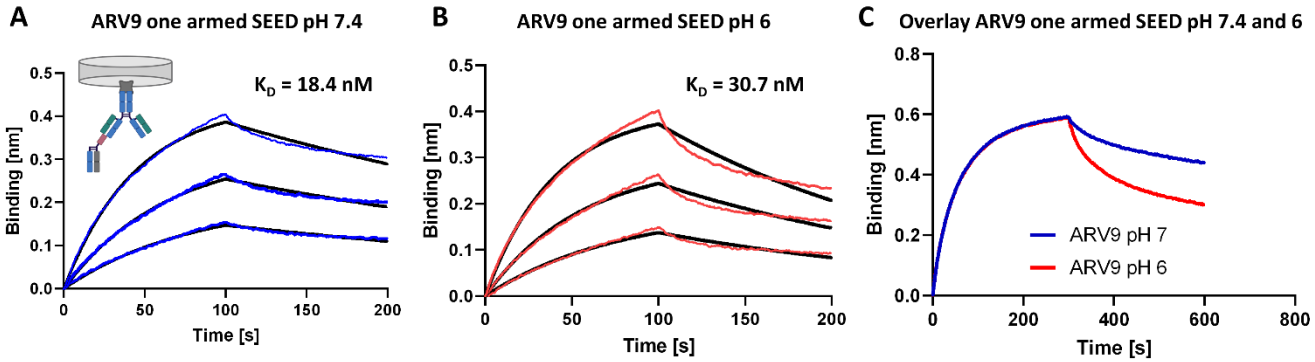

Figure S 11: Binding kinetics of ARV9 under neutral and acidic conditions. The time in seconds is shown on the x-axis, while the binding in nm is depicted on the y-axis. **A)** The binding curves under neutral conditions are shown in blue, while fits for K_D determination are shown in black. **B)** The binding curves under acidic conditions are shown in red, while fits for K_D determination are shown in black. **C)** Overlay between ARV9 binding under neutral and acidic conditions to emphasize differences in dissociation.

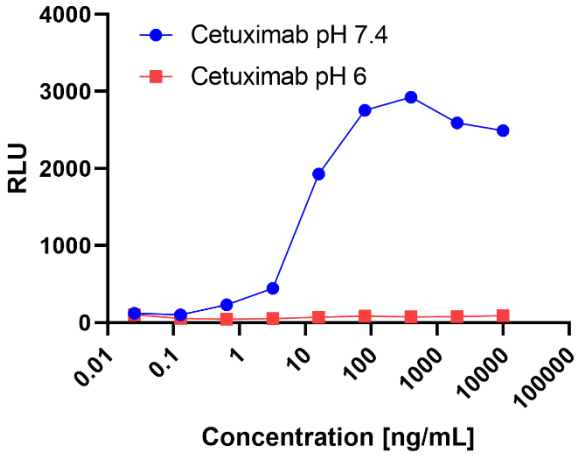

Figure S 12: ADCC reporter assay of cetuximab in HeLa cells at pH 7.4 and 6.0. Relative luminescence units are depicted on the y-axis, while the concentration in ng/mL is shown on the x-axis. RFU of cetuximab at pH 7.4 are displayed by the blue dots and curve, while RFU of cetuximab at pH 6 is represented by the red dots and curve. While cetuximab at pH 6.0 reveals no increase of RFU even at the highest concentration, cetuximab at pH 7.4 shows maximal RFU at 400 ng/mL.

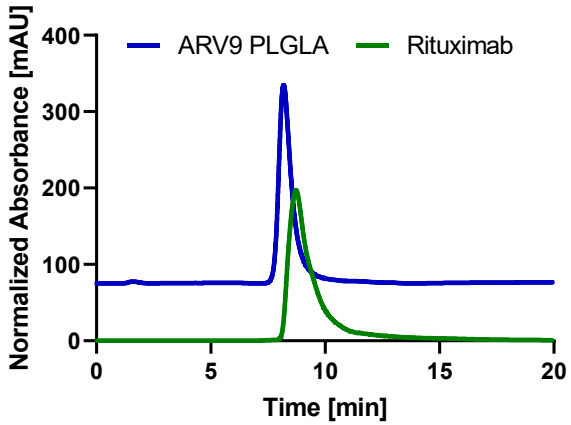

Figure S 13: Analytical SEC analysis of ARV9 PLGLA and rituximab. The rituximab sample is shown in green and reveals a single peak in the range of five to ten minutes. The sample containing ARV9 PLGLA is displayed in blue and exhibits a single peak in the range of five to ten minutes.

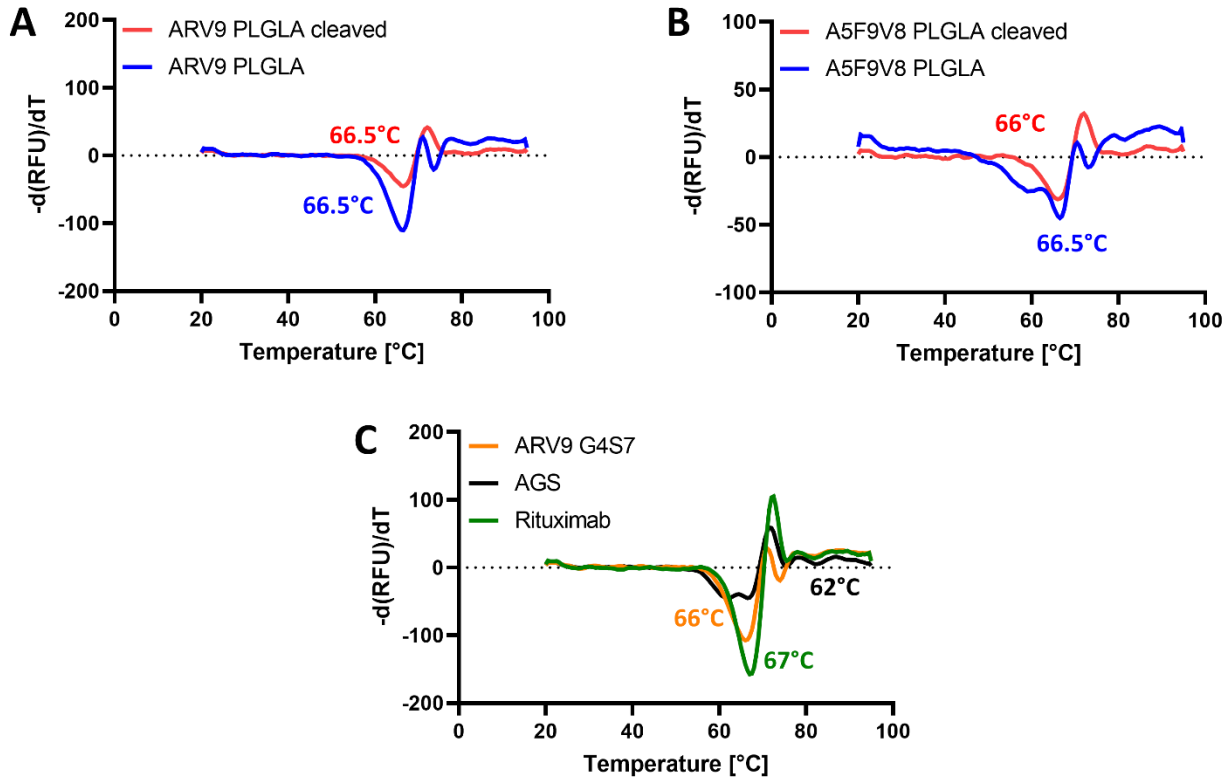

Figure S 14: Melting point analysis of different light chain fusions. The temperature is depicted on the x-axis, while the derivative of fluorescence decrease is shown on the y-axis. **A)** Melting point analysis of ARV9 PLGLA in the non-cleaved and cleaved state with the vNAR removed by protein A chromatography. The red curve represents the derivative of fluorescence decrease for the cleaved and purified sample with a minimum between 60 and 80 °C, while the blue curve displays the derivative of fluorescence decrease for the non-cleaved sample with a minimum between 60 and 80 °C. **B)** Melting point analysis of A5F9V8 PLGLA in the non-cleaved and cleaved state with the vNAR removed by protein A chromatography. The red curve represents the derivative of fluorescence decrease for the cleaved and purified sample with a minimum between 60 and 80 °C, while the blue curve displays the derivative of fluorescence decrease for the non-cleaved sample with a minimum between 60 and 80 °C. **C)** Melting point analysis of ARV9 G4S7, AGS and rituximab in the. The orange curve represents the derivative of fluorescence decrease for ARV9 G4S7 with a minimum between 60 and 80 °C, while the black curve displays the derivative of fluorescence decrease for the AGS sample with a minimum between 60 and 80 °C. The derivative of fluorescence decrease for rituximab is shown in green, with a minimum between 60 and 80 °C.

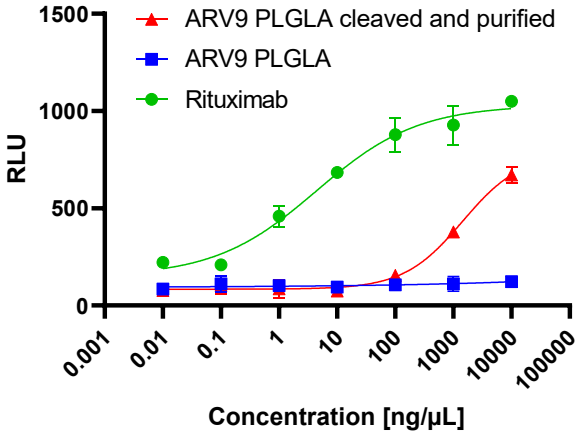

Figure S 15: ADCC reporter assay on Raji cells of rituximab and ARV9 PLGLA construct in the uncleaved as well as cleaved a purified state. Relative luminescence units are depicted on the y-axis, while the concentration in ng/mL is shown on the x-axis. RLU of rituximab are depicted by the green dots and line. The signal of rituximab reveals a sigmoidal curve with plateaus at low and high concentrations. RLU signal of ARV9 PLGLA in the uncleaed as well as cleaved and purified state are displayed in blue and red respectively. While ARV9 PLGLA in the uncleaved state reveals no signal increase, ARV9 PLGLA post cleavage and purification display a signal increase at higher concentrations.

8.5 Supplementary figures and tables for the A6 TCR project

Table S 5: Amino acid sequence alignment of anti-A6 TCR vNARs (AA6Vs) 1,2, 9 and 10. Positions with high consensus are shown in red, whereas positions in blue represent low consensus. Positions indicated in black, reveal no consensus.

Clone	Sequence
AA6V1	MAARLEQTPTTTTKEAGESLTINCVLKGSDYVLGITYWYFTKKGATKKAGLSTGGRYSDTKNTASKSFSLRISDLGVEDSGTYHCIAYSRAGMTRNCGY----IEGGGTILTVK
AA6V2	MAARLEQTPTTTTKEAGESLTINCVLKGSGYGLGKTYWYFTKKGATKKARLSTGGRYSDTKNTASKSFSLRISDLRVEDSGTYHCEAIPYHKLHHRHHNKDHHIEGGGTLVTVN
AA6V9	MAARLEQTPTTTTKEAGESLTINCVLKGSGYGLGITYWYFTKKGATKKASLSTGGRYSDTRNTASKSFSLRISDLRVEDSGTYHCEAWAWDRQNHGFFH----IEGGGTTLTVN
AA6V10	MAARLEQTPTTTTKEAGESLTINCVLKGSGYGLGRTYWYFTKKGATKRASLSTGGRYSDTKNTASKSFSLRISDLRVEDSGTYHCEARHYQWNMQHMYWWLHPIEGGGTLVTVN

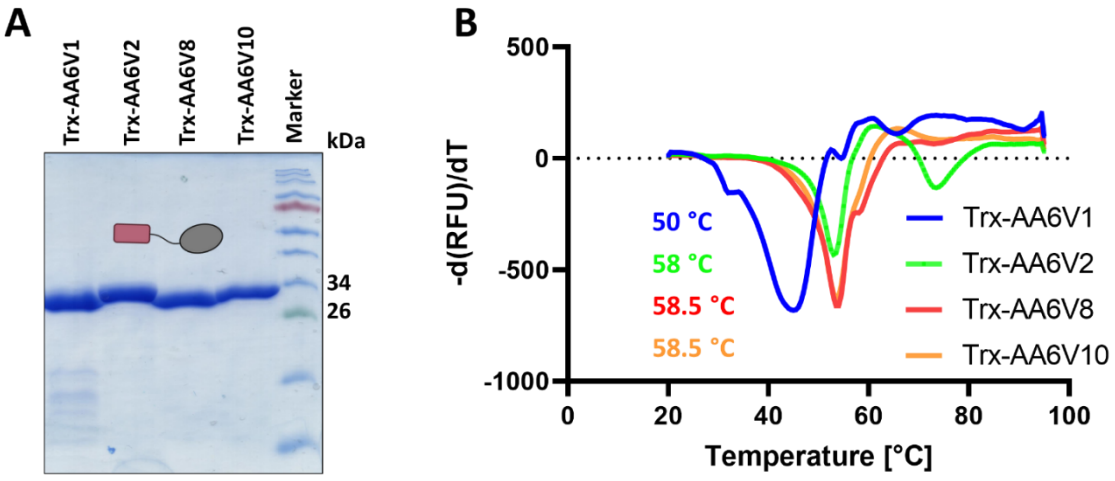

Figure S 16: Analysis of anti-A6 TCR vNAR thioredoxin fusion by reducing SDS-PAGE and thermal shift assay. A) Reducing SDS-PAGE of the anti-A6 TCR thioredoxin fusions. All constructs display a band between 26 and 34 kDa (Calculated mass: Trx-AA6V2: 31 kDa, Trx-AA6V8: 30.4 kDa, Trx-AA6V10: 31.2 kDa). **B)** Melting point analysis of anti-A6 vNARs thioredoxin fusions. The y-axis of the graphs displays the derivative of fluorescence decrease, while the x-axis shows the temperature. Melting curves and melting points of AA6V2, AA6V8 and AA6V10 are shown in blue, green, red and orange respectively.

8.6 Supplementary figures and tables for the 6G11 project

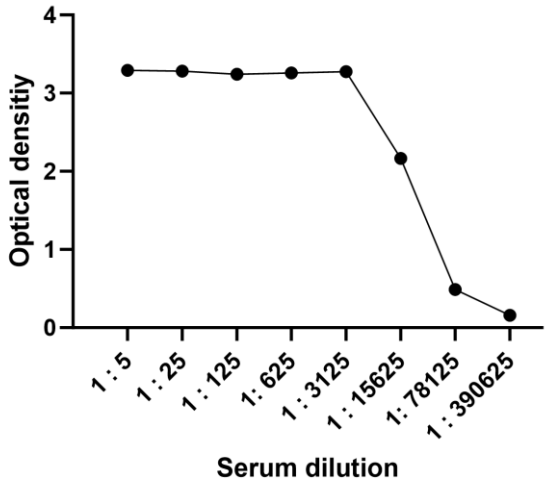

Figure S 17: Titer curve of the chicken immunized with 6G11 scFv. The serum after the fourth immunization was analyzed in an ELISA-based assay with different serum dilutions. The optical density displays a plateau until five consecutive 1:5 dilutions. Afterwards the optical density decreases for the next three dilutions.

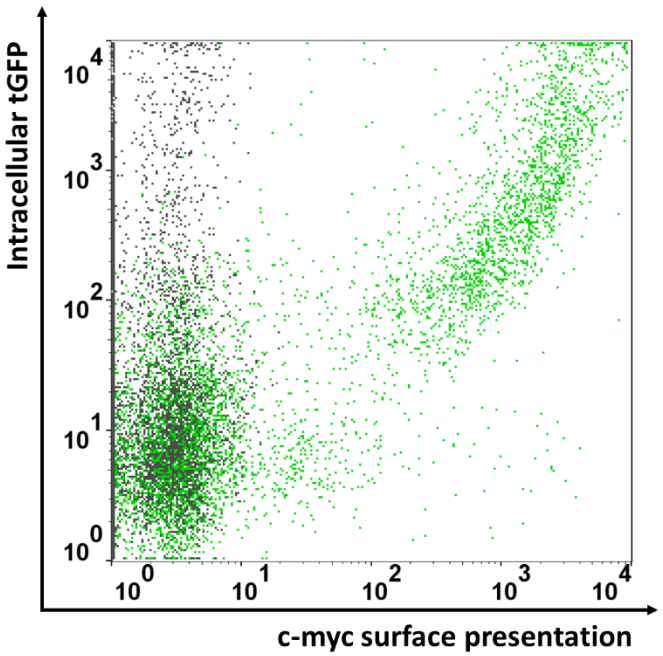

Figure S 18: Correlation between intracellular tGFP signal and c-myc surface presentation. The cells depicted in the dot plots are gated on viable and single cells. The sample incubated without the anti-c-myc antibody is shown in black, while the sample incubated with the anti-c-myc antibody is depicted in green. Intracellular tGFP signal and c-myc surface presentation correlate over a wide range. Correlation in high tGFP expressing cells with c-myc surface presentation is moderate.

Table S 6: Amino acid sequence alignment of A6G11S2B and A6G11S2NC V_H and V_L domains. Positions with high amino acid consensus are shown in red, low consensus is displayed in blue and neutral positions are depicted in black.

Clone	Sequence
A6G11S2B VH	ASAVTLDESGGGLQTPGGGLSLVCKASGFTFSSYSMVWVRQAPSKRLEWVAGIYSSATWTYYAPAVKGRATISRDNGQSTVRLQLNDLRAEDTGTYFCAKTSRSGWTAYSASAIDAWGHGTEVIV
A6G11S2NC VH	ASAVTLDESGGGLQTPGGGLSLVCKASGFSFSDRGMQWVRQAPGKGLEWVAGIDDDDNNTWYATAVKGRATISRDNGQSTVRLQLNSLRAEDTGTYYCAKTPTSYY--WGAAEIDAWGHGTEVIV

Clone	Sequence
A6G11S2B VL	ALTQPSSVSANPGETVKITCSGGSSYYGWYQQKSPGSAPVTVIYSNDKRPSDIPSRFSGSTSGSTATLTITGVQADDEAVYFCGGYDSNIHGGIFGAGTTLTVL
A6G11S2NC VL	ALTQPSSVSANPGETVKITCSGSSGSYGWYQQKAPGSAPVTVIYDNNNRPSNIPSRFSGSLSGSTNTLTITGVQADDEAVYFCGSYEGSSYVGIFGAGTTLTVL

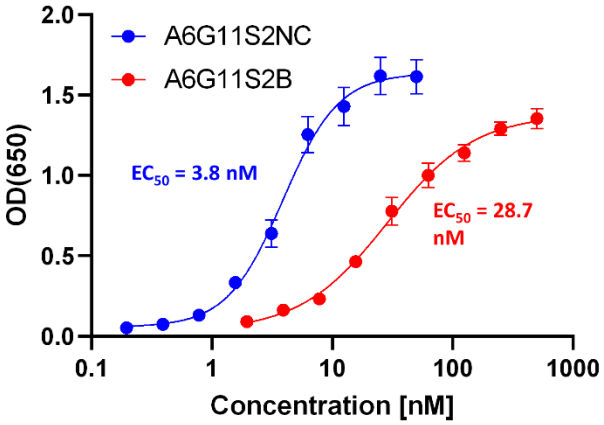

Figure S 19: EC_{50} determination of A6G11S2B and A6G11S2NC *via* ELISA. The optical density at 650 nm is shown in the y-axis, while the concentration is depicted on the x-axis. Binding curves of A6G11S2B and A6G11S2NC are displayed in red and blue respectively. EC_{50}s are indicated in the color of the respective scFv.

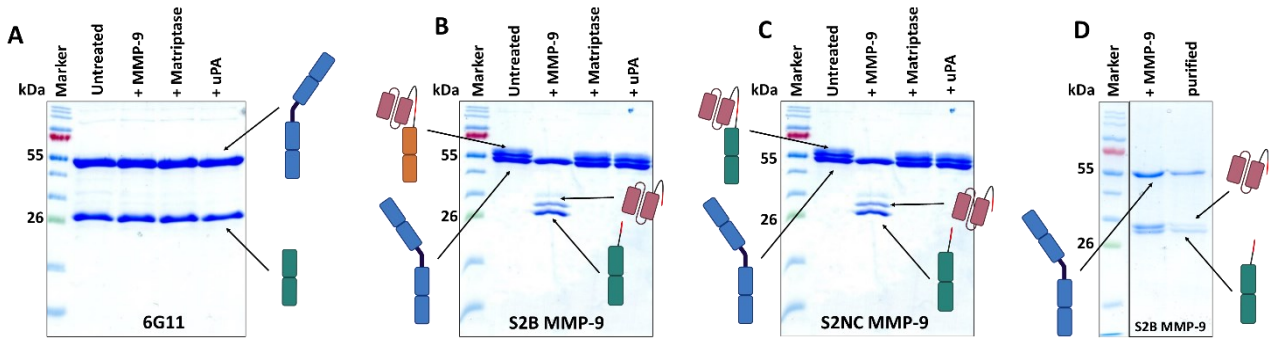

Figure S 20: SDS-PAGE of protease stability testing of 6G11, A6G11S2B and A6G11S2NC light chain fusions. Each construct was incubated over night at 37 °C with either no protease, MMP-9, matriptase or uPA. **A)** Incubation of 6G11 with different proteases. The expected size for the untreated sample is 49.4 kDa for the heavy chain and 23 kDa for the light chain. No matter which protease was used, no cleavage is observed for 6G11. **B)** Incubation of S2B MMP-9 with different proteases. The expected size for the untreated sample is 49.4 kDa for the heavy chain and 50.5 kDa for the light chain. S2B MMP-9 is only cleaved in the presence of MMP-9, while S2B MMP-9 remains intact in the presence of matriptase and uPA. The expected size of the fragments upon cleavage are 26.6 kDa for the scFv fragment and 24 kDa for the light chain fragment. **C)** Incubation of S2NC MMP-9 with different proteases. The expected size for the untreated sample is 49.4 kDa for the heavy chain and 50.3 kDa for the light chain. S2B MMP-9 is only cleaved in the presence of MMP-9, while S2NC MMP-9 remains intact in the presence of matriptase and uPA. The expected size of the fragments upon cleavage are 26.4 kDa for the scFv fragment and 24 kDa for the light chain fragment. **D)** S2B MMP-9 post MMP-9 cleavage and after two purification with the 6G11-based column. The signal intesity of A6G11S2B is about 2-fold decreased compared to the unpurified sample.

8.7 List of figures

8.8 List of tables

8.9 Abbreviations

ADA	Anti-drug-antibody
ADC	Antibody-drug conjugate
ADCC	Antibody-dependent cytotoxicity
ADCP	Antibody-dependent cell-mediated phagocytosis
AID	Activation-induced cytidine deaminase
AKT	Protein kinase B
Ang-2	Angiopoietin-2
APC	Allophycocyanin
APS	Ammonium persulfate
APC	Antigen presenting cell
B ALL	B cell acute lymphoblastic leukemia
BCR	B cell receptor
BiTE	Bispecific T-cell engager
BLI	Biolayer Interferometry
BSA	Bovine serum albumin
C1q	Complement component 1q
CAM	Cell-adhesion molecule
CAR	Chimeric antigen receptor
CD	Cluster of differentiation
CDC	Complement-dependent cytotoxicity
CDR	Complementary determining regions
CEA	Carcinoembryonic antigens
CH	Constant domain heavy chain
CL	Constant domain light chain
CLL	Chronic lymphocytic leukemia
CTLA	Cytotoxic T-lymphocyte-associated protein
c-MET	Hepatocyte growth factor receptor
Da	Dalton
DARPins	Designed ankyrin repeat protein
DC	Dendritic cell
DMEM	Dulbecco´s Modified Eagle´s Medium
DMSO	Dimethyl sulfoxide
DNA	Deoxyribonucleic acid
dsDNA	Double stranded DNA
dsFv	Disulfide-stabilized variable fragment
DTT	1,4-Dithiothreit

dYT	Double concentrated Yeast Tryptone
EBV	Epstein-Barr-Virus
EDTA	Ethylendiaminetetraacetic acid
EGF	Epidermal growth factor
EGFR	Epidermal growth factor receptor
ELISA	Enzyme-linked Immunosorbent Assay
EpCAM	Epithelial cell adhesion molecule
E:T ratio	Effector to target cell ratio
Fab	Fragment antigen binding
FACS	Fluorescence-activated cell sorting
FBS	Fetal bovine serum
Fc	Fragment crystallizable
FcεR	Fc epsilon receptor
FcγR	Fc gamma receptor
FcRn	Neonatal Fc receptor
FDA	Food and drug administration
FITC	Fluorescein isothiocyanate
FOLR1	Folate receptor 1
FR	Framework region
HA	Hemagglutinin antigen
HER2	Epidermal growth factor receptor 2
HIV	Human immunodeficiency viruses
HRP	Horseradish peroxidase
HTLV	Retrovirus-like human T-cell leukemia virus
HV	Hypervariable loop
IFN-γ	Interferon gamma
Ig	Immunoglobulin
IgNAR	Immunoglobulin new antigen receptor
IL	Interleukin
IMAC	Immobilized-metal affinity chromatography
IPTG	Isopropyl-β-D-thiogalactopyranoside
ITAM	Immunoreceptor tyrosine-based activation motif
ITIM	Immunoreceptor tyrosine-based Inhibitory motif
K_D	Equilibrium dissociation constant
LAP	Latency-associated peptide
Lck	Lymphocyte-specific protein-tyrosine kinase
MAPK	Mitogen-activated protein kinase
MCL	Mantle cell lymphoma
MHC	Major histocompatibility complex
MIP-1 α	Macrophage inflammatory protein-1 alpha
MMP	Matrix metalloproteinase
mRNA	Messenger RNA
Nck	Non-catalytic region of tyrosine kinase adaptor protein
NFAT	Nuclear factor of activated T cells
NHL	Non-Hodgkin lymphoma
NK cell	Natural killer cell
NKG2	Natural killer group 2
NM2A	Non-Muscle Myosin 2A
ORF	Open reading frame
PAMP	Pathogen-associated molecular pattern
PCR	Polymerase chain reaction
PD1	Programmed cell death protein 1
PDL1	Programmed cell death protein ligand 1

PE	Phycoerythrin
PAGE	Polyacrylamide gel electrophoresis
PBS	Phosphate buffered saline
PEG	Polyethylene glycol
PEI	Transporter 5™ Transfection Reagent
PI3K	Phosphoinositide 3-kinase
PPR	Pattern recognition receptor
PTCL	Peripheral T cell lymphoma
P/S	Penicillin-Streptomycin
RAC	Radioisotope antibody conjugate
RBC	Red blood cell
RLR	Rig-I-like receptor
rpm	Round per minute
RPMI medium	Roswell Park Memorial Institute medium
RNA	Ribonucleic acid
SB	Super Broth
scFv	Single-chain fragment variable
SEC	Size exclusion chromatography
SDS	Sodium dodecyl sulfate
SEED	Strand-exchange engineered domain
SIRPα	Signal regulatory protein alpha
T ALL	T cell acute lymphoblastic leukemia
TCR	T cell receptor
TdT	Terminal desoxyribonucleotidyl transferase
TGF	Transforming growth factor
tGFP	Turbo green fluorescent protein
TH	T helper cell
TIMP	Tissue inhibitors of MMP
TKR	Tyrosine kinase receptors
TEMED	Tetramethylethylenediamine
TNF	Tumor necrosis factor
TNFSF11	Tumor necrosis factor superfamily member 11
TLR	Toll-like receptor
TRIS	Tris-(hydroxymethyl)-aminomethane
uPA	Urokinase
VEGF-A	Vascular endothelial growth factor A
VH	Variable domain heavy chain
VHH	Variable domain of heavy chain only antibody
VL	Variable domain light chain
vNAR	Variable domain new antigen receptor
v/v	Volume per volume
w/v	Weight per volume

8.10 Danksagung

An dieser Stelle möchte ich mich bei allen Personen bedanken, ohne deren Unterstützung diese Arbeit nicht möglich gewesen wäre. Folgenden Personen gilt besonderer Dank:

An erster Stelle möchte ich **Prof. Dr. Harald Kolmar** für die Möglichkeit danken, meine Doktorarbeit in seiner Arbeitsgruppe anzufertigen. Ein besonderer Dank für deine Unterstützung, dein offenes Ohr und die Motivation die du in unseren Gesprächen immer wieder neu geweckt hast. Du hattest immer eine neue und hilfreiche Idee, egal wie verfahren manches Projekt auch war. Für die Freiheit und Entfaltungsmöglichkeiten während meiner Promotion möchte ich dir ganz besonders danken. Ebenso für die breite methodische Ausbildung, die ich genießen durfte und die ich nicht missen möchte. Du hast neue Ideen und Lösungskonzepte nach Kräften unterstützt und ich freue mich auch in Zukunft auf das ein oder andere Projekt, was wir noch zusammen bearbeiten. Vielen Dank Harald!

Prof. Dr. Evelyn Ullrich möchte ich für die Übernahme des Korreferats danken. Ebenso für die herzliche Aufnahme in deine Arbeitsgruppe, in der ich bereits viel lernen durfte, sowie deine Geduld während der Fertigstellung dieser Arbeit und deine Unterstützung in der gesamten Zeit. Ich freue mich sehr auf unsere zukünftigen Projekte.

Prof. Dr. Dr. Siegfried Neumann möchte ich für die spannenden Gespräche, einen Einblick in einen riesigen Erfahrungsschatz, sowie die Übernahme des ersten Fachprüfers danken.

Prof. Dr. Viktor Stein möchte ich für die Übernahme der Rolle des zweiten Fachprüfers danken.

Prof. Dr. Michael Reggelin danke ich für die Übernahme des Prüfungsvorsitzes.

Vielen Dank auch an **Dr. Andreas Christmann** für die Unterstützung, wenn das FACS einmal wieder Probleme gemacht hat. Beim troubleshooting durfte ich viel von dir lernen.

Ein Dank auch an **Philipp Wendel** für die Neuerstellung der Jurkat A6 TCR Zelllinie und deiner riesigen Unterstützung während deinem Praktikum. Weiterhin möchte ich dir Dank aussprechen für die bisherige Unterstützung und alles, was ich von dir lernen durfte.

Vielen Dank auch an die Praktikanten, Bachlor- und Masterstudenten, die ich betreuen durfte: **Philipp Wendel, Monika Gnatzy, Daniel Schäfer, Darius Zibulski, Gianluca Pohl, Simon Reiners, Philipp Uhl und Sven Gutzeit**. Vielen Dank für eure fleißige Unterstützung bei meinen Projekten.

Ein besonderer Dank geht an **Dominic Happel** für die gemeinsame Arbeit am 6G11 Projekt auch nach Beendigung meiner Laborzeit, ohne deine Unterstützung wäre dieses Projekt nicht so gut gelaufen. Auch für deine Unterstützung über dieses Projekt hinaus und die lustige Zeit im Labor bin ich dir sehr dankbar.

Vielen Dank an **Dr. Ataurehman „Ata“ Ali** und **Dr. Arturo Macarron**. Ohne eure Unterstützung im Labor und die gemeinsam verbrachte Zeit auf der Terrasse, beim Tischkickern und im Büro wären die Tage deutlich langweiliger und weniger lustig gewesen.

Dr. Stefania Carrara möchte ich für die Unterstützung bei allen Fragen zum Thema Zellkultur und der Diskussion von so manchen no mucho bueno Ergebnissen danken.

Ein großer Dank an **Dr. Jan Bogen** für die gemeinsame Laborzeit seit Anfang der Masterarbeit. Vielen Dank für deine Unterstützung mit Rat und Tat bei allen möglichen Projekten und den vielen Diskussionen, aus denen so manches Projekt entstanden ist.

Besonderer Dank gilt auch der Rainbow Six Truppe **Dr. Ata Ali** und **Jorge Romero** für die vielen Abende, die wir im Discord verbracht und uns amüsiert haben.

Vielen Dank an die alte Kickergruppe **Dr. Hendrick Schneider, Dr. Bastian Becker, Dr. Thomas Pirzer, Dr. Lukas „Klaus“ Deweid, Dr. Ata Ali, Dr. Sebastian Bitsch** für die vielen spannenden Spiele, eure Unterstützung und die angenehme Zeit.

Ebenso vielen Dank an die gesammelte Mannschaft vom Arbeitskreis über die ganzen Jahre, ohne euch wäre die Zeit deutlich weniger spannend, lustig und interessant geworden: **Dr. Simon Englert, Dr. Julius Grzeschik, Dr. Benjamin Mattes, Adem Hadjabdelhafid Parisien, Peter Bitsch, Dr. David Fiebig, Dr. Adrian Elter, Carolin Dombrowski, Julia Harwardt, Katrin Schoenfeld, Janna Sturm, Dr. Puyan Rafii, Julia Ettich, Eva Baum, Lara Neureiter, Michael Ulitzka, Sarah Hofmann, Lieke van Gijzel, Dr. Aileen Ebenig, Dr. Anja Hofmann, Dr. Doreen Könning, Dr. Desislava Yanakieva, Dr. Valentina Liebich (geb. Hilberg), Jasmin von Krogh, Susanne Pfaff, Thomas Stipp, Ingo Bork, und Lisa Reinbold.**
Allen nicht aufgeführten Mitgliedern und ehemaligen Mitgliedern des Arbeitskreises danke ich für die gemeinsame Zeit.

Vielen Dank an **Barabra Diestelmann, Dana Schmidt, Janine Becker** und **Cecilia Gorus** für euer unermüdliches Machen und Tun, damit der Arbeitskreis am Laufen bleibt sowie die vielen lieben und aufmunternden Gespräche.

An dieser Stelle ein riesiges Dankschön an meine Freundin **Theresa Landvogt**. Ohne deine Unterstützung seit Beginn des Studiums und ganz besonders während der Doktorarbeit, wäre diese ganze Reise nicht möglich gewesen. Du hast mich immer wieder neu motiviert sowie mir das Durchhaltevermögen und die Kraft gegeben diese Arbeit abzuschließen. Ohne dein Verständnis und deine Hilfe hätte ich das alles nicht geschafft.

Zu guter Letzt, ein riesiges Dankeschön an meine Eltern **Silke** und **Bernd**, meine Schwester **Alina**, sowie den flauschigen Weggefährten **Alpha**, **Freddy**, **Kitty** und **Alberta**. Ohne eure ständige Unterstützung seit Kindesbeinen an und den bedingungslosen Rückhalt auch in schwierigen Zeiten wäre diese Arbeit nicht möglich gewesen und ich würde heute nicht da stehen, wo ich stehe. Ihr habt mir dies alles ermöglicht und dafür bin ich euch unendlich dankbar!

8.11 Affirmations

§8 Abs. 1 lit. c der Promotionsordnung der TU Darmstadt

Ich versichere hiermit, dass die elektronische Version meiner Dissertation mit der schriftlichen Version übereinstimmt und für die Durchführung des Promotionsverfahrens vorliegt.

§8 Abs. 1 lit. d der Promotionsordnung der TU Darmstadt

Ich versichere hiermit, dass zu einem vorherrigen Zeitpunkt noch keine Promotion versucht wurde und zu keinem früheren Zeitpunkt an einer in- oder ausländischen Hochschule eingereicht wurde. In diesem Fall sind nähere Angaben über Zeitpunkt, Hochschule, Dissertationsthema und Ergebnis dieses Versuchs mitzuteilen.

§9 Abs. 1 der Promotionsordnung der TU Darmstadt

Ich versichere hiermit, dass die vorliegende Dissertation selbstständig und nur unter Verwendung der angegebenen Quellen verfasst wurde.

§9 Abs. 2 der Promotionsordnung der TU Darmstadt

Die Arbeit hat bisher noch nicht zu Prüfungszwecken gedient.

Darmstadt, den …….

Jan Habermann